Owner
On Behalf of Kütahya Dumlupınar University
Prof. Dr. Süleyman KIZILTOPRAK (Rector),
On Behalf of Institute of Graduate Studies
Assoc. Prof. Dr. Eray ACAR (Director)

Editorial Board

Journal of Scientific Reports-A started its publication life in 2000 as name of Journal of Science and Technology of Dumlupınar University and is a national peer-reviewed journal published regularly four times a year in March, June, September and December. The language of the journal is English. Articles submitted to the journal are evaluated by at least two referees who are experts in the subject and selected by the editorial board. All articles submitted to the journal are evaluated by the double-blind method. Articles submitted to our journal for review should not be previously published, accepted for publication and in the process of being evaluated for publication in another journal. All responsibility for the articles published in the journal belongs to the author(s).

The journal aims to share scientific studies carried out in the fields of science and engineering at national and international level with scientists and the public. Original research articles, review articles and short notes in science and engineering disciplines are accepted for the journal. Original research articles are expected to contain theoretical and experimental results and should not be published in other journals. In the review articles, it is expected that scientific, technological and current developments on a specific subject are reflected by using an extensive bibliography and made a satisfying evaluation of these. Short notes should be brief writings prepared to announce the first findings of an original study.

Editorial Policy

The journal is open access and the article evaluation period is between 1-2 months.

Advisory Board

JOURNAL OF SCIENTIFIC REPORTS-A
E-ISSN: 2687-6167

CONTENTS

RESEARCH ARTICLES

RESEARCH ARTICLE

Inducing chondrogenic differentiation in ATDC5 cells using a three-dimensional hydrogel with GAG-mimicking properties

Seher Yaylacı[a]*

*[a]Lokman Hekim University, Faculty of Medicine, Department of Medical Biology, Ankara, 06570, Turkey,
ORCID: 0000-0003-3309-2303*

Abstract

This study aims to develop a method using a three-dimensional hydrogel that mimics glycosaminoglycans to accelerate the development of cartilage cells. The hydrogel contains a specific glycosaminoglycan-like peptide sequence with the potential to enhance the effectiveness of chondrogenic differentiation and provide a more efficient approach. In the study, ATDC5 cells were cultured within a synthetic scaffold incorporating peptide amphiphile (PA) nanofibers designed to emulate the structure of glycosaminoglycans in a three-dimensional format for tissue engineering applications. Cellular characterizations were conducted to induce chondrogenic differentiation. ATDC5 cells cultured on GAG-mimicking peptide nanofibers expressed cartilage-specific extracellular matrix components statistically significantly over a 14-day period compared to cells cultured on TCP without insulin induction. Amphiphilic peptide nanofibers offer a valuable approach to replicate glycosaminoglycan properties and support chondrogenic differentiation in ATDC5 cells without the need for growth factors or external stimuli. This approach holds substantial potential for clinical applications in cartilage tissue engineering.
© 2023 DPU All rights reserved.
Keywords: 3D culture; ATDC5 cell; cartilage tissue engineering; GAG-mimicking peptide amphiphile nanofiber;, in vitro chondrogenic differentiation

1. Introduction

The capacity of cartilage tissue to regenerate is restricted because to the absence of blood vessels and nerve supply. Joint degradation can result from acute accidents or degenerative disorders like osteoarthritis. Many approaches, such as tissue engineering, gene therapy, and stem cell therapy, have been studied to support cartilage tissue healing. Scaffold materials, which can be formed from a range of materials including polymers, ceramics, and naturally present extracellular matrix components, are essential to cartilage tissue engineering. These scaffolds facilitate the in vitro culture of cells such as chondrocytes or stem cells, hence promoting the development of

functional cartilage tissue [3–4].

Chondrogenic differentiation is the process by which cells differentiate into cartilage; tissue engineering is particularly interested in this process because it may be applied to repair damaged cartilage. To mimic the environment of natural cartilage more accurately, researchers grew cells in three-dimensional (3D) hydrogels. By transmitting mechanical signals, hydrogels with distinct stiffness and elasticity properties promote chondrogenic growth [5–6]. Peptide-based hydrogels, such as peptide amphiphile nanofibers (PANs), have been investigated for tissue engineering applications; one such application is in progenitor cell chondrogenic development. PANs contain certain peptide groups that are similar to the extracellular matrix of cartilage tissue. One example of this is the induction of chondrogenic cell development in ATDC5 cells with the application of a PAN containing the RGDS peptide sequence present in multiple ECM proteins [7]. One promising strategy for promoting chondrogenic growth would be the application of a hydrogel made of certain peptides, such as sulfated glycosaminoglycans. The structure and activities of naturally occurring glycosaminoglycans in the extracellular matrix of cartilage tissue can be mimicked by a peptide sequence. Chondrogenic differentiation and cartilage tissue regeneration can be enhanced by the application of growth factors, peptide sequences, and appropriate mechanical stimulation [8–10]. In our study we aim to induce chondroprogenitor ATDC5 cells through peptide amphiphile nanofibers without the requirement for external stimulation.

2. Experimentals

2.1. Materials

Lauric acid and DIEA had been supplied by Merck, whereas amino acids and HBTU were obtained from NovaBiochem for the synthesis of PA. All the cell consumables had been supplied by Nest Scientific USA Inc. and Biological Industries (Kibbutz Beit Haemek), and ATDC5 cells were contributed.

2.2. Synthesis of PAs

Three PA molecules (E-PA, K-PA, and GAG-PA) were synthesized using solid-phase Fmoc chemistry. Different resin molecules were employed for each PA molecule. The synthesis steps were executed as detailed in the literature [11]. Following synthesis, the PA molecules underwent purification via an HPLC system. Both PAs were synthesized achieving a purity exceeding 95%. The evaluation of purity was conducted based on the amide content, as determined by absorbance measurements at 220 nm. A common benchmark is that peptide purity, particularly for bioactive peptides, should be above 95% when used in biological assays to ensure that the observed effects are due to the peptide itself and not impurities. An Agilent LC-MS system was utilized for ascertaining the molecular mass and purity of the PAs. Purity was assessed at 220 nm relative to peptide content. One percent solutions of all PA molecules were prepared in a 1:1 (v/v) ratio. The synthesized nanofibers were dried in ethanol at increasing concentrations for the initial ten minutes and subsequently dried using a Tourismis Autosamdri critical dryer.

2.3. Formation of 3-Dimensional peptide hydrogels and cellular viability

To generate 3D peptide hydrogels, E-, K-, and GAG-PA solutions were combined in HEPES buffer at a concentration of 10 nM and a volume of 100 µl. A micro mass culture technique was employed to facilitate chondrogenic differentiation, simulating the three-dimensional cellular interactions occurring during embryogenesis. The cell solution was prepared using K-PA and mixed with 10 nM PA solutions (E- or GAG-PA) in cell culture wells, resulting in a cell-hydrogel composite. In this study, 5×10^6 cells were used per 100 µl of hydrogel, consistent with acceptable ranges established in prior research. Following 3D cell culture formation, cells were incubated for two weeks in a growth media, with media changes occurring every 48 hours. Cellular viability was assessed for

three days using an MTT kit from Roche (catalogue number 11465007001), in accordance with the kit's manual. MTT reagent (0.5 mg/ml) was added to each well. Plates were kept in the dark for four hours before the addition of a solubilization solution to dissolve the formazan crystals. The absorbance was quantified at a wavelength of 570 nm utilizing a BioTek Synergy H1 microplate reader.

2.4. Observing the production of glycosaminoglycans

Post 14-day incubation, hydrogels were fixed in 4% paraformaldehyde for 48 hours at 4°C, dehydrated in ethanol, and cleared in xylene. Resulting samples were sectioned into 5 µm slices using a microtome (Leica RM2125 RTS). Safranin-O and Fast Green were employed for glycosaminoglycan visualization, while Mayer's Hematoxylin and Eosin were used for general staining. Immunohistochemical staining was performed on slides using an antigen retriever (Sigma, C9999) to expose the epitopes. Slides were subsequently blocked and incubated overnight with primary antibodies for Collagen II (Abcam, ab34712). After thorough washing, a secondary antibody (Merck, AP124C) was applied to detect primary antibodies. Finally, cells were washed and analyzed under a fluorescence microscope (ZEISS LSM 510).

2.5. Statistical analyses

All variables were analyzed by calculating their mean and standard error (SEM). A non-parametric Suduki comparison test was employed to evaluate differences between experimental groups. Statistical significance was determined based on p-values less than 0.05. All calculations were performed using GraphPad Prism (San Diego, CA, USA).

3. Results and discussion

The synthesis of both peptide amphiphiles (PAs) resulted in a purity greater than 95%. Purity assessments were performed by quantifying the amide bond content, utilizing absorbance readings at the 220 nm wavelength. It is widely recognized in bioactive peptide research that a purity threshold of 95% is critical for biological assays, as it ensures that the peptides' biological activity is not compromised by contaminating substances. In this study, two distinct 3-dimensional hydrogel environments were generated for culturing ATDC5 cells. The first hydrogel, termed GAG-H, was synthesized by mixing GAG-PA and K-PA at neutral pH and room temperature. The hydrogel designated as Cntrl-H was developed by mixing E-PA with K-PA in a similar set of conditions (refer to Figure 1. Our research introduces peptide frameworks designed to imitate natural glycosaminoglycans (GAGs). This imitation is achieved by producing extended nanofibers adorned with repetitive chemical groups such as carboxylate, hydroxyl, and sulfonate. The GAG-PA peptide used in our study encompasses all these group types, effectively mimicking the characteristics of sulfonated glycosaminoglycans. We've named this peptide focusing on its sulfonate component to distinguish it from other peptides in our research. Scanning electron microscopy revealed that the resultant nanofiber structure closely resembled the natural extracellular matrix in terms of fibril width and porosity (Figure 1d). The purity and efficacy of the synthesized peptides were confirmed through liquid chromatography and mass spectrometry (Figures 1b and 1c). To initiate nanofiber formation, K-PA, a positively charged peptide amphiphile, was employed. The nomenclature of these molecules is based on the charged amino acid residue present at the C-terminus (see Figure 1).
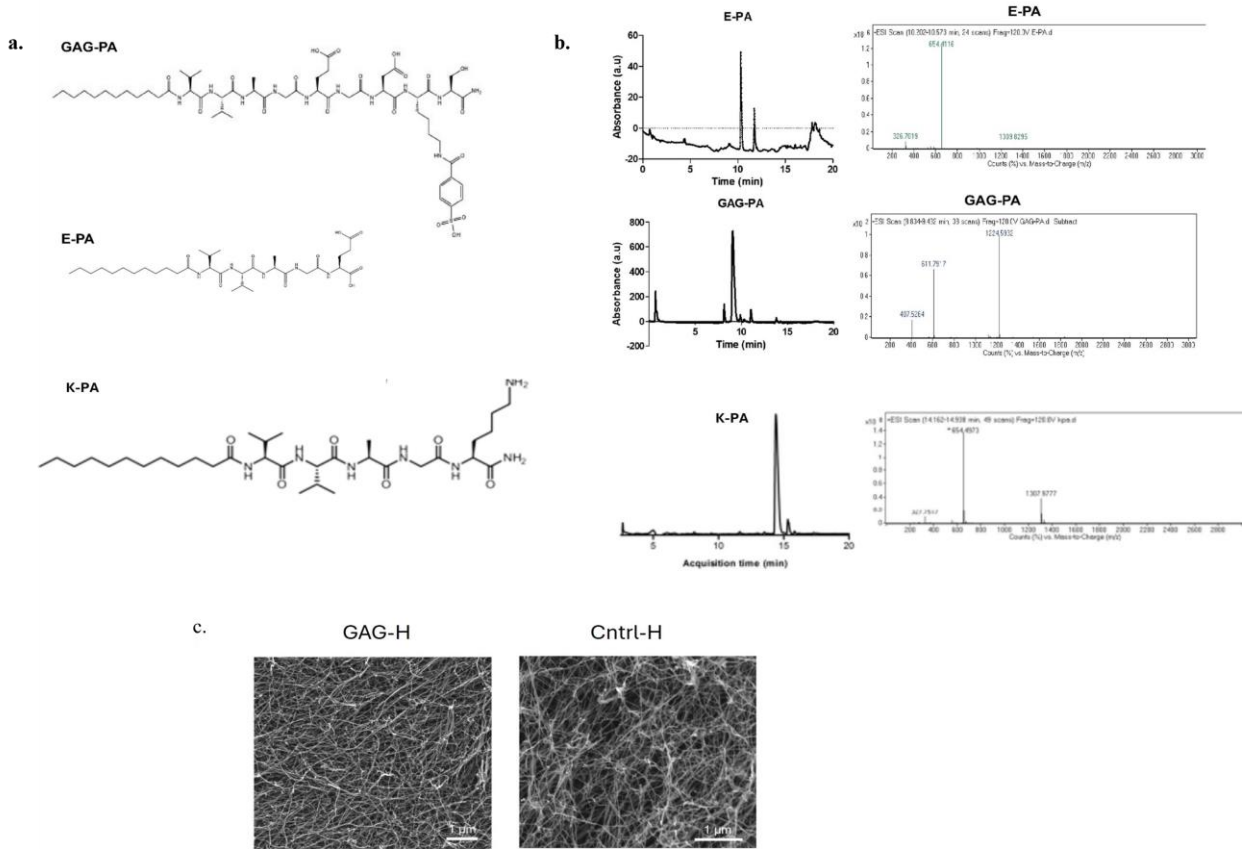
Fig. 1. (a) Chemical representation of PA molecules used in the study. (b) Liquid Chromatogram and (c) Mass Spectroscopy results of PAs. (d) Scanning Electron Microscopy images of PA nanofibers.

Initial cellular viability assessments were conducted on ATDC5 cells cultured in GAG-H and Cntrl-H hydrogels for a period of 3 days. The findings indicated that the hydrogels did not adversely affect ATDC5 cells in contrast to those cultivated on tissue culture plastic (TCP) in a micro mass culture setting (Figure 2a). 3D culture systems are instrumental in simulating the extracellular environment, thereby enhancing cellular interactions, growth factor deposition, directed differentiation, and the maintenance of differentiated states [12]. After 14 days of static culturing, ATDC5 cells formed distinct clusters within the hydrogels, suggesting cell-cell interactions and aggregation (Figures 2b and 2c). Hematoxylin and Eosin staining corroborated the presence of cellular aggregates in both hydrogels on day 14 (Figures 2d, e, f, and g). Notably, this aggregate formation occurred without the addition of insulin, a key inducer for chondrogenic differentiation in ATDC5 cells. Furthermore, the cells synthesized chondrogenic extracellular matrix (ECM), as evidenced by the deposition of glycosaminoglycans and the expression of Collagen II.

a.
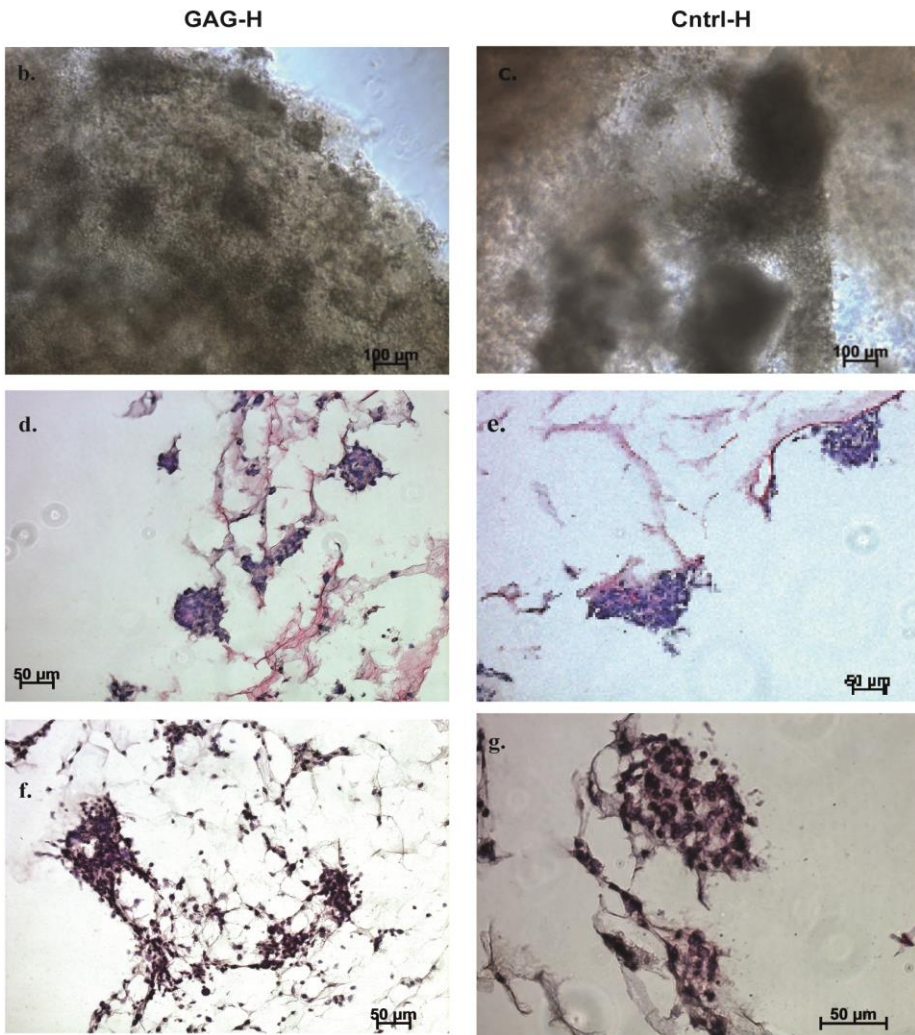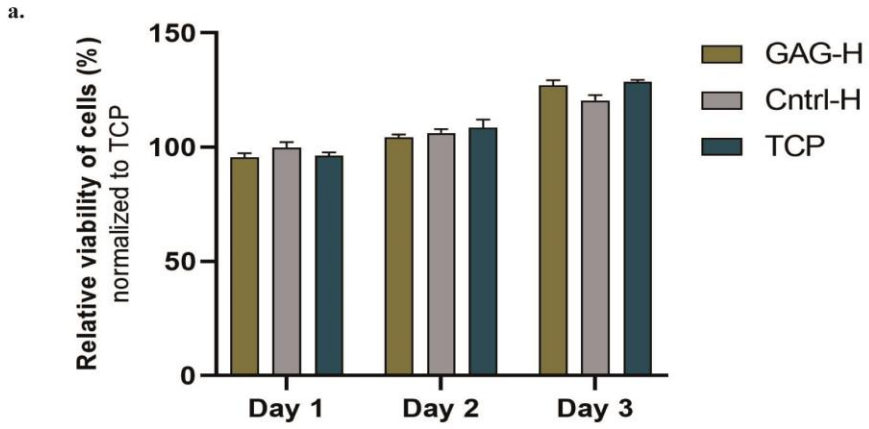
GAG-H

Cntrl-H

Fig. 2. (a) Cell viability on days 1, 2, and 3. (b-c) Comparison of ATDC5 cell behavior in GAG-H and Cntrl-H hydrogels on Day 14. Panels (b-c) display light microscope images of the cells, while panels (d-g) depict aggregate formation using Hematoxylin and Eosin staining in 3D cultures.

Significantly, these outcomes were attained without employing any external inducers, indicating the potential clinical relevance of this approach. Furthermore, the 3D culture system facilitated the formation of aggregates and the synthesis of cartilage-specific proteins, suggesting that the hydrogel environment is conducive to the differentiation of ATDC5 cells into chondrocytes (Figure 3 c-f). Figure 3g shows that the GAG-H gel formulation had a higher GAG/DNA ratio (12.2 ug/ug) and more distinguishable cell aggregates than the Cntrl-H group (8.2 ug/ug). This suggests that the charge and functional groups of the GAG-H hydrogel may play a role in promoting cell-cell interactions and aggregation in terms of chondrogenic differentiation. The analysis of GAG deposition showed faint staining after treatment with chondroitinase (Figure 3a, b), confirming that GAG synthesis occurred in the cells' environment. Overall, these results demonstrate the potential of peptide nanofiber hydrogels as a 3D culture system for differentiating ATDC5 cells into chondrocytes without employing external growth factors or inducers.
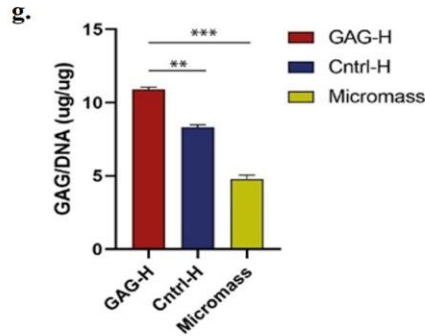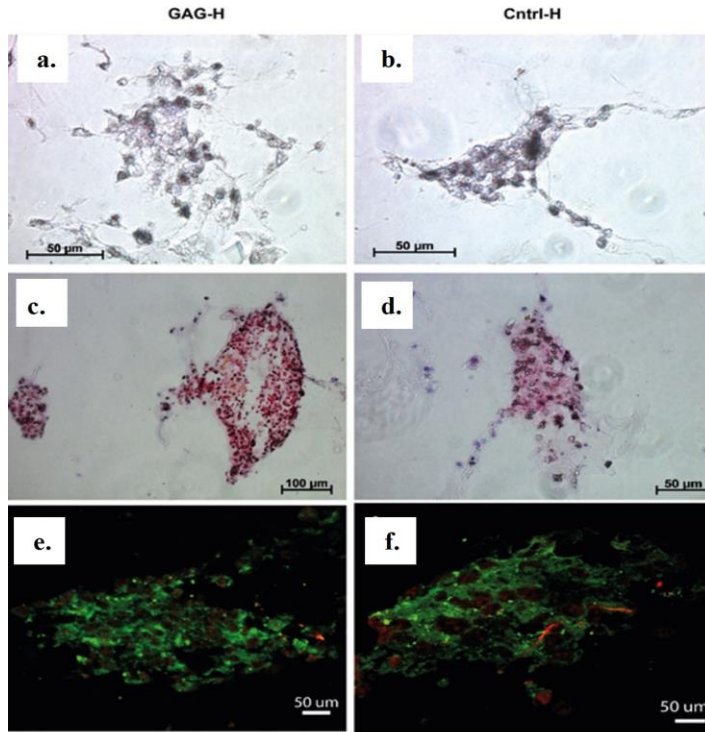
Fig. 3. Characterization of ATDC5 cell behavior in 3D GAG-H and Cntrl-H hydrogels on Day 14. Panels (a-b) and (c-d) show Safranin-O staining with and without chondroitinase treatment, respectively. Panels (e-f) illustrate collagen II staining, (Cy3) and cell nuclei (DAPI-3). (g) GAG/DNA (ug/ug)

The study presented here provides a valuable contribution to the field of tissue engineering by demonstrating the potential of nanofibers that mimic glycosaminoglycans to promote the chondrogenic differentiation of ATDC5 cells. The development of new biomaterials will heavily focus on ECM GAGs, which play a role in various biological functions, including embryonic development, infection, inflammation, wound healing, and cancer. The content and composition of ECM GAGs vary depending on the tissue, age, and pathology [13].

As demonstrated in this study, using synthetic GAG analogues offers a promising approach to address limitations of natural GAGs in hydrogels, such as limited availability, structural heterogeneity, batch-to-batch variability, and

immunogenicity. Several studies focusing on the development of GAG-based hydrogels have examined the use of GAG analogs in tissue engineering. Zhang et al., for instance, used hydrogel to encapsulate chondrocytes for cartilage regeneration, mimicking synthetic hyaluronic acid [14]. Even so, through the manufacture of chondroitin sulfate-mimetic hydrogels, Liu et al. were able to promote chondrogenic development in human mesenchymal stem cells [15]. Kim et al. were mainly looking at how mesenchymal stem cells' chondrogenic development in glycosaminoglycan-based hydrogels was influenced by their type and degree of sulfation. They noticed that the pattern and degree of sulfation had a substantial impact on the synthesis of extracellular matrix and the chondrogenic differentiation of stem cells [16]. Based on these findings, functional groups in GAG-based hydrogels need to be carefully designed and controlled to optimize their ability to promote chondrogenic development. Our study highlights the importance of sulfate/sulfonate groups in a peptide hydrogel as it increases GAG synthesis by ATDC5 cells. Sulfate groups can be incorporated into hydrogels and promote cell differentiation. Recently, Huang et al. conducted a study that fully sulfated sodium cellulose sulfate (NaCS) could be used as a scaffold for cartilage repair. NaCS increases chondrogenesis in human mesenchymal stem cells, which means that cellulose sulfate can be used as a scaffolding material in cartilage tissue engineering [18].

Our study reveals that these nanofibers effectively imitate the functions and properties of glycosaminoglycans. Through integrating amino acid sequences with carboxylate, hydroxyl, and sulfonate groups, we engineered a hydrogel system that fosters chondrogenic differentiation in ATDC5 cells, eliminating the need for external growth factors. Notably, the GAG-H hydrogel with sulfonate surpasses the CNTR-H hydrogel in enhancing chondrogenic cell differentiation. This innovation leads to the development of diverse, multifunctional GAG-like materials, providing a promising alternative to natural GAGs in tissue engineering applications.

4. Conclusion

Our research results demonstrate that adding sulfate/sulfonate groups to peptide hydrogels can increase GAG production and provide a useful substitute for natural GAG products in tissue engineering. Through the development of a hydrogel system that mimics the characteristics of naturally occurring GAGs, we have demonstrated the encouraging potential of these artificial analogs in promoting cell differentiation and extracellular matrix synthesis.

Ethical Approval

Ethical approval for this study was not required. Secondary cell line cultures were utilized in this investigation.

Author Contribution

S.Y. organized and performed all experiments and wrote the manuscript.

Acknowledgements

References

[1] P. B. Lewis, L. P. McCarty, R. W. Kang, B. J. Cole, "Basic science and treatment options for articular cartilage injuries," *J Orthop Sports Phys Ther*, vol. 36, no. 10, pp. 717-727, 2006, doi:10.2519/jospt.2006.2175.
[2] P. J. Boscainos, A. E. Gross, C. F. Kellett, "Surgical options for articular defects of the knee," *Expert Review of Medical Devices*, vol. 4, no. 416, pp. 1-13, doi: 10.1586/17434440.3.5.585.
[3] B. Johnstone, M. Alini, M. Cucchiarini, G. R. Dodge, D. Eglin, F. Guilak, "Tissue engineering for articular cartilage repair – The state of the

art," *European Cells and Materials*, vol. 25, pp. 248-267, 2013.

[4] A. Matsiko, T. Levingstone, F. O'Brien, "Advanced strategies for articular cartilage defect repair," *Materials* (Basel), vol. 6, no. 2, pp. 637-668, 2013, doi:10.3390/ma6020637.

[5] E. B. Hunziker, "Articular cartilage repair: basic science and clinical progress," *Osteoarthritis Cartilage*, vol. 10, no. 6, pp. 432-463, 2002, doi:10.1053/joca.2002.080.

[6] C. Gaissmaier, J. L. Koh, K. Weise, J. Mollenhauer, "Future perspectives of articular cartilage repair," *Injury*, vol. 39, Suppl 1, pp. S114-20, 2008, doi:10.1016/j.injury.2008.01.033.

[7] R. S. Tare, D. Howard, J. C. Pound, H. I. Roach, R. O. C. Oreffo, "ATDC5: An ideal cell line for development of tissue engineering strategies aimed at cartilage generation," *Eur Cells Mater*, vol. 10, no. 22, pp. 2262, 2005.

[8] H. J. Kwon, K. Yasuda, Y. Ohmiya, K. Honma, Y. M. Chen, J. P. Gong, "In vitro differentiation of chondrogenic ATDC5 cells is enhanced by culturing on synthetic hydrogels with various charge densities," *Acta Biomater*, vol. 6, no. 2, pp. 494-501, 2010, doi:10.1016/j.actbio.2009.07.033.

[9] A. K. Kudva, F. P. Luyten, J. Patterson, "In vitro screening of molecularly engineered polyethylene glycol hydrogels for cartilage tissue engineering using periosteum-derived and ATDC5 cells," *Int J Mol Sci*, vol. 19, no. 11, pp. 3341, 2018, doi:10.3390/IJMS19113341.

[10] S. E. Paramonov, H. Jun, J. D. Hartgerink, "Self-assembly of peptide-amphiphile nanofibers: the roles of hydrogen bonding and amphiphilic packing," *J. Am. Chem. Soc,* vol. 11, pp. 7291-7298, 2006.

[11] S. U. Yaylaci, M. Sen, O. Bulut, E. Arslan, M. O. Guler, A. B. Tekinay, "Chondrogenic differentiation of mesenchymal stem cells on glycosaminoglycan-mimetic peptide nanofibers," *ACS Biomater Sci Eng*, vol. 2, no. 5, pp. 871-878, 2016, doi:10.1021/acsbiomaterials.6b00099.

[12] C. Henrionnet, Y. Wang, E. Roeder, et al., "Effect of dynamic loading on MSCs chondrogenic differentiation in 3-D alginate culture," Biomed Mater Eng, vol. 22, no. 4, pp. 209-218, 2012, doi:10.3233/BME-2012-0710.Neves, M. I., Araújo, M., Moroni, L., da Silva, R. M. P., & Barrias, C. C. "Glycosaminoglycan-inspired biomaterials for the development of bioactive hydrogel networks." *Molecules*, 25(4), 978, (2020). doi:10.3390/molecules25040978

[13] M. I. Neves, M. Araújo, L. Moroni, R. M. P. da Silva, C. C. Barrias, "Glycosaminoglycan-inspired biomaterials for the development of bioactive hydrogel networks," *Molecules*, vol. 25, no. 4, 978, 2020, doi:10.3390/molecules25040978.

[14] J. Zhang, W. Liu, L. Schnitzler, et al., "A hyaluronic acid-mimicking hydrogel for the in situ encapsulation of chondrocytes and the promotion of cartilage regeneration," *Biomaterials*, vol. 268, 120546, 2021, doi:10.1016/j.biomaterials.2020.120546.

[15] X. Liu, J. Liang, Y. Li, et al., "Chondroitin sulfate mimetic hydrogels promote chondrogenic differentiation of human mesenchymal stem cells," *Mater Sci Eng C Mater Biol Appl*, vol. 107, 110281, 2020, doi:10.1016/j.msec.2019.110281.

[16] Y. Kim, J. Yoo, H. Kim, K. Kim, D. Kim, G. Kim, "Influence of sulfation pattern and degree on chondrogenic differentiation of mesenchymal stem cells on glycosaminoglycan-based hydrogels," *J Ind Eng Chem*, vol. 90, pp. 314-323, 2020, doi:10.1016/j.jiec.2020.07.027.

[17] J. H. Lee, X. Luo, X. Ren, et al., "A heparan sulfate device for the regeneration of osteochondral defects," *Tissue Engineering Part A*, vol. 25, no. 5-6, pp. 352-363, 2019, doi:10.1089/ten.TEA.2018.0171.

[18] G. P. Huang, A. Molina, N. Tran, G. Collins, T. L. Arinzeh, "Investigating cellulose derived glycosaminoglycan mimetic scaffolds for cartilage tissue engineering applications," *Journal of Tissue Engineering and Regenerative Medicine*, vol. 12, no. 1, e592-e603, 2018, https://doi.org/10.1002/term.2331.

RESEARCH ARTICLE

Thoughts of the February 20, 2023 Defne aftershock

Hatice Durmuş[a]*

[a]Kütahya Dumlupınar University, Engineering Faculty, Department of Geological Engineering, Kütahya. ORCID: 0000-0003-4337-7302

Abstract

On February 6 2023, two large earthquakes with magnitudes of Mw 7.8 (Pazarcık) and Mw 7.6 (Elbistan) occurred consecutively along the East Anatolian Fault Zone in eastern Turkey, causing enormous casualties and heavy damage. This devastating sequence of earthquakes was followed by the Defne aftershock on February 20 near Antakya province, which increased the damage and loss of life. In this study, the teleseismic broadband P velocity waveforms have been inverted in order to obtain the coseismic finite-fault slip distribution of the February 20, 2023 Defne aftershock. It was found that the rupture was controlled by the failure of a single asperity with the largest displacement of approximately 0.75 m, which occurred between 6 and 20 km depth. The source mechanism indicated a dominant left-lateral faulting with a significant normal component and released a total seismic moment of 5.85×10^{18} Nt.m. Coseismic Coulomb stress changes modelling showed that the Defne aftershock rupture was triggered by the earthquake sequence and that the February 6 Pazarcık earthquake had a dominant effect. In the stress modelling carried out on the Dead Sea Fault, the northern segment of the fault remained in the region of significant positive stress loading. Considering the positive stress load over 1 bar created by the earthquake sequence and the Defne aftershock ruptures, as well as the fact that no major earthquake has occurred for more than 600 years, it is clear that the probability of rupture in the northern part has increased significantly and the seismic hazard is high.

1. Introduction

On 6 February 2023, two devastating earthquakes struck south-central Turkey and ruptured the southwestern part of the East Anatolian Fault Zone (EAFZ). The first earthquake was the Mw 7.8 Pazarcık earthquake (at 4:17 am

———————

* Corresponding author:
  E-mail address: hatice.durmus@dpu.edu.tr

GMT), followed by the Mw 7.6 Elbistan earthquake (at 10:24 pm GMT) (Fig. 1). These earthquakes were the largest since the 1939 Erzincan earthquake and were felt across a large part of Turkey, resulting in widespread destruction, loss of life, and economic damage. The earthquakes affected about 450 kilometres from Adana in the west to Diyarbakır in the east and 300 kilometres from Malatya in the north to Syria in the south. It affected eleven provinces, including Kahramanmaraş, Adana, Hatay, Gaziantep, Adıyaman, Diyarbakır, Malatya, Şanlıurfa, Kilis, Osmaniye, and Elazığ, where approximately 13.5 million people reside [1]. In the report published by the Presidency Strategy and Budget of the Republic of Türkiye, it was stated that more than 48 thousand people lost their lives, and more than half a million buildings were destroyed or severely damaged as a result of the earthquakes [2]. According to the World Health Organization's July 2023 report, more than 50,000 people lost their lives, 45.968 in Turkey and 5.900 in Syria, more than 107,000 people were injured, and 3 million people had to leave their homes [3].
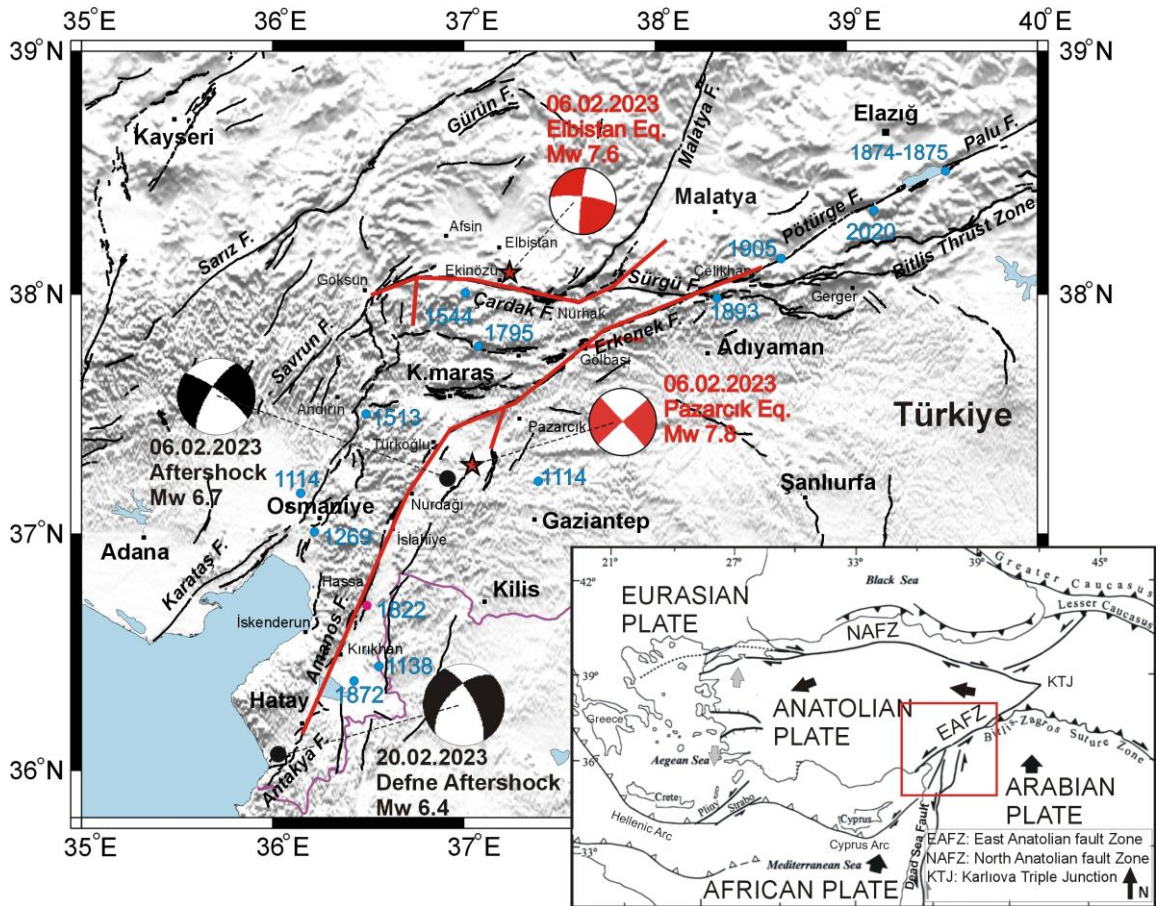
Fig. 1. Major tectonic elements of Turkey (inset) and the seismotectonic of eastern Turkey. Large arrows in the inset map indicate the direction of relative plate motions. The earthquake source mechanisms and epicentres are taken from the catalogue of the Disaster and Emergency Management Authority (AFAD). The active faults are compiled from [4] and [5]. Red lines are surface ruptures of February 6, Pazarcık and Elbistan earthquakes taken from [6]. The map's information was collated from [6-14].

Turkey's main tectonic structures result from the movement between the Arabian, African, Eurasian, and Anatolian plates. In the east, the Arabian Plate converges towards the Anatolian Plate in the northwest direction at a rate 18 mm/year [15, 16] (Fig. 1 inset map). With this convergent movement, the Anatolia was compressed and thickened, and after the compression reached a level that the continental crust could not bear, the Anatolian plate moved westward along two important strike-slip fault systems. [7, 17-19]. The fault systems under consideration are, respectively, the North Anatolian Fault Zone (NAFZ), which exhibits a right lateral strike-slip motion and the East Anatolian Fault Zone (EAFZ), which displays a left lateral strike-slip motion. (Fig.1 inset map). The NAFZ, 1.200 km long, extends from the Karlıova triple junction (KTJ), intersecting with the EAF in the Karlıova region, to the Marmara Sea [20-24] and has a slip rate of approximately 24 mm/year [15, 16, 25]. The EAFZ, on the other hand, extends for about 580 km from the KTJ to the Dead Sea fault in the southwest (Fig. 1). It also has a Northern Branch, which branches off the main fault immediately west of Çelikhan and extends through the Adana Basin to the Mediterranean Sea. (Figs. 1) [5, 24, 26, 27]. GPS studies indicate a slip rate of 9-10 mm/yr for the EAFZ [15, 16, 25], of which about one third is contributed by the Northern Branch after the bifurcation. [10, 26, 28, 29]. Based on data from field studies, a geological slip rate of about 8 mm/yr has also been proposed. [5, 30].

In the 20th and 21st centuries, the NAF was ruptured in a series of earthquakes, beginning with the 1939 Erzincan earthquake and continuing with the 1999 Mw7.9 Izmit and Mw7.2 Düzce earthquakes, which extended as far as the Gulf of Izmit in western Turkey [20, 31, 32]. The historical and instrumental records show that this region has been affected by devastating earthquakes for almost 2,000 years. [20, 33-36]. Significant earthquakes that occurred in the historical period on the segments forming the EAFZ were respectively 29 November 1114 (M> 7.8), 28 March 1513 (M > 7.4), 1822 Antakya Earthquake (M_S= 7.5), 1866 Karlıova-Bingöl Earthquake (M_S = 7.2), 1872 earthquake (M_S = 7.2), 1874 (M_S = 7.1) and 1875 (M_S = 6.7) earthquakes and 2 March 1893 Malatya Earthquake (M_S = 7.1) [37] (Fig. 1). Compared to its activities in the 19th century, the EAFZ was relatively quiet in the 20th century [8, 37]. In the 20th century, the only earthquakes along the EAFZ were the 1905 Malatya and 1971 Bingöl earthquakes. The recent occurrence of the 2003 Bingöl, 2010 Başyurt and 2020 Sivrice-Doğanyol earthquakes and the current occurrence of the 2023 Pazarcık (Mw=7.8) and Elbistan (Mw=7.6) earthquakes suggest that the fault is much more active in the 21st century [14, 39, 40]. Historical earthquakes [8] and Coulomb stress change modelling [38, 41-43] along the EAFZ indicate that the fault segment between Gölbaşı and Türkoğlu creates a seismic gap. At the same time, paleoseismological studies have revealed the existence of a high seismic hazard risk along the southwestern part of the EAFZ after hundreds of years of silence [44]. The data from the trenches that have been dug along the fault indicate that the earthquakes of 1114 and 1513 were the most recent earthquakes to rupture the gap [45]. The 6 February Maraş earthquakes occurred in this seismic gap, which has remained silent for more than 500 years, and the 1114, 1513, 1544 earthquake ruptures and a part of the 1893 earthquake rupture broke again.

Due to the earthquakes, many aftershocks occurred in the region. One of these is the largest aftershock with a magnitude of Mw=6.7, which occurred southwest of the Pazarcık earthquake epicentre, immediately after the 6 February Pazarcık earthquake (Fig. 1). The other is the Defne aftershock with an instrumental magnitude of Mw=6.4, which occurred on February 20, 2023, around Yayladağı (Hatay) at 20.04 local time, two weeks after the February 6 earthquakes. The epicenter of the Defne aftershock is situated on the Antakya Fault Zone [46], a dip-slip normal fault characterised by a left-lateral strike-slip component. This fault zone extends approximately 45 km in length (Fig. 1). Due to this aftershock, 6 people died and 294 people were injured, 18 of them seriously [47]. The hypocentral and source parameters of these earthquakes estimated by different seismological organizations and previous studies given Table 1.

Earthquake sequences that result in large-magnitude events separated by short-time intervals can cause great loss of life and destruction (for example, the 2019 Ridgecrest earthquakes, the 2022 Iran earthquake sequence and the 2022 Taiwan earthquakes). In addition, major aftershocks that occur after the main shock can increase the damage caused by the main shock and cause even greater loss of life and destruction. An example of this is the February 22, 2011 Christchurch earthquake. While no loss of life was observed during the 2011 Christchurch mainshock, 182 deaths occurred due to the devastation that occurred after the aftershock, as the aftershock hypocenter was located

shallower and right under the town of Christchurch [51]. Another example in this context is the November 9, 2011 Edremit aftershock (Mw = 5.7), which occurred after the October 23, 2011 Van earthquake (Mw=7.1) [52, 53]. Although there was relatively little destruction and loss of life in the city centre of Van during the main shock in the 2011 Van earthquake series, the Edremit aftershock particularly affected the city of Van, causing additional destruction and loss of life. The most recent and striking example is the February 6 Pazarcık and Elbistan earthquakes, which occurred in our country. While the occurrence of two major devastating earthquakes 9 hours apart caused great loss of life and damage in a wide area covering 11 provinces, the loss of life and damage increased even more, especially in Hatay province, with the Defne aftershock that occurred two weeks later on February 20. In this context, the fact that two earthquakes occurred within 9 hours and were followed by the Defne aftershock two weeks later makes it valuable to reveal the triggering relationship between these three earthquakes.

It has been suggested that changes in the Coulomb failure stress occur in such a way as to trigger earthquakes [54, 55]. In the past, many crucial studies have been conducted showing that positive Coulomb failure stress plays a role in bringing the fault closer to failure and, therefore, earthquake occurrence, while negative Coulomb failure stress plays a role in delaying subsequent earthquakes [56-68]. In addition, aftershock distribution characteristics can be determined by modelling Coulomb stress changes after the main shock [60, 65, 69-72]. In this context, calculations of the change in Coulomb stress are of great importance for understanding the time-dependent interactions between earthquakes and assessing seismic hazards. In this study, the spatial distribution of the coseismic finite fault rupture of the February 20, 2023, Defne earthquake was obtained, and the triggering effect of the February 6 earthquake sequence (the February 6 Pazarcık earthquake, the largest aftershock and the February 6 Elbistan earthquake) on the rupture of the Defne earthquake was revealed.

Table 1. Various seismological organisations and previous studies have estimated hypocentral and source parameters.

	Lat (°)	Long (°)	Mw	Strike (°) NP1/NP2	Dip (°) NP1/NP2	Rake (°) NP1/NP2	Depth (km)	Max. slip (m)	Seismic Moment (Nt.m)
February 6, 2023, Pazarcık Earthquake									
USGS-NEIC	37.226	37.014	7.8	228/318	89/89	-1/-179	17,5		5.389×10^{20}
GCMT	37.55	37.45	7.8	51/143	70/86	-4/-160	15.1		5.8×10^{20}
KOERI	37.13	37.13	7.7	222/324	64/65	-27/-152	10		3.78×10^{20}
AFAD	37.288	37.043	7.7	233/140	74/77	18/168	8.6		
[46]									6.39×10^{20}
[6]			7.8	43	88	0		9.7	5.62×10^{20}
[48]			7.8					8	5.4×10^{20}
[50]			7.82					9	7.1×10^{20}
[49]			7.8					9	6.51×10^{20}
February 6, 2023, Largest Aftershock									
USGS-NEIC	37.189	36.893	6.7				9.8		
GCMT	37.21	36.84	6.8	212/306	73/78	-13/-163	26.2		1.85×10^{19}
KOERİ	37.2337	36.7805	6.6				5		
AFAD	37.304	36.92	6.6	300/187	70/43	-128/-30	6.2		
February 6, 2023, Elbistan Earthquake									
USGS-NEIC	38.011	37.196	7.5	277/186	78/87	4/168	13.5		2.637×10^{20}
GCMT	38.08	37.22	7.7	264/0	46/83	-9/-136	12		4.53×10^{20}
KOERI	38.05	37.26	7.6	273/6	67/81	-9/-157	10		2.73×10^{20}
AFAD	38.089	37.239	7.6	358/90	73/86	174/13	7		
[46]									3.23×10^{20}
[6]			7.7	261	70	-4		8.1	4.53×10^{20}
[48]								5	3.3×10^{20}
[50]			7.7	282	70	0		10	5.0×10^{20}
[49]			7.6					7	3.64×10^{20}
February 20, 2023, Defne Aftershock									
USGS-NEIC	36.162	36.025	6.3	333/225	69/53	-139/-27	11.5		4.09×10^{18}
GCMT	36.06	36.03	6.3	226/328	42/79	-16/-131	12		4.08×10^{18}

KOERI	36.10	36.13	6.4	330/225	68/56	-143/-25	16		3.63 x10^{18}
AFAD	36.037	36.021	6.4	214/332	57/55	-44/-138	21.73		
[48]			6.4	237	55	12		0.93	
[6]				231	47.5	-0.2		1	
This study				225	53	-27	13.4	0.75	5.85x10^{18}

USGS-NEIC: United States Geological Survey-National Earthquake Information Center; GCMT: Global Centroid Moment Tensor Project; KOERI: Kandilli Observatory and Earthquake Research Institute; AFAD: Republic of Turkey Ministry of Interior Disaster and Emergency Management Authority

2. Finite-fault inversion, model parametrization and results

For the finite-fault analysis of the February 20 Defne aftershock, 21 teleseismic broadband displacement P waveforms recorded by the Global Digital Seismograph Network (GDSN) and obtained from the Incorporated Research Institutions for Seismology (IRIS) were used. The slip distribution model was obtained via the linear finite-fault inversion method, a technique that has been employed for several decades to determine rupture characteristics of earthquakes (see references [73-79] for more detail). In applying the method, a two-dimensional model fault plane is first defined to represent the source of the earthquake (fault length and fault width). This is followed by the division of the model fault plane into subfaults, which enables the spatial distribution of slip to be determined. Accordingly, for the rupture of the Defne aftershock, a single-segment rectangular fault plane of 50 x 25 km^2 was selected and divided into 50 square subfaults (Fig. 2a, along strike 10, along down dip 5). The strike, dip and rake angle of the initial model fault plane were taken as 225°, 53° and -27°, respectively, by considering the source mechanism solutions given in Table 1 and placed within the crustal velocity field. The hypocenter location (36.110°N, 26.062°E) and hypocenter depth (13.4 km) given by the USGS were taken as the starting point of the rupture, and many inversion attempts were made. To simulate rupture front propagation along the model fault plane, 25-point sources were uniformly distributed on each subfaults and point source responses were calculated by applying Generalized Ray Theory [80]. The elastic responses obtained in this way were summed with the appropriate time delay, and artificial seismograms were calculated for each station (Fig. 2b).
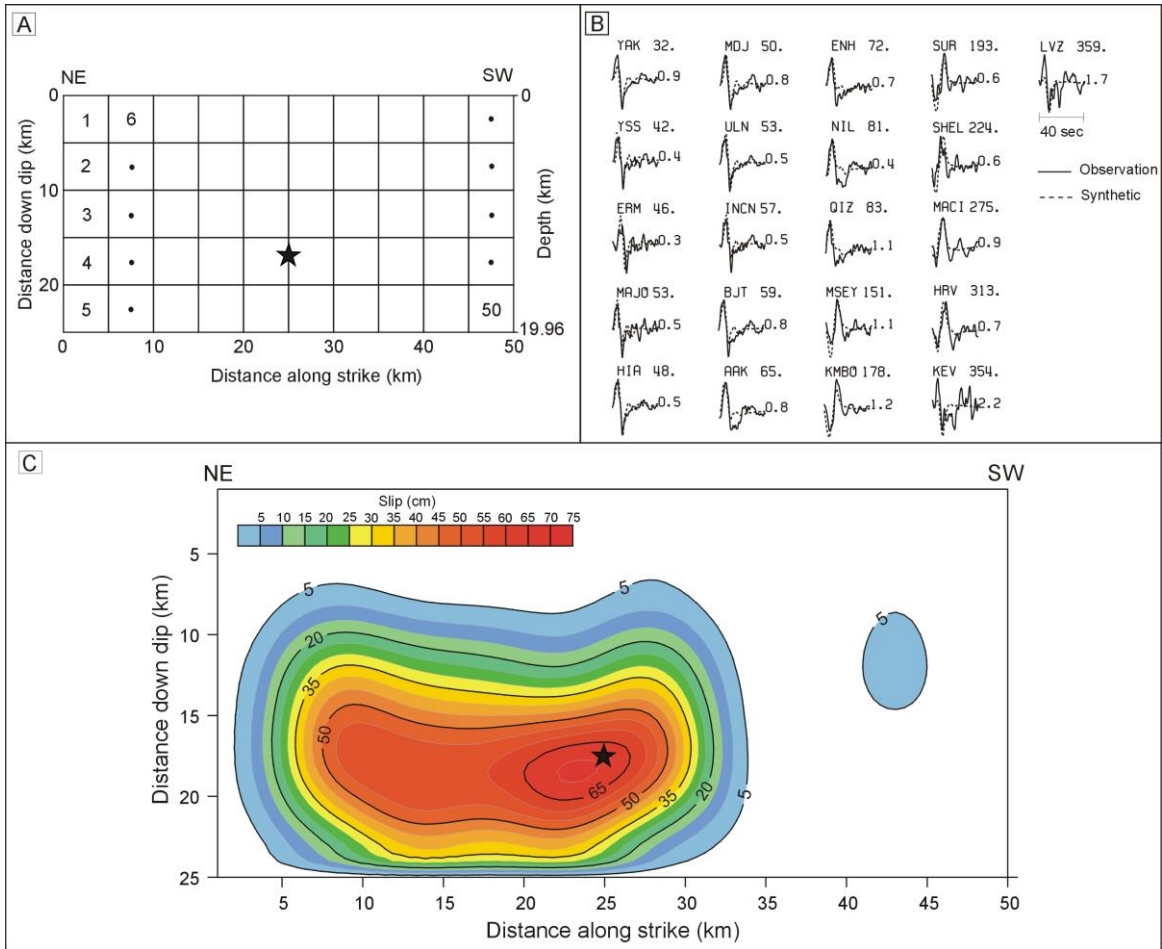
Fig. 2. (a) Defne aftershock model fault plane parameterizations used in the study; (b) comparison of the predicted P and SH waveforms calculated for the slip model and (c) preferred co-seismic slip distribution obtained from the finite-fault analysis. The slips are contoured at 5 cm intervals and only slips that are greater than 5 cm have a contoured. Solid stars represent the hypocenters.

Comparison of observed waveforms and fault segment synthetic waveforms Ax≅b the system of linear equations is over-defined. Here, matrix A is the matrix of fault segment synthetic seismograms, and b is the matrix of observed seismograms at each station combined. x is the solution matrix containing the slip weights to be assigned to each fault segment to ensure the agreement between the synthetic and the observed seismograms, and the Householder least squares inversion method was used for its calculation. Six-time windows were used in the inversion, and the source rise-time function within each time window was represented by an equilateral triangle with a rise and fall of 0.4 s, allowing a total rise time of 4.8 s at each point on the fault plane. Using this time window approach to modeling allows for variations in rupture velocity and slip rise time on the model fault plane, allowing for accurate modeling of complex source properties. The initial rupture velocity for the inversion was taken as 3.0 km/s ([81] emphasized that the rupture velocity varies between 70% and 90% of the S-wave velocity for many earthquakes), but inversions were also attempted for different rupture velocities. A detailed description of the method is given by [73] and [76].

In order to obtain the best fitting slip distribution model to the data, a large number of inversion experiments were performed for different source parameters and different values of rupture velocity and focal depth. Accordingly, the model with a rupture velocity of 3.3 km/s, a focal depth of 13.4 km, and strike, dip, and rake angles of 225°, 53° and -27°, respectively, gave the best fit to the data. A comparison of the observed and synthetic waveforms and the slip distribution pattern of the resulting model are given in Figs. 2b and c, respectively. The unconformity between observed and synthetic waveforms for different inversion trials is defined as the L2 Euclidian norm (‖b-Ax‖) [82].

The finite-fault slip distribution model of the Defne aftershock indicates that the rupture was caused by the failure of a single fault asperity. Covering an area of 35 km x 18 km between depths of 6 and 20 km, the largest slip reached 0.75 m near the hypocenter. The rupture was confined at the hypocenter and proceeded unilaterally towards the northeast. It released a total seismic moment of 5.85×10^{18} Nt.m (Mw=6.4).

3. Coulomb stress changes modeling

When earthquakes occur, they cause a change in the stress state on the neighbouring faults around them, and in this way, they can trigger an earthquake that will occur around the mainshock, bringing it forward or delaying it [57, 60 83-68]. Many studies have shown that there is a stress-triggering relationship between medium and large earthquake sequences (etc. 1999 İzmit (Mw7.4) and Düzce (Mw7.2) earthquake sequence [79]; 2015 Nepal (Mw7.8) and Mw7.1 earthquake sequence [89]; 2019 Ridgecrest (M6.4) and Mw7.1 earthquake sequence [90-92]) and that there is a relationship between successive mainshock-aftershock occurrences and earthquake stress changes [61, 63, 64, 72].

Coulomb failure criteria are widely used to characterize the conditions under which failure occurs and;

$$\Delta\sigma_f = \Delta\tau + \mu'\Delta\sigma_n \tag{1}$$

is expressed by the relation. Here, $\Delta\tau$ and $\Delta\sigma_n$ changes in shear stress and normal stress on the target fault plane, μ' is the effective friction coefficient, including the unknown effects of pore water pressure [60, 63]. It is emphasized that μ' is a value ranging between 0.2-0.8 and has no critical effect on Coulomb stress calculations, and taking it as 0.4 reduces the margin of error in modeling results by 25% [60, 61, 97, 98]. Accordingly, μ' value was taken as 0.4, Young's modulus as 8×10^5 bar and Poisson's ratio as 0.25 in all stress calculations performed within the scope of the study. Stress changes were calculated using [99]'s coseismic elastic dislocation model by considering earthquake ruptures as rectangular dislocation surfaces in an elastic semi-infinite medium. A Coulomb stress change value greater than zero (positive) indicates that fracture has become probable, while a negative value indicates the opposite. The Coulomb 3.2 package program was used for the calculations [68, 100], and the increase in stress is represented in red and the decrease in blue.

The focal and source parameters (strike, dip, rake and fault dimension) of the earthquakes that constitute the source in the coseismic coulomb stress change calculations are summarized in Table 2 (the February 6 Pazarcık, the largest aftershock, the February 6 Elbistan and the Defne aftershock). For the February 6 Pazarcık and Elbistan earthquakes, the fault slip distribution model obtained by [6] based on coseismic InSAR and GPS displacements was used. The homogeneous rupture model dimensions (fault length x fault width) and the maximum slip value for the largest aftershock were determined as 30 km x13 km and -0.90 cm, respectively (depending on the magnitude (Mw=6.7)) based on the empirical relations of [101]. Fault parameters given by GCMT were used for the determined rupture model, and this fault plane was placed in the source region.

Table 2. Source earthquake rupture parameters in Coulomb stress change modelling.

Earthquake Name	Date	Lat. Lon. (º)	M_w	Strike (º)		Dip (º)	Rake (º)	Fault length (km)	Fault width (km)	Max Slip (m)	Ref.
				Source Earthquakes							
February 6 Pazarcık	06.02.2023	37.288 37.043	7.8	S1	21.1	88	0	175	20.00	Variable	[6]
				S2	34.3						
				S3	66.9						
				S4	50.7						
				S5	67.7						
				S6	205						
				S7	8.3						
				S8	92.3						
Largest Aftershock	06.02.2023	37.189 36.893	6.7	212*		73*	-13*	30	13	-0.90	[101] *GCMT
February 6 Elbistan	06.02.2023	38.089 37.239	7.6	S1	249.1	70	-4	150	21.28	Variable	[6]
				S2	269.4						
				S3	281.9						
				S4	245.1						
				S5	231.4						
				S6	2.3						
Defne Aftershock	20.02.2023	36.110 36.062	6.4	225		53	-27	35	25	Variable	This study

The map view of the Coulomb stress change models calculated to investigate whether the February 6 earthquake sequence triggered the Defne aftershock rupture is shown in Figs. 3 and 4. Stress patterns were calculated on the Defne aftershock rupture plane, from which we obtained the slip distribution model (Strike=225°, Dip=53°, Rake=-27°), and for a depth of 13.4 km corresponding to its hypocenter depth. Fig. 3a shows the stress changes calculated for the February 6 Pazarcık earthquake, Fig. 3b for the largest aftershock and Fig. 3c for the February 6 Elbistan earthquake.

Fig. 3 shows that the rupture plane of the Defne aftershock was subjected to positive stress due to the February 6 Pazarcık and the largest aftershock earthquakes and negative stress due to the February 6 Elbistan earthquake. This suggests that the February 6 Pazarcık and the largest aftershock earthquakes triggered the rupture of the Defne aftershock. In order to reveal the triggering stress effect of each earthquake, stress values were calculated at different epicentral locations (Fig. 3) and hypocentral depths given by USGS, GCMT, AFAD and KOERİ for the Defne aftershock (Table 3). The high positive Coulomb stress values calculated at all hypocentral locations revealed that the rupture of the Defne aftershock was predominantly caused by the triggering effect of the rupture of the February 6 Pazarcık earthquake.
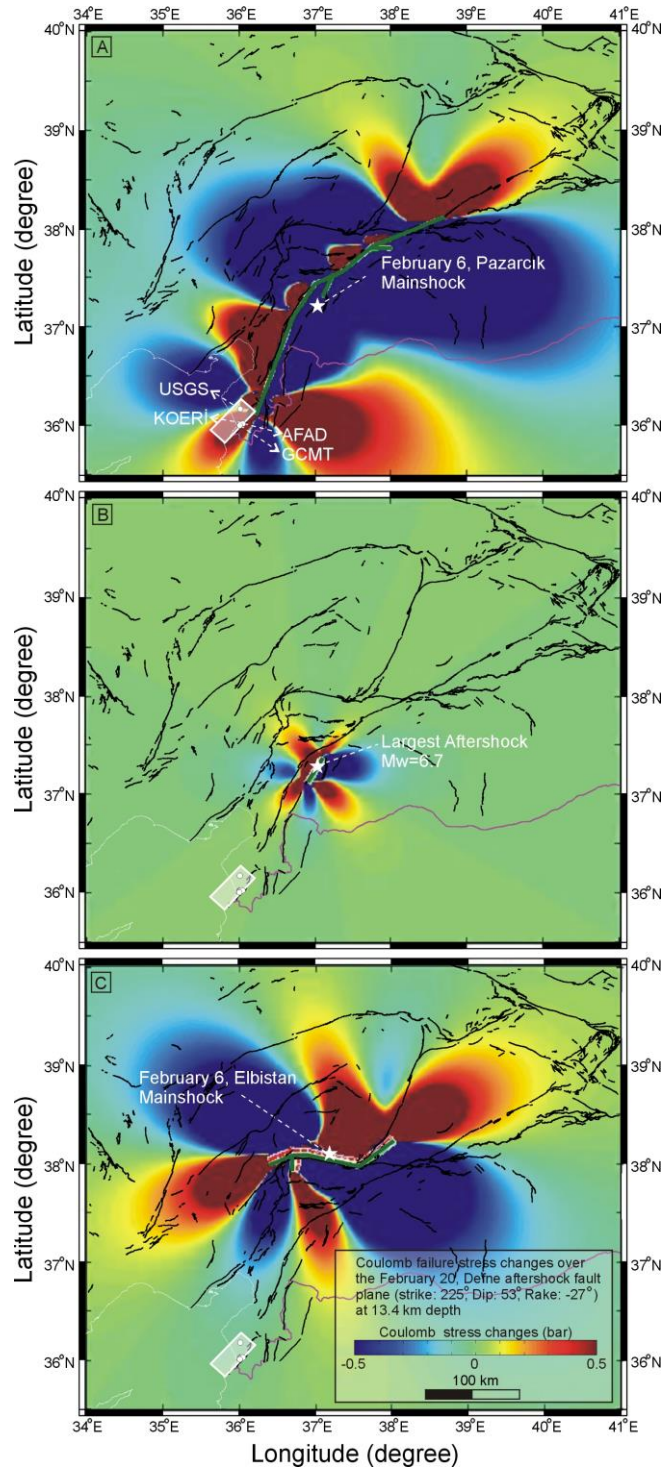
Fig. 3. Map view of Coulomb stress change over the Defne aftershock fault plane caused by (a) the February 6 Pazarcık; (b) the largest aftershock; (c) the February 6 Elbistan earthquake. Green lines are fault planes on the surface for earthquakes. The white rectangle is the Defne aftershock fault plane. White circles indicate the location of the Defne aftershock by USGS, KOERİ, AFAD and GCMT, respectively. White stars are earthquake epicentres according to AFAD.

In order to examine the combined effects of the earthquakes, Fig. 4a shows the map image of the Coulomb stress change model calculated on the rupture plane of the Defne aftershock due to February 6 Pazarcık and the largest aftershock earthquakes. Fig. 4b shows the map image of the Coulomb stress change models calculated on the rupture plane of the Defne aftershock due to the February 6 earthquake sequence. When Figs. 4a and b are analyzed, it is noteworthy that the rupture plane of the Defne aftershock is located in the area of positive Coulomb stress increase.
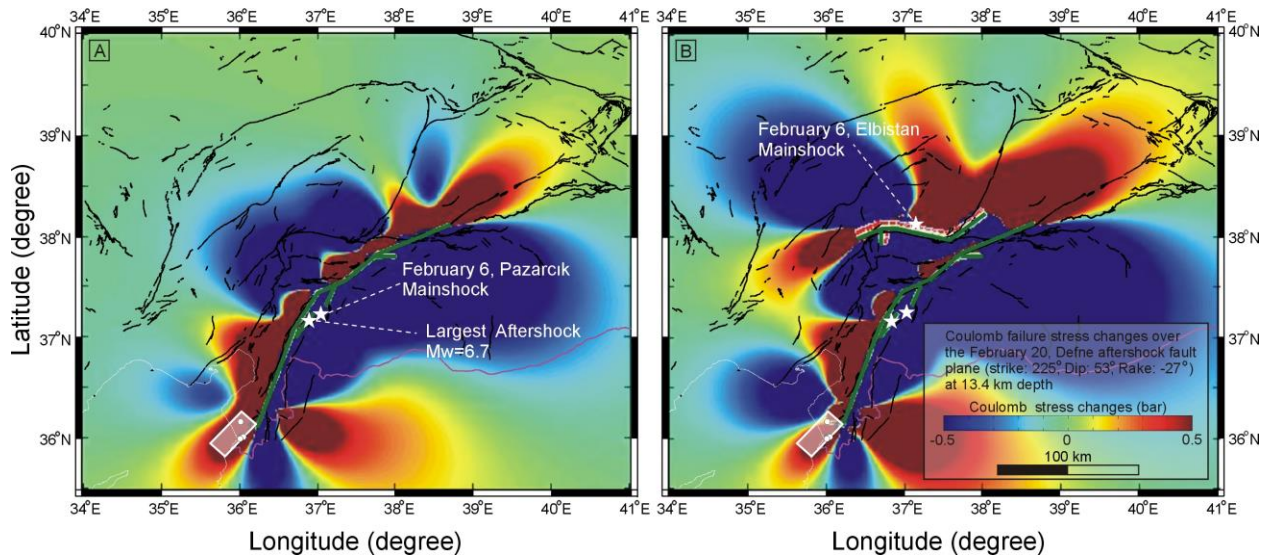
Fig. 4. The map view illustrates the change in Coulomb stress changes over the Defne aftershock fault plane resulting from (a) the February 6, Pazarcık and the largest aftershock earthquakes; (b) the earthquake sequence. See labels within the figures caption of Fig. 3 for the other details.

In order to determine the triggering relationship of earthquake ruptures on neighboring faults, Coulomb stress changes were calculated on the DSF, which extends in the N-S direction just south of the February 6, earthquake sequence and the Defne aftershock ruptures (Fig. 5). The direction of the plane where the stress changes were calculated for the DSF was determined from the map trace (180°), and the dip and rake angle were taken as 87° and 0°, respectively [102]. Calculations were made for a depth of 10 km. Firstly, the Coulomb stress change model was calculated on the DSF where the February 6 earthquake sequence and the Defne aftershock earthquakes were defined as the source fault, and it was noted that a positive stress field of over 1 bar was formed in the northern part (Fig. 5a). When the stress change model was calculated only due to the rupture of the Defne aftershock, a very low positive stress field was obtained in the same part (Fig. 5b).

Stress values were calculated at four different points (Fig. 5; P1, P2, P3 and P4) to determine the spatial distribution of stress changes along the northern part of the DSF (Table 3). Accordingly, points P1 and P2 on the western segment in the northern part of the DSF were predominantly loaded with positive stress above 1 bar due to the February 6 Pazarcık earthquake, while point P4 was loaded with positive stress around 0.5 bar. While the rupture

of the Defne aftershock created a negative stress field in the south, it had a very small positive stress loading effect on points P1 and P3 in the north (Fig. 5, Table 3).
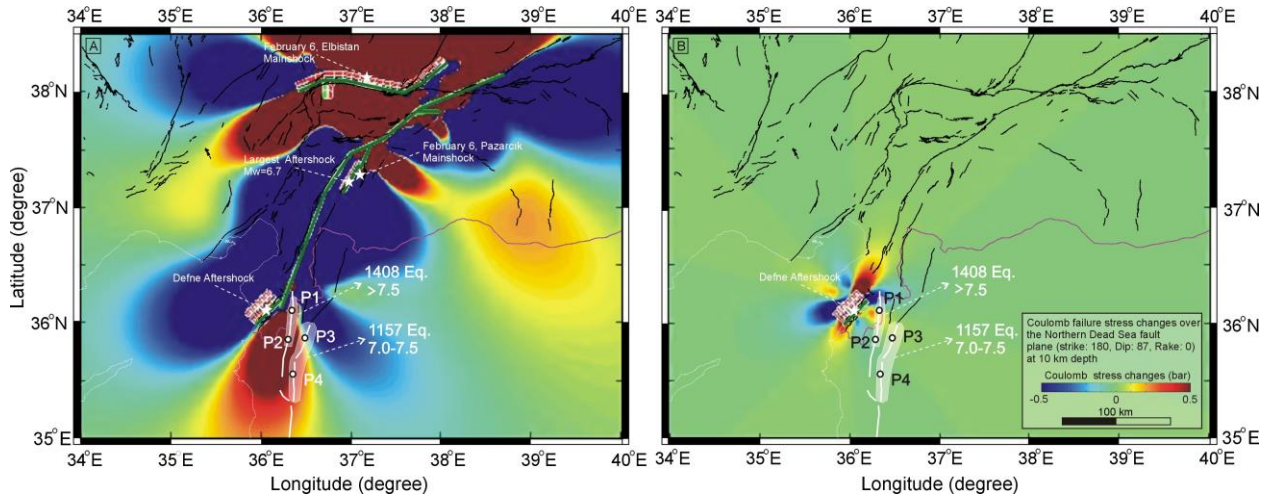
Fig. 5. Map view of Coulomb stress change over the northern part of the DSF caused by (a) February 6, earthquake sequence and the Defne aftershock earthquakes; (b) the Defne aftershock. White circles indicate the points for which the stress values are sampled (see Table 3). Fault traces of the DSF were taken from [104].

4. Discussion

In this study, the finite-fault slip distribution model of the Defne aftershock is derived from the inversion of broadband teleseismic P waveforms. The coseismic slip distribution model shown in Fig. 2c indicates that the Defne aftershock rupture occurred with a maximum slip of 0.75 m, with a single fault asperity over a fault area of 35 km by 18 km. The rupture started at the hypocenter, propagated unilaterally to the NE and released a total seismic moment of 5.85×10^{18} Nt.m. The finite-fault slip distribution model is relatively similar to the slip distribution models obtained by [6] and [48] based on InSAR data, except for the maximum amount of slip. Their slip distribution models show a slip value of about 1 meter around the hypocenter, while the finite-fault slip distribution model shows a relatively low slip value of 0.75 m. All the obtained models show that the rupture propagated to the NE and completed its maximum slip in an area including Hatay province. This explains why the loss of life and damage from the Defne aftershock was more severe in Hatay.

The Coulomb stress change maps created to investigate whether the rupture of the Defne aftershock occurred due to stress triggering revealed that the rupture of the Defne aftershock occurred in the area of positive stress loading (Fig. 3). The February 6 Pazarcık and the largest aftershock created a triggering positive stress load on the rupture plane of the Defne aftershock, while the February 6, Elbistan earthquake created a negative stress shadow. [40] and [84] emphasized that the triggering threshold for a critical fault close to failure is 0.1- 0.5 bar. Accordingly, when Table 3 is analyzed, the triggering effect of the February 6, Pazarcık earthquake on the rupture of the Defne earthquake is clearly seen (>1 bar). Positive stress values ranging from 0.002 to 0.005 bar originating from the largest aftershock indicate that this stress effect is negligible. The February 6 Elbistan earthquake created a stress shadow between -0.030- -0.040 bar at all epicenter locations given. This is interpreted as the rupture of the February 6 Elbistan earthquake with very low negative stress values did not have a delaying effect on the rupture of the Defne aftershock.

In order to reveal the combined effect of earthquake ruptures in Coulomb stress modeling further, calculations were made on the Defne aftershock rupture due to both the February 6 Pazarcık and the largest aftershock earthquakes and the February 6 earthquake sequence. The stress models showed that the rupture of the Defne aftershock is located in the positive stress field for both cases (Fig. 4). When stress values were calculated for the Defne aftershock at different hypocentral locations, high positive stress values close to each other were obtained (Table 3). Accordingly, the stress values calculated at USGS, GCMT, AFAD and KOERİ hypocentral locations for the February 6 Pazarcık and the largest aftershock earthquakes are 0.234 bar, 2.009 bar, 1.912 bar and 1.097 bar, respectively, while the stress values obtained by taking into account the February 6 Elbistan earthquake are 0.116 bar, 2.121 bar, 1.878 bar and 1.107 bar, respectively. It is noteworthy that these high-stress values are almost the same as the stress values calculated only for the February 6 Pazarcık earthquake (Table 3). This suggests that the stress shadow created by the February 6 Elbistan earthquake had a negligible effect in delaying the rupture of the Defne aftershock and that the Defne aftershock rupture was predominantly triggered by the rupture of the February 6 Pazarcık earthquake. [6] and [103] emphasized that the Defne aftershock was triggered by the February 6 Pazarcık earthquake with a significant positive stress load in the epicenter region.

Table 3. The Coulomb stress change values calculated for different scenarios and locations.

		USGS (225/53/-27)			
		USGS	**GCMT**	**AFAD**	**KOERİ**
	Long (°):	36.025	36.06	36.037	36.10
	Lat (°):	36.162	36.03	36.021	36.13
	Calculation Depth (km):	11.5	12	21.73	16
For Figures 3 and 4		*Coulomb stress changes (bar)*			
	06 February Pazarcık Eq.	0.198	2.041	1.923	1.075
	Largest aftershock_6.7	0.005	0.002	0.002	0.004
	06 February Elbistan Eq.	-0.038	-0.029	-0.037	-0.038
	06 February Pazarcık+ Largest Aftershock	0.234	2.009	1.912	1.097
	06 February Pazarcık Eq. Largest Aftershock 06 February Elbistan Eq.	0.116	2.121	1.878	1.107
		Dead Sea Fault Plane (180/87/0)			
		P1	**P2**	**P3**	**P4**
	Long (°):	36.356	36.356	36.532	36.405
	Lat (°):	35.955	35.844	35.884	35.578
	Calculation Depth (km):	10			
For Figure 5		*Coulomb stress changes (bar)*			
	06 February Pazarcık Eq.	1.258	1.161	-0.306	0.486
	Largest aftershock_6.7	0.010	0.009	0.010	0.005
	06 February Elbistan Eq.	-0.001	-0.004	-0.018	-0.009
	Defne aftershock	0.060	-0.006	0.033	-0.015
	06 February Pazarcık Eq. Largest aftershock_6.7 06 February Elbistan Eq.	1.255	1.079	-0.279	0.448

In all stress models obtained in Fig. 5, the finite-fault slip distribution model we obtained for the rupture of the Defne aftershock was used. The Coulomb stress model calculated on the DSF due to the February 6 earthquake sequence, including the Defne aftershock, revealed that the northern part of the DSF is loaded with positive stress (Fig. 5a). This positive stress loading field indicates that the northern part of the DSF is more likely to rupture in the future. When the stress change model calculated only for the Defne aftershock in Fig. 5b is analyzed, it is noteworthy that the positive stress is negligibly small. Two major earthquakes occurred along the northern part of the DSF, one in the eastern segment in 1157 (M=7.0-7.5) and the other in the western segment in 1408 (M>7.5) [104]. The rupture zones of these earthquakes are shown in Fig. 5 (Transparent white areas). Points P1 and P2 are

selected on the 1408 earthquake rupture and points P3 and P4 are selected on the 1157 earthquake rupture. When Table 3 is examined, it is noteworthy that the 1408 fracture with high stress values (1.255 bar for the P1 point and 1.079 bar for the P2 point) is loaded with a triggering positive stress and the stress load is predominantly caused by the rupture of the February 6 Pazarcık earthquake. Although the rupture of the Defne aftershock created a stress load of 0.33 bar on point P3, it could not carry the stress shadow created by the February 6, earthquake to positive. Accordingly, point P3 is located in the stress shadow with a stress value of -0.279 bar. The stress load of 0.448 bar on point P4, located south of the 1157 rupture, is predominantly due to the rupture of the February 6 Pazarcık earthquake. The rupture of the Defne aftershock created a stress shadow of -0.015 bar at this point. On the other hand, the February 6 Elbistan earthquake created a stress shadow at all points, but this was not enough to delay a fault rupture. This is explained by the location of the February 6 Elbistan earthquake rupture and the distance from the points where stress calculations were performed. The absence of a large-scale earthquake north of the DSF for more than 600 years, the positive Coulomb stress changes values caused predominantly by the February 6 Pazarcık earthquake, and the negligible effect of the Defne aftershock rupture have increased the probability of future rupture in this part of the fault, perhaps bringing it forward. Therefore, special attention should be paid to this fault.

5. Conclusions

Here, a finite-fault slip distribution model was obtained from the inversion of the teleseismic P waveforms of the February 20, 2023, Defne aftershock, which occurred shortly after the devastating February 6 Pazarcık and Elbistan earthquakes. The slip model showed that the rupture was caused by the rupture of an asperity located between 6-12 km depth with a maximum displacement of about 0.75 m. The rupture propagated unilaterally from the hypocenter to the NE. A total seismic moment of 5.85×10^{18} Nt.m was released. Coulomb stress change modeling showed that the high positive stress load from the rupture of the February 6 Pazarcık earthquake played the dominant triggering role in the rupture of the Defne aftershock. In addition, stress variation modeling on the DSF showed high positive stress values in the northern part. The positive stress load and the fact that no major earthquake has occurred for a long time showed that the seismic risk for the northern part of the DSF is high.

Author Contribution

The writing of the manuscript and all analyses were performed by Hatice Durmuş.

Acknowledgements

References

[1] Afet ve Acil durum Yönetimi Deprem Dairesi Başkanlığı, "06 Şubat 2023 Pazarcık-Elbistan Kahramanmaraş (Mw:7.7-Mw:7.6) Depremleri Raporu", [Online] https://deprem.afad.gov.tr/assets/pdf/Kahramanmara%C5%9F%20Depremi%20%20Raporu_02.06.2023.pdf [Access date: 05 February 2024]
[2] T.C. Cumhurbaşkanlığı Strateji ve Bütçe Başkanlığı, "Kahramanmaraş ve Hatay Depremleri Raporu", [Online] https://www.sbb.gov.tr/2023-kahramanmaras-ve-hatay-depremleri-raporu/ [Access date: 15 February 2024]
[3] World Healty Organization, "Emergency situation report", https://www.who.int/europe/emergencies/situations/turkiye-and-syria-earthquakes/situation-reports, [Access date: 25 January 2024]
[4] F. Şaroğlu, O. Emre, I. Kuscu, "Active fault map of Turkey", General Directorate of Mineral Research and Exploration, [Access date: 25 January 2024]
[5] T. Y. Duman and Ö. Emre, "The East Anatolian Fault: geometry, segmentation and jog characteristics", *Geological Society, London, Special Publications*, 372.1: 495-529, 2013, doi.org/10.1144/SP372.14.
[6] J.J. Zhao, Q. Chen, Y.H. Yang, & Q. Xu, "Coseismic faulting model and post-seismic surface motion of the 2023 Turkey–Syria earthquake doublet revealed by InSAR and GPS measurements," *Remote Sensing*, 15.13: 3327, 2023, doi.org/10.3390/rs15133327.

[7] A. A. Barka and K. Kadinsky- Cade, "Strike- slip fault geometry in Turkey and its influence on earthquake activity," *Tectonics*, 7.3: 663-684, 1988, doi.org/10.1029/TC007i003p00663.

[8] N. N. Ambraseys, "Temporary seismic quiescence: SE Turkey," *Geophysical Journal International*, 96.2: 311-331, 1989, doi.org/10.1111/j.1365-246X.1989.tb04453.x.

[9] T. Taymaz, H. Eyidoğan, & J. Jackson, Source parameters of large earthquakes in the East Anatolian Fault Zone (Turkey). *Geop J. Int.*, *106*(3), 537-550, 1991.

[10] Ö. Emre, T. Y. Duman, S. Özalp, H. Elmacı, Ş. Olgun, & F. Şaroğlu, "Active fault map of Turkey with explanatory text". *General directorate of mineral research and exploration special publication series*, *30, 2013*.

[11] O. Tan, Z. Pabuçcu, M. C. Tapırdamaz, S. İnan, S. Ergintav, H. Eyidoğan,... & F. Kuluöztürk, "Aftershock study and seismotectonic implications of the 8 March 2010 Kovancılar (Elazığ, Turkey) earthquake (MW= 6.1)", *Geophysical Research Letters*, *38*(11), 2011.

[12] M. Utkucu, E. Budakoğlu & M. Çabuk, "Teleseismic finite-fault inversion of two M w= 6.4 earthquakes along the East Anatolian Fault Zone in Turkey: the 1998 Adana and 2003 Bingöl earthquakes". *Arabian Journal of Geosciences*, *11*, 1-14, 2018.

[13] M. Utkucu, "Türkiye'de Zaman Bağımlı Deprem Gerilme Etkileşimlerinin Modellenmesi ve Deprem Tehlikesi Üzerine Çıkarımlar" *TÜBİTAK Proje No: 121Y271, 2023*.

[14] A. Hubert-Ferrari, L. Lamair, S. Hage, S. Schmidt, M.N. Çağatay, & U. Avşar, "A 3800 yr paleoseismic record (Lake Hazar sediments, eastern Turkey): Implications for the East Anatolian Fault seismic cycle," *Earth and Planetary Science Letters*, 538: 116152, 2020, doi.org/10.1016/j.epsl.2020.116152.

[15] S. Mcclusky, S. Balassanian, A. Barka, C. Demir, S. Ergintav, I. Georgiev & G. Veis, "Global Positioning System constraints on plate kinematics and dynamics in the eastern Mediterranean and Caucasus," *Journal of Geophysical Research: Solid Earth*, 105.B3: 5695-5719, 2000, doi.org/10.1029/1999JB900351.

[16] R. Reilinger, S. McClusky, P. Vernant, S. Lawrence, S. Ergintav, R. Cakmak & G. Karam, "GPS constraints on continental deformation in the Africa- Arabia- Eurasia continental collision zone and implications for the dynamics of plate interactions," *Journal of Geophysical Research: Solid Earth*, 111.B5, 2006, doi:10.1029/2005JB004051.

[17] A. Hubert-Ferrari, G. King, I. Manighetti, R. Armijo, B. Meyer, & P. Tapponnier, "Long-term elasticity in the continental lithosphere; modelling the Aden Ridge propagation and the Anatolian extrusion process," *Geophysical Journal International*, 153.1: 111-132, 2003, doi.org/10.1046/j.1365-246X.2003.01872.x.

[18] O. Tatar, J.D.A. Piper, H. Gürsoy, A. Heimann, & F. Koçbulut, "Neotectonic deformation in the transition zone between the Dead Sea Transform and the East Anatolian Fault Zone, Southern Turkey: a palaeomagnetic study of the Karasu Rift Volcanism," *Tectonophysics*, 385.1-4: 17-43, 2004, doi.org/10.1016/j.tecto.2004.04.005

[19] A.M.C. Şengör, O. Tüysüz, C. Imren, M. Sakınç, H. Eyidoğan, N. Görür,... & C. Rangin, "The North Anatolian fault: A new look," *Annu. Rev. Earth Planet. Sci.*, 33: 37-112, 2005, doi.org/10.1146/annurev.earth.32.101802.120415.

[20] N. N. Ambraseys, "Some characteristic features of the Anatolian fault zone," *Tectonophysics*, 9.2-3: 143-165, 1970, doi.org/10.1016/0040-1951(70)90014-4.

[21] R. Armijo, B. Meyer, A. Hubert, & A. Barka, "Westward propagation of the North Anatolian fault into the northern Aegean: Timing and kinematics," *Geology*, 27.3: 267-270, 1999, doi.org/10.1130/0091-7613(1999)027<0267:WPOTNA>2.3.CO;2

[22] A. Hubert‐Ferrari, R. Armijo, G. King, B. Meyer, & A. Barka, "Morphology, displacement, and slip rates along the North Anatolian Fault, Turkey," *Journal of Geophysical Research: Solid Earth*, 107.B10: ETG 9-1-ETG 9-33, 2002.

[23] X. Le Pichon, A.C. Şengör, J. Kende, C. İmren, P. Henry, C. Grall, H. & Karabulut, "Propagation of a strike-slip plate boundary within an extensional environment: the westward propagation of the North Anatolian Fault," *Canadian Journal of Earth Sciences*, 53.11: 1416-1439, 2016, doi.org/10.1139/cjes-2015-0129.

[24] M. Cengiz, S. Karabulut, "A two-stage deformation of the Anatolian Plate deduced from Paleomagnetic signals: The initial age of the Anatolian's escape". *Turkish Journal of Earth Sciences*, *33*(3), 243-259, 2024.

[25] B. Aktug, H. Ozener, A. Dogru, A. Sabuncu, B. Turgut, K. Halicioglu,... & E. Havazli, "Slip rates and seismic potential on the East Anatolian Fault System using an improved GPS velocity field," *Journal of Geodynamics*, 94: 1-12, 2016, doi.org/10.1016/j.jog.2016.01.001.

[26] R. Westaway, "Kinematic consistency between the Dead Sea Fault Zone and the Neogene and Quaternary left-lateral faulting in SE Turkey". *Tectonophysics*, *391*(1-4), 2004, 203-237.

[27] A. Seyrek, T. Demir, R. Westaway, H. Guillou, S. Scaillet, T. S. White, & D. R. Bridgland, "The kinematics of central-southern Turkey and northwest Syria revisited". *Tectonophysics*, 2014, *618*, 35-66.

[28] E. Altunel, M. Meghraoui, V. Karabacak, S. H. Akyüz, M. Ferry, Ç. Yalçıner, & M. Munschy, "Archaeological sites (tell and road) offset by the dead sea fault in the Amik Basin, southern Turkey". *Geophysical Journal International*, *179*(3), 1313-1329, 2009.

[29] Y. Mahmoud, F. Masson, M. Meghraoui, Z. Cakir, A. Alchalbi, H. Yavasoglu, & S. Inan, "Kinematic study at the junction of the East Anatolian fault and the Dead Sea fault from GPS measurements". *Journal of Geodynamics*, *67*, 30-39, 2013.

[30] E. Herece "Atlas of the East Anatolian Fault (1:500,000)". General Directorate of Mineral Research and Exploration of Turkey (MTA), Ankara, Turkey. Special Publication Series 13:13,359, 2008.

[31] R.D. Hartleb, J.F. Dolan, H.S. Akyüz, & B. Yerli, "A 2000-year-long paleoseismologic record of earthquakes along the central North Anatolian Fault, from trenches at Alayurt, Turkey," *Bulletin of the Seismological Society of America*, 93.5: 1935-1954, 2003, doi.org/10.1785/0120010271.

[32] M. Bohnhoff, P. Martínez-Garzón, F. Bulut, E. Stierle, & Y. Ben-Zion, "Maximum earthquake magnitudes along different sections of the North Anatolian fault zone," *Tectonophysics*, 674: 147-165, 2016, doi.org/10.1016/j.tecto.2016.02.028.

[33] B. Willis, "Dead Sea problem: rift valley or ramp valley?", *Bulletin of the Geological Society of America*, *39*(2), 490-542, 1928.

[34], K. Ergin "A catalogue of earthquakes for Turkey and surrounding area (11AD to 1964AD)". *Tech. Univ. Mining Eng. Fac. Publ.*, *24*, 189, 1967.

[35] J. P. Poirier, & M. A. Taher, "Historical seismicity in the near and Middle East, North Africa, and Spain from Arabic documents (VIIth-XVIIIth century)". *Bulletin of the Seismological Society of America*, *70*(6), 2185-2201, 1980.

[36] H. Soysal, S. Sipahioğlu, D. Kolçak, & Y. Altınok, Türkiye ve çevresinin tarihsel deprem kataloğu. *TÜBİTAK Proje No: TBAG*, *341*, 124, (1981).

[37] N. N. Ambraseys, & J. A. Jackson, "Faulting associated with historical and recent earthquakes in the Eastern Mediterranean region". *Geophysical Journal International*, *133*(2), 390-406, 1998.

[38] S.S. Nalbant, J. McCloskey, S. Steacy, & A.A. Barka, "Stress accumulation and increased seismic risk in eastern Turkey," *Earth and Planetary Science Letters*, 195.3-4: 291-298, 2002, doi.org/10.1016/S0012-821X(01)00592-1.

[39] Ö. Yönlü, & V. Karabacak, "Surface rupture history and 18 kyr long slip rate along the Pazarcık segment of the East Anatolian Fault". *Journal of the Geological Society*, *181*(1), jgs2023-056, 2024.

[40] R. E. Tatevossian, N. G. Mokrushina, A. N. Ovsyuchenko, & A. S. Larkov, "Historical Earthquake on the North-Eastern Extension of the East Anatolian Fault". *Izvestiya, Physics of the Solid Earth*, *59*(6), 878-887, 2023.

[41] H. Karabulut, S. E. Güvercin, J. Hollingsworth, & A. Ö. Konca, "Long silence on the East Anatolian Fault Zone (Southern Turkey) ends with devastating double earthquakes (6 February 2023) over a seismic gap: implications for the seismic potential in the Eastern Mediterranean region". *Journal of the Geological Society*, *180*(3), jgs2023-021, 2023.

[42] H. Alkan, A. Büyüksaraç, & Ö. Bektaş, "Investigation of earthquake sequence and stress transfer in the Eastern Anatolia Fault Zone by Coulomb stress analysis". Turkish Journal of Earth Sciences, 33(1), 56-68, 2024.

[43] R.E. Tatevossian, N.G. Mokrushina, A.N. Ovsyuchenko, & A.S. Larkov, "Historical Earthquake on the North-Eastern Extension of the East Anatolian Fault". *Izvestiya, Physics of the Solid Earth*, *59*(6), 878-887, 2023.

[44] Ö. Yönlü, V. Karabacak, E. Altunel, H.S. Akyüz, "Paleoseismological slip rate on the East Anatolian fault zone around Türkoğlu," *International Earth Science Colloquium on the Aegean Region, IESCA-2012,* 2012, p. 1-5.

[45] Yönlü, Ö. (2012). Doğu Anadolu Fay Zonunun Gölbaşı (Adıyaman) İle Karataş (Adana) arasındaki kesiminin geç kuvaterner aktivitesi.

[46] S. Li, X. Wang, T. Tao, Y. Zhu, X. Qu, Z. Li, & S. Song, "Source Model of the 2023 Turkey Earthquake Sequence Imaged by Sentinel-1 and GPS Measurements: Implications for Heterogeneous Fault Behavior along the East Anatolian Fault Zone," *Remote Sensing*, 15.10: 2618, 2023, doi.org/10.3390/rs15102618.

[47] AFAD (Şubat 2023). 06 Şubat 2023 Kahramanmaraş (Pazarcık ve Elbistan) Depremleri Saha Çalışmaları Ön Değerlendirme Raporu, Deprem Dairesi Başkanlığı, Available:https://deprem.afad.gov.tr/assets/pdf/Arazi_Onrapor_28022023_surum1_revize.pdf

[48] S. Barbot, H. Luo, T. Wang, Y. Hamiel, O. Piatibratova, M.T. Javed,... & G. Gurbuz, "Slip distribution of the February 6, 2023 Mw 7.8 and Mw 7.6, Kahramanmaraş, Turkey earthquake sequence in the East Anatolian fault zone," *Seismica*, ISSN 2816-9387 volume 2.3, 2023, *doi.org/10.26443/seismica.v2i3.502*.

[49] D. Melgar, T. Taymaz, A. Ganas, B.W. Crowell, T. Öcalan, M. Kahraman,... & C. Altuntaş, "Sub-and super-shear ruptures during the 2023 Mw 7.8 and Mw 7.6 earthquake doublet in SE Türkiye," *Seismica,* vol. 2.3, 2023, doi.org/10.26443/seismica.v2i3.387.

[50] C. Liu, T. Lay, R. Wang, T. Taymaz, Z. Xie, X. Xiong, & C. Erman, "Complex multi-fault rupture and triggering during the 2023 earthquake doublet in southeastern Türkiye," *Nature Communications,* 14:5564, 2023, doi.org/10.1038/s41467-023-41404-5

[51] J.R. Elliott, E.K. Nissen, P.C. England, J.A. Jackson, S. Lamb, Z. Li, & B. Parsons, "Slip in the 2010–2011 Canterbury earthquakes, New Zealand," *Journal of Geophysical Research: Solid Earth*, 117.B3, 2012, doi.org/10.1029/2011JB008868.

[52] M. Utkucu, "23 October 2011 Van, Eastern Anatolia, earthquake (M_w 7.1) and seismotectonics of Lake Van area," *Journal of seismology*, 17: 783-805, 2013, doi.org/10.1007/s10950-012-9354-z.

[53] M. Utkucu, H. Durmuş, H. Yalçın, E. Budakoğlu, & E. Işık, "Coulomb static stress changes before and after the 23 October 2011 Van, eastern Turkey, earthquake (M W= 7.1): implications for the earthquake hazard mitigation," *Natural Hazards and Earth System Sciences*, 13.7: 1889-1902, 2013, doi.org/10.5194/nhess-13-1889-2013.

[54] R.S. Stein, "Earthquake conversations," *Scientific American*, January 2003, 288.1: 72-79.

[55] A.M. Freed, "Earthquake triggering by static, dynamic, and postseismic stress transfer," *Annu. Rev. Earth Planet. Sci.*, 33: 335-367, 2005, doi.org/10.1146/annurev.earth.33.092203.122505.

[56] R.A. Harris and R.W. Simpson, "Changes in static stress on southern California faults after the 1992 Landers earthquake," *Nature*, 360.6401: 251-254, 1992, doi.org/10.1038/360251a0.

[57] R.S. Stein, G.C.P. King, J. Lin, "Change in failure stress on the southern San Andreas fault system caused by the 1992 magnitude= 7.4 Landers earthquake," *Science*, 258.5086: 1328-1332, 1992, doi: 10.1126/science.258.5086.1328.

[58] R.S. Stein, G.C.P, King, J. Lin, "Stress triggering of the 1994 M= 6.7 Northridge, California, earthquake by its predecessors," *Science*, 265.5177: 1432-1435, 1994, doi: 10.1126/science.265.5177.14.

[59] R.S. Stein, A.A. Barka, J.H. Dieterich, "Progressive failure on the North Anatolian fault since 1939 by earthquake stress triggering," *Geophysical Journal International*, 128.3: 594-604, 1997, doi.org/10.1111/j.1365-246X.1997.tb05321.x.

[60] G.C.P. King, R.S. Stein, J. Lin, "Static stress changes and the triggering of earthquakes," *Bulletin of the Seismological Society of America*, 84.3: 935-953, 1994, doi.org/10.1785/BSSA0840030935.

[61] G.C.P. King, "Fault interaction, earthquake stress changes, and the evolution of seismicity," *Earthquake Seismology*, 4: 225-255, 2007, doi.org/ 10. 1016/ B978- 04445 2748-6. 00069-9.

[62] A. Hubert, G. King, R. Armijo, B. Meyer, & D. Papanastasiou, "Fault re-activation, stress interaction and rupture propagation of the 1981 Corinth earthquake sequence," *Earth and Planetary Science Letters*, 142.3-4: 573-585, 1996, doi.org/10.1016/0012-821X(96)00108-2.

[63] R.A. Harris, "Introduction to special section: Stress triggers, stress shadows, and implications for seismic hazard," *Journal of Geophysical*

Res: Solid Earth, 103.B10:24347-24358, 1998, doi.org/10.1029/98JB01576.

[64] S.S. Nalbant, A. Hubert, G.C.P. King, "Stress coupling between earthquakes in northwest Turkey and the north Aegean Sea," *Journal of Geophysical Research: Solid Earth*, 103.B10: 24469-24486, 1998, doi.org/10.1029/98JB01491.

[65] S. Toda, R.S. Stein, P.A. Reasenberg, J.H. Dieterich, & A. Yoshida, "Stress transferred by the 1995 Mw= 6.9 Kobe, Japan, shock: Effect on aftershocks and future earthquake probabilities," *Journal of Geophysical Research: Solid Earth*, 103.B10: 24543-24565, 1998, doi.org/10.1029/98JB00765

[66] A. Hubert-Ferrari, A. Barka, E. Jacques, S.S. Nalbant, B. Meyer, R. Armijo & G.C. King, "Seismic hazard in the Marmara Sea region following the 17 August 1999 Izmit earthquake," *Nature*, March 2000, 404.6775: 269-273.

[67] F. Pollitz, M. Vergnolle, E. Calais, "Fault interaction and stress triggering of twentieth century earthquakes in Mongolia," *Journal of Geophysical Research: Solid Earth*, 108.B10, 2003, doi.org/10.1029/2002JB002375.

[68] J. Lin and R.S. Stein, "Stress triggering in thrust and subduction earthquakes and stress interaction between the southern San Andreas and nearby thrust and strike- slip faults," *Journal of Geophysical Research: Solid Earth*, 109.B2, 2004, doi.org/10.1029/2003JB002607.

[69] T. Parsons and D.S. Dreger, "Static- stress impact of the 1992 Landers earthquake sequence on nucleation and slip at the site of the 1999 M= 7.1 Hector Mine earthquake, southern California," G*eophysical research letters*, 27.13: 1949-1952, 2000, doi.org/10.1029/1999GL011272

[70] M. Wyss and S. Wiemer, "Change in the probability for earthquakes in southern California due to the Landers magnitude 7.3 earthquake," *Science*, 290.5495: 1334-1338, 2000, doi: 10.1126/science.290.5495.13.

[71] H. Durmuş, "İran depremlerinin faylanma özelliklerinin ve deprem gerilme etkileşimlerinin modellenmesi." Doktora Tezi, Sakarya Üniversitesi Fen Bilimleri Enstitüsü, 2014.

[72] M. Utkucu, H. Durmuş, S. Nalbant, "Stress history controls the spatial pattern of aftershocks: case studies from strike-slip earthquakes," *International Journal of Earth Sciences*, 106: 1841-1861, 2017, doi.org/10.1007/s00531-016-1389-x.

[73] S.H. Hartzell and T.H. Heaton, "Inversion of strong ground motion and teleseismic waveform data for the fault rupture history of the 1979 Imperial Valley, California, earthquake," *Bulletin of the Seismological Society of America*, 73.6A: 1553-1583, 1983, doi.org/10.1785/BSSA07306A1553.

[74] S.H. Hartzell, G.S. Stewart, C. Mendoza, "Comparison of L 1 and L 2 norms in a teleseismic waveform inversion for the slip history of the Loma Prieta, California, earthquake," *Bulletin of the Seismological Society of America*, 81.5: 1518-1539, 1991, doi.org/10.1785/BSSA0810051518.

[75] D.J. Wald, D.V. Helmberger, T.H. Heaton, "Rupture model of the 1989 Loma Prieta earthquake from the inversion of strong-motion and broadband teleseismic data," *Bulletin of the Seismological Society of America*, 81.5: 1540-1572, 1991, doi.org/10.1785/BSSA0810051540.

[76] D.J. Wald and T.H. Heaton, "Spatial and temporal distribution of slip for the 1992 Landers, California, earthquake," *Bulletin of the Seismological Society of America*, 84.3: 668-691, 1994, doi.org/10.1785/BSSA0840030668.

[77] C. Mendoza, "Coseismic slip of two large Mexican earthquakes from teleseismic body waveforms: Implications for asperity interaction in the Michoacan plate boundary segment," *Journal of Geophysical Research: Solid Earth*, 98.B5: 8197-8210, 1993, doi.org/10.1029/93JB00021.

[78] C. Mendoza, "Finite-fault analysis of the 1979 March 14 Petatlan, Mexico, earthquake using teleseismic P waveforms," *Geophysical Journal International*, 121.3: 675-683, 1995.

[79] M. Utkucu, *et al.* "Slip distribution and stress changes associated with the 1999 November 12, Düzce (Turkey) earthquake (Mw= 7.1)," *Geophysical Journal International*, 153.1: 229-241, 2003.

[80] C.A. Langston and D.V. Helmberger, "A procedure for modelling shallow dislocation sources," *Geophysical Journal International*, 42.1: 117-130, 1975, doi.org/10.1111/j.1365-246X.1975.tb05854.x.

[81] C. Mendoza, & S.H. Hartzell, 1988. Inversion for slip distribution using teleseismic Pwaveforms: North Palm Springs, Borah Peak and Michoacan earthquakes, *Bull. seism. Soc. Am.,* 78, 1092–1111.

[82] W. Menke, "Geophysical Data Analysis: Discrete Inverse Theory," International Geophysics Series, Vol. 45, Academic Press, Inc., San Diego, California 92101, ISBN -0-12-490921-3, 1989.

[83] S.S. Nalbant, A.A. Barka, Ö. Alptekin, "Failure stress change caused by the 1992 Erzincan earthquake (Ms= 6.8)," *Geophysical research letters*, 23.13: 1561-1564, 1996, doi.org/10.1029/96GL01323.

[84] R. S. Stein, "The role of stress transfer in earthquake occurrence," *Nature*, 402.6762: 605-609, 1999, doi.org/10.1038/45144.

[85] S. Toda and R.S. Stein, "Toggling of seismicity by the 1997 Kagoshima earthquake couplet: a demonstration of time-dependent stress transfer," *Journal of Geophysical Res.: Solid Earth*, 108. B12, 2003, doi.org/10.1U029/2003JB002527

[86] O. Heidbach and Z. Ben-Avraham, "Stress evolution and seismic hazard of the Dead Sea fault system," *Earth and Planetary Science Letters*, 257.1-2: 299-312, 2007, doi.org/10.1016/j.epsl.2007.02.042.

[87] X. Liu, Q. Chen, Y. Yang, Q. Xu, J. Zhao, L. Xu, & R. Liu, "The 2021 Mw7. 4 Maduo earthquake: Coseismic slip model, triggering effect of historical earthquakes and implications for adjacent fault rupture potential," *Journal of Geodynamics*, 151: 101920, 2022, doi.org/10.1016/j.jog.2022.101920.

[88] M. Utkucu, F. Uzunca, H. Durmuş, S.S. Nalbant, C. İpek, & Ş. Ramazanoğlu, "The M w= 5.8 2019 Silivri earthquake, NW Türkiye: is it a warning beacon for a big one?," *International Journal of Earth Sciences*, 2024, 113.1: 107-124.

[89] C. Liu, P. Dong, Y. Shi, "Stress change from the 2015 Mw 7.8 Gorkha earthquake and increased hazard in the southern Tibetan Plateau," *Physics of the Earth and Planetary Interiors*, 267: 1-8, 2017, doi.org/10.1016/j.pepi.2017.04.002.

[90] W.D. Barnhart, G.P. Hayes, R.D. Gold, "The July 2019 Ridgecrest, California, earthquake sequence: Kinematics of slip and stressing in cross- fault ruptures," *Geophysical Research Letters*, 46.21: 11859-11867, 2019, doi.org/10.1029/2019GL084741

[91] S. Li, G. Chen, T. Tao, P. He, K. Ding, R. Zou,... & Q. Wang, "The 2019 M w 6.4 and M w 7.1 Ridgecrest earthquake sequence in eastern California: Rupture on a conjugate fault structure revealed by GPS and InSAR measurements," *Geophysical Journal International*, 221.3: 1651-1666, 2020, doi.org/10.1093/gji/ggaa099.

[92] D.E. Goldberg, D. Melgar, V.J. Sahakian, A.M. Thomas, X. Xu, B.W. Crowell, & J Geng, "Complex rupture of an immature fault zone: A simultaneous kinematic model of the 2019 Ridgecrest, CA earthquakes," *Geophysical Research Letters*, 47.3, 2020, doi.org/10.1029/2019GL086382.

[93] S. Steacy, J. Gomberg, M. Cocco, "Introduction to special section: Stress transfer, earthquake triggering, and time- dependent seismic hazard," *Journal of Geophysical Research: Solid Earth*, 110.B5, 2005, doi.org/10.1029/2005JB003692.

[94] P.S. Raju, V.K. Gahalaut, K.M. Ravi, "Phodong (Sikkim) earthquake of 14 February 2006 and its aftershocks-Coulomb stress analysis," *Journal of Geodynamics*, 46.1-2: 63-67, 2008, doi.org/10.1016/j.jog.2008.04.001.

[95] S. Lasocki, V.G. Karakostas, E.E. Papadimitriou, "Assessing the role of stress transfer on aftershock locations," *Journal of Geophysical Research: Solid Earth*, 114.B11, 2009, doi.org/ 10.1029/2008JB006022.

[96] T. Sato, S. Hiratsuka, J. Mori, "Coulomb stress change for the normal-fault aftershocks triggered near the Japan Trench by the 2011 M w 9.0 Tohoku-Oki earthquake," *Earth, planets and space*, 64: 1239-1243, 2012, doi.org/10.5047/eps.2012.04.003.

[97] M. Cocco, C. Nostro, G. Ekström, "Static stress changes and fault interaction during the 1997 Umbria-Marche earthquake sequence," *Journal of Seismology*, 4: 501-516, 2000, doi.org/10.1023/A:1026507917308.

[98] S. Steacy, D. Marsan, S.S. Nalbant, & J. McCloskey, "Sensitivity of static stress calculations to the earthquake slip distribution," J*ournal of Geophysical Research: Solid Earth*, 2004, 109.B4, doi.org/10.1029/2002JB002365.

[99] Y. Okada, "Internal deformation due to shear and tensile faults in a half-space," *Bulletin of the seismological society of America*, 82.2: 1018-1040, 1992, doi.org/10.1785/BSSA0820021018.

[100] S. Toda, R.S. Stein, K.R. Dinger, S. Bozkurt, "Forecasting the evolution of seismicity in southern California: Animations built on earthquake stress transfer," *Journal of Geophysical Research: Solid Earth*, 110.B5, 2005, doi.org/10.1029/2004JB003415

[101] D.L. Wells and K.J. Coppersmith, "New empirical relationships among magnitude, rupture length, rupture width, rupture area, and surface displacement," *Bulletin of the seismological Society of America*, 84.4: 974-1002, 1994, https://doi.org/10.1785/BSSA0840040974

[102] Ö., Emre, T. Y., Duman, S., Özalp, F., Şaroğlu, Ş., Olgun, H., Elmacı, & T. Çan, "Active fault database of Turkey," *Bulletin of Earthquake Engineering*, 16.8: 3229-3275, 2018, doi.org/10.1007/s10518-016-0041-2.

[103] M. Utkucu, F. Uzunca, H. Durmuş, S. Nalbant, & S. Sert, "The 2023 Pazarcık (Mw=7.8) and Elbistan (Mw=7.6), Kahramanmaraş Earthquakes in the southeast, Türkiye", [Online], http://www.aym.sakarya.edu.tr/2023/02/24/the-2023-pazarcik-mw7-8-and-elbistan-mw7-6-kahramanmaras-earthquakes-in-the-southeast-turkiye/ 22 February 2023, [Access date: 25 January 2024].

[104] M. Meghraoui, F. Gomez, R. Sbeinati, J. Van der Woerd, M. Mouty, A.N. Darkal, & M. Barazangi, "Evidence for 830 years of seismic quiescence from palaeoseismology, archaeoseismology and historical seismicity along the Dead Sea fault in Syria," *Earth and Planetary Science Letters*, 210.1-2: 35-52, 2003, doi.org/10.1016/S0012-821X(03)00144-4.

[105] P. Wessel and W.H.F. Smith, "New, improved version of Generic Mapping Tools released," *Eos, Transactions American Geophysical Union*, 79.47: 579-579, 1998, doi.org/10.1029/98EO00426.

RESEARCH ARTICLE

Mathematical modelling and performance analysis of an AEM electrolyzer

Salih Obut[a],*

aYildiz Technical University,Department of Mechatronics Engineering, İstanbul 34349, Türkiye, sobut@yildiz.edu.tr
ORCID: 0000-0002-9833-8151

Abstract

In this study, an analytical model including electrochemical reactions and mass transfer in an anion-exchange membrane electrolyzer (AEMEL) has been developed by considering water sorption/desorption in electrodes. The model developed was used to investigate the performance of the AEMEL in terms of efficiency, transport phenomena and operating parameters. The numerical results revealed that the voltage losses in the AEMEL are mainly due to activation losses. The effects of important parameters such as membrane thickness, operating pressure on cell performance, and species transport were also investigated. The results also revealed that the AEMEL performance improves with decreasing membrane thickness, but the membrane thickness should be considered together with hydrogen permeability and differential operating pressure to operate the electrolyzer safely.

1. Introduction

Hydrogen is defined as the clean energy carrier of the future. Hydrogen presents several benefits over fossil fuels as an energy carrier; one of them is the hydrogen energy content (120 MJ/kg), which is higher than most fuels (e.g.

* Corresponding author. Tel.: +90-535-884-2154; fax: +90-212-383-2975.
  E-mail address: sobut@yildiz.edu.tr

.

natural gas 48.7 MJ/kg). In addition, the use of hydrogen in industry has the potential to eliminate the greenhouse gas emission problems caused by the use of fossil fuels.

Hydrogen can be produced from fossil-based sources as well as water by various methods such as thermal, photocatalytic etc. processes. Nowadays, electrolysis of water with renewable energy sources is seen as a sustainable and cost-effective solution for green hydrogen production and intensive research and development activities are carried out on electrolyzers [1,2].

There are three important low-temperature electrolyzer technologies in hydrogen production; alkaline electrolyzer (AEL), proton-exchange membrane electrolyzer (PEMEL) and anion-exchange membrane electrolyzer (AEMEL). AELs are seen as the most mature technology. Although they are economical in initial investment cost, they require high electrolyte concentrations, and purification and pressurization of hydrogen at the electrolyzer exit. Compared to AEL technology, PEMELs have the advantage of high hydrogen outlet pressure and high purity due to the use of membrane as the anode-cathode separator material in their structures. However, materials, such as Pt, Pd, and Ir, used in PEMELs significantly increase the initial investment costs of these electrolyzers. On the other hand, AEMELs are seen as an alternative that combines the advantages of both alkaline and PEMELs. AEMEL, like PEMEL, have a membrane as separator in their structure and therefore can provide hydrogen of high purity and pressure at the output. Additionally, unlike AEL, they can be operated with a very low concentration of electrolyte solution, that reduces corrosion, and with lower priced catalysts based on Cu, Ni, Co, and Fe. Therefore, due to these advantages among electrolyzer technologies, intensive research and development studies are carried out on AEM electrolyzer in the last decades.

Mathematical modelling is an important tool used in improving the performance and examining the behavior of complex physicochemical processes. Design and optimization of AEMELs, which are still at low technology readiness level (TRL), through mathematical modeling are gaining importance. There are limited number of publications in the literature on modelling AEMELs [3-8]. An et al. [3] examined the effects of liquid saturation, exchange current density and membrane thickness on the performance of an AEMEL. Nafchi et al. [4] investigated different parameters such as cell temperature and cathode pressure levels of AEM. Vidales et al. [5] developed a model that considers mass transfer and electrochemistry together to evaluate the effects of electrolyzer parameters. The model was then validated and effect of the operating parameters of electrolyzer such as electrolyte concentration, temperature, and operating pressure were evaluated. Liu et al. [6] presented a two-phase one-dimensional AEMEL model that is extended from their previous work. The results indicated that electrolyte concentration has more impact on oxygen evolution reaction (OER) kinetics than AEM conductivity. Stainslaw et al. [7] analyzed the effect of electrolyte composition and they found that the conductivity of membrane has insignificant impact on the electrolyzer performance. Kim et al. [8] presented a deterministic model and a feasibility analysis of a 10 MW AEMEL system. The results revealed that the levelised cost of hydrogen (LCOH) of AEMEL would be comparable to that of PEMEL when the lifetime of AEMEL is brought to the same level as PEMEL.

In the present study, an isothermal analytical model is proposed to assess the performance of an AEMEL. The developed model considers transport within gas phase, liquid phase and ionomer/membrane phase together with electrochemical effects. In contrast to the lumped models in the literature, the model was developed to include the ionomer phase sorption/desorption rates explicitly. In this way, it is possible to model the decrease of membrane water content on the cathode electrode due to increasing current density, i.e. electro-osmotic drag effect, and thus the loss of performance of AEMEL. The model is then used to predict current-voltage polarization, efficiency and product stream compositions of the electrolyzer. The governing model equations were solved in the MATLAB environment and the model was validated with literature data. The performance of the electrolyzer was analyzed for different membrane thicknesses and different operating pressures through parametric analysis.

2. Mathematical model

The AEM electrolyzer model can be obtained by combining the mass transport and the electrochemical model equations. The electrochemical model equations are written for prediction of the operating voltage of the cell, considering voltage losses in the cell, such as activation losses, ohmic losses, etc. The mass transport equations are used to predict the transport of water across the membrane, the consumption production rates of the components at the anode and at the layer, and the transport of OH⁻ and water molecules across the membrane. By solving set of these coupled equations, the cell voltage, efficiency and product gas stream compositions can be predicted at different current densities.

A typical AEM electrolyzer cell has a membrane, anode and cathode electrodes (catalyst and diffusion layers) and bipolar plates on which flow channels are engraved. The electrolyte solution, i.e. typically aqueous KOH solution, is fed to the electrolyzer anode side while no solution is delivered to the electrolyzer cathode side. The water in the electrolyte solution in anode is transferred to the other side of the membrane to meet the water demand of the hydrogen evolution reaction (HER). The water transferred to the cathode side is reduced to hydroxide and hydrogen by the HER in the electrode (Equation 1). The resulting hydroxide ions pass to the anode side through the AEM and are oxidized in the anode electrode (Equation 2) to release oxygen (Fig. 1). Oxygen and hydrogen formed within the two sides of the electrolyzer leave the electrolyzer cell through the flow channels in the bipolar plates. Fluid flow in the anode flow channels is multiphase (i.e. mostly oxygen + KOH solution), whereas in the cathode flow channels, which are not supplied with KOH solution, only gas-phase flow is present (dry operation).

Anode: $$2OH^- \rightarrow H_2O + \frac{1}{2}O_2 + 2e^- \qquad (1)$$

Cathode: $$2H_2O + 2e^- \rightarrow 2OH^- + H_2 \qquad (2)$$
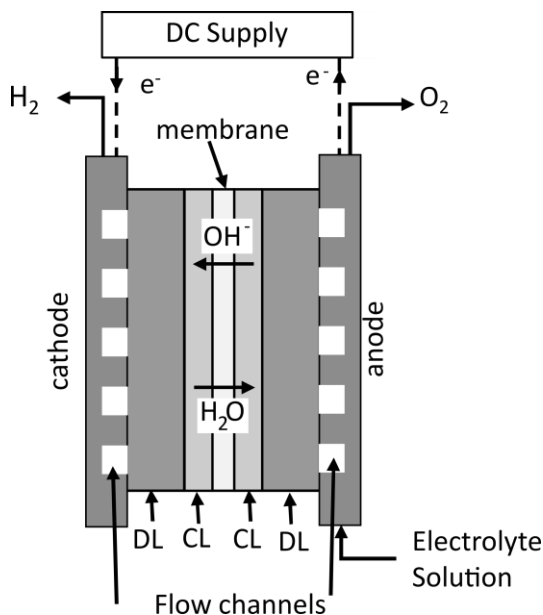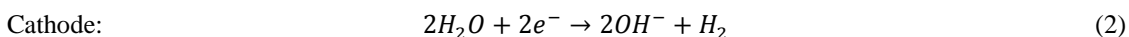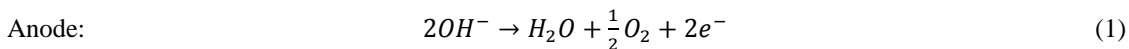
Fig. 1. Structure of a single cell AEMEL.

2.1. Electrochemical equations

The electrochemical behavior of an electrolyzer can be described by the following current-voltage (I-V) model, including the most important voltage losses that determine the cell voltage, E_{cell}

$$E_{cell} = E_{rev} + \eta_{act} + \eta_{ohm} + \eta_{conc} \tag{3}$$

where E_{rev} is the reversible cell voltage, η_{act} is the activation losses or overpotential, η_{ohm} is the ohmic losses or overpotential, and η_{conc} is the mass transfer losses or overpotential. The other overpotentials such as bubble overpotential etc. were neglected.

The reversible cell voltage, $E_{rev}(T,P)$, of an electrolyzer system in which hydrogen and oxygen evolution reactions present is governed by the Nernst equation

$$E_{rev}(T,P) = E_{rev}^0(T) + \frac{RT}{2F} ln \left(\frac{\Pi p_p}{\Pi p_r} \right) \tag{4}$$

where $E_{rev}^0(T)$ is the reversible cell voltage (V), R is the ideal gas constant, F is Faraday's constant, p_r and p_p are reactants and products partial pressures. Reversible cell potential, $E_{rev}^0(T)$ in voltage, can be calculated by using [9]

$$E_{rev}^0(T) = 1.481 - 0.000846T(K) \tag{5}$$

for $H_2O_{(l)}$ at 25°C. The reversible cell voltage, $E_{rev}(T,P)$ in V, is given as a function of pressure and temperature [9]

$$E_{rev}(T,P) = 1.481 - 0.000846T(K) + 0.0000431T(K)ln \left(\frac{p_{H_2}p_{O_2}^{0.5}}{p_{H_2O}} \right) \tag{6}$$

where p_{H_2}, p_{O_2}, and p_{H_2O} are corresponding species partial pressures, respectively. The activation overpotential, η_{act}, is the potential required to overcome the activation energies of the HER and OER occurred at cathode and at anode of an electrolyzer. The activation overpotential can be explicitly calculated as follows

$$\eta_{act} = \eta_{act,an} + \eta_{act,ca} = \frac{RT}{\alpha_{an}F} \, arcsinh \left(\frac{i}{2j_{o,an}} \right) + \frac{RT}{\alpha_{ca}F} \, arcsinh \left(\frac{i}{2j_{o,ca}} \right) \tag{7}$$

where α represents the charge coefficient and j_o represents the apparent exchange current density value which is function of the physical properties of electrodes, i.e. roughness, and the exchange current density at reference temperature and operating temperature [10].

The ohmic overpotential, η_{ohm}, is arising due to the current-carrying components resistance to electron transport and ion-conducting media resistance to ion transport. The ohmic overpotential is given by Ohm's law

$$\eta_{ohm} = R_{cell}I = (R_{el} + R_{ion})I \tag{8}$$

where R_{cell} is the ohmic resistance of the cell and I is the current. In Equation 8, R_{el} is the resistance of electron conducting media, i.e. bipolar plates and electrodes, and R_{ion} is the total resistance of ion conducting media, i.e. ionomer phase and electrolyte solution in electrodes and membrane, within cell. In this study, because electron

transport resistances are expected to be lower than that of ion transport resistances, for simplicity, only the resistance of ion conducting media is considered

$$R_{ion} = R_{mem} + R_{ion,an} + R_{ion,ca} \tag{9}$$

where R_{mem}, $R_{ion,an}$, and $R_{ion,ca}$ corresponds ionic resistances of membrane, anode catalyst layer (ACL) and cathode catalyst layer (CCL), respectively, i.e. ionomer and electrolyte resistances for anode and only ionomer resistance in cathode. Resistance of membrane is given by

$$R_{mem} = \frac{\delta_{mem}}{\sigma_{mem}A} \tag{10}$$

where δ_{mem} is the membrane thickness, σ_{mem} is the membrane conductivity and A represents cell active area. Similarly, catalyst layer (CL) ionic resistances are calculated by

$$R_{ion,an} = \left[\frac{\delta_{CL}}{\sigma_{ion}^{eff}A} + \frac{\delta_{CL}}{\sigma_{KOH}^{eff}A}\right]^{-1} \tag{11}$$

$$R_{ion,ca} = \frac{\delta_{CL}}{\sigma_{ion}^{eff}A} \tag{12}$$

where δ_{CL} is the CL thickness, σ_{ion}^{eff} and σ_{KOH}^{eff} are effective ionomer and electrolyte solution conductivities, respectively, that are corrected by Bruggeman relation [11]. In anode catalyst layer, it is assumed that resistance of ionomer phase and KOH solution was considered as parallel resistances.

The mass transfer overpotential, η_{conc}, represents the losses due to diffusion processes and sometimes called as concentration losses or overpotential. In this study, it is assumed that concentration overpotential is negligible; therefore, this term is neglected in the present model.

2.2. Mass transport equations

The mass transfer in the AEM electrolyzer cell was obtained by writing the mass balances of each species for each phase in anode, cathode, and membrane. On the anode side, mass balances of H_2, O_2 and H_2O in the gas phase and mass balances of KOH and water in the liquid phase were considered. On the cathode side, mass balances were established for H_2 and H_2O in the gas stream. In order to resolve H_2O transport between two sides of the electrolyzer cell, mass balance of dissolved water in ionomer/membrane was established for ACL and CCL and membrane. Furthermore, the mass balances were linked to the electrochemical model by means of the production and consumption rate equations of hydrogen, oxygen and water in the ACL and CCL.

The molar generation rate and consumption rate of H_2, O_2 and H_2O can be written according to Faraday's law. For the anode side where O_2 and H_2O generated

$$N_{O_2,an}^{gen} = \frac{I}{4F} \tag{12}$$

$$N_{H_2O,an}^{gen} = \frac{I}{2F} \tag{13}$$

and for cathode side where H_2 generated and H_2O consumed

$$N_{H_2,ca}^{gen} = \frac{I}{2F} \tag{14}$$

$$N_{H_2O,ca}^{cons} = \frac{I}{F} \tag{15}$$

The mass balance of species in anode side can be written for gas and liquid phases separately. For gas phase, hydrogen balance is

$$N_{H_2,an}^{in} - N_{H_2,an}^{out} + N_{H_2,mem}^{perm} = 0 \tag{16}$$

where superscripts *in* and *out* represents inlet and outlet flow rates. Hydrogen crossover through the membrane, $N_{H_2,mem}^{perm}$, is given by

$$N_{H_2,mem}^{perm} = k_{H_2} \frac{A}{\delta_{mem}} (P_{ca} - P_{an}) \tag{17}$$

where k_{H_2} is the permeability of hydrogen, P_{ca} and P_{an} are cathode and anode pressures. For gas phase, O_2 balance is

$$N_{O_2,an}^{in} - N_{O_2,an}^{out} + N_{O_2,an}^{gen} = 0 \tag{18}$$

where O_2 generation is given by Equation 12. Similarly, for the gas phase H_2O mass balance

$$N_{H_2O,an}^{in} - N_{H_2O,an}^{out} + N_{H_2O,an}^{phase} = 0 \tag{19}$$

where $N_{H_2O,an}^{phase}$ account for water transfer from liquid phase to gas phase in anode side. In this model, because aqueous KOH solution is fed to the anode side, it is assumed that the anode outlet gas is saturated with water until it leaves the cell. With the aid of this assumption, the mass transfer rate from liquid phase to gas phase, $N_{H_2O,an}^{phase}$, was calculated during the simultaneous solution of the anode and cathode mass balances. For anode side liquid phase, KOH and water balances are written

$$N_{KOH,an}^{in} - N_{KOH,an}^{out} = 0 \tag{20}$$

$$N_{H_2O_l,an}^{in} - N_{H_2O_l,an}^{out} - N_{H_2O,an}^{phase} - N_{H_2O,an}^{sorp} = 0 \tag{21}$$

where $N_{H_2O,an}^{sorp}$ represent water transfer from liquid phase to ionomer phase within ACL. Because aqueous KOH solution was fed to the anode side, the ionomer in the ACL was considered fully saturated. Again, similar to the liquid-gas water transfer rate in anode, the sorption rate of water will be calculated by solving two side mass balances above simultaneously.

The mass balance for cathode side of the cell can be written. For gas phase, H_2 and H_2O balances are given below

$$N_{H_2,ca}^{in} - N_{H_2,ca}^{out} + N_{H_2,ca}^{gen} - N_{H_2,mem}^{perm} = 0 \tag{22}$$

$$N_{H_2O,ca}^{in} - N_{H_2O,ca}^{out} + N_{H_2O,ca}^{desorp} = 0 \tag{23}$$

where $N_{H_2O,ca}^{desorp}$ is the desorption rate of dissolved water from ionomer phase to gas phase which is given by

$$N_{H_2O,ca}^{desorp} = \gamma_{dw}(C_{dw,ca} - C_{dw,ca}^{eq})V_{CL,ca} \tag{24}$$

Rate constant for membrane/ionomer desorption/sorption process, γ_{dw}, is taken as 100 s^{-1} [12,13]. The actual and the equilibrium dissolved water concentrations are denoted by $C_{dw,ca}$ and $C_{dw,ca}^{eq}$, respectively. Catalyst layer volume, $V_{CL,ca}$, is simply product of active area and cathode catalyst layer thickness. Equilibrium dissolved water concentration can be calculated by [14]

$$C_{dw}^{eq} = p_m \lambda^{eq} \tag{25}$$

where p_m is the product of membrane dry density, ρ_{dry}, and ion exchange capacity (IEC) and λ^{eq} is the equilibrium water content, that is defined as the number of water molecules per positively charged (cationic) functional groups (FG) within membrane [15].

The dissolved water transport through membrane/ionomer can be written in terms of diffusion, electro-osmotic drag (EOD) effect, and hydraulic pressure (HP) effect. Thus, net rate of dissolved water transport from ACL to CCL

$$N_{H_2O,mem}^{net} = N_{H_2O,mem}^{diff} - N_{H_2O,mem}^{eod} - N_{H_2O,mem}^{perm} \tag{26}$$

where $N_{H_2O,mem}^{net}$ is the rate of net molar transport of dissolved water, $N_{H_2O,mem}^{diff}$ is the molar transport rate of dissolved water by diffusion from ACL to CCL, $N_{H_2O,mem}^{eod}$ is the rate of molar transport H_2O from CCL to ACL due to EOD and $N_{H_2O,mem}^{perm}$ is the molar transport rate of dissolved water from the CCL to the ACL due to the pressure differential.

The diffusion rate of water is calculated by Fick's law in the CCL assuming fully hydrated conditions for membrane

$$N_{H_2O,mem}^{diff} = N_{H_2O,ca}^{diff} = D_w A(C_{dw,mem}^{eq} - C_{dw,ca})/\delta_{CL,ca}^{eff} \tag{27}$$

where D_w is the water diffusion coefficient of in the ionomer phase, $\delta_{CL,ca}^{eff}$ is the effective diffusion path within CCL, which is taken to be half of the thickness of the cathode catalyst layer. $C_{dw,mem}^{eq}$ is the equilibrium dissolved water concentration within wet membrane and $C_{dw,ca}$ is the dissolved water concentration in the ionomer phase of CCL.

The H_2O transport due to EOD is related to the flux of hydroxides migrating from the CCL to ACL through the AEM and can be expressed as

$$N_{H_2O,mem}^{eod} = n_d \frac{I}{F} \tag{27}$$

where n_d is the EOD coefficient (mol H$_2$O / mol OH$^-$). Electro-osmotic drag coefficient is function of H_2O content of ionomer/membrane and for the simplicity it is taken as 5 mol H$_2$O / mol OH$^-$ [16].

The H_2O transport rate from the CCL to the ACL through the membrane can be calculated using Darcy's law

$$N_{H_2O,mem}^{perm} = K_D \frac{A}{\delta_{mem}} (P_c - P_a) \frac{\rho_{H_2O}}{\mu_{H_2O}}$$ (28)

where K_D is the H_2O permeability of membrane.

Dissolved water balance for anode side can be written in terms of net molar transport rate of dissolved water as

$$N_{H_2O,an}^{sorp} + N_{H_2O,an}^{gen} - N_{H_2O,mem}^{net} = 0$$ (29)

where $N_{H_2O,an}^{gen}$ is the generation of water by Equation 1 in anode. Similarly, for cathode dissolved water balance can be written

$$N_{H_2O,mem}^{net} - N_{H_2O,ca}^{cons} - N_{H_2O,ca}^{desorp} = 0$$ (30)

where $N_{H_2O,ca}^{cons}$ is the consumption of water by Equation 2 in cathode.

2.3. Solution methodology

Mass transport model and electrochemical model given in the previous section were solved by MATLAB. The baseline model and operating parameters are given in Table 1 and Table 2, respectively. In the next section, the validation of model and series of parametric analysis regarding the AEMEL performance are presented.

Table 1. The model parameters.

Parameter	Value	Unit	Reference
R	8.314	J mol^{-1} K^{-1}	
F	96,485.3	A s mol^{-1}	
Density of water, ρ_{H_2O}	998.04	kg m^{-3}	
Water viscosity, μ_{H_2O}	5.465×10^{-4}	kg m^{-1} s^{-1}	
Membrane Darcy water permeability, K_D	1×10^{-20}	m^2	[17], [18]
Vapor equilibrated membrane water content, λ	Eqns. 27-29 in [16]	$\frac{mol\ H_2O}{mol\ FG}$	[16]
Wet membrane water content, λ^{eq}	18.5	$\frac{mol\ H_2O}{mol\ FG}$	[16]
Apparent OER exchg. current density, $j_{0,an}$	1.9	mA cm^{-2}	[19]
Apparent HER exchg. current density, $j_{0,ca}$	5.6×10^{-2}	mA cm^{-2}	[20]
Diffusion coefficient of water, D_w	Eqns. 30-31 in [16]	m^2 s^{-1}	[16]
Electro-osmotic drag coefficient, n_d	5	$\frac{mol\ H_2O}{mol\ OH^-}$	[16]
Thickness of membrane, δ_{mem}	28	μm	[16]
Membrane IEC	1.8	meq g^{-1}	[16]
ACL thickness, $\delta_{CL,an}$	30	μm	Assumption
CCL thickness, $\delta_{CL,ca}$	15	μm	Assumption
ACL porosity, $\epsilon_{CL,an}$	0.2		Assumption
CCL porosity, $\epsilon_{CL,ca}$	0.1		Assumption
Ionomer volume fraction of ACL, $\epsilon_{ion,CL,an}$	0.6		Assumption
Ionomer volume fraction of CCL, $\epsilon_{ion,CL,ca}$	0.6		Assumption
Hydrogen permeability, k_{H_2}	5.6×10^{-17}	mol s^{-1} cm^{-1} Pa^{-1}	[21]

| Conductivity of KOH solution | Eqn. 2 in [22] | S cm^{-1} | [22] |
| Cell active area, A | 25 | cm^2 | |

Table 2. AEMEL operating parameters.

Parameter	Value	Unit
Temperature, T	50	°C
Anode pressure, P_a	1	bar
Cathode pressure, P_a	1	bar
Concentration of KOH solution	10	mM
Feed flow rate of KOH solution	20	ml min^{-1}

3. Results and discussions

In this part, firstly, the validation of the model using literature data is presented. Then, the effects of parameters such as membrane thickness and operating pressure on the cell performance and species transport are presented.

3.1. Model validation

Before performing parametric analysis with the developed model, the predictive ability of the model was evaluated by comparing the polarization curve generated by the model with the experimental polarization curve of the dry cathode AEM electrolyzer in [23] under the same conditions. Fig. 2 shows that the polarization curve predicted by the model is in good agreement with the experimental data. In the next part, numerical results for the effects of operating pressure and of membrane thickness and are presented, respectively.
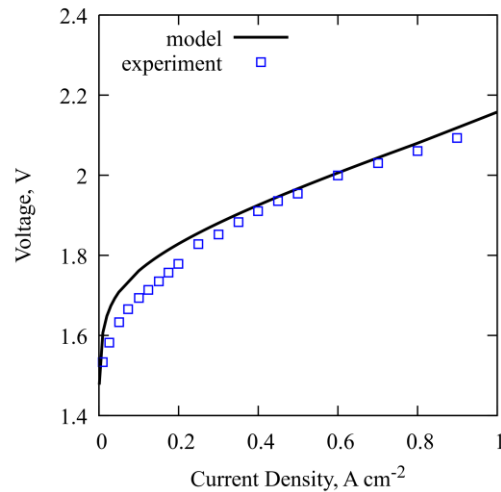
Fig. 2. Developed model polarization curve and experimental data [23].

3.2. Effect of membrane thickness

In AEMELs, membrane thickness has an impact on the ionic resistance of the cell, water transport, and hydrogen permeability through the membrane. While reducing the membrane thickness, it improves performance by reducing

the ionic resistance and increasing the amount of H_2O transported from the ACL to the CCL. It can also increase hydrogen transfer from the cathode side to the anode side for cells operating with a pressure difference between the cathode and anode. This could pose a safety issue and reduce Faraday efficiency. Therefore, cell polarization curves were estimated by using the validated model for two different cases where the membrane thickness was halved and doubled compared to the initial case. According to Fig. 3, the cell performance improves inversely proportional to the membrane thickness and the increase in performance with decreasing membrane thickness has been observed in many modeling [3, 5] and experimental studies [24-26] in the literature. Improvement is mainly due to ionic resistance, i.e. ohmic overpotential and this is evident from the increase in the slope of the polarization curve at high current densities. The effect of thickness of membrane was also studied for cells operating with a pressure difference between the cathode side and anode side. In this case, electrolyzer performance was predicted for 30 bar pressure difference ($\Delta P = P_c - P_a = 30\ bar$) between cathode and anode (Fig. 4). The results in Fig. 4(a) show that both Faraday efficiency and DC efficiency of the cell (based on higher heating value, HHV, of H_2) decreases with decreasing membrane thickness as a result of increasing hydrogen crossover (Fig. 4(b)). At 0.5 mA cm^{-2} current density and with 28 μm membrane thickness, anode product gas may contain 3.9% vol. hydrogen (Fig. 4(b)) which is very close to lower explosive limit (LEL) limit [27], 4% in 1 bar. For atmospheric operation, the amount of H_2 in O_2 was experimentally found to be about 0.14% vol. [23], however, H_2 permeation will be much higher for a pressure difference of 30 bar. Considering that the H_2 flux increases in direct proportion to the pressure difference, H_2 in O_2 is likely to be around 4% for 30 bar pressure difference operation, which agrees with the 3.9% value obtained from this modeling study. In order to reach hydrogen content in anode gas below LEL limit, current density values greater than approximately 1 A/cm^2 is required. For the safe operation of the AEM electrolyzer with a reasonable threshold, i.e. 2% below LEL limit, nearly 1 A cm^{-2} is required for membrane thickness of 28 μm.
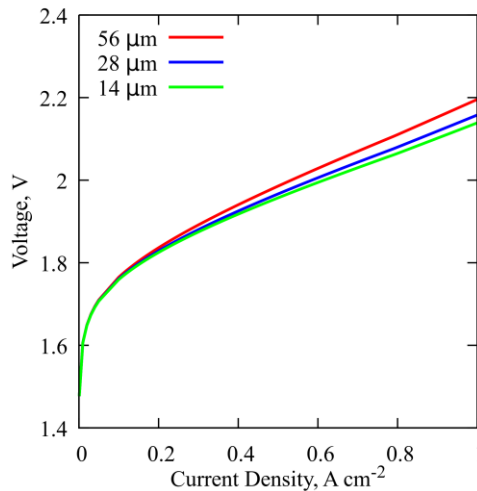
Fig. 3. Polarization curves for different membrane thicknesses.
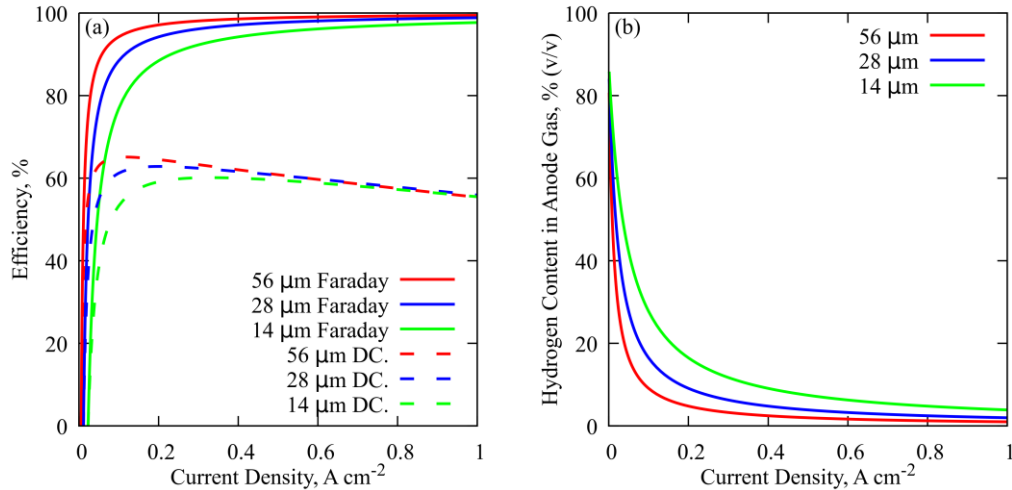
Fig. 4. (a) Faraday efficiency (continuous line) and DC efficiency (dashed line), (b) hydrogen mole percentages for different membrane thicknesses at 30 bar pressure difference between cathode side and anode side.

3.3. Effect of operating pressure

Another operating parameter that affects the performance of an AEM electrolyzer operating in dry cathode mode is the cathode and anode side pressure difference at the same membrane thickness. The cathode side pressure of AEMELs is tried to be kept high to prevent the need for additional pressurization of the produced hydrogen. However, this situation has negative effects. First, as it can be seen by the Nernst equation, the electrolyzer cell operating voltage increases as the effect of the increasing pressure difference. Additionally, increasing differential pressure increases the hydrogen cross-over from the cathode to the anode, reducing the Faraday efficiency. Finally, due to the increasing cathode-anode differential pressure, water transfer increases from cathode side to the anode side, and this can reduce the cathode side ionomer water content along with the decreasing relative humidity especially at high current densities. This increases the cell resistance to ion transport and causes performance decrease.

Effect of cathode-anode pressure difference on AEM electrolyzer performance is shown in Fig. 5(a). Because a high operating pressure directly increases the open circuit voltage, the cell polarization curve tends to increase at high pressure differences. However, while this effect is evident up to 15 bar pressure difference from atmospheric operation, it is not evident between 15 and 30 bar pressure difference. In their study, Nafchi et al. [4] also found that the cell operating voltage increased with increasing cathode side pressure and this increase was much less pronounced after 10 bar cathode pressure. Besides the effects of pressure increase, the increasing cathode-anode pressure difference increases the amount of water hydraulically passing from the cathode side to the anode side, thereby reducing the H_2O content of the cathode side ionomer phase and thus increasing the ohmic polarization. Additionally, the humidity of the cathode product gas will decrease as an effect of decreasing net water transport to the CCL. Water content of the CCL ionomer phase is shown in Fig. 5(b). As can be seen, with increasing cathode-anode pressure difference, the water content and therefore the conductivity of the cathode ionomer phase decreases. This can be understood from the fact that the polarization curves in Fig. 5(a) slope upward in the high current density region.
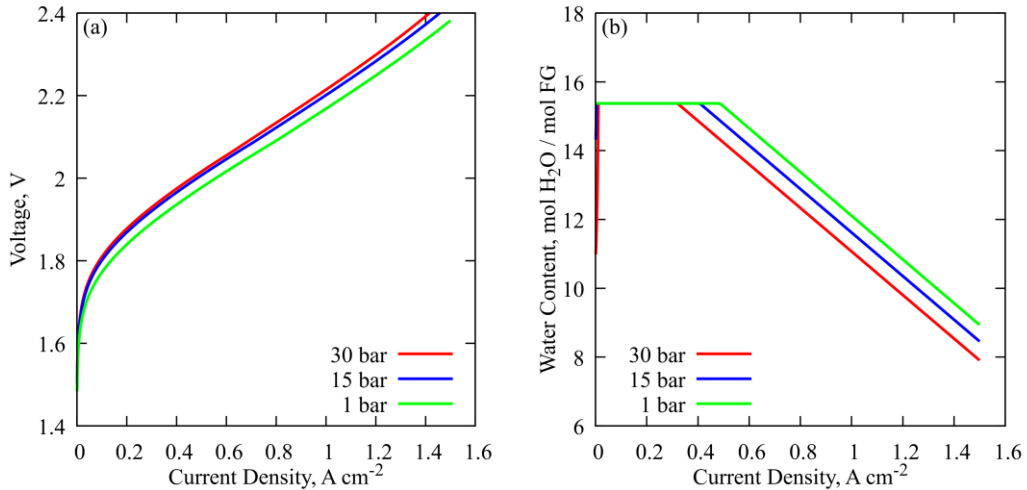
Fig. 5. (a) Polarization curves, (b) cathode side ionomer phase water contents for various pressure differential between cathode and anode.

4. Conclusions

In this study, an analytical model was developed to predict the performance of an AEMEL fed with aqueous KOH solution to anode. The developed model was validated with literature data and then analyses were carried out with the help of the model for two important parameters that determine the AEM electrolyzer performance. Accordingly, as the membrane thickness decreases, both the AEMEL cell voltage and the Faraday and DC efficiency of the cell decreases. Higher operating pressure of cathode side is one of the advantages of AEMEL technology, however, at high pressure differences between the cathode and anode side, such as 30 bar, a gas mixture with H_2 content above 4% vol. may form at the anode outlet, which poses a safety risk. Therefore, the most suitable membrane thickness should be selected according to the operating conditions by considering the compromise between cell voltage, efficiency and cell operating safety. On the other hand, when the pressure is increased at constant membrane thickness, it is found that the AEMEL polarization curves tend to increase upward more at high current densities above 1 A cm^{-2} as a result of decreased cathode side membrane water content. Thus, especially for large active area electrolyzer stacks drying of cathode side should be properly handled and this requires higher dimensional model of AEMEL to see the local drying effects. In order to better understand local effects at the cell level, studies are ongoing to adapt the model to two-dimensions and eventually to three-dimensions.

Author contribution

The writing of the manuscript and all analyses were performed by Salih Obut.

Acknowledgements

References

[1] IRENA, "World Energy Transitions Outlook 2023: 1.5°C Pathway," Abu Dhabi, 2023. [Online]. Available: https://www.irena.org/Publications/2023/Jun/World-Energy-Transitions-Outlook-2023 Accessed: Feb. 7, 2024.

[2] IEA, "Global Hydrogen Review 2023," Paris, 2023. [Online]. Available: https://www.iea.org/reports/global-hydrogen-review-2023. Accessed: Feb. 7, 2024.

[3] L. An, T. S. Zhao, Z. H. Chai, P. Tan, and L. Zeng, "Mathematical modeling of an anion-exchange membrane water electrolyzer for hydrogen production," *Int. J. Hydrogen Energy*, vol. 39, no. 35, pp. 19869-19876, 2014.

[4] F. M. Nafchi, E. Afshari, and E. Baniasadi, "Anion exchange membrane water electrolysis: Numerical modeling and electrochemical performance analysis," *Int. J. Hydrogen Energy*, vol. 52, pp. 306-321, 2024.

[5] A. G. Vidales, N. C. Millan, and C. Bock, "Modeling of anion exchange membrane water electrolyzers: The influence of operating parameters," *Chem. Eng. Res. Des.*, vol. 194, pp. 636-648, 2023.

[6] J. Liu, Z. Kang, D. Li, M. Pak, S. Alia, et al., "Elucidating the role of hydroxide electrolyte on anion-exchange-membrane water electrolyzer performance," *J. Electrochem. Soc.*, vol. 168, no. 5, p. 054522, 2021.

[7] L. N. Stanislaw, M. R. Gerhardt, and A. Z. Weber, "Modeling electrolyte composition effects on anion-exchange-membrane water electrolyzer performance," *ECS Trans.*, vol. 92, no. 8, p. 767, 2019.

[8] M. Kim, D. Lee, M. Qi, and J. Kim, "Techno-economic analysis of anion exchange membrane electrolysis process for green hydrogen production under uncertainty," *Energy Conv. Manage.*, vol. 302, p. 118134, 2024.

[9] C. Lamy and P. Millet, "A critical review on the definitions used to calculate the energy efficiency coefficients of water electrolysis cells working under near ambient temperature conditions," *J. Pow. Sour.,* vol. 447, p. 227350, 2020.

[10] V. Liso, G. Savoia, S. S. Araya, G. Cinti, and S. K. Kær, "Modelling and experimental analysis of a polymer electrolyte membrane water electrolysis cell at different operating temperatures," *Energies*, vol. 11, no. 12, p. 3273, 2018.

[11] W. Olbrich, T. Kadyk, U. Sauter, M. Eikerling, and J. Gostick, "Structure and conductivity of ionomer in PEM fuel cell catalyst layers: a model-based analysis," *Sci. Rep.*, vol. 13, no. 1, p. 14127, 2023.

[12] A. Vorobev, O. Zikanov, and T. Shamim, "A computational model of a PEM fuel cell with finite vapor absorption rate," *J. Pow. Sour.*, vol. 166, no. 1, pp. 92-103, 2007.

[13] H. Wu, X. Li, and P. Berg, "On the modeling of water transport in polymer electrolyte membrane fuel cells," *Electrochim. Acta*, vol. 54, no. 27, pp. 6913-6927, 2009.

[14] Y. Zheng, U. Ash, R. P. Pandey, A. G. Ozioko, et al., "Water uptake study of anion exchange membranes," *Macromolecules*, vol. 51, no. 9, pp. 3264-3278, 2018.

[15] M. L. Disabb-Miller, Z. D. Johnson, and M. A. Hickner, "Ion motion in anion and proton-conducting triblock copolymers," *Macromolecules*, vol. 46, no. 3, pp. 949-956, 2013.

[16] Y. S. Li, T. S. Zhao, and W. W. Yang, "Measurements of water uptake and transport properties in anion-exchange membranes," *Int. J. Hydrogen Energy*, vol. 35, no. 11, pp. 5656-5665, 2010.

[17] P. Trinke, B. Bensmann, S. Reichstein, R. Hanke-Rauschenbach, and K. Sundmacher, "Hydrogen permeation in PEM electrolyzer cells operated at asymmetric pressure conditions," *J. Electrochem. Soc.*, vol. 163, no. 11, p. F3164, 2016.

[18] X. Luo, A. Wright, T. Weissbach, and S. Holdcroft, "Water permeation through anion exchange membranes," *J. Pow. Sour.,* vol. 375, pp. 442-451, 2018.

[19] S. Fu, J. Song, C. Zhu, G. L. Xu, K. Amine, et al., "Ultrafine and highly disordered Ni2Fe1 nanofoams enabled highly efficient oxygen evolution reaction in alkaline electrolyte," *Nano Energy*, vol. 44, pp. 319-326, 2018.

[20] N. Mahmood, Y. Yao, J. W. Zhang, L. Pan, X. Zhang, et al., "Electrocatalysts for hydrogen evolution in alkaline electrolytes: mechanisms, challenges, and prospective solutions," *Adv. Sci.*, vol. 5, no. 2, p. 1700464, 2018.

[21] D. Henkensmeier, M. Najibah, C. Harms, J. Žitka, et al., "Overview: State-of-the art commercial membranes for anion exchange membrane water electrolysis," *J. Electrochem. En. Conv. Stor.*, vol. 18, no. 2, p. 024001, 2021.

[22] R. J. Gilliam, J. W. Graydon, D. W. Kirk, and S. J. Thorpe, "A review of specific conductivities of potassium hydroxide solutions for various concentrations and temperatures," *Int. J. Hydrogen Energy*, vol. 32, no. 3, pp. 359-364, 2007.

[23] H. Ito, N. Kawaguchi, S. Someya, T. Munakata, et al., "Experimental investigation of electrolytic solution for anion exchange membrane water electrolysis," *Int. J. Hydrogen Energy*, vol. 43, no. 36, pp. 17030-17039, 2018.

[24] P. Fortin, T. Khoza, X. Cao, S. Y. Martinsen, A. O. Barnett, et al., "High-performance alkaline water electrolysis using Aemion™ anion exchange membranes," *J. Pow. Sour.*, vol. 451, p. 227814, 2020.

[25] I. Vincent, A. Kruger, and D. Bessarabov, "Hydrogen production by water electrolysis with an ultrathin anion-exchange membrane (AEM)," *Int. J Electrochem Sci.,* vol. 13, no. 12, pp. 11347-11358, 2018.

[26] I. V. Pushkareva, A. S. Pushkarev, S. A. Grigoriev, P. Modisha, and D. G. Bessarabov, "Comparative study of anion exchange membranes for low-cost water electrolysis," *Int. J. Hydrogen Energy*, vol. 45, no. 49, pp. 26070-26079, 2020.

[27] V. Schröder, B. Emonts, H. Janßen, and H. P. Schulze, "Explosion limits of hydrogen/oxygen mixtures at initial pressures up to 200 bar," *Chem. Eng. Tech.: Ind. Chemistry‐ Plant Equip. Proc. Eng.‐ Biotech.,* vol. 27, no. 8, pp. 847-851, 2004.

RESEARCH ARTICLE

Forecasting urban forest recreation areas in Turkey using machine learning methods

Mehmet Cüneyt Özbalcı[a,*], Sena Dikici[b], Turgay Tugay Bilgin[c]

[a]*Bursa Technical University, Bursa, 16310, Türkiye, ORCID: 0000-0003-4499-0061*
[b]*Bursa Technical University, Bursa, 16310, Türkiye, ORCID: 0000-0002-1759-6045*
[c]*Bursa Technical University, Bursa, 16310, Türkiye, ORCID: 0000-0002-9245-5728*

Abstract

Recreation is the process of revitalizing and renewing human existence through optional activities, serving as a broad description. It has prominently arisen as a reaction to personal requirements for stress reduction, especially in developed urban areas. Engaging in this recreational activity provides a way to utilize one's spare time, providing refreshment for both the physical and mental aspects, whether done alone or with others, in countryside or city environments. Urban forests are important leisure places within city environments. An expanded presence of urban forest places can greatly enhance the general well-being of society. The estimation of urban forest areas in the future may receive increased attention, leading to measures to extend current areas or prepare for future activities and services. We utilized official statistics from the years 2013 to 2021, sourced from the Republic of Turkey official website. Ministry of Agriculture and Forestry's General Directorate of Forestry. We used statistics that contained information about urban forests, classified as Type D recreational areas, to create a dataset. We performed provincial-level area projections for the year 2021. Using the KNIME platform, we used three different analysis techniques: linear regression analysis, gradient-boosted regression trees and artificial neural networks. It is seen that the results of linear regression and artificial neural networks are close to each other and give good results. The peak performance was attained using artificial neural networks, resulting in an R^2 score of 0.99. This study differs from other similar projects by concentrating on calculating urban forest recreational spaces per province throughout Turkey, using data provided by government agencies. The accomplishments highlight the ability to make reliable predictions about future forest resources by using analogous forecasts in the upcoming years.

*Corresponding author.
e-mail: mehmet.ozbalci@btu.edu.tr

1. Introduction

The benefits of nature-based tourism and outdoor recreation are growing. It is commonly known that spending time outside and in natural settings enhances people's health and wellbeing. For reasons like fostering a sense of connection with one's natural and cultural heritage, strengthening social bonds, fostering indigenous identity, and boosting the economy, it is critical to increase public awareness of the need to conserve natural places [1]. As awareness of these benefits has increased over time, natural areas have become a focal point of interest and focus for society. Recreation is the activities that people voluntarily do in their free time in order to reach the fitness of their physical and mental health in order to lead a healthy and productive life. Recreation is considered as an important contribution to physical and mental health. Parks and forest areas are considered to be important recreation areas for societies [2]. Nowadays, it is necessary to increase the organization and services in recreation areas for the entertainment and recreation needs of people living in cities or to intensify the studies depending on the increase in recreation areas. The need for recreation areas is increasing in order to strengthen the human-environment relationship of the society around the city [3]. Because there aren't many places to relax in cities, especially the larger ones, people choose to move to seaside locations. Recreational spaces are essential for satiating emotional and spiritual requirements as well as providing the energy required for daily productivity [4]. Urban forests are valued as significant recreational spaces. Because of this, a rise in recreational places benefits society, but a fall has the opposite effect. The protection of urban recreation areas and our natural assets is of great importance for society. Urban forests and natural resources are vital for our future. Scientific studies should draw attention to this issue and emphasize its importance.

When various regression studies are examined, it is observed that linear regression and artificial neural networks are frequently used and successful results are obtained [5], [6], [7], [8], [9], [10], [11]. It is also thought that the GBRT (Gradient Boosted Regression Trees) algorithm may be another algorithm to be preferred after experimental observations. The study utilized official information obtained from the Ministry of Agriculture and Forestry's General Directorate of Forestry website. The KNIME platform was utilized to predict the area in hectares of Type D (urban forest) regions in Turkey for the upcoming year through the use of linear regression analysis, gradient boosted regression tree, and artificial neural network (ANN) approaches. The evaluation criteria indicated that the approaches successfully forecasted the results. The goal is to enhance the existing literature by predicting recreational areas using linear regression analysis, gradient boosted regression tree, and ANN.

1.1. Literature survey

Data from 399 watersheds in 15 wildfires that burned in Colorado, Idaho, Montana, and New Mexico between 2000 and 2002 were analyzed by Ruppert et al. in their study. The study demonstrated how debris flows in landscapes that have recently seen fires can be predicted using logistic regression. This was achieved by examining more than 35 independent factors related to burn severity, geology, slope, precipitation, and soil properties [5]. Using information from a survey of 2449 persons, a representative sample of the Norwegian population, Bjerke et al. assessed the relationship between interest in 15 outdoor recreational activities and environmental attitudes. It was observed that there was an opposite relationship between age and score. In addition, women were found to score higher than men. In addition, it was determined that there was a complex relationship between predictor variables and recreational interests [6]. Human population density and activity are the primary drivers of land use change. Urban growth modeling has gained a lot of interest since it aids in understanding the processes underlying changes in land use, which in turn aids in the development of pertinent policies. Nong Yu and Du Qingyun used logistic regression to model urban expansion in Jiayu County, Hubei Province, China. The model accuracy is displayed by the relative operating characteristic (ROC), which has a curve of 0.891 and a standard error of 0.001. According to the findings, the model does a good job of simulating urban growth at the county level [7]. Bivariate and regression analysis techniques were used in a study to assess the association between the utilization of recreational places on

campus and the individual variables of university students, such as exercise practices, social physical anxiety, and self-efficacy. The Cronbach's alpha coefficient is the internal consistency coefficient that is determined by calculating the pairwise correlation between test items. The study's evaluation criterion was the Cronbach's alpha coefficient, and a value of 0.91 was attained [8]. The length and timing of a plant's growth stages vary from place to region according on climate, which affects chickpea phenology. It was proposed that a strong prediction might be made jointly about the geographical origin of accession and the local environmental circumstances in the growing region. They put up a novel forecasting model for the blossoming period of wild chickpeas cultivated in Turkey under four distinct environmental circumstances and in 21 distinct seasons. The study employed the nonlinear regression method, and the R^2 value was found to be 0.97 [9]. Another study analyzed many factors to understand the changes in forest acreage in the Mediterranean Region between 2004 and 2019. Data on factors such as precipitation, temperature, land surface temperature, ozone, fire, urban areas and population were obtained. Using this data, the factors that most affect the changes in forest areas were analyzed by multiple linear regression method. The analysis's findings demonstrated that the strongest factor causing loss in forest areas is forest fires [10]. Zelin Liu et al. compared the three machine learning techniques of support vector machines (SVM), ANN and decision trees. Their applications in forest ecology in the last decade were compared. Models of species distribution, carbon cycles, hazard assessment and prediction, and other forest management applications are the items that are compared [11]. In the study by Qingxia Zhao et al. parameters of forests were estimated using various regression methods. Four different machine learning algorithms were used. These are: SVM, ANN, RF, and classification and regression tree (CART) to determine how well they could predict the forest parameters of black locust plantations on the Loess Plateau. The findings demonstrated that, for all forest parameter estimations, RF provided the maximum accuracy, SVM and ANN approaches performed moderately, and the CART method yielded the lowest accuracy. The highest R^2 values was 0.85 and the lowest relative root mean square error (RRMSE) was 0.18 [12]. Three distinct data sets were employed in the investigation of forest degradation detection. BFAST method was used and two machine learning methods, SVM and RF, were used. The findings demonstrate that the SVM approach, when applied to the entire forest dataset, achieves the maximum accuracy. It was found that the latter model was more accurate than the magnitude threshold model [13]. Snezhana G. Gocheva-Ilieva et al. suggest a new method for modeling air pollutant data using RF and AutoRegressive Integrated Moving Average (ARIMA) methods. First, the pollutant's RF model is made and examined in connection to meteorological factors. After that, univariate ARIMA is used to model its residuals and correct it. The method is used for nine years and three months' worth of hourly data for seven air pollutants (CO, NO, NO_2, NOx, O_3, PM_{10} and SO_2) in Dimitrovgrad, Bulgaria. Three time variables and six meteorological variables were included as predictors. High-performing models were produced, with R^2 values between 90% and 98% [14]. Maryam Pourshamsi et al. employed machine learning techniques to improve the estimates of forest canopy height using LiDAR measurements by utilizing baseline polarimetric interferometric SAR (PolInSAR) data. Multiple baseline merging was performed using a support vector. The methodology was created by combining two datasets. The method was analyzed on NASA AfriSAR. The accuracy of the resulting estimated height approximation (R^2 = 0.81, RMSE = 7.1 m) was measured as the previously introduced multiple baseline fusion approach (R^2 = 0.67, RMSE = 9.2 m) [15]. In this study by Xiaobang Liu et al. For the dataset, 30-m Landsat-8 data and merged 1-m GaoFen-2 (GF-2) satellite imagery were used. In the Three North Regions of China, the fractional forest cover was estimated using a variety of machine learning algorithms. Based on the findings of the 10-fold cross-validation, all nonlinear algorithms perform well, with an R^2 value of more than 0.8 and a root-mean-square error of less than 0.05. The RF outperformed the light gradient assisted machine in the boosting ensemble (R^2 = 0.992, RMSE = 0.022) and the bagging ensemble (R^2 = 0.993, RMSE = 0.020). Additionally, the study's findings demonstrate that the RF method is the best choice for estimating fractional forest cover and serve as a guide for the following research. [16]. Manley and Egoh developed a model to predict how non-urban recreation will change due to climate change. The model shows that current patterns will worsen in the future due to climate change, with cottage recreation areas becoming more suitable and unpopular cottage recreation areas becoming less suitable for recreation. At various intervals from 2030 to 2099, recreation areas have been forecasted for some

regions in the state of California [17]. Chen et al. uses logistic regression (LR), decision tree (DT), and random forest (RF) models to analyze landslide susceptibility in forest-covered regions in Lin'an, China. It identifies key predictive factors like forest type (FT), maximum daily rainfall (MDR), distance to road (DTRD), understory vegetation height (UVH), and the normalized differential vegetation index (NDVI). Hickory plantations have the highest susceptibility, and the RF model proves to be the most accurate for predicting high-susceptibility zones. This research helps understand landslide risks, especially when transitioning from natural forests to plantations, and guides disaster mitigation and prevention strategies [18]. Adhikari et al. conducted a comparative study evaluating various modeling methods including Least Squares Regression, Adaptive Least Absolute Shrinkage and Selection Operator (ALASSO), Random Forest, and Generalized Additive Model Selection for predicting attributes of urban forest areas such as volume, basal area, and dominant height. The experimental results showed R² values of 88% for volume, 83% for basal area and 83% for dominant height, respectively [19]. Forest land categories typically collide with other land use types during societal development, resulting in environmental repercussions. As a result, study into changes in forest land categories has become a more international priority. As urbanization trends increase, regional land use modeling studies become increasingly significant in identifying possible forest ecological security concerns. This study, which uses land use data from the Ganjiang River basin, looks at the distribution of land use categories and how they've changed from 2000 to 2020. It estimates the land use pattern of the basin in 2040 and looks into the features of forest land types that transfer using the CA-Markov model. The results indicate that the transfer between different subcategories of forest land, which was particularly widespread in the high-altitude mountainous portions of the basin in the south and west, was the most significant trend in the development of land use between 2000 and 2020. With a kappa value of 0.92, the land use pattern prediction model created in this work suggests that the projections are accurate and trustworthy [20].

2. Material and method

2.1. KNIME data analytics tool

KNIME, an open source, modular data mining software, includes many possibilities such as data analysis, statistical evaluation, clustering, classification, and reporting. Operations are carried out using nodes in KNIME, which distinguishes out for its usability and user-oriented interface. The application provides a wide range of data science services and includes statistical analysis modules, learning algorithms, and clustering algorithms. The user can manually handle every stage of the process using the modules, from uploading the raw data to pre-processing, segmenting, and formatting the data to applying the appropriate algorithms. Data from files with the .txt, .csv, .arff and .table extensions can be imported into KNIME. The software offers a wide range of visualization features [21].

2.2. Dataset

The data used in the study were collected from the official website of the General Directorate of Forestry of the Ministry of Agriculture and Forestry of the Republic of Turkey, covering the years 2013 to 2020. The data set contains the total number of hectares of A, B, C, and D category recreational spaces from 2007 to 2021. Types A, B, and C designate recreational spaces, whereas type D designates urban woods. This study examined the transformation of type D data due to the high value attributed to urban forest assets. The dataset contains the number of urban forest and their hectare equivalents. Analysis was conducted on data from 2013 to 2021 to utilize the most recent information. A projection for 2021 was created and accomplishments were assessed based on data up to 2020. The dataset is around 20 kilobytes in size. The file with numerical data for all provinces in our country was converted to xlsx format and prepared for processing. 70% of the data is allocated for training, while the remaining 30% is designated for testing. To ensure reliability in the results, missing recreation data in the provinces were replaced with the mean values of the row data in the dataset. The study could not estimate statistics for Adana,

Aksaray, Kilis, Muş, Yozgat, and Gümüşhane provinces due to unavailability of information [22]. The information of some cities belonging to the dataset is given in the figure below.

Table 1. A fragment of the content of the data in the dataset.

Cities	Number of Areas	Area in Hectares
İstanbul	12	1783,59
Tekirdağ	3	211,90
Edirne	2	81,50
Kırklareli	2	122,87
Balıkesir	1	15,00

2.3. Analysis methods

2.3.1 Regression analysis

The functional depiction of the relationship between the dependent variable and the independent variable or variables is known as regression analysis [23]. In regression analysis, working with as much data as possible increases the likelihood of consistent results. The consistency of the available data within itself is also an important factor for the result to be successful. Regression analysis is used extensively in fields of study that are open to statistical and empirical studies such as finance, marketing and health. In order to obtain the desired results, the data used should not be underfit or overfit. When the learning process fails miserably with the training data, the test data yields inconsistent results, which is known as underfitting. Typically, underfitting is seen when there is an excessive amount of noisy data. When the training set's state is retained by the learning process through memorization, this is known as overfitting, and bad test data findings are the outcome.

2.3.2 Linear regression analysis

Predicting the value of a variable based on the values of other variables is the basis of linear regression analysis. Independent variables are those that are not employed in the prediction of the dependent variable, while the variable or variables to be forecasted form dependent variables [24].

Linear regression analysis consists of two basic concepts. These are simple linear regression and multiple linear regression. In simple regression analysis, it shows the linear relationship between only one explanatory variable and the response variable [25]. In a simple linear regression model, Y is the response variable, X_i is the explanatory variable, $\beta 0$ and $\beta 1$ are the unknown parameters of the variable, and e is the error term due to chance. In this case, the simple linear regression model is calculated as given in Eq. 1:

$$Y = \beta_0 + \beta_1 X_{i_1} + e_i \quad i = 1,2,..n \tag{1}$$

Regarding a multivariate linear regression model with n observations and p explanatory variables;

$$Y_i = \beta_0 + \beta_1 X_{i_1} + \beta_2 X_{i_2} + \ldots + \beta_p X_{i_p} + e_i \quad i = 1,2,..n \tag{2}$$

The R^2 value in regression analysis is a metric that indicates the predictive performance of the model. This value is associated with the extent to which the independent variables affect the dependent variable. The values that R^2 can take vary between 0 and 1. The higher this value is, the better the regression model fit [26].

2.3.3 Gradient boosted regression tree (GBRT)

The GBRT technique can be used to solve regression and classification issues. Regression problems show that this approach performs remarkably well. As a result, it has emerged as one of regression analysis's most often used algorithms. GBRT is made up of three main components. These three are the additive model, the weak learner, and the loss function. The goal of the problem solution must be the main emphasis in order to determine the loss function [27]. The GBRT model employs an algorithm that is focused on building individual decision trees. The model is improved through training the decision trees. Training the decision trees results in the generation of an objective function. Here, maximizing the desired features by iterative splitting is the key goal [28]. One popular method of binary classification is to measure node purity during the splitting process. Here, the purity index is referred to as the gini index. Figure 1 illustrates how the proper value will be chosen at each step based on the gini index, which will determine the most appropriate decision.
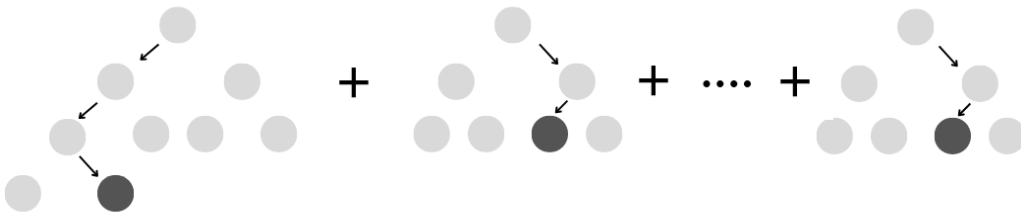
Fig. 1. Structural visualization of the GBRT algorithm with many decision trees [29].

2.3.4 Artificial neural networks (ANN)

The architecture of ANN, essentially imitates that of the human brain. Its relational structure is comparable to human neuronal connections. Neurons are made up of three layers: input, hidden, and output. A collection of interconnected nodes made up of artificial neurons makes up an ANN [30]. Each link has the ability to transmit a signal from one artificial neuron to another, just like synapses do in the brain. After processing the signal, the receiving neuron can communicate with other neurons [31]. Data filtering, interpretation, association, prediction, and classification are all done with ANN [32]. The illustration of the ANN's layers and connections between them is provided below.
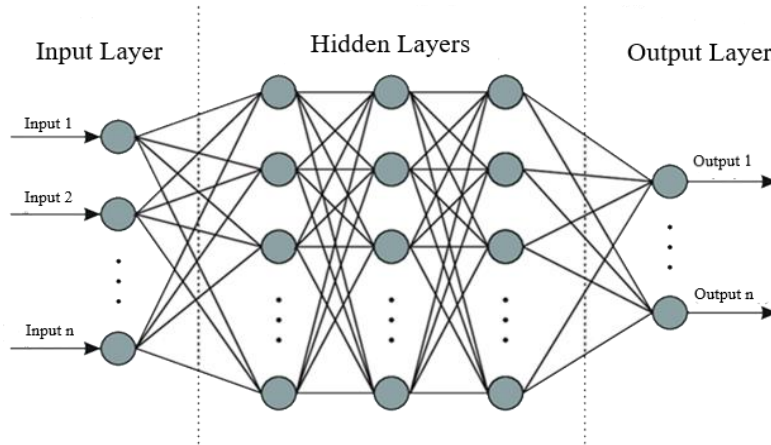
Fig. 2. Layers of ANN and their relational structure [33].

In the initial step of an ANN, a result is obtained by multiplying the input data by the predetermined weights. The impact of inputs on the desired outcomes can be changed in this way. The activation function is the one that takes the weighted sum of the inputs from the preceding layer and outputs a value. Activation functions that are most widely used and favored are sigmoid and ReLU.

2.4 Performance metrics

In this study, R^2, mean absolute error value, square of mean errors, root mean square roots error and mean absolute percentage error were calculated for performance measures [34,35].

2.4.1 R^2 value

The R^2 value is a measure of the success of the regression model fit. The closer this value is to 1, the lower the error rate. The calculation is performed according to Equation 3.

$$R^2 = 1 - \frac{\sum (y_i - \hat{y}_i)^2}{\sum (y_i - \bar{y}_i)^2} \tag{3}$$

Here, y_i denotes the actual value of y, $\hat{y}_i$ is denotes the predicted value of y, $\bar{y}_i$ denotes the mean value of y.

2.4.2 Mean squared error (MSE)

MSE is the difference of the mean squares between the actual values and the predicted values. The calculation is performed according to Equation 4.

$$MSE = \frac{1}{n} \sum_{i=1}^{n} (y_i - \hat{y}_i)^2 \tag{4}$$

2.4.3 Root mean squared error (RMSE)

RMSE is a measure of the average of the square roots of erroneous estimates. The calculation is performed according to Equation 5.

$$\text{RMSE} = \sqrt{\frac{1}{n}\sum_{i=1}^{n} y_i^2} \qquad (5)$$

2.4.4 Mean absolute error (MAE)

MAE is a quantity that expresses the sum of the absolute error value. The calculation is performed according to Equation 6.

$$\text{MAE} = \frac{1}{n}\sum_{i=1}^{n} |y_i - y| \qquad (6)$$

2.4.5 Mean absolute percentage error (MAPE)

MAPE is the error rate of the accuracy of the statistical estimate. It is a measure of the accuracy of the estimate. The calculation is performed according to Equation 7.

$$\text{MAPE} = \frac{1}{n}\sum_{i=1}^{n} \left|\frac{\hat{y}_i - y_i}{y_i}\right| \qquad (7)$$

2.4.6. Standard deviation (STD. DEV.)

Standard deviation is the square root of variance. The ideal situation is when the standard deviation is the lowest.

$$s = \sqrt{\frac{\sum (x_i - \bar{x})^2}{(N-1)}} \qquad (8)$$

3. Result and discussion

The study employs GBRT, ANN, and linear regression to predict the D-type urban recreation spaces for 2021 based on province-specific data from 2013 and 2020. The selected algorithms were applied to the data using the nodes in the KNIME software. Below are system flow diagrams created using KNIME software. Figures 3, 5, and 7. Hatay province had missing data for 2013 and 2014, while Siirt had missing data for 2013. To address this, missing data was excluded by calculating the average for each technique based on the rows (provinces), ensuring consistent and reliable analysis. The data underwent the decimal scaling normalization technique. Decimal scaling normalization involves dividing the data by a power of 10 to reduce it to a number less than 1. Equation 9 gives the equation for the normalizing process, which involves decimal scaling.

$$A' = \frac{A_i}{10^j} \qquad (9)$$

Methods such as Z-score normalization, which require normally distributed data for best performance, are less appropriate given our data's non-normal distribution. Decimal scaling, on the other hand, is more appropriate for datasets with uncertain or non-normal distributions because it does not make any assumptions about the data's distribution. Maintaining the independence of each province's data is also essential because the data from one does not affect the data from another. By normalizing each value according to its own order of magnitude, decimal scaling successfully addresses this issue instead of utilizing group statistical measures like standard deviation and mean, which may cause biases if the data points were interdependent. This approach ensures that the unique characteristics of the forest area data in each province are preserved without the distortion that might occur with other normalization techniques.

The normalized data is represented by A', the value to be normalized is represented by A_i, and the value that reduces A' to 1 is represented by J. The J value for Normalization by Decimal Scaling is determined automatically by KNIME in its current edition. This J value cannot be manually set or determined by researchers. Based on the highest absolute value of every feature in the dataset, the software chooses the best J, making sure that the greatest absolute value is less than 1 after scaling. The efficient standardization of data through this automated approach eliminates the need for user participation in defining scaling parameters, hence streamlining the data preprocessing procedures. This implies, however, that users' control over this step of the KNIME data normalization process is restricted.

The data was divided into training and test sets after normalizing the data. Figures 4, 6, and 7 display comparisons of the training and test data obtained at different rates during the study. The same processes for handling missing data, normalizing data, and dividing data were used to all three approaches. Figure 3 displays the flow diagram of the linear regression approach.
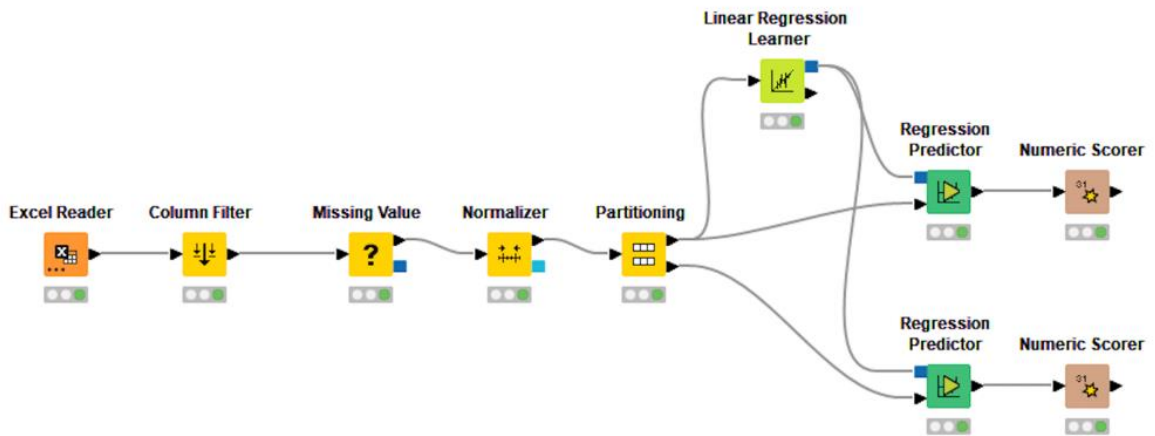
Fig. 3. Flow diagram of linear regression model in KNIME tool.

The flow diagram generated by the Knime tool for the linear regression method is shown in Figure 3. The Knime tool utilizes a node called "Linear Regression Learner" for implementing the linear regression approach. Merely the target column for prediction is chosen in this node. The study focuses on column 2021. The predictor node is named "Regression Predictor". The predictor utilizes data from before 2021 to generate forecast results for 2021. Performance values are determined by the disparities between the expected and actual data.

48

The study on linear regression involved analyzing training and test data at various proportions. Figure 4 presents a comparison of the data obtained.
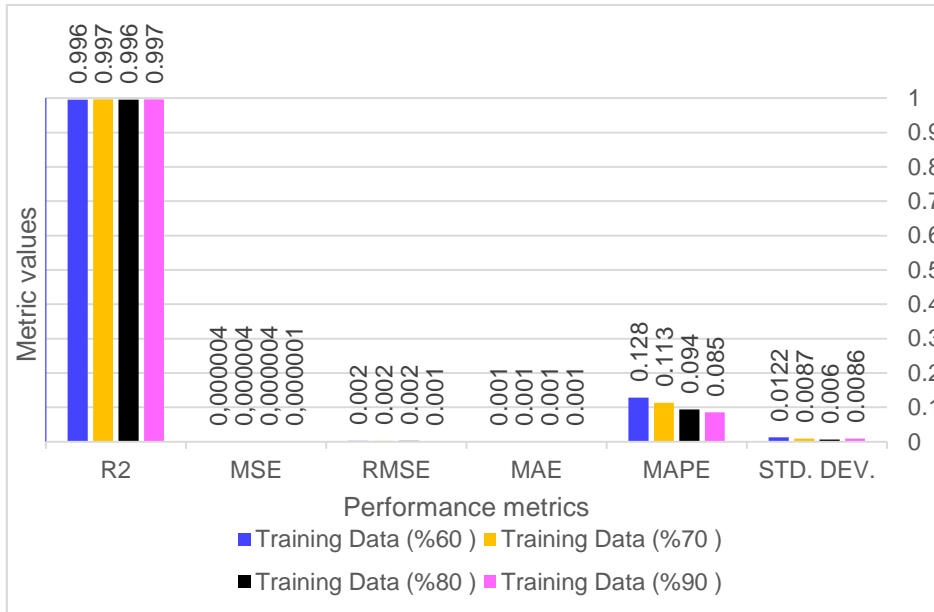
Fig. 4. Results from various training and test data set percentages using the linear regression approach.

Experimentation utilizing various percentages of training and test data showed that the best results for the linear regression technique were obtained when 90% of the data was utilized for training. The results display almost perfect explanatory power across all training set percentages, with R^2 values close to 1, indicating that the model excellently captures the variance of the dependent variable regardless of the data set size.

Looking at the mean squared error (MSE) and the root mean squared error (RMSE), the values are exceptionally low across all training data scenarios, ranging from 0.0002 to 0.0001 for MSE and consistently at 0.001 for RMSE. These metrics signify that the model's predictions are very close to the actual values, highlighting a high degree of accuracy and consistency. MAE values are between 0.0007 and 0.0008 and MAPE values are between 0.085 and 0.128. The standard deviation value is between 0.006 and 0.008. The low levels of these values indicate the success of the model.
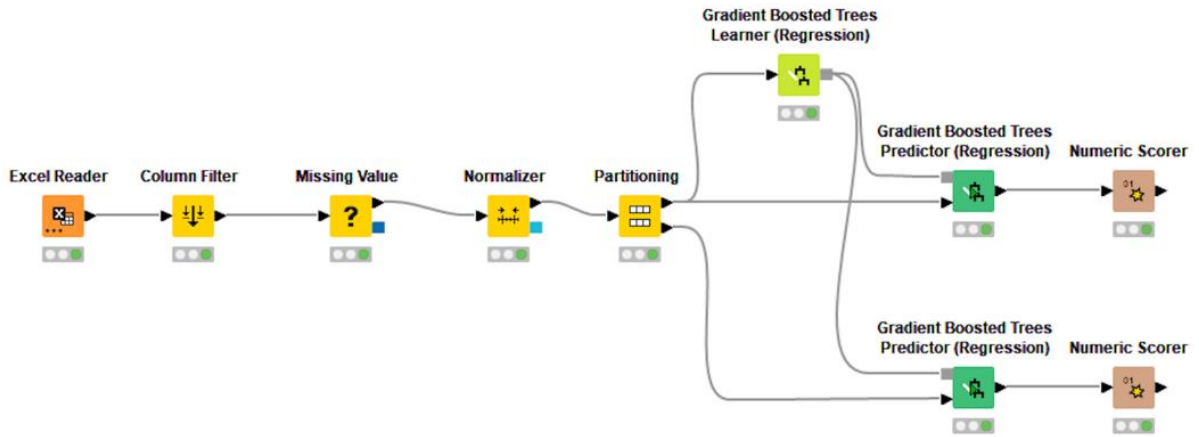
Fig. 5. Flow diagram of GBRT model in Knime program.

Figure 5 illustrates the flow diagram of the gradient boosted regression tree technique generated with the Knime tool. To enable the gradient boosted regression Tree to understand the dataset, the "Gradient Boosted Tree Learner" node is necessary. This node has a maximum tree depth set at four levels. The learning rate is established at 0.05 and the number of models is determined at 100. The target column is designated as the latter part of 2021. The "Gradient Boosted Trees Predictor" node was utilized by the predictor. The R^2, MSE, RMSE, MAE, and MAPE values were calculated by comparing the predicted values from the predictor node with the actual 2021 data. The values were acquired using the "Numeric Scorer" node. Figure 6 displays the outcomes of the gradient boosted regression tree approach using various percentages of training and test data. While conducting the experiments, tree depth was determined as 4. Learning rate was taken as 0.05. Alpha value was 0.95.
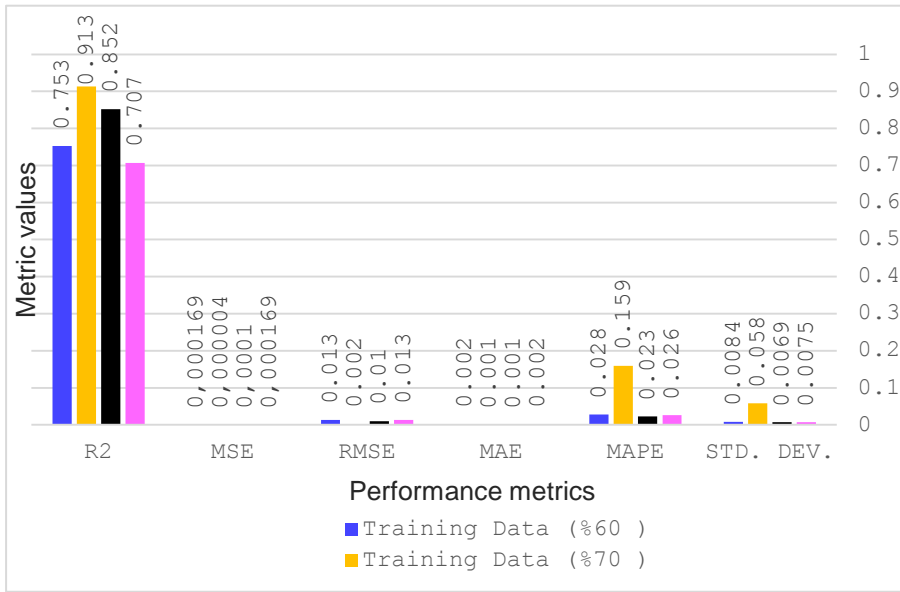
Fig. 6. Results from various training and test data set percentages using the gradient boosted regression tree approach.

The gradient boosted regression tree approach yielded optimal results by allocating 70% of the dataset for training and 30% for testing. Gradient enhanced regression tree method shows a significant disparity in results between training and test data compared to linear regression. In addition, GBRT has been observed that the performance of the model decreases as the training set size increases. Low values obtained from the metrics indicate that the generalizability of the model decreases. When the training set size increases significantly, the model may overfit the training data. This leads to low performance on unseen test sets. Figure 7 displays the flow diagram for the ANN technique using the Knime tool. Cross-validation was used to calculate the results. Cross-validation is performed with the X-Partitioner node.
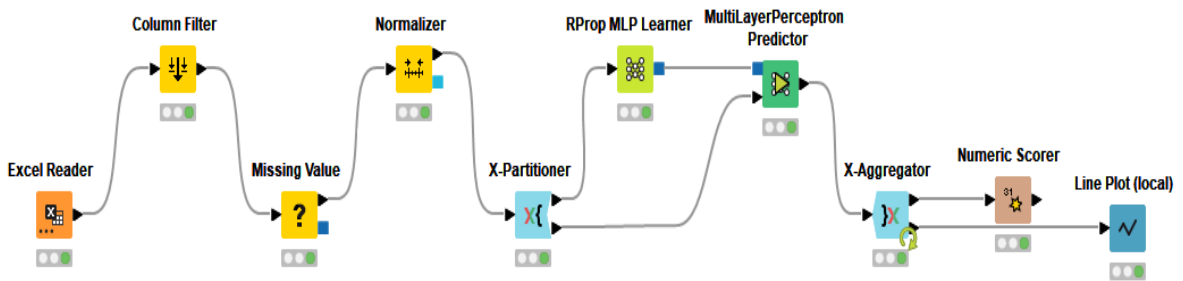
Fig. 7. Flow diagram of MLP model in Knime tool.

The neural network results were confirmed using cross-validation. The cross-validation method made use of the "X-Partitioner" node included in the Knime tool. The data was divided into ten divisions and random sampling was conducted. The "RProp MLP Learner" node was utilized in the ANN method to analyze the dataset in the learning phase. The parameters were as follows: 100 iterations were performed using a neural network with three hidden layers, each containing 100 neurons, and the goal class column was set to 2021. Figure 8 shows the results of the cross-validation process.
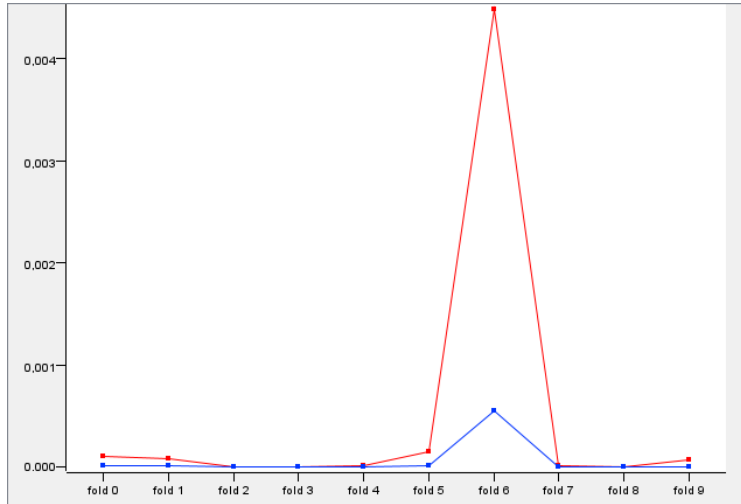
Fig.8. MSE values obtained as a result of cross-validation on multilayer perceptron (red is total MSE, blue is average MSE).

The variance in MSE values among folds is deemed acceptable given the scarcity of provincial data in Turkey and the limited historical data available on the official website. Cluster 6 had the lowest MSE value among the sub-datasets, whereas cluster 8 had the highest MSE value. MSE value suggests a favorable outcome based on the average value.

Figure 9 displays a comparison of the three approaches in the study based on R^2, MSE, RMSE, MAE, MAPE and STD. DEV. values using a bar chart. The Knime nodes used for training are set to repeat a maximum of 50 times with random seed. The node named Numeric scorer gives the best results and their standard deviations when displaying the results.
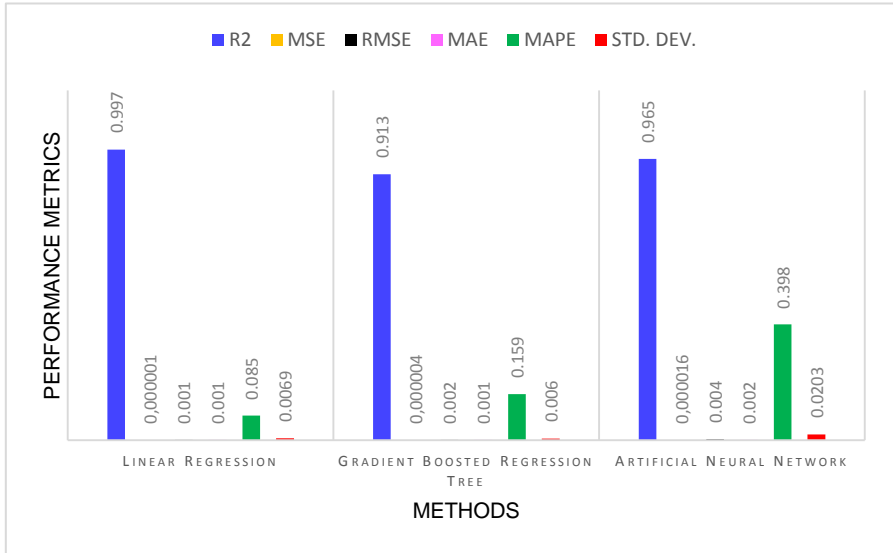
Fig. 9. Comparison of three methods based on R^2, MSE, RMSE, MAE, MAPE and STD. DEV. values.

The analysis findings from the training and test data sets indicate that the predictions made by each approach are within an acceptable range. The linear regression technique yielded the highest R^2 score in the experiments. The ANN approach had the highest rate for estimating the variance of the dependent variable from the independent factors. Performance evaluation of the model is clearer when the R^2 analysis is combined with additional techniques, especially MSE. As the data points approach the regression line, the MSE decreases and eventually approaches zero. Models that predict with less error are more accurate. In both the training and test datasets of this study, the MSE value for each of the three models is approximately 0. The RMSE value represents the square root of the MSE value. It simplifies the comprehension of exceedingly large numbers. Optimal RMSE values are those that approach zero. RMSE values between 0.001 and 0.004 are considered ideal for our study. An ideal range of 0.001-0.002 was identified for the MAE values, which indicate the average absolute difference between the observed data values. MAPE was 0.398 for the ANN, 0.159 for the gradient boosted regression tree, and 0.085 for linear regression. The linear regression approach yielded the best result when all assessment factors were taken into account, similar to the MAPE value.

The high R^2 score obtained with the linear regression technique shows that this method is quite effective for this dataset. However, the artificial neural network (ANN) approach, despite achieving a slightly lower R^2 score, showed a strong ability to capture the variability in the data and proved to be a reliable alternative especially for more complex data patterns. The results obtained are also consistent with previous studies where artificial neural networks were preferred due to their flexibility and accuracy.

Unlike other studies, this research emphasizes how machine learning can be used in environmental management by using these methods to predict urban forest recreation areas. The results obtained demonstrate the effectiveness of these methods and provide a basis for investigating ways to combine them with other advanced techniques to provide greater accuracy.

The impact of the findings is not limited to statistical estimates alone, but also provides valuable information for urban planners and policy makers. It can contribute to making more informed decisions on urban development and environmental protection by accurately predicting recreation area needs. It also highlights the importance of

integrating machine learning tools into traditional urban planning approaches to deal with the contemporary problems of our rapidly urbanizing world.

4. Conclusion

This study aimed to forecast the provincial recreational areas inside urban forests in Turkey and analyze future forest resources using official statistics from 2013 to 2020. Three methods, namely linear regression, gradient boosted regression tree, and ANN, were applied to the data using the KNIME platform. The metrics used to evaluate the performance of the methods are R^2, MSE, RMSE, MAE, MAPE, respectively. The most successful method was linear regression. Inferences from this study can be used in the planning and conservation of forest assets. It is believed that this study makes an important contribution to the literature in terms of protecting existing forest assets and preserving the ecosystem in its natural state. In this study, which emphasizes the protection of forest assets, it has been shown that computer science can be used functionally in this regard. If larger and more detailed data sets can be obtained, much more detailed analyzes will be possible. The limitations of this study are that the study was carried out within the scope of specified areas and within certain parameters.

It has been seen that this study is important in terms of making predictions about future forest assets. Such studies are important in order to take measures to protect our natural assets, which are extremely important for us. There are similar studies in the literature. However, this study has a special importance as it is a country-based study and draws attention to the issue of urban recreation areas, which is one of the main problems of the country.

Accessing larger data sets of the study will enable more in-depth analyses. Efficient actions can be taken to implement the required strategies for forest resources. Accessing greater data sets will enable more intricate analyses. This will enable efficient strategies to be implemented for managing forest resources.

The findings from the study are instructive in the area of the use of machine learning techniques in the prediction of urban forest recreation areas in Turkey. The efficacy of linear regression, gradient-assisted regression tree and artificial neural network methods in this field has been demonstrated.

Using three different methods and various performance metrics, this study shows the effectiveness of artificial neural networks with the highest performance. In addition to the satisfactory results obtained, it is predicted that the methods used in the study will give successful results in more complex and detailed data sets. This study, which can be a guide for future studies, stands out especially as it is a study on the characteristic structures of the cities of countries.

Another critical importance of the study is that it provides guidance for conservation policies related to forest areas. Based on the results of the study, it is possible to take some measures to protect and increase our forest areas in the future. It is also considered to be of particular importance in terms of encouraging the protection and development of our natural resources. The main limitations of this study are that there are some missing data in the dataset and it does not contain too much detail. This situation can be improved and pave the way for more comprehensive studies. For future studies, existing methods can be improved or different machine learning algorithms can be used.

While our study provides a solid basis for estimating urban forest recreation areas, it is important to recognize several limitations. The biggest limitation is that the dataset only covers the years 2013-2020. Not including data from older years or additional variables such as socio-economic factors may limit the generalizability of the findings. Moreover, focusing only on provincial level data may miss differences at the local level (e.g. district or neighborhood level).

For future research, expanding the dataset to include a wider range of variables and more recent data could significantly improve the predictive performance of the model. Furthermore, applying different machine learning algorithms such as Random Forests, Support Vector Machines, or hybrid models combining multiple approaches can provide a more comprehensive understanding of the factors influencing urban forest recreation areas.

Another area to explore in the future is the integration of spatial analysis techniques such as Geographic Information Systems (GIS) with machine learning models. This can enable more precise spatial predictions and a better understanding of the geographical distribution of urban forest resources. Furthermore, long-term studies that track changes over time can provide important insights into the dynamic nature of urban recreation areas and the long-term impact of urbanization on these areas. By addressing these limitations and exploring these issues, future studies can build on existing findings to provide more detailed and actionable insights for urban forest management and policy development.

Author contribution

M.C.Ö., S.D. and T.T.B. actively participated in conducting the experimental studies and writing the manuscript.

Acknowledge

References

[1] P. L. Winter, S. Selin, L. Cerveny and K. Bricker, "Outdoor recreation, nature-based tourism, and sustainability," *Sustainability*, vol. 12, no. 1, pp. 81, 2019, doi: 10.3390/su12010081.

[2] Ç. Kılıçaslan, "Ortaca kenti rekreasyon alanlarının mevcut durumu ve Muğla Üniversitesi Ortaca Meslek Yüksekokulu öğrencilerinin rekreasyon alanlarına yönelik beklentileri," *Düzce Üniversitesi Ormancılık Dergisi*, vol 4, no. 1-2, pp. 3-16, 2008.

[3] S. Uzun and H. Müderrisoğlu, "Kirsal ve kentsel alanlardaki parklarda kullanici memnuniyeti; Gölcük orman içi dinlenme alanı ve İnönü Parkı örneği," *Düzce Üniversitesi Orman Fakültesi Ormancılık Dergisi*, vol. 3, no. 2, pp. 84-101, 2007.

[4] H. Akyüz, M. Kul and F. Yaşartürk, "Rekreasyon açısından ormanlar ve çevre," *International Journal of Sport Culture and Science*, vol 2, no. (Special Issue 1), pp. 881-890, 2016.

[5] M. G. Rupert, S. H. Cannon and J. E. Gartner, "Using logistic regression to predict the probability of debris flows occurring in areas recently burned by wild land fires," *US Geological Survey Open-File Report*, vol. 500, no. 1, 2003.

[6] T. Bjerke, C. T. and J. Kleiven, "Outdoor recreation interests and environmental attitudes in Norway," *Managing leisure*, vol. 11, no. 2, pp. 116-128, 2006, doi: 10.1080/13606710500520197.

[7] Y. Nong and Q. Du, "Urban growth pattern modeling using logistic regression," *Geo-spatial Information Science*, vol. 14, no. 1, pp. 62-67, 2011, doi: 10.1007/s11806-011-0427-x.

[8] H. M. Shaikh, M. S. Patterson, B. Lanning, M. R. Umstattd Meyer and C. A. Patterson, "Assessing college students 'use of campus recreation facilities through individual and environmental factors," *Recreational Sports Journal*, vol. 42, no. 2, pp. 145-159, 2018, doi: 10.1123/rsj.2017-0.

[9] K. Kozlov, A. Singh, J. Berger *et al.* "Non-linear regression models for time to flowering in wild chickpea combine genetic and climatic factors," *BMC Plant Biol,* vol. 19, no. 94, pp. 1-14, 2019.

[10] N. Başaran, D. K. Matcı and U. Avdan, "Using multiple linear regression to analyze changes in forest area: the case study of Akdeniz Region," *International Journal of Engineering and Geosciences*, vol. 7, no. 3, pp. 247-263, 2022, doi: 10.26833/ijeg.976418.

[11] Z. Liu, C. Peng, T. Work, J. N. Candau, A. DesRochers and D. Kneeshaw, "Application of machine-learning methods in forest ecology: recent progress and future challenges," *Environmental Reviews,* vol. 26, no 4, pp. 339-350, 2018, doi: 10.1139/er-2018-0034.

[12] Q. Zhao, S. Yu, F. Zhao, L. Tian and Z. Zhao, "Comparison of machine learning algorithms for forest parameter estimations and application for forest quality assessments," *Forest Ecology and Management*, vol. 434, pp. 224-234, 2019, doi: 10.1016/j.foreco.2018.12.019.

[13] J.V. Solórzano and Y. Gao, "Forest disturbance detection with seasonal and trend model components and machine learning algorithms," *Remote Sensing*, vol. 14, no. 3, pp. 803, 2022, doi: 10.3390/rs14030803.

[14] S. G. Gocheva-Ilieva, A. V. Ivanov and I. E. Livieris, "High performance machine learning models of large scale air pollution data in urban area," *Cybernetics and Information Technologies*, vol. 20, no. 6, pp. 49-60, 2020, doi: 10.2478/cait-2020-0060.

[15] M. Pourshamsi, M. Garcia, M. Lavalle and H. Balzter, "A machine-learning approach to PolInSAR and LiDAR data fusion for improved tropical forest canopy height estimation using NASA AfriSAR Campaign data," *IEEE Journal of Selected Topics in Applied Earth Observations and Remote Sensing*, vol. 11, no. 10, pp. 3453-3463, 2018, doi: 10.1109/JSTARS.2018.2868119.

[16] X. Liu, S. Liang, B. Li, H. Ma and T. He, "Mapping 30 m fractional forest cover over China's Three-North Region from Landsat-8 data using ensemble machine learning methods," *Remote Sensing*, vol. 13, no. 13, pp. 2592, 2021, doi: 10.3390/rs13132592.

[17] K. Manley, and B. N. Egoh," Mapping and modeling the impact of climate change on recreational ecosystem services using machine learning and big data", *Environmental Research Letters*, vol. 17, no. 5, pp 054025, 2022.

[18] C. Chen, Z. Shen, Y. Weng, S. You, J. Lin, S. Li, and K. Wang, "Modeling Landslide Susceptibility in Forest-Covered Areas in Lin'an, China, Using Logistical Regression, a Decision Tree, and Random Forests", *Remote Sensing*, vol. 15 no. 18, pp 4378, 2023.

[19] A. Adhikari, C. R. Montes, and A. Peduzzi, "A comparison of modeling methods for predicting forest attributes using LiDAR metrics", *Remote Sensing*, vol. 15, no. 5, pp 1284, 2023.

[20] Y. Zhou, J. Hu, M. Liu, and G. Xie, "Predicting Sub-Forest Type Transition Characteristics Using Canopy Density: An Analysis of the Ganjiang River Basin Case Study", *Forests*, vol. 15, no. 2, pp 274, 2024.

[21] M. Kaya and S. A. Özel, "Açık kaynak kodlu veri madenciliği yazılımlarının karşılaştırılması," *Akademik Bilişim*, pp. 1-8, 2014.

[22] Republic of Turkey Ministry of Agriculture and Forestry General Directorate of Forestry, "Official statistics." ogm.com, https://www.ogm.gov.tr/tr/e-kutuphane/resmi-istatistikler (accesed Feb. 1, 2023).

[23] A.O. Sykes, "An introduction to regression analysis," *Coase-Sandow Working Paper Series in Law and Economics*, 1993.

[24] S. Kılıç, "Doğrusal regresyon analizi," *Journal of Mood Disorders*, vol. 3, no. 2, pp. 90-92, 2013, doi: 10.5455/jmood.20130624120840.

[25] S. Dörterler, "Developing a prediction model with the Battle Royale Optimization Algorithm," in *International Research in Engineering Sciences III*, vol. 1, M. Kamanlı, Eds. Konya, Turkey: Egitim Publishing, 2022, pp. 5-19.

[26] D. Maulud and A. M. Abdulazeez, "A review on linear regression comprehensive in machine learning," *Journal of Applied Science and Technology Trends*, vol. 1, no. 4, pp. 140-147, 2020, doi: 10.38094/jastt1457.

[27] Ö. G. Uzut and S. Buyrukoğlu, "Veri madenciliği algoritmalari ile gayrimenkul fiyatlarinin tahmini," *Euroasia Journal of Mathematics, Engineering, Natural & Medical Sciences*, vol. 7, no. 9, pp. 77-84, doi: 10.38065/euroasiaorg.81.

[28] H. Alshari, A. Saleh and A. Odabas, "CPU performansı için gradyan artırımlı karar ağacı algoritmalarının karşılaştırılması," *Erciyes Üniversitesi Fen Bilimleri Enstitüsü Fen Bilimleri Dergisi*, vol. 37, no. 1, pp. 157-168, 2021.

[29] Y. Shin, "Application of boosting regression trees to preliminary cost estimation in building construction projects," *Computational intelligence and neuroscience*, vol. 2015, pp. 1-1, 2015, doi: 10.1155/2015/149702.

[30] İ. Pençe, A. Kalkan and M. Ş. Çeşmeli, "Turkey sanayi elektrik enerjisi tüketiminin 2017-2023 dönemi için yapay sinir ağları ile tahmini," *Mehmet Akif Ersoy Üniversitesi Uygulamalı Bilimler Dergisi*, vol. 3, no. 2, pp. 206-228, 2019, doi: 10.31200/makuubd.538878.

[31] R. M. Sadek, S. A. Mohammed, A. R. K. Abunbehan, A. K. H. A. Ghattas, M. R. Badawi, M. N. Mortaja and S. S. Abu-Naser, "Parkinson's disease prediction using artificial neural network," *International Journal of Academic Health and Medical Research*, vol. 3, no. 1, pp. 1-8, 2019.

[32] K. Öztürk and M. E. Şahin, "Yapay sinir ağları ve yapay zekâ'ya genel bir bakış," *Takvim-i Vekayi*, vol. 6, no. 2, pp. 25-36, 2018.

[33] K. Y. Lee, K. H. Kim, J. J. Kang, S. J. Choi, Y. S. Im, Y. D. Lee, and Y. S. Lim, "Comparison and analysis of linear regression & artificial neural network*", International Journal of Applied Engineering Research*, vol. 12, no. 20, pp. 9820-9825, 2017.

[34] D. Özdemir, S. Dörterler and D. Aydın, "A new modified artificial bee colony algorithm for energy demand forecasting problem," *Neural Computing and Applications*, vol. 34, no. 20, pp.17455-17471, 2022.

[35] D. Özdemir and S. Dörterler, "An adaptive search equation-based artificial bee colony algorithm for transportation energy demand forecasting," *Turkish Journal of Electrical Engineering and Computer Sciences*, vol. 30, no. 4, pp. 1251-1268, 2022.

RESEARCH ARTICLE

Enhanced license plate recognition using deep learning and block-based approach

Gülistan ARSLAN[a]*, Fırat AYDEMİR[b], Seyfullah ARSLAN[c]

[a]*Kütahya Dumlupınar University, Faculty of Engineering, Computer Engineering Dept., 43100, Kütahya, Türkiye*
ORCID: 0000-0001-6498-1635
[b]*Kütahya Dumlupınar University, Faculty of Engineering, Computer Engineering Dept., 43100, Kütahya, Türkiye*
ORCID: 0000-0002-8965-1429
[c]*Kütahya Dumlupınar University, Faculty of Engineering, Computer Engineering Dept., 43100, Kütahya, Türkiye*
ORCID: 0000-0002-2573-273X

Abstract

This study investigates the effectiveness of current deep learning techniques in license plate detection and makes essential contributions. Instead of classifying the characters on Turkish license plates with a single classifier, the characters are divided into blocks of numbers and letters using various image processing techniques, and a separate classifier is used for each block. The proposed approach improves character classification accuracy and license plate recognition accuracy. This approach eliminated the possibility of misclassifying similar letters and numbers and improved the character classification accuracy from 95.9% to 99.6%. In addition, a new character feature dataset was created, and a deep learning model was trained on this dataset. Integrating this model into the system increased the classification accuracy to 99.7%. The YOLOv8 object detection model, trained using CUDA technology, achieved a mAP of 98.9%. The overall accuracy of the whole system in license plate recognition reached 97.3%. This study proves the effectiveness of current deep learning methods and the proposed block-based character recognition approach in license plate recognition.
© 2023 DPU All rights reserved.
Keywords: License plate recognition; image processing; convolutional neural networks; object detection; deep learning

* Corresponding author. Tel.: +90-274-443-4258
  E-mail address: gulistan.colak@dpu.edu.tr

1. Introduction

Vehicle license plates serve as a unique identification, critical for traffic management and safety in modern societies [1]. Due to their uniqueness, license plates are used as a fundamental tool for registering, tracking, and, where necessary, identification of vehicles. License plates are important in many areas, such as traffic control, security investigations, crime-fighting, and commercial activities. Identifying vehicles that violate traffic rules, identifying drivers exceeding speed limits, optimizing traffic flow, or controlling entry and exit to and from public spaces requires identifying the vehicles' license plates. In this way, traffic accidents can be reduced, traffic congestion can be managed, and overall traffic efficiency can be increased. Since manual identification of vehicle license plates is often time-consuming, error-prone, and inefficient, technological tools such as automatic license plate recognition systems help detect and prevent security threats by instantly recognizing license plate numbers [2]. However, license plate recognition systems that work with traditional image processing methods are sensitive to the adverse effects of weather conditions. In particular, weather conditions such as heavy rain, snow, and fog can reduce license plate visibility and recognition accuracy.

Thus, the high-accuracy license plate recognition system should detect and record the license plates of vehicles. AI-based vehicle license plate recognition systems can help achieve these goals toward efficient management of traffic and security operations. Various image processing techniques and machine learning algorithms are used to detect vehicle license plates in license plate recognition systems. With the recent developments in deep learning, one of the machine learning methods, deep learning-based systems are frequently used in areas such as computer vision, voice recognition, and natural language processing [3]. Deep learning algorithms and image processing techniques have been used to develop more accurate and reliable systems for license plate recognition. [4]. These systems include various techniques such as object detection algorithms, multiple morphological operations, and optical character recognition.

This research aims to design a license plate recognition system that achieves a higher level of accuracy and reliability than the existing works in the literature with the YOLOv8 object detection algorithm [5], [6], which is the latest version of the YOLO [7], [8] and aims to improve deep learning techniques such as CNN-based classifiers for the character classification task.

The main contributions of this study are as follows:

- Instead of using a single classifier for all the characters in the license plate, the license plate image is divided into blocks of numbers and letters, and by using a separate classifier for each block, the character classification accuracy is improved from 95.9% to 99.6% on average for two classes.
- An mAP of 98.9% was achieved with the trained YOLOv8 object detection model.
- The overall license plate recognition accuracy of the system is 97.3%.
- A new character image dataset called License Plate Character Dataset was created for this study.
- To improve the classification accuracy of similar characters, a new dataset containing some pixel-based features of the characters called Pixel-based Character Feature Dataset was created.
- A deep learning model was trained using the dataset containing these pixel-based features and the probability values obtained from this deep learning model were added to the prediction results during testing. With the contribution of this deep learning model, the average classification accuracy was increased to 99.7%.
- The results show that when the classifier based on pixel features alone is used without the CNN classifier, it works with a classification accuracy as high as 90%.

2. Literature review

License plate recognition systems are widely used today, especially in security, traffic management, and automation. The recent development of these systems has been accelerated by the advancement of machine learning

and artificial intelligence technologies [9]. This section presents a literature review on machine learning and deep learning methods used in automatic license plate detection applications.

In license plate recognition systems, one of the first and most essential operations is to locate the license plate in the image. License plates usually have fixed shapes and similar colors [10], and a study using these visual features presents a modified version of the GrabCut algorithm to locate the license plate region [11]. To implement this algorithm, the geometric information of the aspect ratios of the license plates was used, and using a dataset of 500 different vehicle images, 99.8% accuracy was achieved in predicting the location of license plates. However, this method seems quite slow compared to current deep learning methods, with an average license plate detection time of 0.21 seconds. Studies conducted with current deep learning methods have achieved much faster detection times, such as 18.75 ms [12]. Apart from these algorithms, recent deep learning-based object detection algorithms such as YOLO, SSD, and Faster-RCNN have been widely used in license plate detection applications in recent years [13], [14], [15]. These deep learning-based algorithms estimate the coordinate points where the object to be detected is located in the image and the class to which it belongs.

Another essential process for license plate recognition systems is the segmentation and classification of the characters in the localized license plate image. In the algorithms used in license plate recognition systems, the characters in the license plate are first segmented separately. Then, the segmented character images are classified using classifiers such as CNN, and character recognition is performed [16], [17].

In the literature, a Chinese license plate recognition research paper was conducted with license plate region detection using SVM and character classification based on CNN networks. The results show that the detection rate of the license plate region was 99%, and character recognition accuracy was 97.1%. The overall accuracy rate of the system was 95% [18]. In another research work, edge detection and SVM algorithms were used. This method achieved 96% accuracy in license plate recognition [19]. YOLOv5 was used for the detection of license plates in another study, and CNN was used for the recognition of characters in the detected license plates. The overall accuracy rate of this method was 92.8% [20]. In another study using the YOLO object detection algorithm, an average recognition rate of 96.9% was achieved on eight datasets from five different regions [21]. In this work, the Fast-YOLOv2 model was used to detect license plates and classify them according to regions, and the CR-NET [22] model was used to recognize the characters in the detected license plates. Fast-YOLO architecture with the CR-NET model is used in another work for the detection and segmentation of license plates[23]. In a study combining Xception and LSTM networks for license plate recognition, the system achieved an overall accuracy rate of 90.5% [24]. A research work proposed to classify license plates and characters simultaneously with two fully convolutional one-stage object detectors and ResNet50 was used as the backbone network. In this study, 96.4% license plate recognition accuracy was obtained [25]. In a paper using the YOLOv5 algorithm, which is stated to be suitable for real-time use, the license plate recognition accuracy was 93% [26]. Another work used YOLOv3 for license plate detection and the ILPRNET algorithm for license plate recognition and achieved an overall accuracy of 93.6% [27]. A study that used the YOLOv3 algorithm both for license plate detection and character detection achieved a 95.05% accuracy rate in license plate recognition [28]. The newest research on license plate recognition very often applies deep learning methods, especially various versions of the YOLO algorithm [29].

In this study, the last version of YOLO architecture, YOLOv8, is applied to the image to detect the coordinates of license plates in the image. Then characters in the obtained license plate images were segmented and classified using the CNN model.

3. Material and method

Information about datasets and deep learning methods used in the study is given in this section. It also provides the hyperparameters for the trained YOLOv8 and classifier models, evaluation metrics applied during the evaluation of the models, and details of the improvements made.

3.1. Dataset

The YOLOv8 object detection model for license plate detection is trained on a dataset containing 24242 marked license plate images [30]. This dataset includes vehicle images and YOLOv8 annotation files containing the coordinates of the license plates in the image. The dataset consists of 21174 training, 2048 validation, and 1020 test data. These values have remained the same as determined by the researchers who provided the dataset. This dataset is referred to as the License Plate Detection Dataset in this study.

After detecting license plates with the YOLOv8 model, locating the characters on the license plates and determining which character they are is necessary. This classification problem requires another data set consisting of character images. The fonts of the characters on the license plates vary around the world. [31]. Using any other license plate character dataset in the world during the training phase may affect the feature extraction and classification success of Turkish license plate characters. For this reason, there is a need for a dataset containing the license plate characters in Türkiye. Since a dataset containing the license plate characters in Türkiye is needed, this dataset is not taken as ready-made but created by the authors. The characters in the images of the license plates in Türkiye are cropped, grayscaled, and resized to 22x44 dimensions, which are the input dimensions of the classifiers. Finally, all the images were labeled to create a license plate character dataset, and the created dataset is named as License Plate Character Dataset. Sample images from the License Plate Character Dataset are shown in Fig. 1.

The License Plate Character Dataset consists of 16500 images, 500 images for each character. There are 32 character image samples in Fig. 1. Since the same character is used for the number 0 and the letter O in Turkish license plates, the images of this character are used for both the number 0 and the letter O. In this way, the dataset contains a total of 16500 images. Since the proposed method classifies characters as numbers and letters, this dataset is divided into two different sub-datasets: number and letter datasets. The sub-dataset consisting of number images is referred to as License Plate Character Dataset-N, and the sub-dataset consisting of letter images is referred to as License Plate Character Dataset-L. The total number of data and the number of training, test, and validation data of these datasets are shown in Table 1.
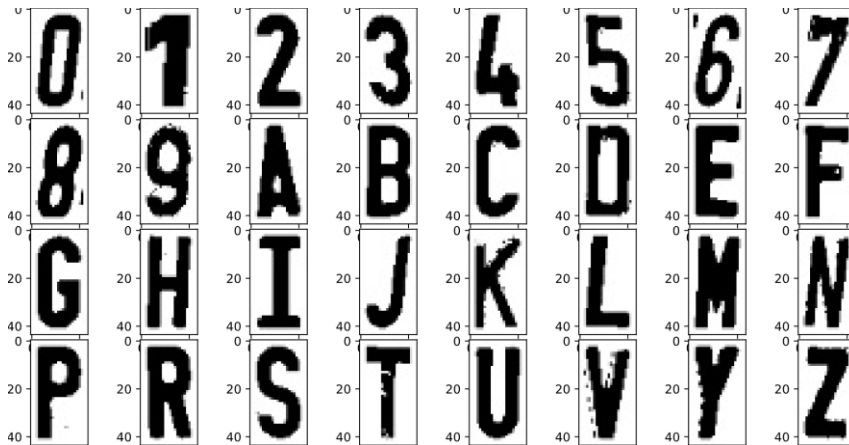
Fig. 1. Sample character images from the License Plate Character Dataset.

In addition to the License Plate Character Dataset, another dataset created by the authors, the Pixel-based Character Feature Dataset contains the data obtained from the pixel-based features of the character images. Eight pixel-based features were extracted for each character image in the License Plate Character Dataset and a new dataset of 16500 rows and nine columns -one for label values- was created.

Data samples from the Pixel-based Character Feature Dataset, are shown in Fig. 2, and the correlation matrix of the data is presented in Fig. 3. Similar to the License Plate Character Dataset, this dataset is divided into number and letter subsets. The sub-dataset consisting of features of number images is called Pixel-based Character Feature Dataset-N and the sub-dataset consisting of features of letter images is called Pixel-based Character Feature Dataset -L.

	Upper Ratio	Lower Ratio	Left Ratio	Right Ratio	Top Left Ratio	Top Right Ratio	Bottom Left Ratio	Bottom Right Ratio	Label
0	0.38	0.62	0.47	0.53	0.17	0.21	0.30	0.32	0
1	0.40	0.60	0.29	0.71	0.04	0.36	0.25	0.35	0
2	0.42	0.58	0.38	0.62	0.09	0.33	0.28	0.29	0
3	0.41	0.59	0.56	0.44	0.24	0.17	0.31	0.27	0
4	0.42	0.58	0.42	0.58	0.14	0.28	0.28	0.30	0
...	...	...	...	...	...	...	...	...	...
9195	0.50	0.50	0.50	0.50	0.19	0.31	0.31	0.18	22
9196	0.52	0.48	0.49	0.51	0.15	0.37	0.34	0.14	22
9197	0.52	0.48	0.52	0.48	0.18	0.34	0.35	0.14	22
9198	0.50	0.50	0.51	0.49	0.20	0.30	0.31	0.19	22
9199	0.51	0.49	0.51	0.49	0.19	0.32	0.32	0.17	22

9200 rows × 9 columns

Fig. 2. Sample of the Pixel-based Character Feature Dataset.
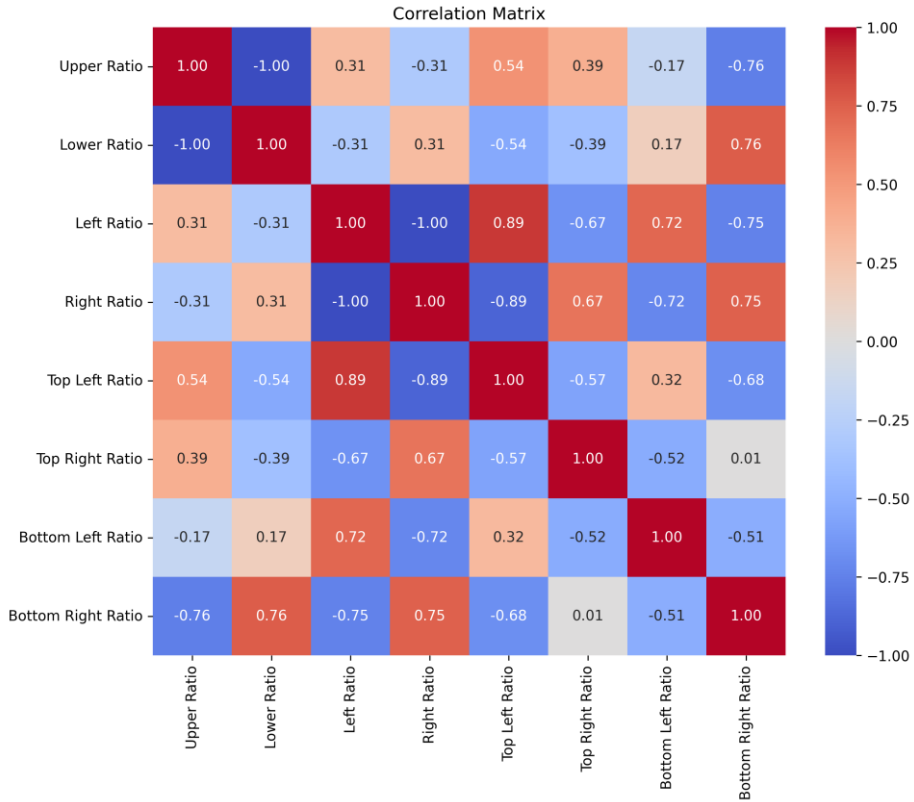
Fig. 3. Correlation matrix of the Pixel-based Character Feature Dataset.

Table 1, presented below, contains information about all the datasets used in this study. The datasets used for character classification are divided into two different sub-datasets, numbers and letters, in accordance with the method proposed in the paper. The proportions of the datasets for training, testing, and validation sub-sets can also be seen in the table.

Table 1. Summary of the datasets used.

Dataset	Total number of data	Training data	Validation data	Test data
License Plate Detection Dataset [30]	24242 (%100)	21174 (%87.3)	2048 (%8.5)	1020 (%4.2)
License Plate Character Dataset-N	5000 (%100)	3500 (%70)	500 (%10)	1000 (%20)
License Plate Character Dataset-L	11500 (%100)	8050 (%70)	1150 (%10)	2300 (%20)
Pixel-based Character Feature Dataset-N	5000 (%100)	3500 (%70)	500 (%10)	1000 (%20)

Pixel-based Character Feature Dataset-L	11500 (%100)	8050 (%70)	1150 (%10)	2300 (%20)

3.2. Proposed model

This section presents the proposed license plate recognition architecture design, the details of the deep learning models used, and the improvements made. To summarize the steps of the license plate recognition process, first, the coordinates of the license plate in the camera image are determined. The license plate region within these coordinates is cropped from the image, and the license plate recognition process is completed due to operations such as character segmentation, cropping, and classification of characters from the image. The model proposed in this study uses a block structure to improve classification accuracy. The structure of the proposed model is shown in Fig. 4.
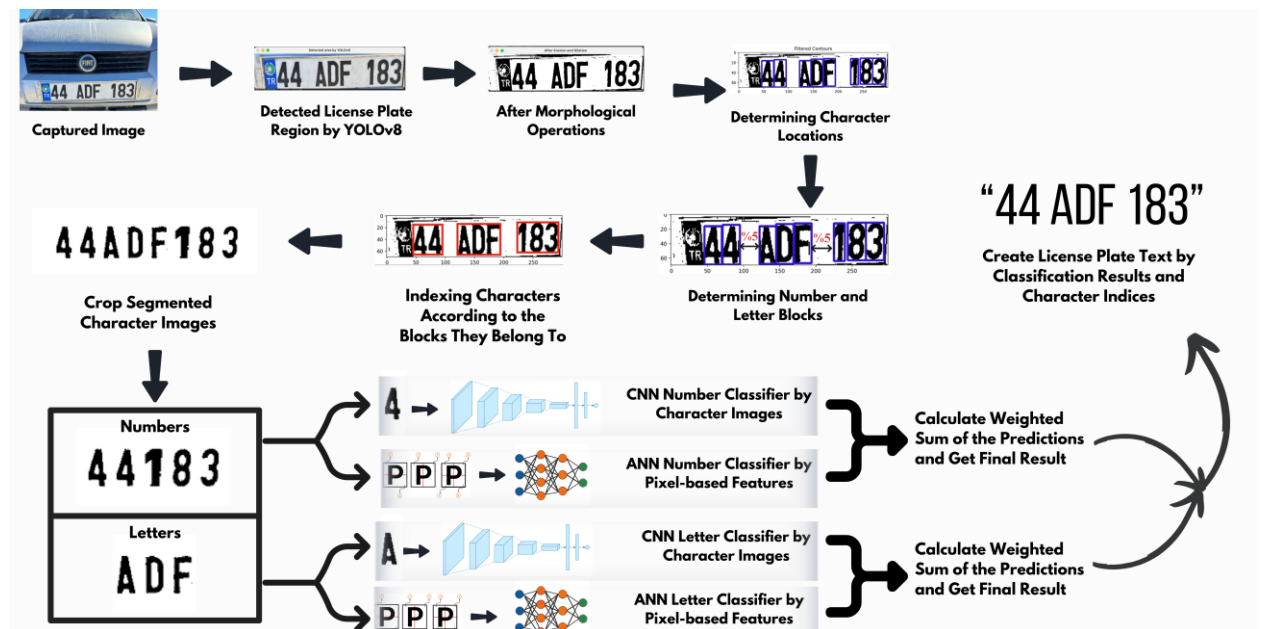
Fig. 4. Proposed model.

3.2.1 License plate detection

The YOLOv8 object detection model is trained to detect license plates in the image. The general structure of the YOLOv8 architecture is presented in Fig. 5.
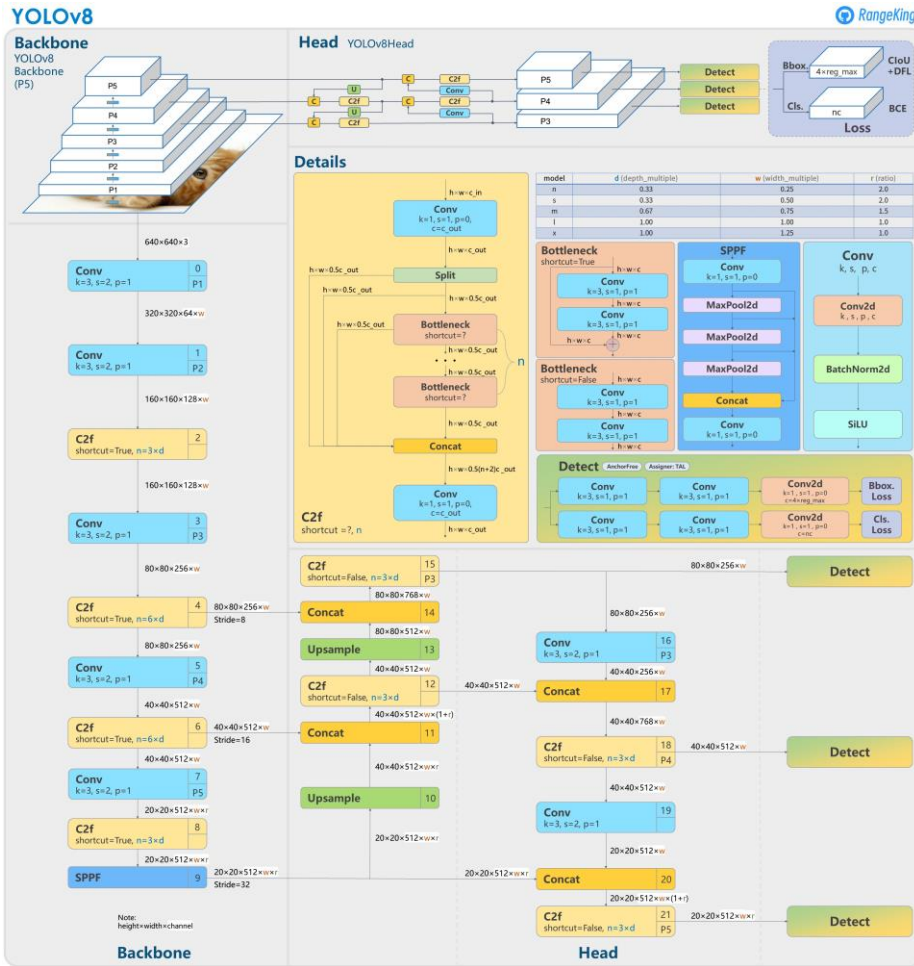
Fig. 5. YOLOv8 architecture [32].

The training was performed on an RTX 3060 graphics card with 3584 CUDA cores using CUDA [33] technology, and the training of the YOLOv8 model took 8 hours and 10 minutes for 21174 images. The parameters of the trained model are presented in Table 2. The trained model was tested on multiple computers. An example of the license plate region detected with the trained YOLOv8 model is shown in Fig. 6.

Table 2. YOLOv8 training hyperparameters.

Parameter	Value
Epoch	100
Batch	8
Optimizer	SGD
Learning rate	0.01

Momentum	0.937
Image size	640x640

Fig. 6. Example of plate region detected with YOLOv8 model.

3.2.2 Character segmentation

After the license plate region is detected and cropped, morphological operations are performed to facilitate the segmentation of the characters on the license plate. First, the image is resized to 300x75. Then, OTSU thresholding [34], erosion with a 3x3 kernel, and dilation with a 3x3 kernel are applied. Erosion and dilation are applied one after the other to reduce noise, emphasize details, and facilitate contour processing. The plate image after the operations is shown in Fig. 7.
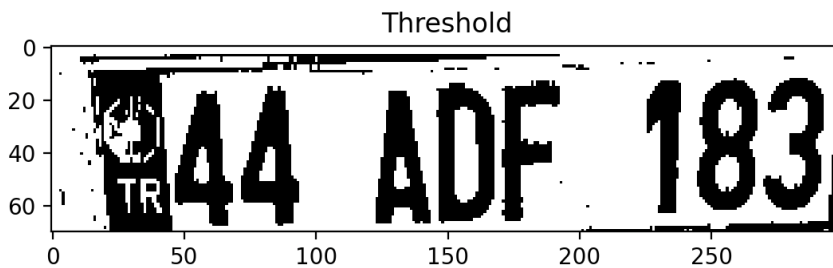
Fig. 7. License plate image after morphological operations.

To locate the characters in the image after thresholding and noise reduction, the contours in the image were found. First, all contours in the image were found with the help of the OpenCV [35] library, and then the contours

65

that may contain characters were filtered. This filtering process was done according to the ratio of the found contour sizes to the total size of the license plate. Upper and lower bounds were set for the height and width of the contours that might contain characters, and then the contours outside these bounds were ignored. The upper and lower bounds were determined after tests with the obtained license plate images. Information about these values can be seen in Table 3.

Table 3. Lower and upper bound values for character contour filtering.

Boundary value type	Boundary value
Width lower bound	w*0.166
Width upper bound	w*0.5
Height lower bound	h*0.1
Height upper bound	h*0.66

In the table, w is the total width of the license plate image, and h is the total height of the license plate image. After these operations, the license plate image contains the filtered contours and shows only the position of the characters that need to be recognized on the license plate. The contour information before and after the filtering process is shown in Fig. 8.
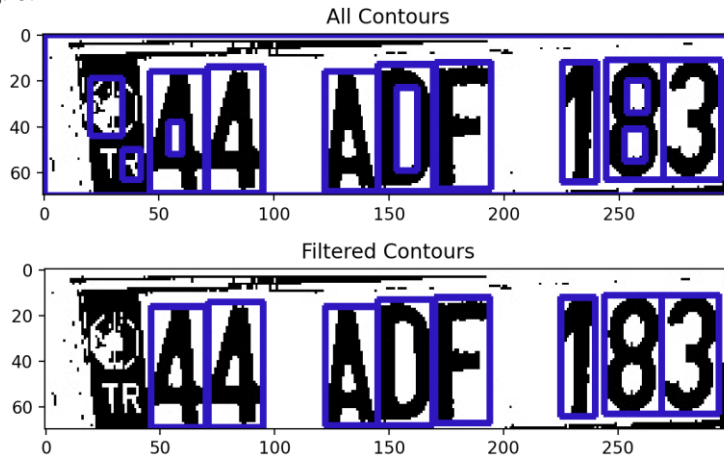
Fig. 8. Contours before and after filtering.

3.2.3 Determination of the blocks

After the positions of the characters are determined, the classification process is started. However, when a single classifier is trained for all characters in the License Plate Character Dataset, the accuracy rate is found to be insufficient, and after the tests, it was determined that similar characters such as 0 and O, 4 and A, and 1 and I affect the recognition accuracy.

In this study, a method for recognizing the letters and numbers on license plates with separate classifiers was developed to improve recognition accuracy. The license plates in Türkiye consist of 3 blocks in total: the first block is a number block indicating the province to which the license plate belongs, the second block is a letter block consisting of 1 to 3 letters, and the last block is a number block again.

With the help of the determined contours, the distance between the characters in the license plate was calculated, and the relevant blocks were determined. As a result of the tests, it was seen that the distance between the blocks was at least 5% of the total width of the plate. Therefore, in cases where the distance between contours is more than 5%, a block change is assumed, and the character images in each block are classified with the help of the relevant classifier. The positions of the blocks on the license plate image and the console outputs of the block detection process are shown in Fig. 9.
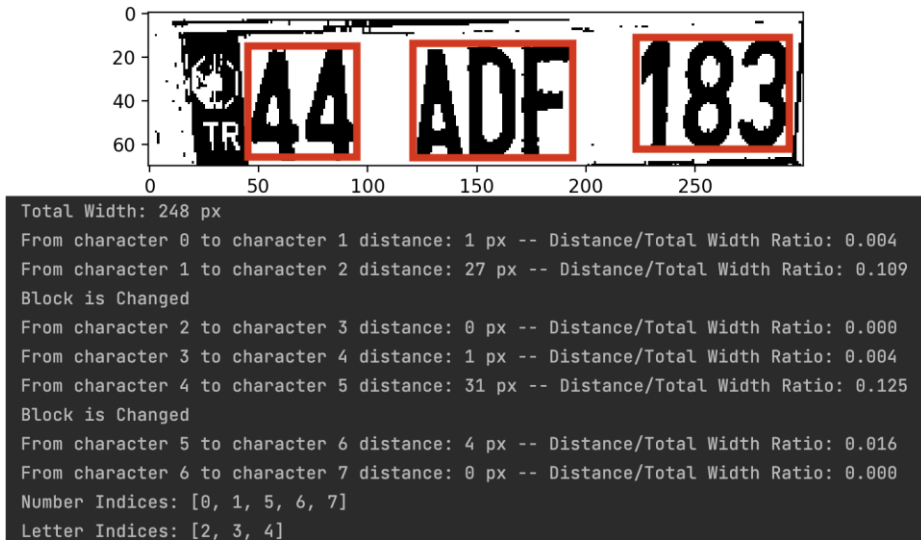
Fig. 9. The process of identifying plate blocks.

3.2.4 Character classification by images

Character recognition is started after determining which classifier the characters should be sent to according to their indexes. A CNN model was created to classify the number and letter images for character recognition. The architecture of the CNN model used for letter classification is shown in Fig. 10.

67

conv2d_input	input:	[(None, 44, 24, 1)]
InputLayer	output:	[(None, 44, 24, 1)]

conv2d	input:	(None, 44, 24, 1)
Conv2D relu	output:	(None, 42, 22, 32)

max_pooling2d	input:	(None, 42, 22, 32)
MaxPooling2D	output:	(None, 21, 11, 32)

conv2d_1	input:	(None, 21, 11, 32)
Conv2D relu	output:	(None, 19, 9, 64)

max_pooling2d_1	input:	(None, 19, 9, 64)
MaxPooling2D	output:	(None, 9, 4, 64)

conv2d_2	input:	(None, 9, 4, 64)
Conv2D relu	output:	(None, 7, 2, 128)

max_pooling2d_2	input:	(None, 7, 2, 128)
MaxPooling2D	output:	(None, 3, 1, 128)

flatten	input:	(None, 3, 1, 128)
Flatten	output:	(None, 384)

dense	input:	(None, 384)
Dense relu	output:	(None, 128)

dense_1	input:	(None, 128)
Dense softmax	output:	(None, 23)

Fig. 10. CNN architecture used for letter classification.

The CNN architecture given above was created for letter classification with a 23-dimensional output layer. The model created for the classification of numbers has the same parts up to the output layer, which is 10-dimensional. The training and data augmentation parameters of the trained models are presented in Table 4.

Table 4. Training and data augmentation parameters of character classifier models.

Parameter	Value
Epoch	10
Batch	16
Optimizer	Adam
Learning rate	0.001
Image size	44x24
Rescale	1/255
Shear range	0.2
Zoom range	0.2
Horizontal flip	True
Loss	Categorical Crossentropy

3.2.5 Character classification by pixel-based features

The recognition process is completed after the detection of the license plate, identification of the blocks in the license plate, and classification of the characters. However, to improve the recognition accuracy, in addition to the block structure, a dataset based on pixel-based features of the images called Pixel-based Character Feature Dataset

was created, and an ANN model was trained to classify them according to this dataset. Fig. 11 shows the selection of 8 pixel-based features extracted from the image.
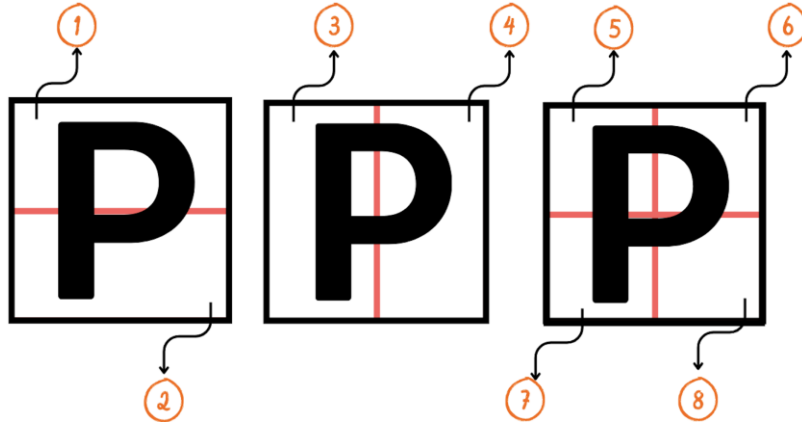
Fig. 11. Selected areas of pixel-based features for character images.

The Pixel-based Character Feature Dataset was created according to the above regions. The character image was first divided horizontally, and the ratio of black pixels in Region 1 to all black pixels in the image was calculated; the same was done for the black pixels in Region 2. Then, the character image was divided vertically, and the ratios of black pixels in Region 3 and Region 4 were calculated. Finally, the image was divided into four equal regions, and the proportion of black pixels in each region was calculated and added to the dataset. The main purpose of dividing the image into 4 regions is to facilitate the discrimination of characters such as the character "P". The pixel ratios may be equal in horizontal or vertical division, but when divided into four regions, it is seen that Region 8 contains fewer black pixels than all other regions. Fig. 12 shows the feature data for the character "P".

	Upper Ratio	Lower Ratio	Left Ratio	Right Ratio	Top Left Ratio	Top Right Ratio	Bottom Left Ratio	Bottom Right Ratio	Label
6277	0.65	0.35	0.62	0.38	0.32	0.33	0.30	0.05	15
6278	0.68	0.32	0.62	0.38	0.35	0.33	0.27	0.05	15
6279	0.66	0.34	0.63	0.37	0.33	0.33	0.31	0.04	15
6280	0.66	0.34	0.63	0.37	0.33	0.33	0.31	0.04	15
6281	0.69	0.31	0.65	0.35	0.36	0.33	0.29	0.02	15
6282	0.56	0.44	0.60	0.40	0.28	0.28	0.32	0.12	15

Fig. 12. Pixel-based feature data for character P.

As expected in the generated dataset, the lowest value is observed in region 8, called the Bottom Right Ratio. In addition, region 1 has more black pixels than region 2, and region 3 has more black pixels than region 4. Using this feature data, the CNN model contributes to the classification of characters such as 0 and D, which are very similar and difficult to classify by the CNN model. The final result is obtained by weighted summing the classification probabilities obtained from the pixel feature data set and the probabilities of the CNN network. In the weighted sum process, the CNN model is given a weight value of 0.9, and the ANN model is given a weight value of 0.1. The neural network's architecture that trained on the Pixel-based Character Feature Dataset is shown in Fig. 13.

dense_4_input	input:	[(None, 8)]
InputLayer	output:	[(None, 8)]

dense_4		input:	(None, 8)
Dense	relu	output:	(None, 64)

dense_5		input:	(None, 64)
Dense	relu	output:	(None, 16)

dense_6		input:	(None, 16)
Dense	relu	output:	(None, 16)

dense_7		input:	(None, 16)
Dense	softmax	output:	(None, 23)
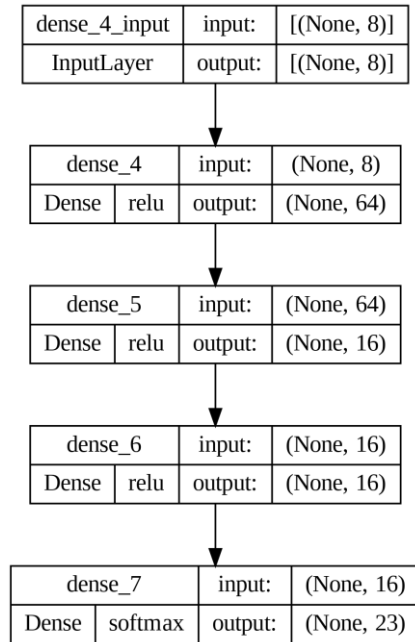
Fig. 13. ANN architecture for character classification based on pixel-based features.

The training parameters of the model used in the classification process are given in Table 5. Evaluation metrics for all models are presented in the next section.

Table 5. Training parameters of the character classification model based on pixel-based features.

Parameter	Value
Epoch	500
Batch	8
Optimizer	Adam
Learning rate	0.001
Loss	Categorical Crossentropy

3.3. Evaluation metrics

This section gives the evaluation metrics of the developed deep learning models. For the YOLOv8 model, Precision, Recall, and Mean Average Precision are some of the critical evaluation criteria. Where P is precision, it denotes the ratio of the TP value of a model to all predicted positive values (TP+FP), hence showing the proportion of samples classified as positive by the model that are positive. Recall R is the model's TP value as a ratio to actual positive values (TP+FN) and determines the number of positive samples that are classed correctly. This means there is a trade-off between these two evaluation metrics. Precision and Recall are calculated respectively as follows [36], [37]:

$$P = \frac{TP}{TP+FP} \tag{1}$$

$$R = \frac{TP}{TP+FN} \tag{2}$$

Average Precision (AP) is the average of the Precision values at different Recall levels, and it indicates the performance of a model at detecting objects at different confidence thresholds. Mean Average Precision (mAP) is the mean of the AP values for all classes, which describes the model's performance. The values of AP and mAP are obtained by [38]:

$$AP = \int_0^1 P(R) \, dR \tag{3}$$

$$mAP = \frac{1}{N}\sum_{i=1}^{N} AP_c \tag{4}$$

In the given equations $P(R)$ is the Precision value at a given Recall level, N is the number of classes, and AP_c is the average Precision value for the class c. For the trained CNN and ANN models, there are several evaluation metrics in addition to Precision and Recall metrics. These are Accuracy (A) and Specificity (S) metrics. Accuracy is the ratio of the sum of the TP and TN values to all samples in the test set and represents the overall correct prediction rate. Specificity is the ratio of the TN value to all true negative values (TN + FP) and measures how accurately truly negative samples are classified. Accuracy and Specificity metrics are calculated as follows respectively [39]:

$$A = \frac{TP+TN}{TP+TN+FP+FN} \tag{5}$$

$$S = \frac{TN}{TN+FP} \tag{6}$$

Categorical Crossentropy (CCE), used in the classification of CNN and ANN models, is a loss function used when there are two or more label classes and is calculated as follows [40]:

$$CCE = -\sum_{C=1}^{M} y_{o,c} \, log(p_{o,c}) \tag{7}$$

In the specified loss function, M represents the number of classes. y is a binary representation (0 or 1) indicating whether the class label c is the correct classification for observation o, and p represents the probability that observation o is predicted to belong to class c. In the next section, we present and discuss the performance of the deep learning models according to these evaluation metrics.

4. Results and discussion

This section presents the performance of the trained deep learning models according to the evaluation metrics. The complexity matrix obtained after training the YOLOv8 model is shown in Fig. 14. The performance values are presented in Table 6.
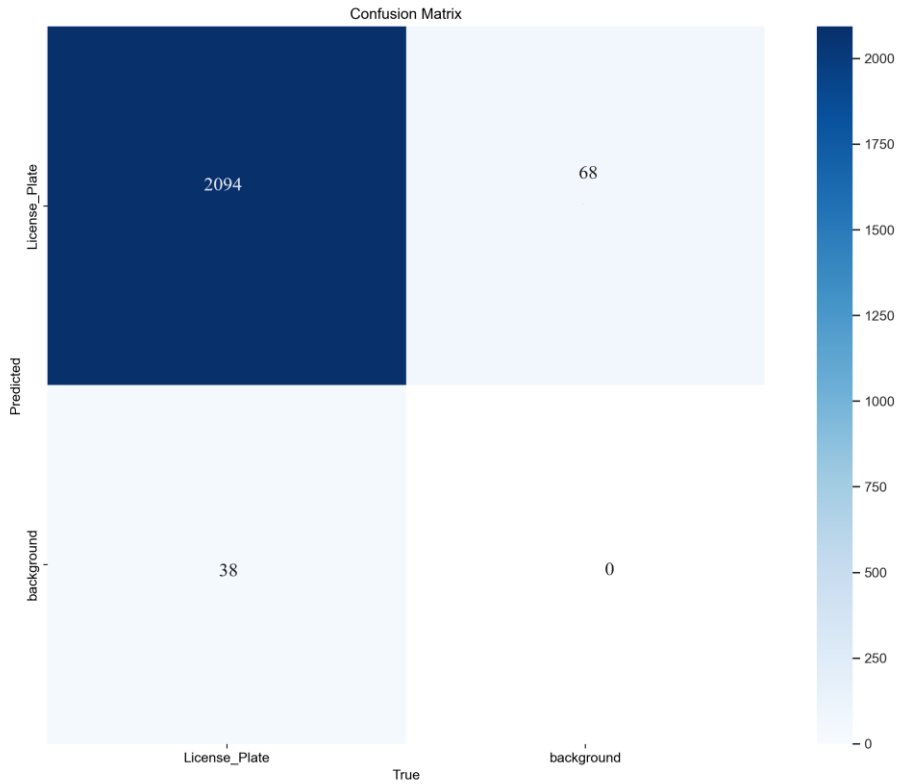
Confusion Matrix

Fig. 14. Confusion matrix of YOLOv8 model.

Table 6. YOLOv8 object detection model test performance values.

Metric	Value
Precision	0.979
Recall	0.973
mAP	0.989

The evaluation results show that the trained model is 98.9% accurate in detecting license plates in the image. To better understand the balance achieved by the model for Precision and Recall metrics, the Precision-Recall curve of the model is presented in Fig. 15.
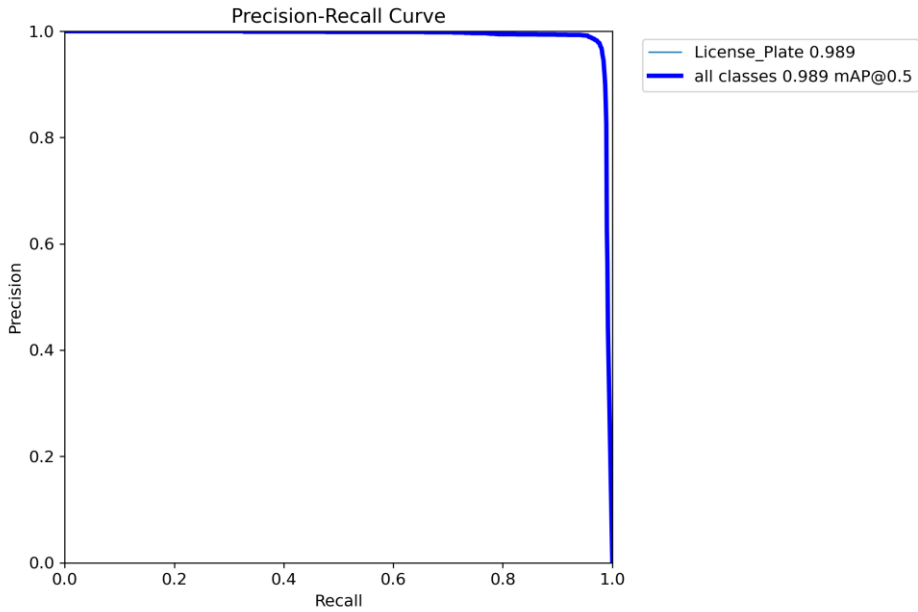
Fig. 15. Precision-Recall curve of YOLOv8 model.

The Precision-Recall curve indicates the trade-off between Precision and Recall for various threshold values. The high area under the curve indicates that both Recall and Precision values are high. Here, high Precision is associated with a low FP rate, and high Recall is associated with a low FN rate. Graphs of the changes in all evaluation metrics during training can be seen in Fig. 16.
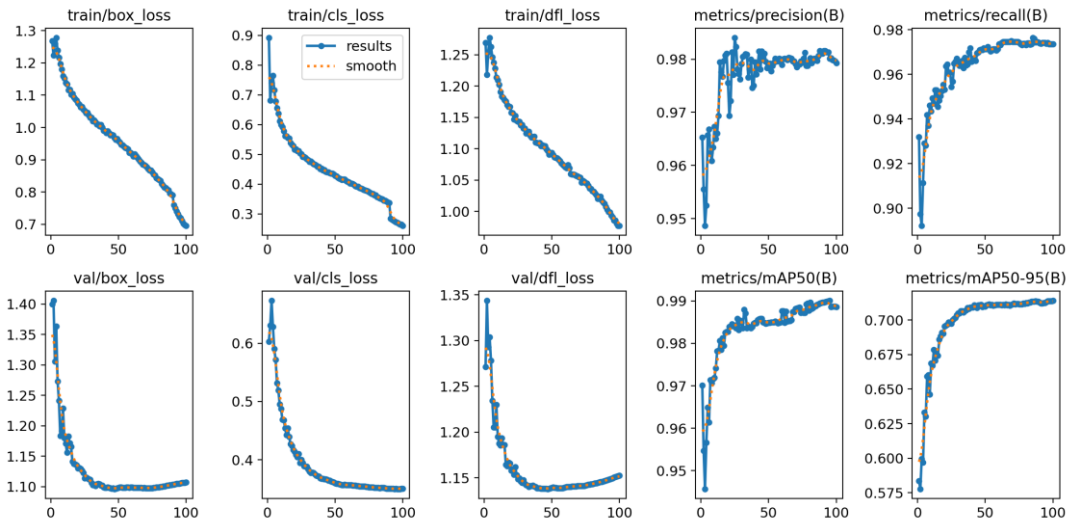
Fig. 16. Training and validation performances of the YOLOv8 model.

When the results are analyzed, it is seen that the loss values in the training and validation phases decrease sharply after the first 20 epochs and the mAP value increases. Considering the data size and the noisy samples in the data, it is seen that the trained model achieves very successful results. After the training of the license plate detection model was completed, the training of the CNN models that classify the number and letter images on the license plate was completed. In order to make a comparison, we first trained a single classifier that classifies all characters with the same architecture. Then, two separate classifiers were trained for letters and numbers, and their performances were analyzed. The accuracy and loss values obtained during the training of the classifier that classifies all characters are given in Fig. 17. The accuracy and loss values obtained during the training of the classifiers that classify numbers and letters separately are shown in Fig. 18.
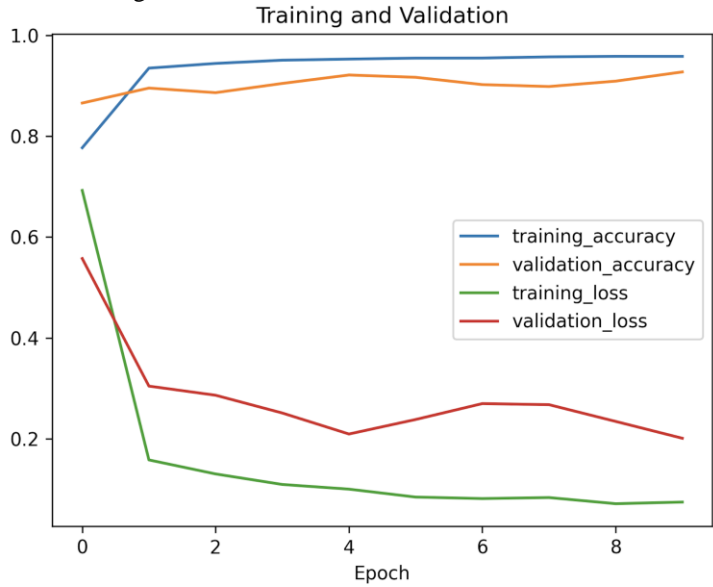
Fig. 17. Training graph of the single CNN model classifying all characters
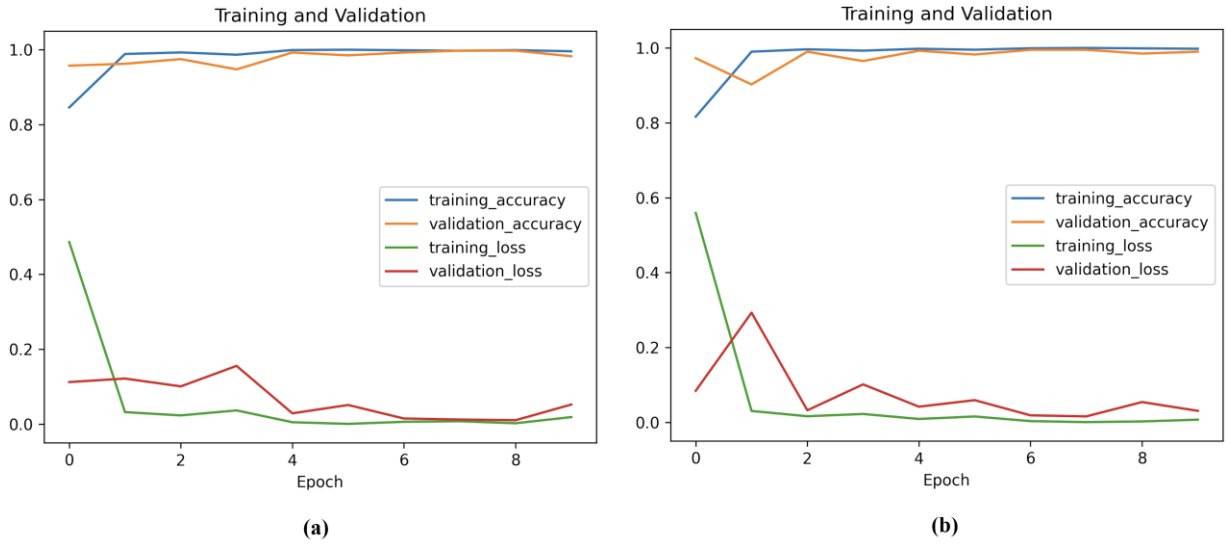
Fig. 18. Training graphs of the letter classifier CNN model (a) and the number classifier CNN model (b).

When the training graphs are analyzed, it can be seen that using two different classifiers, number and letter classifiers, has higher accuracy and much lower loss values than a single classifier. The complexity matrices obtained from the tests of these classifiers on the test data are given below. Fig. 19 shows the complexity matrix of the single classifier, and Fig. 20 shows the complexity matrices of the proposed two-classifier structure.
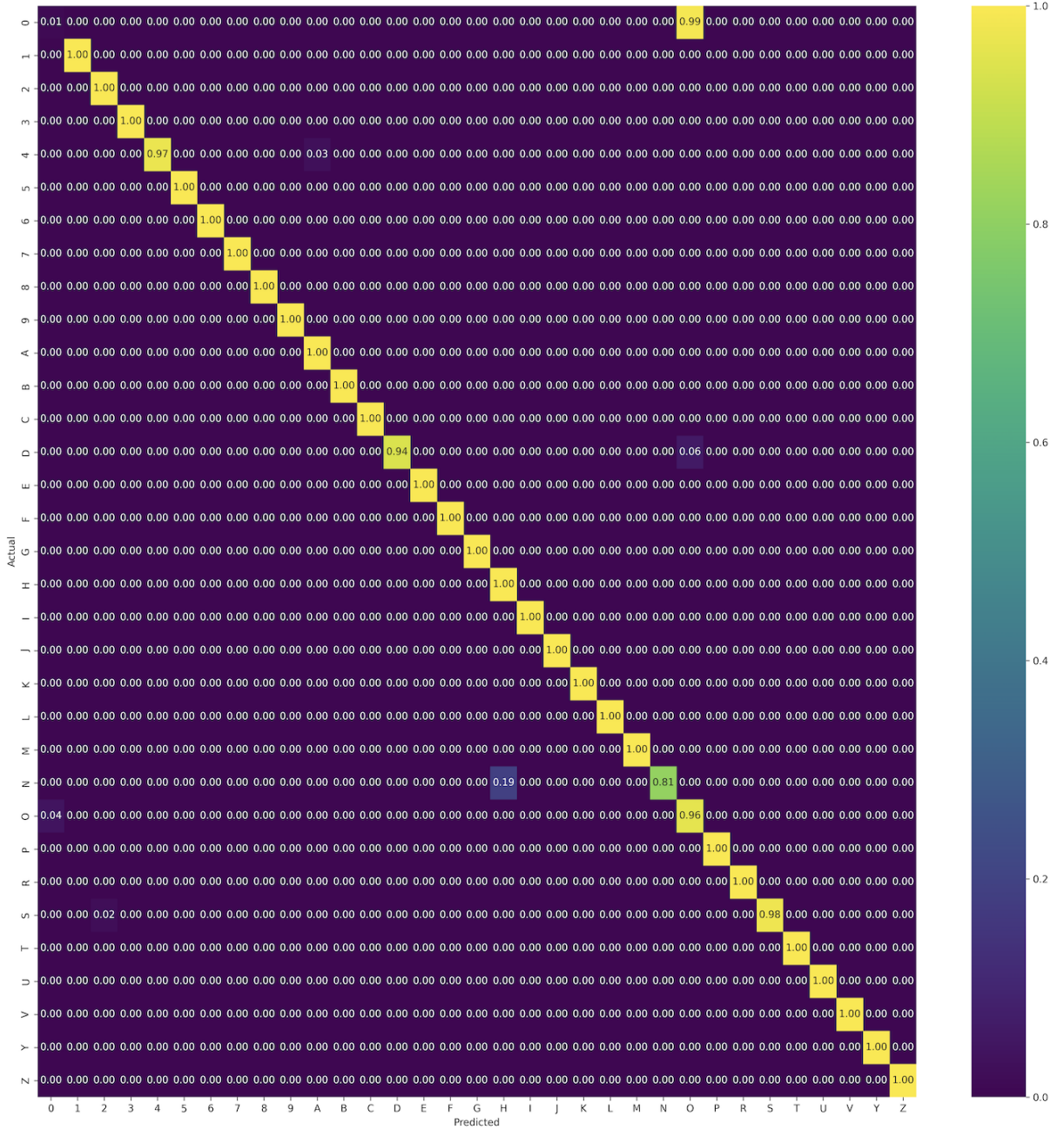
Fig. 19. Complexity matrix of the single CNN model classifying all characters.

(a)

(b)
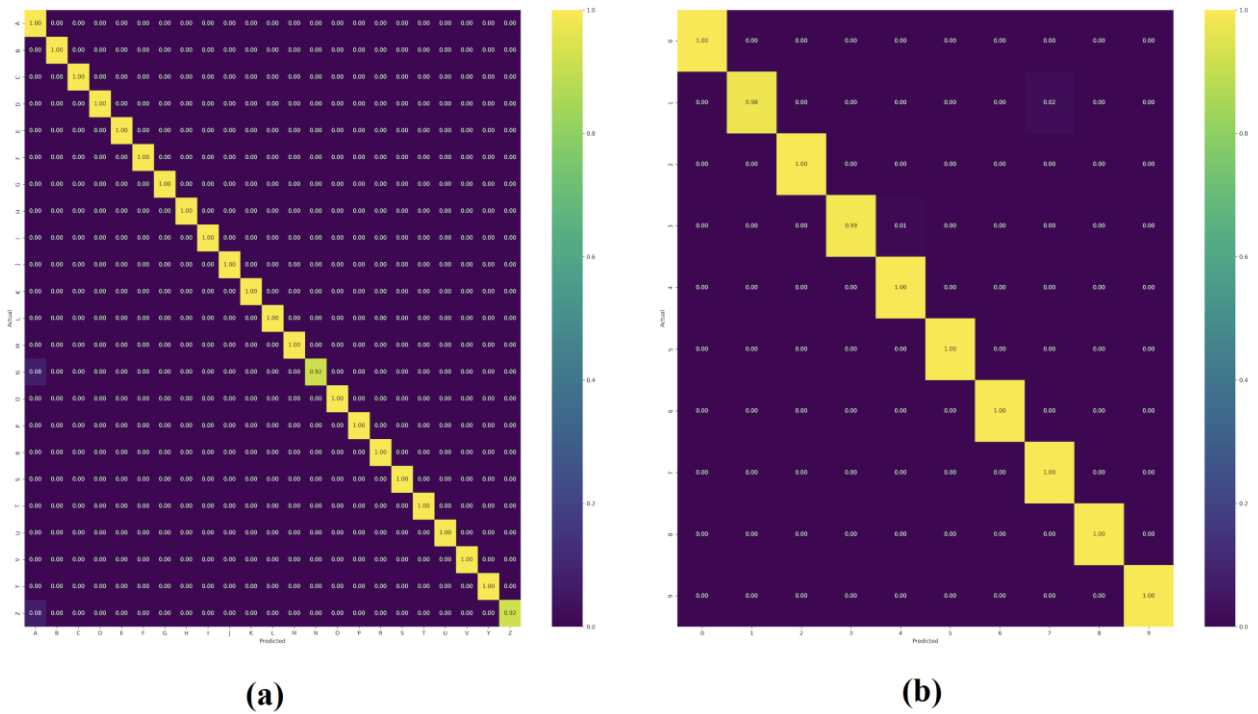
Fig. 20. Complexity matrices of the letter classifier CNN model (a) and the number classifier CNN model (b).

When the complexity matrices are examined, it is seen that the model that classifies all characters classifies almost all of the '0' characters as the letter 'O' and has a high misclassification rate in the classification of 'N' and 'H' characters. It is seen that the models trained separately for letters and numbers make predictions with much higher accuracy. The performance values obtained from the complexity matrix of the models can be seen in Table 7.

Table 7. Test performance of CNN classifiers.

Metric	Precision	Recall	Specificity	Accuracy
All Characters Classifier	0.95	0.96	0.95	0.959
Letter Classifier	0.99	0.99	0.98	0.993
Number Classifier	0.99	0.99	0.99	0.999

When the results are analyzed, it is seen that the proposed method of dividing the license plate into blocks and using different classifiers for each block achieves a very high accuracy rate compared to the traditional method of classifying all characters with a single classifier. In addition to the CNN models, ANN models that classify using pixel-based features were also trained and tested. The training graphs can be seen in Fig. 21, and the complexity matrix values obtained after the test can be seen in Fig. 22.
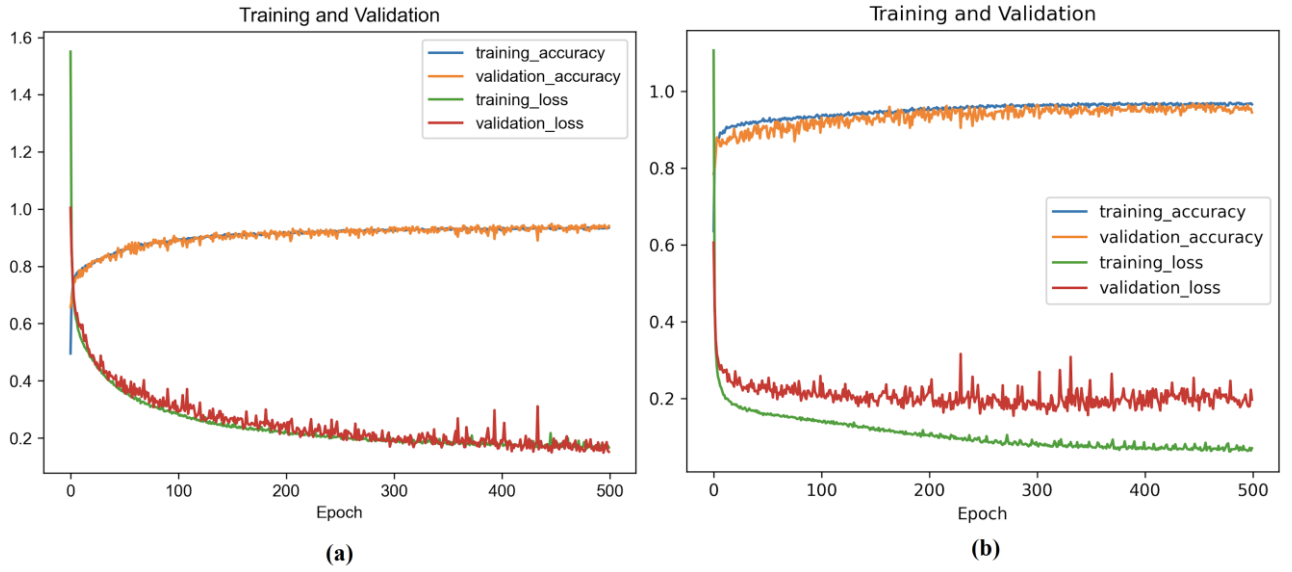
Fig. 21. Training plots of letter classifier ANN model (a) and number classifier ANN model (b).
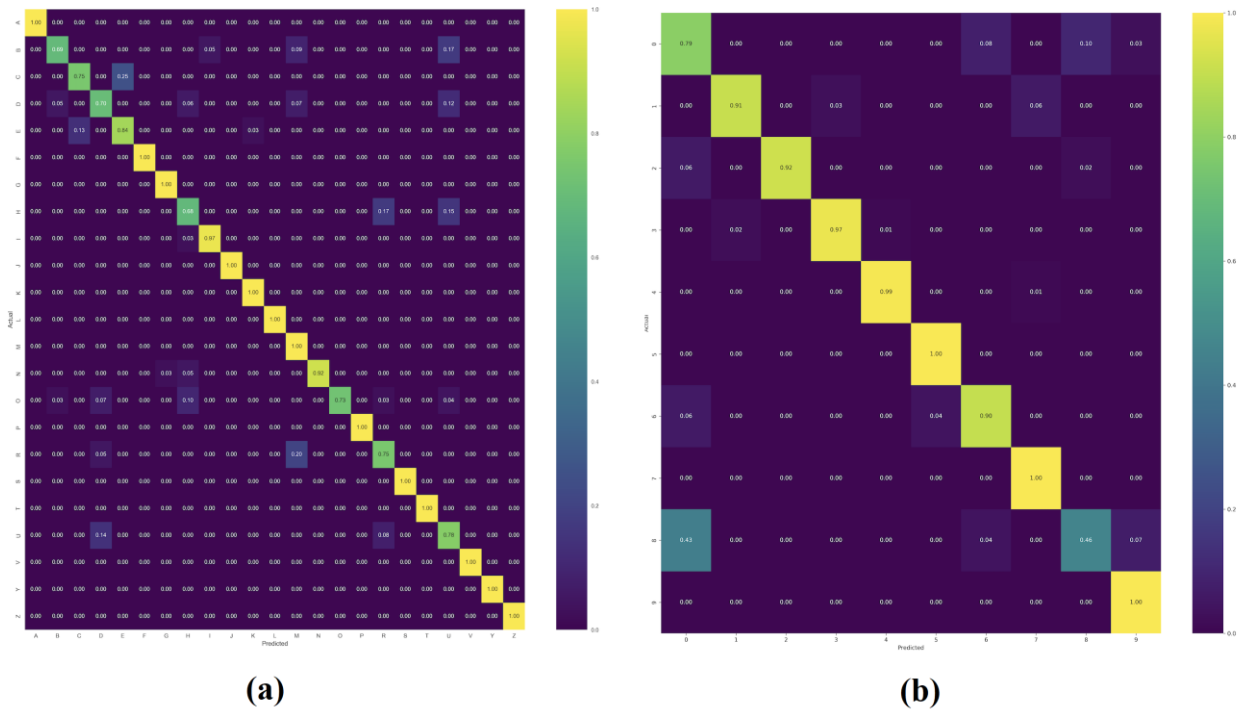
Fig. 22. Complexity matrices of the letter classifier ANN model (a) and the number classifier ANN model (b).

When the training graphs and complexity matrices are examined, it is seen that although the accuracy of the ANN model is high and the loss value is low during classification, the loss values are high when the validation data is used. This shows that the model is subject to overfitting; it cannot generalize the data well enough. However, the letter classifier ANN model performed well despite the low data size and limited feature diversity. When the complexity matrices are analyzed, it is seen that there is difficulty in classifying symmetrical characters in both horizontal and vertical axes. For example, it is noticeable that incorrect predictions were made between the characters '0' and '8'. The performance values of the trained ANN models are given in Table 8.

Table 8. Test performance of ANN classifiers.

Metric	Precision	Recall	Specificity	Accuracy
Letter Classifier	0.91	0.90	0.90	0.90
Number Classifier	0.90	0.89	0.89	0.89

Although the accuracy values are relatively low, sufficient classification accuracy is achieved with low computational cost and low data set size using eight simple features extracted from the image. As a result of the weighted sum of the probability values obtained from CNN and ANN models, the accuracy rate in the character classification process was increased from 99.6% to 99.7%.

After these steps, there is one last step left to be done. This is to reveal the license plate text by combining the characters obtained from the classification results of the character images on the license plate. A vehicle image with license plate recognition completed is shown in Fig. 23.

Fig. 23. Image of a vehicle with completed license plate recognition.

As a result of the tests, the system's overall license plate recognition accuracy was found to be 97.3%. Table 9 compares the results obtained with those of other studies in the literature.

Table 9. Comparison of the proposed method with other studies in the literature.

Study	License Plate Detection (mAP)	Character Recognition Accuracy	Overall License Plate Recognition Accuracy
Cheng et al. [18]	**0.990**	0.971	0.950
Khan et al. [20]	0.950	0.928	0.928
Tourani et al. [28]	0.978	0.991	0.950
Zaafouri et al. [41]	0.955	0.994	0.945
Proposed Model	0.989	**0.997**	**0.973**

The comparison shows that the classification process using the proposed block structure outperforms the studies in the literature in terms of license plate recognition accuracy. Although the detection accuracy of license plates is 0.1% higher in only one study, the proposed model outperforms this study in overall license plate recognition accuracy by giving much better results in recognizing the characters in the detected license plates. In addition, the fact that the YOLOv8 model, which is the most up-to-date object detection algorithm in the literature, was efficiently trained using CUDA cores with a large amount of data and achieved a high detection rate significantly affected the accuracy of the license plate recognition system. The approach of classifying the classification process by dividing it into sub-problems instead of using a single model provides solutions with low computational cost due to the use of smaller size models and high accuracy value due to the reduction in complexity.

5. Conclusion

This work contributes to using current deep-learning methods for license plate detection. Among the main contributions, instead of classifying the characters in the license plate with a single character classifier, the license plate image is divided into blocks of numbers and letters so that separate classifiers are used for numbers and separate classifiers for letters.

This approach reduces the probability of misrecognizing similar characters such as 0 and O, 4 and A, 1 and I to zero. Character classification accuracy increased from 95.9% for a single classifier to 99.6% on average using two classifiers. In addition, a new character feature dataset, Pixel-based Character Feature Dataset was created to improve character classification accuracy. The addition of the deep learning model trained using the new dataset containing pixel-based features increased the classification accuracy of the system to 99.7%. Furthermore, a high mAP value of 98.9% was achieved with the trained YOLOv8 object detection model. The overall license plate recognition accuracy of the system was 97.3%. All these findings demonstrate the effectiveness and accuracy of deep learning methods used in license plate detection.

Future research could address issues such as increasing the model's generalization capability by using more data, developing a detailed object detection algorithm to improve small object detection performance, or conducting field studies to improve system performance in conditions that make camera images unfavorable for image processing. Such studies could lead to more comprehensive steps toward improving the reliability and usability of license plate recognition systems.

Acknowledgements

University. The sample vehicle license plate shown in the study belongs to the authors, and no ethical violations were made.

References

[1] M. Arora, A. Jain, S. Rustagi, and T. Yadav, "Automatic number plate recognition system using optical character recognition," *International Journal of Scientific Research in Computer Science, Engineering and Information Technology*, pp. 986–992, 2019.

[2] B. Lavanya and G. Lalitha, "Multileveled ALPR using Block-Binary-Pixel-Sum Descriptor and Linear SVC," *International Journal of Advanced Computer Science and Applications*, vol. 13, no. 5, 2022.

[3] Y. Kumar, K. Kaur, and G. Singh, "Machine learning aspects and its applications towards different research areas," in *2020 International conference on computation, automation and knowledge management (ICCAKM)*, IEEE, 2020, pp. 150–156.

[4] W. Weihong and T. Jiaoyang, "Research on license plate recognition algorithms based on deep learning in complex environment," *IEEE Access*, vol. 8, pp. 91661–91675, 2020.

[5] S. Rahman, J. H. Rony, J. Uddin, and M. A. Samad, "Real-Time Obstacle Detection with YOLOv8 in a WSN Using UAV Aerial Photography," *J Imaging*, vol. 9, no. 10, p. 216, 2023.

[6] G. Jocher, A. Chaurasia, and J. Qiu, "Ultralytics YOLOv8," 2023. [Online]. Available: https://github.com/ultralytics/ultralytics

[7] J. Redmon, S. Divvala, R. Girshick, and A. Farhadi, "You only look once: Unified, real-time object detection," in *Proceedings of the IEEE conference on computer vision and pattern recognition*, 2016, pp. 779–788.

[8 C.-Y. Wang, A. Bochkovskiy, and H.-Y. M. Liao, "YOLOv7: Trainable bag-of-freebies sets new state-of-the-art for real-time object detectors," in *Proceedings of the IEEE/CVF Conference on Computer Vision and Pattern Recognition*, 2023, pp. 7464–7475.

[9] G. Aslı and A. DOĞAN, "License Plate Recognition System Based on Artificial Intelligence with Different Approach," *El-Cezeri*, vol. 10, no. 1, pp. 121–136, 2023.

[10] H. Shi and D. Zhao, "License Plate Recognition System Based on Improved YOLOv5 and GRU," *IEEE Access*, vol. 11, pp. 10429–10439, 2023.

[11] A. O. Salau, T. K. Yesufu, and B. S. Ogundare, "Vehicle plate number localization using a modified GrabCut algorithm," *Journal of King Saud University-Computer and Information Sciences*, vol. 33, no. 4, pp. 399–407, 2021.

[12] T.-A. Pham, "Effective deep neural networks for license plate detection and recognition," *Vis Comput*, vol. 39, no. 3, pp. 927–941, 2023.

[13] N. Duan, J. Cui, L. Liu, and L. Zheng, "An end to end recognition for license plates using convolutional neural networks," *IEEE Intelligent Transportation Systems Magazine*, vol. 13, no. 2, pp. 177–188, 2019.

[14] N. Awalgaonkar, P. Bartakke, and R. Chaugule, "Automatic license plate recognition system using ssd," in *2021 International Symposium of Asian Control Association on Intelligent Robotics and Industrial Automation (IRIA)*, IEEE, 2021, pp. 394–399.

[15] N. P. Ap, T. Vigneshwaran, M. S. Arappradhan, and R. Madhanraj, "Automatic number plate detection in vehicles using faster R-CNN," in *2020 International conference on system, computation, automation and networking (ICSCAN)*, IEEE, 2020, pp. 1–6.

[16] B. Pu, "Research on Chinese license plate recognition algorithm based on convolution neural network," in *Journal of Physics: Conference Series*, IOP Publishing, 2021, p. 032055.

[17] M. Driss, I. Almomani, R. Al-Suhaimi, and H. Al-Harbi, "Automatic Saudi Arabian License Plate Detection and Recognition Using Deep Convolutional Neural Networks," in *International Conference of Reliable Information and Communication Technology*, Springer, 2021, pp. 3–15.

[18] C. Cheng, L. Mei, and J. Zhang, "License plate recognition via deep convolutional neural network," in *IOP Conference Series: Earth and Environmental Science*, IOP Publishing, 2018, p. 062030.

[19] A. Singh and P. Singh, "License Plate Recognition for Traffic Management," *Journal of Management and Service Science (JMSS)*, vol. 1, no. 2, pp. 1–14, 2021.

[20] I. R. Khan *et al.*, "Automatic License Plate Recognition in Real-World Traffic Videos Captured in Unconstrained Environment by a Mobile Camera," *Electronics (Basel)*, vol. 11, no. 9, p. 1408, 2022.

[21] R. Laroca, L. A. Zanlorensi, G. R. Gonçalves, E. Todt, W. R. Schwartz, and D. Menotti, "An efficient and layout- independent automatic license plate recognition system based on the YOLO detector," *IET Intelligent Transport Systems*, vol. 15, no. 4, pp. 483–503, 2021.

[22] S. Montazzolli and C. Jung, "Real-time brazilian license plate detection and recognition using deep convolutional neural networks," in *2017 30th SIBGRAPI conference on graphics, patterns and images (SIBGRAPI)*, IEEE, 2017, pp. 55–62.

[23] S. M. Silva and C. R. Jung, "Real-time license plate detection and recognition using deep convolutional neural networks," *J Vis Commun Image Represent*, vol. 71, p. 102773, 2020.

[24] L. Zhang, P. Wang, H. Li, Z. Li, C. Shen, and Y. Zhang, "A Robust Attentional Framework for License Plate Recognition in the Wild," *IEEE Transactions on Intelligent Transportation Systems*, vol. 22, no. 11, pp. 6967–6976, Nov. 2021, doi: 10.1109/TITS.2020.3000072.

[25] Q. Huang, Z. Cai, and T. Lan, "A Single Neural Network for Mixed Style License Plate Detection and Recognition," *IEEE Access*, vol. 9, pp. 21777–21785, 2021, doi: 10.1109/ACCESS.2021.3055243.

[26] J. A *et al.*, "Enhancing Public Safety through License Plate Recognition for Counter terrorism through Deep Learning Technique," in *2023 4th International Conference on Signal Processing and Communication (ICSPC)*, IEEE, Mar. 2023, pp. 96–100. doi: 10.1109/ICSPC57692.2023.10125687.

[27] Y. Zou *et al.*, "License plate detection and recognition based on YOLOv3 and ILPRNET," *Signal Image Video Process*, vol. 16, no. 2, pp.

473–480, Mar. 2022, doi: 10.1007/s11760-021-01981-8.

[28] A. Tourani, A. Shahbahrami, S. Soroori, S. Khazaee, and C. Y. Suen, "A robust deep learning approach for automatic iranian vehicle license plate detection and recognition for surveillance systems," *IEEE Access*, vol. 8, pp. 201317–201330, 2020.

[29] M. M. Khan, M. U. Ilyas, I. R. Khan, S. M. Alshomrani, and S. Rahardja, "A review of license plate recognition methods employing neural networks," *IEEE Access*, 2023.

[30] P. Roboflow Universe, "License Plate Recognition Dataset." Accessed: Mar. 02, 2024. [Online]. Available: https://universe.roboflow.com/roboflow-universe-projects/license-plate-recognition-rxg4e

[31] R. K. Varma P, S. Ganta, H. K. B, and P. Svsrk, "A Novel Method for Indian Vehicle Registration Number Plate Detection and Recognition using Image Processing Techniques," *Procedia Comput Sci*, vol. 167, pp. 2623–2633, 2020, doi: 10.1016/j.procs.2020.03.324.

[32] K. Range, "YOLOv8 by RangeKing." Accessed: Aug. 09, 2024. [Online]. Available: https://github.com/RangeKing

[33] R. G. Jha and A. Samlodia, "GPU-acceleration of tensor renormalization with PyTorch using CUDA," *Comput Phys Commun*, vol. 294, p. 108941, 2024.

[34] Z. Y. Tan, S. N. Basah, H. Yazid, and M. J. A. Safar, "Performance analysis of Otsu thresholding for sign language segmentation," *Multimed Tools Appl*, vol. 80, pp. 21499–21520, 2021.

[35] J. Sigut, M. Castro, R. Arnay, and M. Sigut, "OpenCV basics: A mobile application to support the teaching of computer vision concepts," *IEEE Transactions on Education*, vol. 63, no. 4, pp. 328–335, 2020.

[36] S. Dörterler, "Hybridization of k-means and meta-heuristics algorithms for heart disease diagnosis," *New Trends in Engineering and Applied Natural Sciences*, p. 55, 2022.

[37] S. Dörterler, H. Dumlu, D. Özdemir, and H. Temurtaş, "Hybridization of Meta-heuristic Algorithms with K-Means for Clustering Analysis: Case of Medical Datasets," *Gazi Journal of Engineering Sciences*, vol. 10, no. 1, pp. 1–11, Apr. 2024, doi: 10.30855/gmbd.0705N01.

[38] M. Safran, A. Alajmi, and S. Alfarhood, "Efficient Multistage License Plate Detection and Recognition Using YOLOv8 and CNN for Smart Parking Systems," *J Sens*, vol. 2024, 2024.

[39] F. Aydemir and S. Arslan, "A System Design With Deep Learning and IoT to Ensure Education Continuity for Post-COVID," *IEEE Transactions on Consumer Electronics*, 2023.

[40] O. Sahin, "Music Genre Classification Based on Song Titles with Long Short-Term Memory," in *2023 IEEE International Students' Conference on Electrical, Electronics and Computer Science (SCEECS)*, IEEE, 2023, pp. 1-5.

[41] A. Zaafouri, M. Sayadi, and W. Wu, "A Vehicle License Plate Detection and Recognition Method Using Log Gabor Features and Convolutional Neural Networks," *Cybern Syst*, vol. 54, no. 1, pp. 88–103, 2023.

RESEARCH ARTICLE

Microstrip Patch Antenna Design for 5G and Beyond Wireless Communication Systems

Bahar BARISER[a], Inci UMAKOGLU[b,*], Mustafa NAMDAR[c], Arif BASGUMUS[d]

[a]Kutahya Dumlupınar University, Department of Electrical and Electronics Engineering, 43100, Kutahya, Turkey
ORCID: 0000-0002-2173-7314
[b]Kutahya Dumlupınar University, Department of Electrical and Electronics Engineering, 43100, Kutahya, Turkey
ORCID: 0000-0002-2786-5421
[c]Kutahya Dumlupınar University, Department of Electrical and Electronics Engineering, 43100, Kutahya, Turkey
ORCID: 0000-0002-3522-4608
[d]Bursa Uludag University, Department of Electrical and Electronics Engineering, 16059, Bursa, Turkey,
ORCID: 0000- 0002-0611-3220

Abstract

This paper gives a theoretical evaluation on how feeder lengths are appropriate for distinct conductor materials using rectangular microstrip patch antenna shape with the help of finite integration techniques (FIT). In this study, the ground surface width is 5.6mm and the ground surface length is 4.65 mm for the rectangular microstrip patch antenna. The length of the patch is 3.44 mm while the patch width is 4.40 mm. The substrate thickness is at 0.20 mm, the patch thickness is 0.035 mm the additional inner feed length is 1.05 mm and the microstrip line feed width is 0.6 mm. Antenna of rectangular microstrip patch type has been designed to work in the 20 – 36 frequency band and working frequency of the proposed antenna is 28 GHz. Compared to the use of a single conductor on the surface of the designed patch antenna, three different conductor materials-copper, gold, and aluminum-were applied to the patch surface of the antenna. The return loss (S11), voltage standing wave ratio (VSWR), bandwidth (BW), directivity and gain of the microstrip antenna parameters are studied using finite integration method Computer Simulation Technology (CST) based on nine different feed lengths in microstrip antenna design. When analyzing the feature of the simulation, the optimal S11 can be observed at the 28 resonant frequencies in the copper conductor. According to the analysis results, for copper conductor the best S11 was obtained at a resonant frequency of 28.03 GHz. The value of S11 is -31.19 dB and the BW value is 968 MHz. For the gold conductor the high return loss is achieved using the at the resonated frequency of 28.01 GHz. S11 value is -32 dB and the BW value is 972 MHz Aluminum conductor has the highest value of S11 with a resonant frequency of 28.01 GHz as shown in -33.29 dB and BW value is 976 MHz. Unsurprisingly, the characterization of the conductor deposition on each structure shows that aluminum conductor yielded the best S11 among all the conductor types. The VSWR is equal to 1.05 for copper conductor at resonant frequency of 28.03 GHz, 1.05 at gold conductor at a resonant frequency of 28.01 and 1.04 for aluminum conductor at a resonant frequency of 28.01 GHz. The maximum directivity values that have been attained in the three-dimensional (3D) representation of the copper conductor, gold and aluminum conductor antennas are nearly 6.99

Corresponding author. Tel.: + 0 (274) 443 43 43; fax: + 0 (274) 265 20 13.
E-mail address: inci.umakoglu@dpu.edu.tr

dBi, respectively. The maximum values of the gain are obtained for the 3D representation of copper, gold and aluminum conductor antennas are 6.61, 6.60 and 6.58 dBi, respectively.

1. Introduction

Wireless communication is a technology employed for transmitting information or data, typically through the use of electromagnetic signals [1]. Currently, wireless communication is one of the rapidly growing and influential sectors of human life and its usage is expanding [2]. Fifth generation (5G) elevates the wireless communication network in terms of its features which include high speed communications, faster data transfer, low delay or latency, and dependable connections [3].

The impact of the progressive development of wireless communication has been illustrated by introducing a new, unique approach to both improve communication reliability and the utilization of the NOMA system with the help of UAV assistance [4]. Studying the outcomes of the radio wave signal transmission scheme called the orthogonal time frequency space non-orthogonal multiple access (OTFS-NOMA) in highly mobile users for 5G wireless communication and analyzing its effects on the reliability and effectiveness of mobility-based programs has brought into the light one of the highly significant wireless application zones for 5G [5, 6]. Cited in the article are the fairly appealing findings in ergodic capacity estimation with artificial neural networks in conjunction to underscore the role of innovation in CNS for reliability [7]. Specifically, this survey investigates the 5G wireless communication by assessing the bit error rate (BER) of downlink NOMA systems. Regarding reliability and efficiency, this analysis elucidated the imperative role played by the 5G wireless communication systems [8]. In this way, through the analysis of previous studies, it can be concluded that microstrip antennas have the potential to fulfill the demands of 5G communication systems [9]. From examining the functions of microstrip antennas and from the assessments of the capability of microstrip antennas to meet the demands of the 5G application, an efficient microstrip antenna design with wide bandwidth was proposed [10]. Patch antennas are also known as microstrip antennas; they are becoming more prevalent in almost all wireless communication applications including space communications [11]. With the increasing technology in communication engineering, there is a rise in the complication of the shape of antennas which the analytical methods cannot offer a full explanation; thus, computational electromagnetic models are used to solve them fully. This reveals the general situation with the antenna structures and field radiation that make it hardly possible to obtain a full solution of the antenna problems using solely the analytical methods it is necessary to apply the computational electromagnetic models (CEM) in addition [12]. This paper has shown that finite difference method, the finite element method (FEM) and the integral equations method used to solve Maxwell's equations are important numerical methods that can be employed when handling these equations. These methods involve using Maxwell's equations to recalculate the electric and magnetic fields within a body confined by a set of physical boundary conditions. This leads us to the core of this mathematical formulation: Maxwell's equations are at the heart of this description. These equations make the foundation of electricity and magnetism which are composed of four laws [13]. Finite integration technique (FIT) has been introduced to solve Maxwell's equations for six-component fields on a finite region of space. It presents a numerical solution of Maxwell's equations and uses a differential formulation of Maxwell's equations adopting the finite difference method [14]. From the above analysis, it can be ascertained that the FIT method has been applied in analyzing antennas and antenna arrays. One of these procedures is where Maxwell's equations are solved employing the finite element method. The aforementioned technique, which is derived from FEM and used to model and analyze antenna structures and surrounding fields, is useful for evaluating complicated antenna structures and gives the theoretical framework for using numerical solutions [15]. Computer Simulation Technology (CST) Microwave Studio – this is an electromagnetic simulation software package used in the engineering field. A detailed study of feed lengths that are likely to determine the performance of the microstrip patch antennas has been done [16]. This paper aims at analyzing the performances as well as designing techniques of the antennas commonly used in high-frequency 5G communication technology [17]. This paper focuses on the analysis of the effect of feed length on the microstrip patch antennas and how that may affect their efficiency. Generally, an antenna feed length longer than the current half-wavelength adds more current at each turn in the magnetic loop, thus enhancing the effectiveness of the antenna

as compared to shorter feed lengths that decrease the efficiency of the antenna. These results support the assertion that the feed length is a factor among the larger considerations in the design of microstrip patch antennas [18].

In this study, a microstrip patch antenna of rectangular shape is designed at 28 GHz with various conductor thicknesses, but having the same geometrical parameters and with various feed lengths of the antenna in the 20-36 GHz for 5G wireless communication systems in the CST environment. As observed from the previous simulation results where graphical representations of the three materials used for patch conductors are presented, it is clear that the three materials match the desired operating frequency and operating potential. On analyzing the above graphs based on the return loss (S11), it is also found that all the conductors used here provide the optimum results at the feed length of 1.05 mm. It was seen that return loss depends on conductor type and the best conductor was aluminum, gold and copper.

The rest of the paper is composed of the following sections. In section 2, improving upon the propagation characteristics of signals through microstrip patch antennas is demonstrated by simulating sophisticated electromagnetic fields by FIT. First, it discusses the theory that is relevant to the microstrip patch antenna design. In section 3, the design and simulation of rectangular microstrip patch antenna for wireless communication is described. Thus, the roles of the mentioned 5G antenna parameters of S11, voltage standing wave ratio, bandwidth (BW), gain, and directivity in CST simulation are analyzed in the antenna for various conductor patches and feed lengths in the range of 20-36 GHz with the operating resonance at 28 GHz. Based on the simulation results in section 4, the best conductor patch and the optimal feed length are presented.

2. Microstrip Patch Antenna (MPA) Design

The differential formulation of Maxwell's equations can be solved by the FIT. FIT employs something called finite integration as the mechanism for analyzing the behavior of electromagnetic fields. As suggested by its name, FIT is an efficient method of taking a limited number of measurements of the strengths of the electromagnetic fields and computing the measured fields. Using the finite difference method, the derivatives of the fields are approximated in a numerical form, and in this manner, a numerical solution to Maxwell's equation is derived. This method is applied where the real situations of electric and magnetic fields are desired and in the resolution of high precision such as lithography [19].

The microstrip antenna is made of an upper metal strip as its top layer. This is a thin strip of metal that provides the primary framework of the antenna, and its function is to code and send electromagnetic waves. They are generally formed of conductive materials. A link that connects various parts of a single software program or a related group of programs is also referred to as a patch. The middle layer is made of a dielectric material whereas the top layer is made of a conductor material called metal. The interlayer affects the electrical characteristics of the antennas and assists in their operating efficiency. The lowest layer of the radiating system in the case of transmitting antennas is a substrate or a reflective surface placed under the antenna. This layer gives directed radiation and enhances the ability of the antenna in its operation [20]. In the design process of microstrip patch antennas for 5G/B5G (beyond fifth generation) applications, performance criteria such as frequency, bandwidth, gain and directivity has been evaluated. These criteria affect the antenna performance to be used in 5G/B5G applications [21]. Modular antenna arrays designed in the 5G field have been shown to have high performance in real-world applications in terms of antenna performance, cost-effectiveness, scalability and application [22]. The simplest kind of microstrip patch antenna is illustrated in Figure 1.
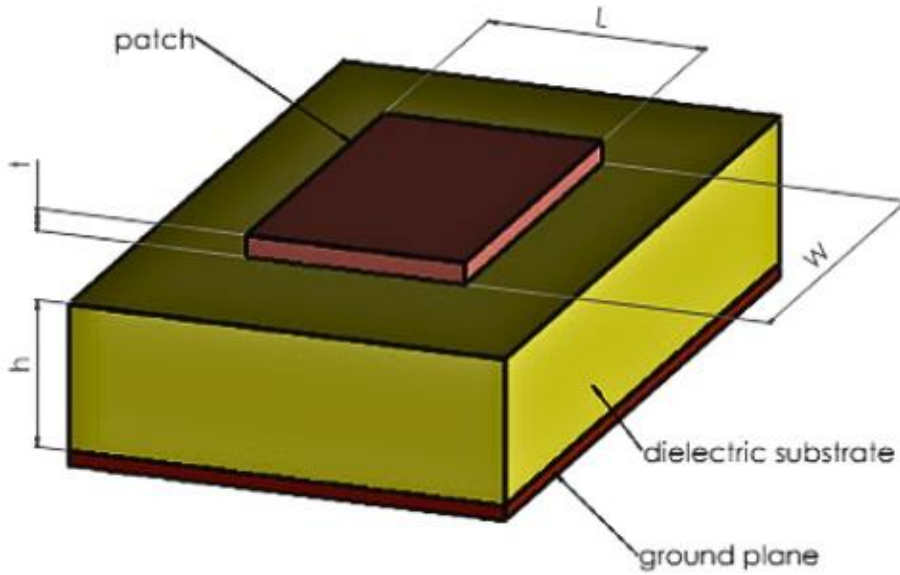
Fig. 1. Microstrip patch antenna structure.

In the operation of microstrip antennas, achieving optimal performance requires careful selection and placement of the feed point and SMA port to facilitate efficient reception and transmission of RF signals by the antenna. In this investigation, a 50-ohm SMA port serves as the feed interface. The feed structure for the microstrip patch antenna is shown in Figure 2.
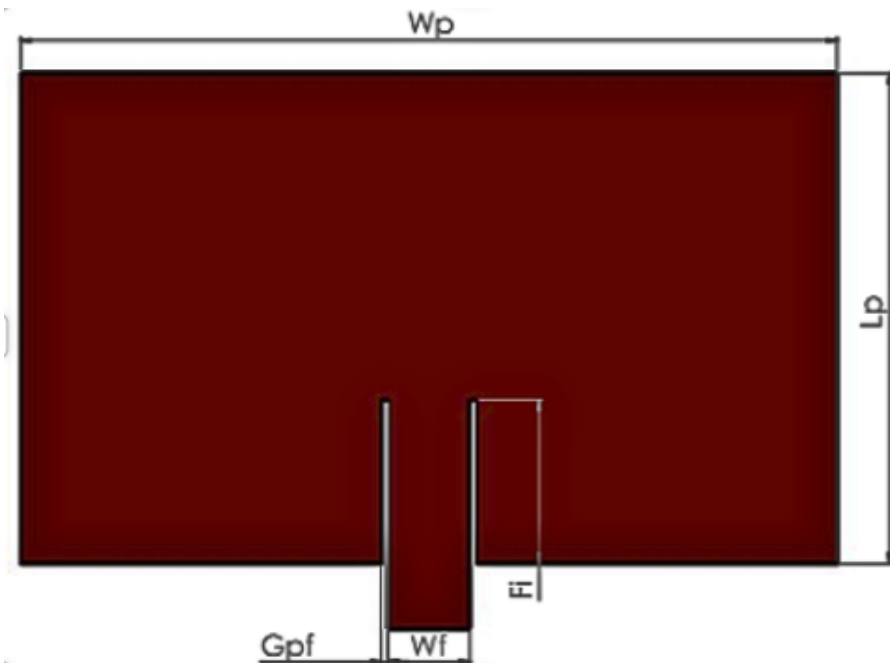
Fig. 2. Microstrip patch structure with patch feed.

A microstrip patch structure is used with a patch feed. The width (W) and length (L) of the antenna patch are determined using Equation (1);

$$W = \frac{c}{2f_o \sqrt{\frac{\varepsilon_r+1}{2}}} . \tag{1}$$

To calculate the length (L_{eff}), we first determine the dielectric constant (ε_{reff}) from the Equation (3) and substitute it into Equation (2);

$$L = \frac{c}{2f_o \sqrt{\varepsilon_{eff}}} . \tag{2}$$

The effective dielectric constant is determined using the formula in Equation (3);

$$\varepsilon_{eff} = \frac{\varepsilon_r+1}{2} + \frac{\varepsilon_r-1}{2} + (1 + 12\frac{h}{w})^{-1/2}. \tag{3}$$

The total length is derived using the following formula;

$$\triangle L = 0.412 \frac{(\varepsilon_{eff}+0.3)(\frac{w}{h}+0.264)}{(\varepsilon_{eff}-0.258)(\frac{w}{h}-0.8)} . \tag{4}$$

The length extension ($\triangle L$) is calculated as;

$$\triangle L = L_{eff} - 2 \triangle L . \tag{5}$$

The length of the inner part can be determined through the formula defined as [23];

$$F_i = \frac{6h_s}{2} . \tag{6}$$

3. Antenna Design and Analysis for 5G & Beyond Wireless Communication

The objective of this research is to present an innovative microstrip antenna for 5G wireless networks that offer better radiation characteristics and is convenient in terms of dimension and mechanical stability. Thus, defining 28 GHz as a resonant frequency in this study. Rogers5880 is employed for dielectric layer material. The layer thickness of can be noted that for H = 0.2 mm and the dielectric constant Er =2.2. From the resonance frequency equations, the respective dimensions of the WP and LP antennas are found, and patch size is calculated as 4.4 mm and 3.44 mm, respectively. The ground plane dimensions are WG= 5.6 mm and LG=4.65 mm. The proposed internal feed length is calculated using Equations (1)-(6). The feed length F=1.05 mm, the feed length width WF=0.6 mm, the gap between the patch and the feed line G=0.1 mm. The design of the antenna structure presented in this work with the help of CST is shown in Figure 3.
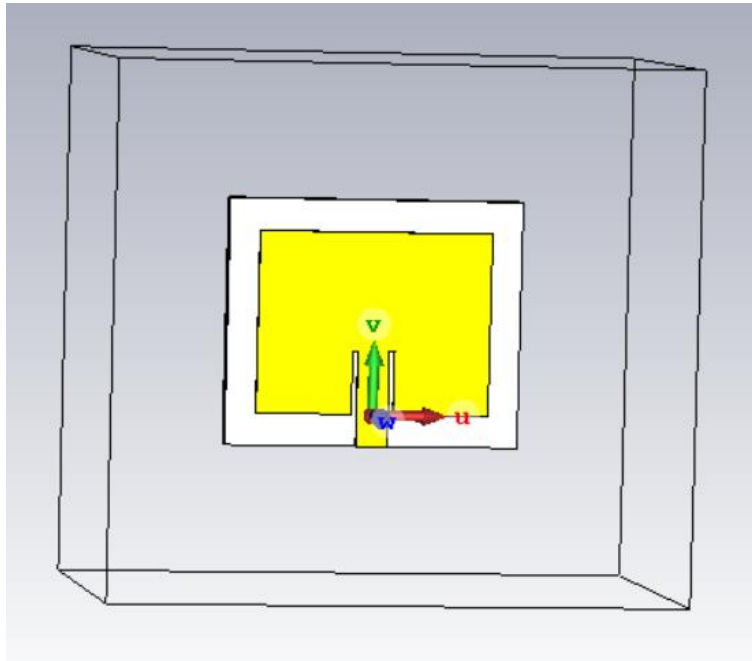
Fig. 3. Structure of the designed antennas.

The antenna dimensions used for the rectangular patch microstrip antenna design are shown in Table 1.

Table 1. Design parameters and dimensions of the proposed antenna.

Parameters	Definition	Value (mm)
WG	Floor and Surface Width	5.60
LG	Floor and Surface Length	4.65
WP	Patch Width	4.40
LP	Patch Length	3.44
H	Thickness of the substrate	0.20
MT	Patch thickness	0.035
Gpf	Gap between patch and feed line	0.10
Fi	Inner feed length	1.05
WF	Microstrip line feed width	0.60

The antenna designs utilize copper, aluminum and gold conductors in their construction. The measurements for S11, VSWR, BW and antenna radiation patterns are conducted for each conductor type across nine feed lengths using the calculated patch antenna dimensions.

The return loss graphs for the copper, gold, and aluminum conductors are shown respectively in Figure 4, 5 and 6.
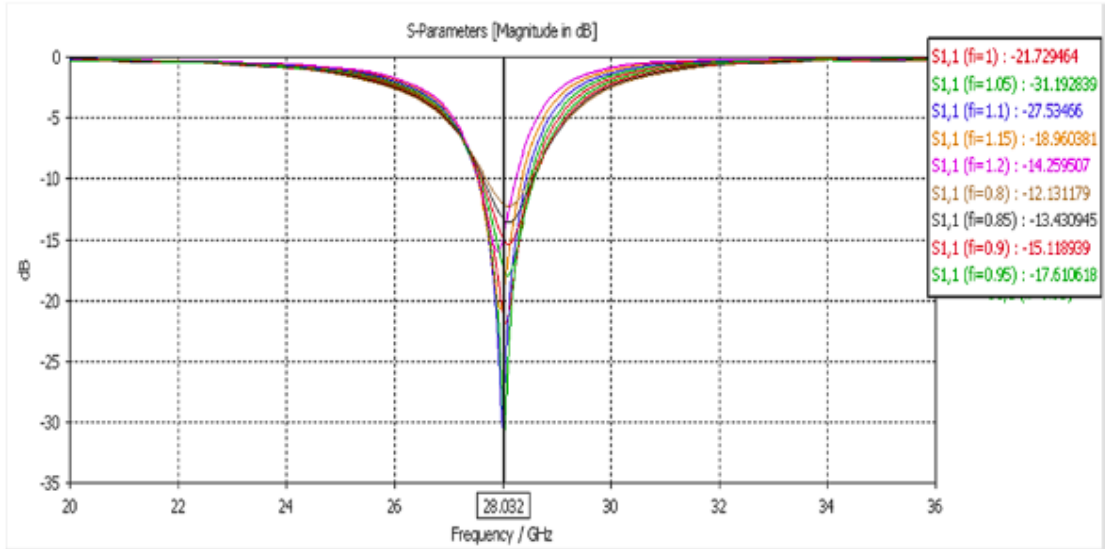
Fig. 4. Return loss for the copper conductor.
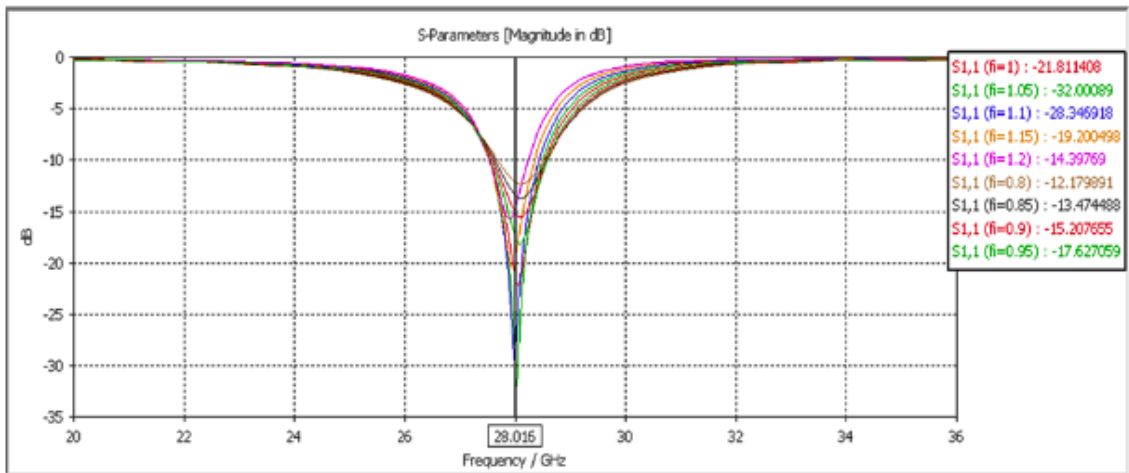
Fig. 5. Return loss for the gold conductor.
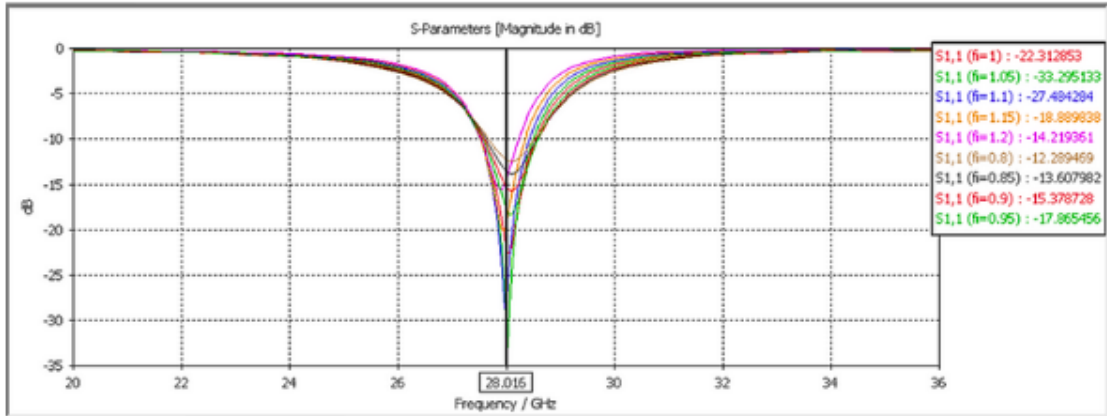
Fig. 6. Return loss for the aluminum conductor.

VSWR is a critical parameter indicating voltage variations along the transmission line. The graphs illustrating VSWR are presented in Figures 7-9.
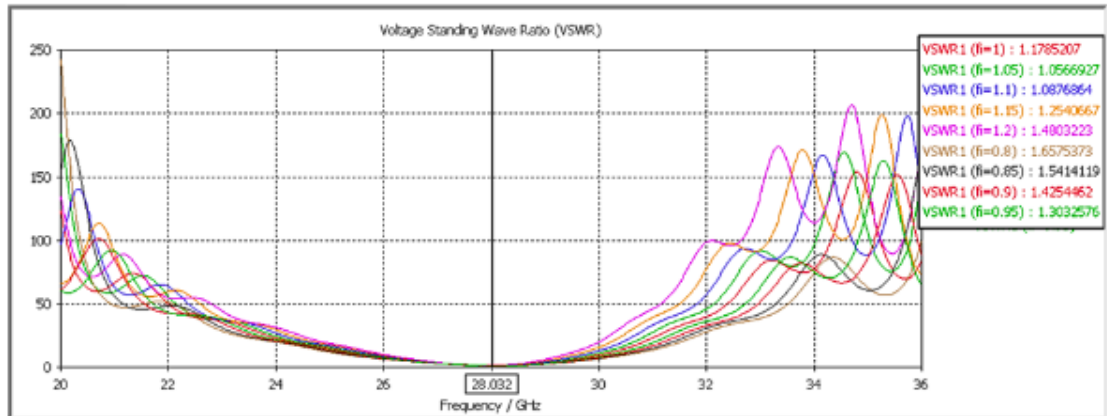
Fig. 7. VSWRs for the copper conductor at nine different feed lengths.
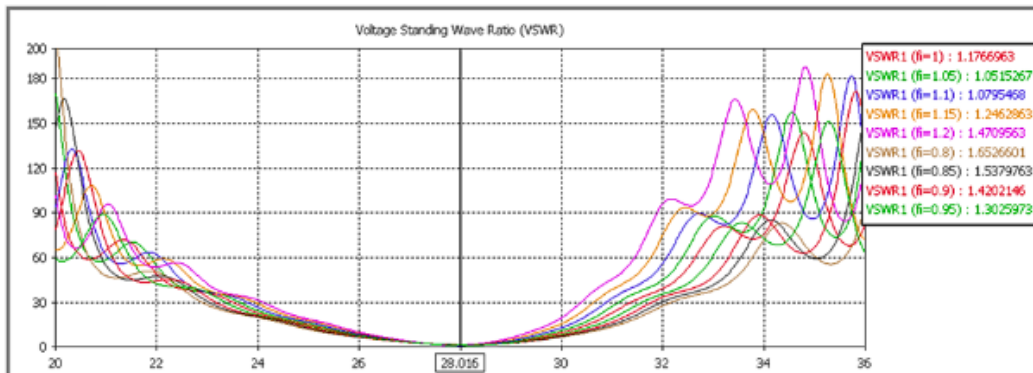
Fig. 8 VSWRs for the gold conductor at nine different feed lengths.
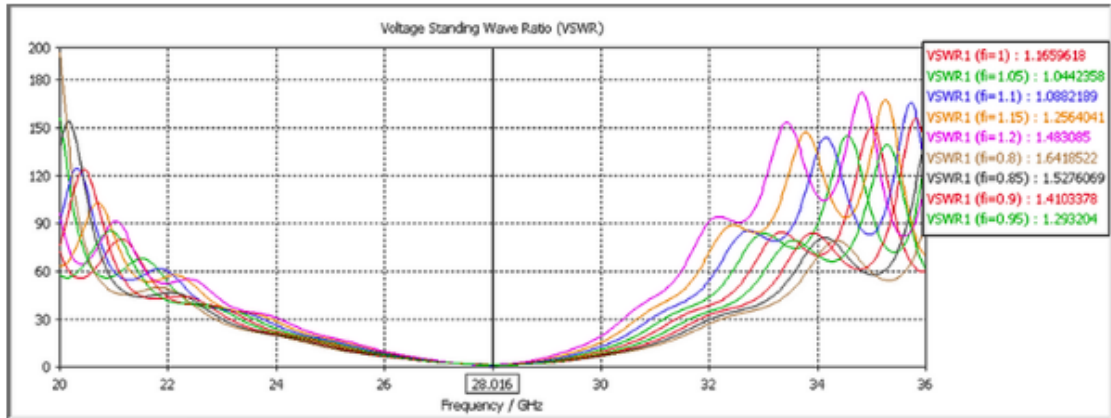
Fig. 9 VSWRs for the aluminum conductor at nine different feed lengths.

S11, VSWR, Frequency (Fr) and BW values for three different conductors at nine different feed lengths are shown in Table 2.

Table 2. S11, VSWR and BW values of different conductor antennas for different feed lengths.

Conductor Material	Inner feed length	S11(dB)	VSWR	Fr (GHz)	BW (MHz)
	fi:0.8mm	-12.13	1.65	28.03	814
	fi:0.85mm	-13.43	1.54	28.03	950
	fi:0.9mm	-5.11	1.42	28.03	973
	fi:0.95mm	-17.61	1.30	28.03	1002
Copper	fi: 1mm	-21.72	1.17	28.03	996
	fi:1.05mm	-31.19	1.05	28.03	968
	fi:1.1mm	-27.53	1.08	28.03	908
	fi:1.15mm	-18.96	1.25	28.03	820
	fi:1.2mm	-14.25	1.48	28.03	693
	fi:0.8mm	-12.17	1.65	28.01	828
	fi:0.85mm	-13.47	1.53	28.01	927
	fi:0.9mm	-15.20	1.42	28.01	987
	fi:0.95mm	-17.62	1.30	28.01	1018
Gold	fi: 1mm	-21.81	1.17	28.01	1002
	fi:1.05mm	-32.00	1.05	28.01	972
	fi:1.1mm	-28.34	1.07	28.01	910
	fi:1.15mm	-19.20	1.24	28.01	820
	fi:1.2mm	-14.39	1.47	28.01	692
	fi:0.8mm	-12.28	1.64	28.01	843
	fi:0.85mm	-13.60	1.52	28.01	939
	fi:0.9mm	-15.37	1.41	28.01	996
	fi:0.95mm	-17.86	1.29	28.01	1017
Aluminum	fi: 1mm	-22.31	1.16	28.01	991
	fi:1.05mm	-33.29	1.04	28.01	976
	fi:1.1mm	-27.48	1.08	28.01	914
	fi:1.15mm	-18.88	1.25	28.01	822
	fi:1.2mm	-14.21	1.48	28.01	690

In Table 2 we observe that, for a feed length (Fi) of 0.8 mm the resonance frequency of the microstrip patch antenna with copper conductor is 28.03 GHz, with a S11 of -12.13 dB a VSWR value of 1.65 and a BW of 814 MHz. The resonance frequency for the antenna with the gold conductor is slightly lower at 28.01 GHz with an S11 value of -12.17 dB VSWR value of 1.65 and bandwidth of 828 MHz. Similarly, the microstrip patch antenna with aluminum conductor also resonates at around 28.01 GHz with an S11 value of -12.28 dB VSWR value at 1.64 and BW reaching up to 843 MHz.

91

For a feed length (Fi) increased to 0.85 mm, the S11 varies as follows: for the copper conductor, it is -13.43 dB with a VSWR of 1.54 and a bandwidth of 950 MHz; for the gold conductor, it is -13.47 dB with a VSWR of 1.53 and a bandwidth of 927 MHz; and for the aluminum conductor, it reaches -13.60 dB with a VSWR of 1.52 and a bandwidth of 939 MHz.

When the feed length is 0.9 mm, for the copper conductor microstrip patch antenna the S11 is -5.11 dB with a VSWR of 1.42 and a BW of 973 MHz. For the gold conductor microstrip patch antenna, the S11 is -15.20 dB with a VSWR value of 1.42 and a BW of 987 MHz. Meanwhile, for the aluminum conductor microstrip patch antenna the S11 is -15.37 dB with a VSWR of 1.41, and a BW of 996 MHz.

As shown in Table 2, this is at the feedlength of 0.95 mm, the copper conductor microstrip patch antenna gain an attractive S11 value at -17.61 dB with VSWR value of 1.30. BW at 1002 MHz. The S11 value at -17.62 dB, VSWR at 1.30 and BW at 1018 MHz obtained for the gold conductor microstrip patch antenna The S11 value of the aluminum-conductor microstrip patch antenna is -17.86 dB, the VSWR value is 1.29, and the bandwidth is 1017 MHz.

The S11, VSWR, and BW are -21.72 dB, 1.17 and 996 MHz, respectively, for the copper conductor microstrip patch antenna when the feed length is 1 mm. For the gold conductor variant, the S11 value is -21.81 dB, with a VSWR of 1.17 and a bandwidth BW of 1002 MHz. An aluminum conductor microstrip patch antenna has S11=-22.31 dB, VSWR=1.16, and BW=991 MHz.

The S11 of the copper conductor microstrip patch antenna, for a feed length of 1.05 mm, is -31.19 dB, with a VSWR of 1.05, and the proposed antenna has a BW of 968 MHz. The gold conductor version returned an S11 of -32 dB VSWR 1.05 up to 972 MHz, while the aluminum conductor type has an S11 of -33.29 dB VSWR 1.04 with BW reaching approximately 976 MHz.

With the feed length set to be at 1.1 mm, observations for the copper conductor microstrip patch antenna include an S11 reading of around -27.53 dB along with a VSWR value about 1.,08 within a BW that reaches up to, around approximately 908 MHz. The gold conductor microstrip patch antenna has an S11 value of -28.34 dB a VSWR value of 1.07 and a BW of 910 MHz. For the aluminum conductor microstrip patch antenna, the S11 value is -27.48 dB the VSWR value is 1.08. The BW is 914 MHz.

When the Fi measures 1.15 mm, the copper conductor microstrip patch antenna exhibits an S11 value of -18.96 dB a VSWR value of 1.25, and a BW of 908 MHz. In comparison for the gold conductor microstrip patch antenna at this feed length, we observe an S11value of -19.20 dB with a VSWR of 1.24 and a BW of 820 MHz; while for the aluminum conductor version, it is depicted that the S11 value of 18.88 dB with a VSWR of 1.25 and a BW of 822 MHz.

With a feed length set at 1.2 mm, the copper conductor microstrip patch antenna exhibits an S11 value of -14.25 dB alongside a VSWR value of 1.48 and a BW spanning 693 MHz. The gold conductor microstrip patch antenna records a S11 value at -14.39 dB with a VSWR value of 1.47 and BW reaching up to 692 MHz; similarly, the aluminum conductor variant showcases a S11 reading at -14.21 dB with a VSWR figure of 1.48 and BW capped at 690 MHz.

The path of the antenna radiation is a mathematical description of antenna radiation fields in the long-range direction at different spatial positions. This model helps in evaluating the nature of density of the radiated power of the antenna and details the emission from the antenna at great distances of the electromagnetic waves. The antenna selection model is determined by factors such as the antenna dimensions, operating frequency, and the feeding techniques and influence of the environment. Thus, the antenna radiation pattern is used for the assessment of the performance and efficiency of the antenna in the communication system and constitutes an important element of a communication system. The conductor cross-sectional representations from three distinct current-carrying forms are presented in Figures 10-12.

Farfield Directivity Abs (Phi=90)

— farfield (f=28) [1]

Frequency = 28 GHz
Main lobe magnitude =   7 dBi
Main lobe direction =   4.0 deg.
Angular width (3 dB) = 88.7 deg.
Side lobe level = -16.3 dB

Theta / Degree vs. dBi
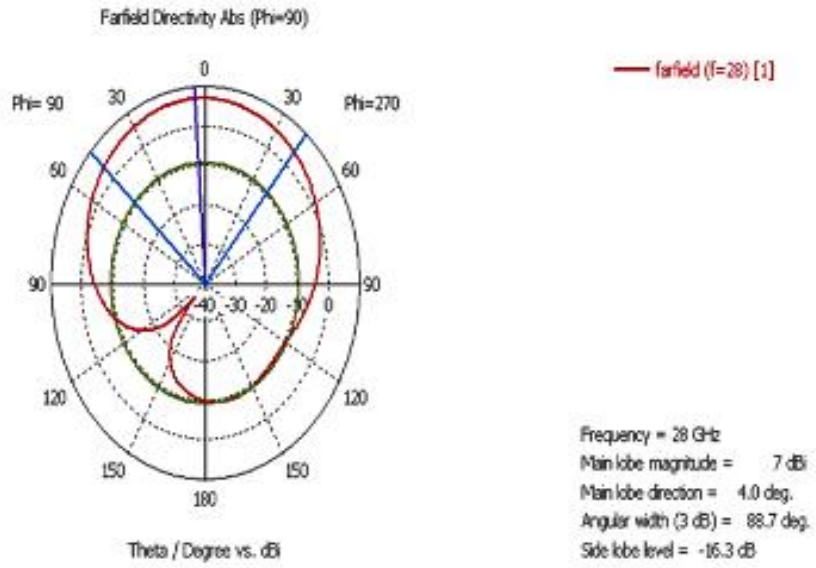
Fig. 10. 2D antenna radiation pattern for the copper conductor.

Farfield Directivity Abs (Phi=90)

— farfield (f=28) [1]

Frequency = 28 GHz
Main lobe magnitude =   7 dBi
Main lobe direction =   4.0 deg.
Angular width (3 dB) = 88.7 deg.
Side lobe level = -16.3 dB

Theta / Degree vs. dBi
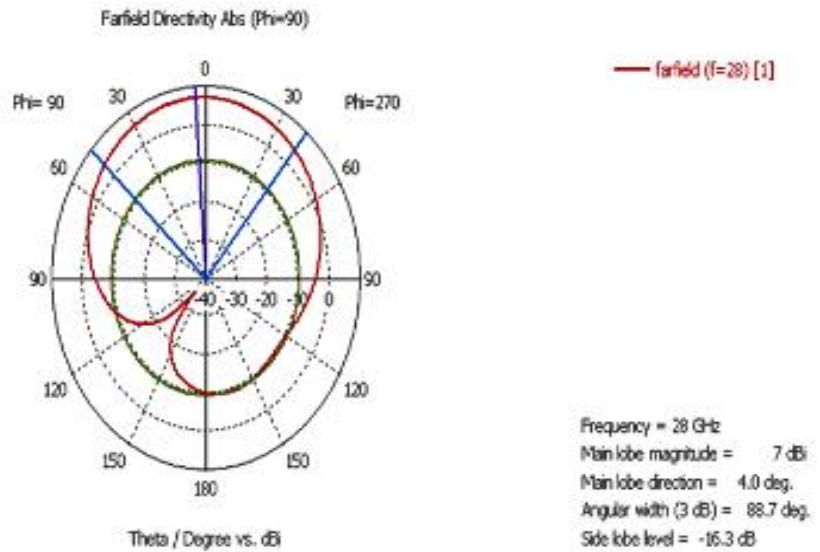
Fig. 11. 2D antenna radiation pattern for the gold conductor.
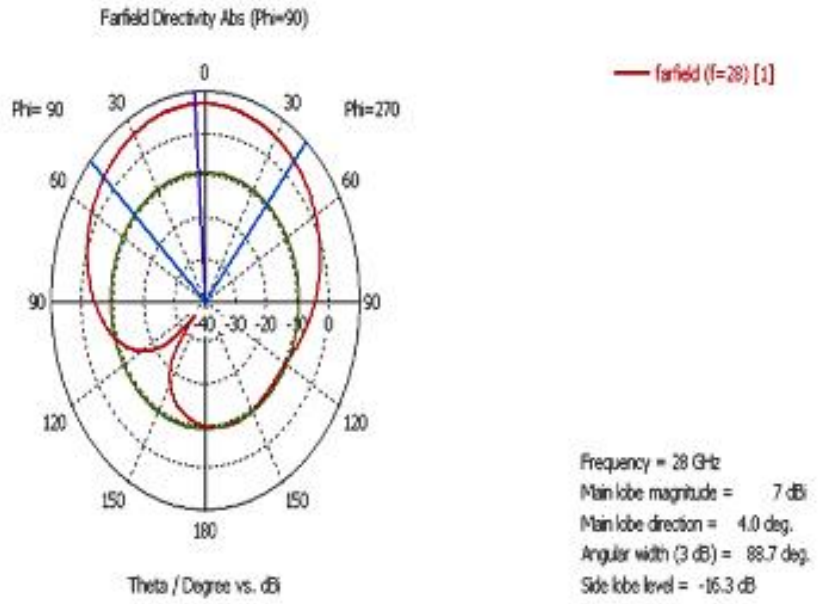
Fig. 12. 2D antenna radiation pattern for the aluminum conductor.

The three-dimensional (3D) directivity representation of the antennas design can be seen in Figure 13-15.
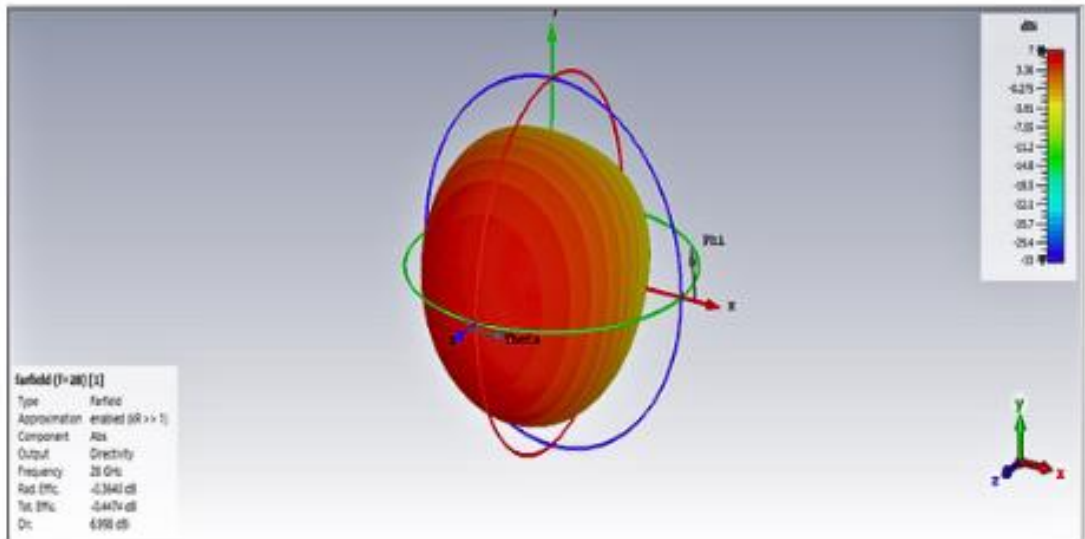
Fig. 13. 3D directivity pattern of the copper conductor antenna.
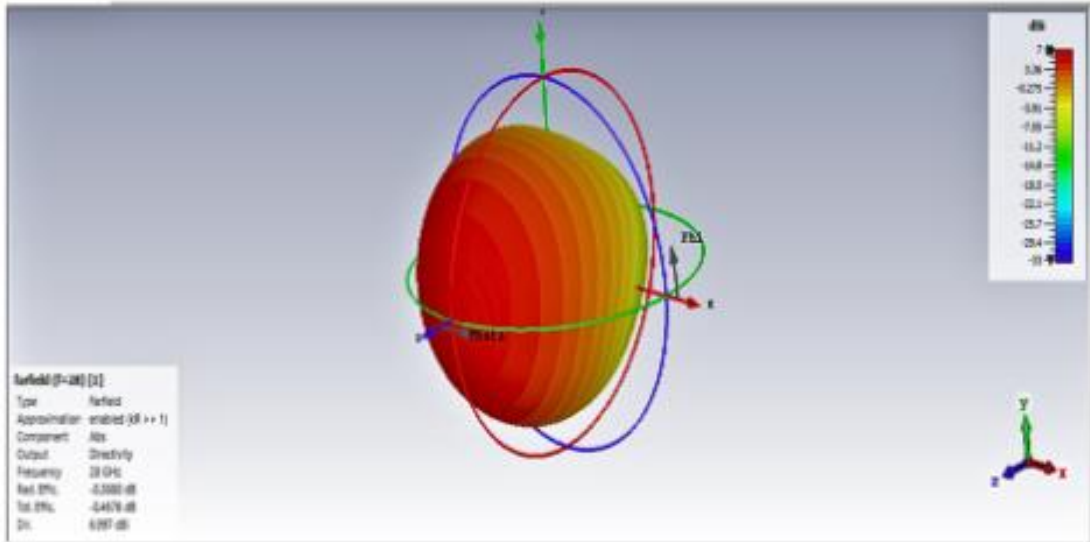
Fig. 14. 3D directivity pattern of the gold conductor antenna.
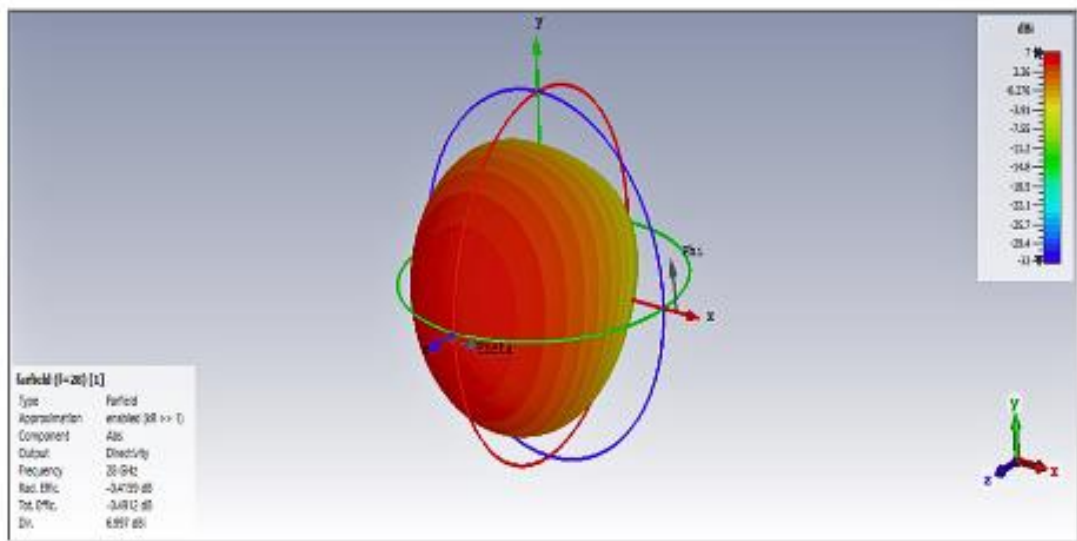
Fig. 15. 3D directivity pattern of the aluminum conductor antenna.

The maximum directivity values in their three representations are approximately at about 6.99 dBi for copper conductor, gold conductor and aluminum conductor antennas.

Additionally, Figures 16-18 exhibits three-dimensional representations of gain patterns, for these antennas.
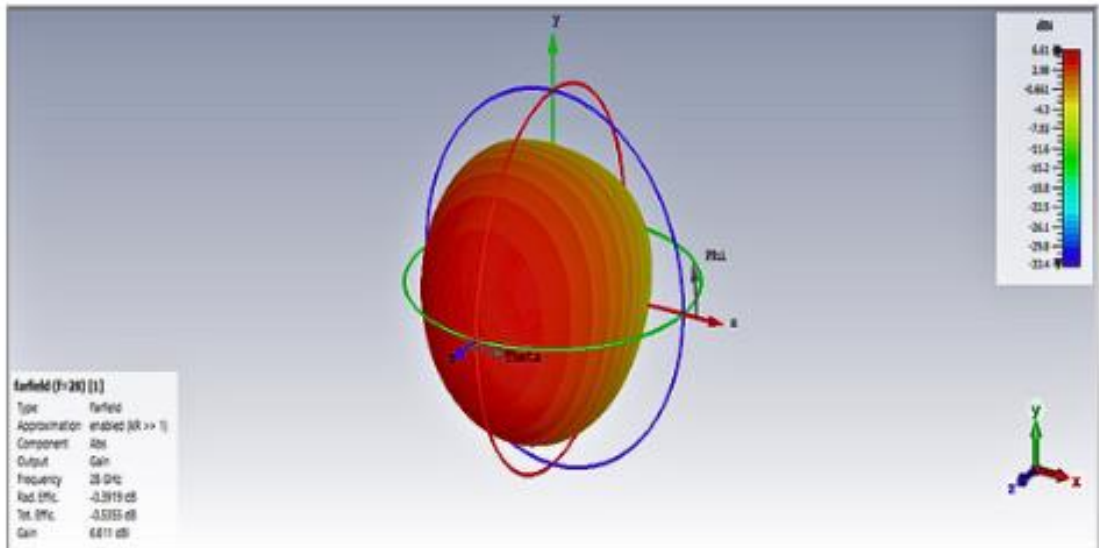
Fig. 16. 3D gain pattern of the copper conductor antenna.
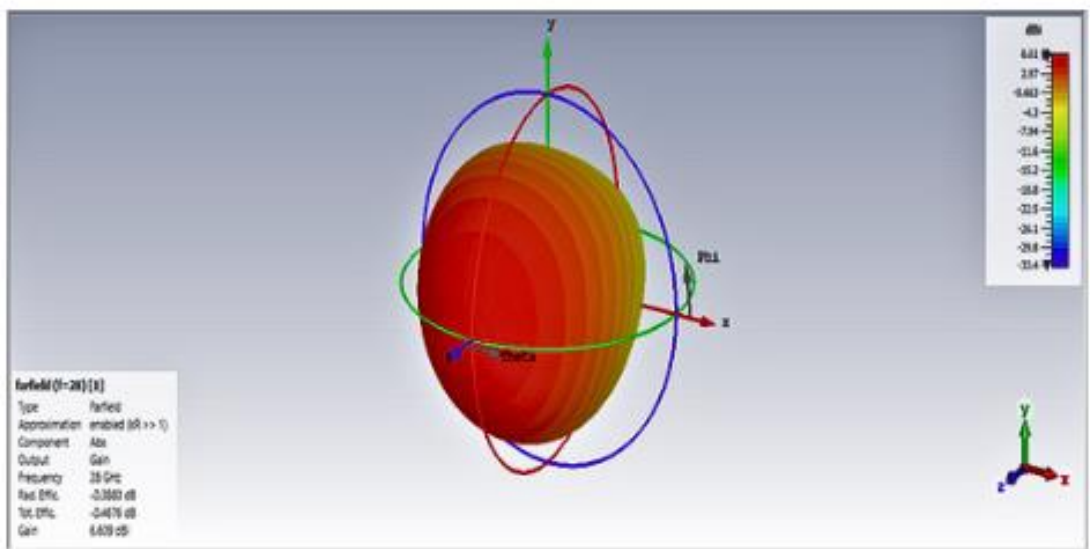
Fig. 17. 3D gain pattern of the gold conductor antenna.
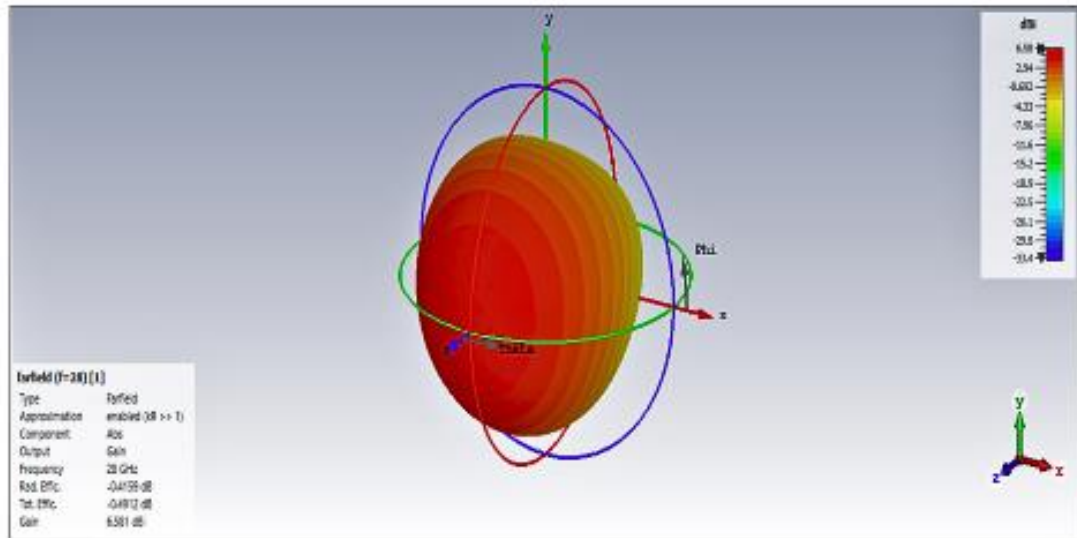
Fig. 18. 3D gain pattern of the aluminum conductor antenna.

The maximum gain values of the 3D representation for the copper-conductor, gold-conductor and aluminum-conductor antennas are 6.61, 6.60 and 6.58 dBi, respectively.

4. Conclusions

In this study, a microstrip patch antenna of rectangular shape is designed at 28 GHz with various conductor thicknesses but having the same geometrical parameters and with various feed lengths of the antenna in the 20-32 GHz for 5G wireless communication systems in the CST environment. As observed from the previous simulation results where graphical representations of the three materials used for patch conductors are presented, it is clear that the three materials dovetails into the desired operating frequency and operating potential. On analyzing the above graphs based on the return loss, it is also found that all the conductors used here provide the optimum results at the feed length of 1.05 mm It was observed that the return loss varies with the type of conductor, with aluminum being the most effective, followed by gold and copper.

There is much influence of the various types of conductors used on the material of the antenna patch and the feed lengths used in microstrip patch antenna based on the findings of this study. We determined that a feed length of 1.05 mm yields the optimal return loss compared to the three conductor types assessed in this study. For the copper conductor, they were able to attain a return loss of -31.19 dB at a resonant frequency of 28.03 GHz and BW 968 MHz. The gold conductor is slightly better at a center frequency of about 28.01 GHz obtaining a S11 of -32 dB and a bandwidth of 972 MHz. However, the aluminum conductor achieved the superior S11 of -33.29 dB at the same resonant frequency 28.01 GHz with the greatest BW 976 MHz among all three conductors. Fortunately, the analysis results show that at the respective resonant frequencies of the three conductors, the VSWR level remains at the low value of 1.05. A VSWR of 2 or less indicates high efficiency in antenna operation. Based on these findings, microstrip patch antennas with optimized feed lengths and various conductors are expected to exhibit improved radiation characteristics suitable for 5G applications.

Acknowledgements

References

[1] M. Shafi, A. Hashimoto, M. Umehira, S. Ogose, and T. Murase, "Wireless communications in the twenty-first century: A perspective," *Proc. IEEE*, vol. 85, no. 10, pp. 1622-1638, Oct. 1997, doi: 10.1109/5.640770.

[2] S. Kumar, "Mobile communications: Global trends in the 21st century," *Int. J. Mobile Commun.*, vol. 2, no. 1, pp. 67-86, 2005, doi: 10.1504/IJMC.2004.004488.

[3] J. Pisarov and G. Mester, "The impact of 5G technology on life in the 21st century," *IPSI Trans. Adv. Res.*, vol. 16, no. 2, pp. 11-14, 2020.

[4] I. Umakoglu, M. Namdar, and A. Basgumus, "UAV-Assisted Cooperative NOMA System with the *n*th Best Relay Selection," *Adv. Electr. Comput. Eng.,* vol. 23, no. 3, pp. 39-46, 2023, doi: 10.4316/AECE.2023.03005.

[5] I. Umakoglu, M. Namdar, and A. Basgumus, "Performance Evaluation of OTFS-NOMA Scheme for High Mobility Users," *Sakarya Univ. J. Comput. Inf. Sci.,* vol. 6, no. 3, pp. 253-260, 2023, doi: 10.35377/saucis...1391813.

[6] I. Umakoglu, M. Namdar and A. Basgumus, "Deep Learning-Assisted Signal Detection for OTFS-NOMA Systems," *IEEE Access*, pp. 1-11, doi: 10.1109/ACCESS.2024.3449812.

[7] M. Namdar, A. Guney, F. K. Bardak, and A. Basgumus, "Ergodic Capacity Estimation with Artificial Neural Networks in NOMA-based Cognitive Radio Systems," *Springer Arab. J. Sci. Eng.,* vol. 49, pp. 6459-6468, 2024, doi: 10.1007/s13369-023-08279-6.

[8] A. Basgumus, F. Kocak, and M. Namdar, "BER Performance Analysis for Downlink NOMA Systems over Cascaded Nakagami-m Fading Channels," *Springer Ann. Telecommun.,* vol. 79, pp. 447-453, 2024. doi: 10.1007/s12243-023-01002-4.

[9] S. K. Ezzulddin, S. O. Hasan, and M. M. Ameen, "Microstrip patch antenna design, simulation and fabrication for 5G applications," *Simul. Model. Pract. Theory,* vol. 116, p. 102497, 2022, doi: 10.1016/j.simpat.2022.102497.

[10] P. Balachandran, A. Nidadavolu, O. P. Kumar, S. Vincent, and T. Ali, "A Microstrip Patch Antenna with Enhanced Bandwidth for Millimeter Wave 5G Application," *J. Phys.: Conf. Ser.,* vol. 1706, no. 1, p. 012101, 2020, doi:10.1088/1742-6596/1706/1/012101.

[11] B. Tutuncu, "Microstrip Antenna for 5G Communication: Design and Performance Analysis," in Proc. 2020 Int. Congr. Human-Comput. Interact., *Optim. Robot. Appl. (HORA)*, 2020, pp. 1-4, doi: 10.1109/HORA49412.2020.9152855.

[12] P. Elliot, "The applied computational electromagnetics society," *IEEE Antennas Propag. Mag.,* vol. 33, no. 1, pp. 18–19, 1991, doi: 10.1109/74.80657.

[13] M. N. Sadiku, Elements of Electromagnetics, 4th ed., Oxford Univ. Press, 2009.

[14] T. Weiland, "A discretization model for the solution of Maxwell's equations for six-component fields," *Arch. Elektron. Uebertragungstech.,* vol. 31, pp. 116-120, 1977.

[15] M. J. Jian and J. R. Douglas, Finite Element Analysis of Antennas and Arrays, John Wiley & Sons, Inc., 2009.

[16] T. S. Aina, O. O. Akinte, and B. A. Iyaomolere, "Investigation on performance of microstrip patch antenna for a practical wireless local area network (WLAN) application," *Int. J. Res. Appl. Sci. Eng. Technol. (IJRASET),* vol. 10, no. I, pp. 221–226, 2022, doi: 10.22214/ijraset.2022.39799.

[17] M. Khasiyev, "28 GHz frekansında 5G kablosuz haberleşme için S-şekilli mikroşerit anten tasarımı ve analizi," Yüksek Lisans Tezi, Bursa Uludağ Üniversitesi, 2023.

[18] H. M. Bhatt, "Study on the effect of ınset feed length on radiation characteristic of rectangular microstrip patch antenna," in S. Lathigara, H. M. Bhatt, and V. Unadkat (Eds.), *Proc. Natl. Conf. Emerg. Trends Comput., Electr. Electron. (ETCEE-2015)*, Rajkot, 2015.

[19] R. Zhabiz, The Finite Integration Technique (FIT) and the Application in Lithography Simulations, Friedrich-Alexander Univ., 2011.

[20] C. A. Balanis, Antenna Theory: Analysis and Design, John Wiley & Sons Ltd., 2016.

[21] H. Attar, R. S. Agieb, A. Amer, A. Solyman, and M. S. Aziz, "Microstrip Patch Antenna Design and Implementation for 5G/B5G Applications", *2022 International Engineering Conference on Electrical, Energy, and Artificial Intelligence (EICEEAI)*, Zarqa, Jordan, 2022, pp. 1-6, doi: 10.1109/EICEEAI56378.2022.10050499.

[22] A. Ashraff, T. Gunawan, M. Kartıwı, L. Nur, B. Nurgoho and R. Astutı, "Advancements and Challenges in Scalable Modular Antenna Arrays for 5G Massive MIMO Networks ", *IEEE Access*, vol. 12, pp. 57895 − 57916, doi: 10.1109/ACCESS.2024.3391945.

[23] A. S. Chaurasia, A. K. Shankhwar and A. Singh, "Design of Novel Patch Antenna using CST Software," *2021 Second International Conference on Electronics and Sustainable Commun. Systems (ICESC)*, 2021, pp. 586-591, doi: 10.1109/ICESC51422.2021.9532843.

RESEARCH ARTICLE

Diffusion limited aggregation via Python: Dendritic structures and algorithmic art

Çağdaş Allahverdi[a,*], Yıldız Özfırat Allahverdi[b]

[a]*Toros University, Faculty of Engineering, Department of Software Engineering, Mezitli Campus, 33210, Mezitli, Mersin, Türkiye,*
ORCID: 0000-0002-6825-5099.
[b]*Mersin University, Faculty of Fine Arts, Department of Painting, Ciftlikkoy Campus, 33343, Yenişehir, Mersin, Türkiye,*
ORCID: 0000-0001-9794-6510

Abstract

Diffusion limited aggregation (DLA) has attracted much attention due to its simplicity and broad applications in physics such as nano and microparticle aggregations. In this study, the algorithm of DLA is written with Python. Python's Turtle library is used to plot the aggregate on the computer monitor as it grows. The algorithm is run on the Raspberry Pi. A cheap and portable medium is created for DLA simulation. Two different options are placed in the algorithm. The first path does not allow the primary particle to turn outside of the aggregate after the collision. However, the second one allows the percolation of the primary particle both inside and outside of the aggregate. The spherical dendritic structures consisting of 500-2000 primary particles are obtained by the algorithm. The fractal dimension of these structures is around 1.68. Their porosity is found below 50%. Their gyration radii are also calculated. Beyond scientific investigation, examples of algorithmic art using these dendritic structures are also given.
Keywords: Diffusion limited aggregation; Random walk; Fractal dimension; Porosity; Raspberry Pi; Algorithmic art

 * Corresponding author. Tel.: +90-324-325-3300 ; fax: +90-324-325-3301 .
  E-mail address: cagdas.allahverdi@toros.edu.tr
  http://dx.doi.org/10.1016/j.cviu.2017.00.000
.

1. Introduction

Diffusion limited aggregation (DLA) is the gathering of particles in random manner. DLA has an importance from the point of view of science and algorithmic art. Flocculation [1], nanoparticle aggregation [2], bacterial growth [3], Hele-Shaw fingering [4], and dielectric breakdown [5] can be imitated by using DLA. Witten and Sander generated aggregate patterns including around 3000 particles on a square lattice [6]. Woźniak et al. approximated this model to a much more realistic one [7]. Mroczka et al. derived radius of gyration and fractal dimension of silicon dioxide and soot aggregates from their light scattering intensities [8]. The effect of the number of primary particles, step length, and appearance radius on morphology and structure of aggregates was investigated by Liu et al [9]. Wang et al. compared fractal dimensions obtained from box-counting and power law methods of DLA [10]. Computer runtimes for the formation of DLA structures were studied on single and multiple CPU cores by Zsaki [11]. In DLA, only one particle moves around randomly and sticks to the targeted aggregate after colliding with it. However, many particles move around randomly, collide, and stick together in diffusion limited cluster aggregation (DLCA). Some authors studied their physical systems using DLA and DLCA [12-14].

In this study, the algorithm of DLA has been written by using Python programming language and run on Raspberry Pi 4 Model B microprocessor. Indeed, Raspberry Pi 4 is a small and low-cost single-board computer [15]. The Turtle library of Python has been used to draw sticking aggregates instantaneously on the computer monitor. Thus, DLA can be easily worked and demonstrated via this cheap equipment. The physical parameters such as fractal dimension, gyration, birth, and death radii, and working principle of the DLA have been explained in the paper. The DLA algorithm for the simulation of aggregation of non-overlapping circular (spherical at 3D) hard particles has been depicted. A mathematical explanation is given for the position adjustments of colliding circular particles. Aggregates have been grown in two different modes by keeping their fractal dimension within a certain range (1.60-1.80). These modes are i) no chance of percolation for the particle after the collision and ii) a chance of percolation for the particle after the collision. In addition, some artistic studies of these dendritic structures are given in the text.

2. Theory

The theory explained by Woźniak et al. has been taken as reference in this work [7]. However, it has been modified and the position adjustment of the particles has been clarified. In DLA, a seed particle is placed at the origin of a cartesian coordinate system. A particle is sent from a point on the perimeter of a circle at a certain distance from the center. Herein, this circle will be called birth circle, and its radius will be birth radius (R_{bi}). This particle moves randomly in the cartesian coordinate system. This is a random walk. When it collides with the seed at the center, it sticks to the seed and adjusts itself to form tangential circles. Then, another particle is sent from the birth circle. The birth radius is not constant. It is greater than the bounding radius (R_{bo}), that is $R_{bi}>R_{bo}$. The bounding radius is the radius of the circle which covers the aggregate growing from the seed. There is also a death circle. The radius of the death circle, that is death radius (R_{de}), restricts the particle movement. If the particle passes from inside to outside of the death circle, it is annihilated, and a new particle is sent from the birth circle. This process is repeated to enlarge the aggregate. Figure 1 shows this process.
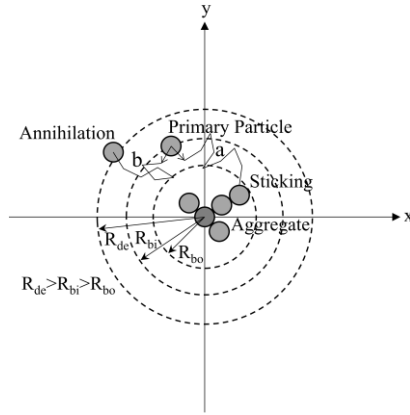
Fig. 1. Diffusion limited aggregation. Growth of the aggregate is shown by sticking. Primary particle following path a is stuck to the aggregate or following path b is annihilated. R_{de}, R_{bi} and R_{bo} are death, birth, and bounding radii, respectively.

In our aggregation growth, $R_{bi}=2.0R_{bo}$ and $R_{de}=3.0R_{bo}$ have been used. R_{bo} encircles the aggregate and can be written as in Equation 1.

$$R_{bo} = maximum\left(\sqrt{x_i^2 + y_i^2}\right) + R_0 \qquad (1)$$

where x_i is the x-coordinate of ith particle in the aggregate, y_i is the y-coordinate of ith particle in the aggregate and R_0 is the radius of the primary particle (see Figure 2).
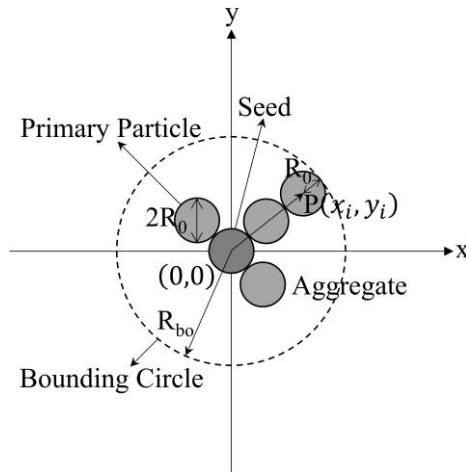
Fig. 2. Bounding circle. $P(x_i,y_i)$ shows the cartesian coordinate of the particle. R_0 and R_{bo} are the radii of the primary particle and bounding circle, respectively.

The fractal dimension (the Hausdorff dimension) of fractal structures is given by Equation 2.

$$D_f = \frac{\log\left(\frac{N}{k_0}\right)}{\log\left(\frac{R_{g,N}}{R_0}\right)} \tag{2}$$

where N is the number of primary particles, k_0 is the scaling prefactor, $R_{g,N}$ is the gyration radius and R_0 is the radius of the primary particle and D_f is the fractal dimension. $R_0=2.0$ and $N=500,1000,2000$ have been used. D_f has been kept between 1.60 and 1.80 (1.70±0.10). $R_{g,N}$ has been calculated according to Equation 3.

$$R_{g,N} = \sqrt{\frac{1}{N}\sum_{i=1}^{N}[(x_i - x_{CM})^2 + (y_i - y_{CM})^2]} \tag{3}$$

where x_{CM} is x-coordinate of the center of mass of the aggregate and y_{CM} is y-coordinate of the center of mass of the aggregate. Assuming the primary particles are same, x_{CM} and y_{CM} are calculated using Equations 4 and 5, respectively.

$$x_{CM} = \frac{\sum_{i=1}^{N} m_0 x_i}{\sum_{i=1}^{N} m_0} = \frac{1}{N}\sum_{i=1}^{N} x_i \tag{4}$$

$$y_{CM} = \frac{\sum_{i=1}^{N} m_0 y_i}{\sum_{i=1}^{N} m_0} = \frac{1}{N}\sum_{i=1}^{N} y_i \tag{5}$$

where m_0 is the mass of the primary particle.

The colliding two particles can be made tangential by using the equations of analytic geometry in the 2D Euclidean space. Figure 3 shows colliding and position adjustment of two primary particles. They will be called particle 1 and particle 2. Particle 1 is randomly moving individual particle and particle 2 is a primary particle of the aggregate. x_{1a}, x_1, y_{1a}, y_1, x_2, y_2, and θ are adjusted x-coordinate of particle 1, x-coordinate of particle 1 before the adjustment, adjusted y-coordinate of particle 1, y-coordinate of particle 1 before the adjustment, x-coordinate of particle 2, y-coordinate of particle 2, and the angle of incidence of particle 1 respectively.
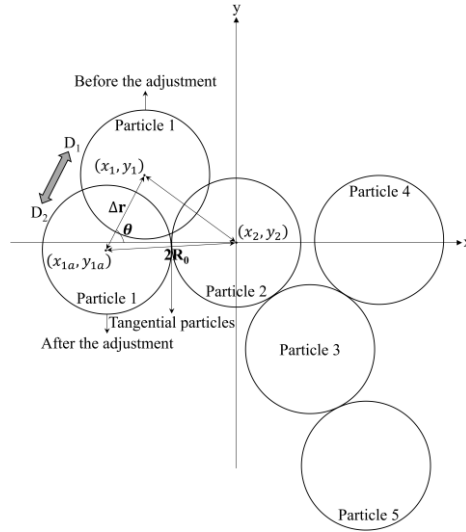
Fig. 3. Adjustment of the position of particle 1 relative to the aggregate. Particles 2, 3, 4, and 5 are the member particles of the aggregate. After the collision of particle 1 with particle 2, particle 1 is moved by Δr in the direction of D_2. Particle 1 and particle 2 are tangent to each other and so particle 1 becomes a new member of the aggregate. $2R_0$ is the diameter of the particle.

As seen from Figure 3, the distance between the centers of particle 1 and particle 2 after the adjustment must be $2R_0$. Equation 6 indicates that particle 1 and particle 2 are tangential.

$$(x_{1a} - x_2)^2 + (y_{1a} - y_2)^2 = 4R_0^2 \tag{6}$$

Equation of the line connecting the center of particle 1 before the adjustment to the center of particle 1 after the adjustment is written as follows.

$$y(x) = mx + n = (tan\theta)x + n \tag{7}$$

where m is the slope of the line and n is the y-intercept of the line. (x_{1a}, y_{1a}) and (x_1, y_1) coordinates satisfy Equation 7.

$$y_{1a} = (tan\theta)x_{1a} + n \tag{8}$$

$$y_1 = (tan\theta)x_1 + n \tag{9}$$

$$n = y_1 - (tan\theta)x_1 \tag{10}$$

If Equation 8 is written in Equation 6 and Equation 6 is arranged in the form of quadratic equation, Equation 11 is obtained.

$$(1 + tan^2\theta)x_{1a}^2 + 2(ntan\theta - x_2 - y_2 tan\theta)x_{1a} + (x_2^2 + y_2^2 + n^2 - 2ny_2 - 4R_0^2) = 0 \tag{11}$$

Herein, the solution of Equation 11 is given as follows.

$$a = 1 + tan^2\theta \tag{12}$$

$$b = 2(ntan\theta - x_2 - y_2tan\theta) \tag{13}$$

$$c = x_2^2 + y_2^2 + n^2 - 2ny_2 - 4R_0^2 \tag{14}$$

$$x_{1a} = \frac{-b \pm \sqrt{b^2 - 4ac}}{2a} \tag{15}$$

x_{1a} can be calculated using Equation 15. Equation 15 gives two solutions, but the displacement from (x_{1a},y_{1a}) and (x_1,y_1) must be equal or smaller than the step length of the particle 1 which is $2R_0$ in this study. Therefore, the solution satisfying Equations 16, 17 and 18 is chosen. Here, n and y_{1a} are calculated by Equations 10 and 8.

$$\Delta r = \sqrt{(x_{1a} - x_1)^2 + (y_{1a} - y_1)^2} \le 2R_0 \tag{16}$$

$$x_{prev} < x_{1a} < x_1 \tag{17}$$

$$y_{prev} < y_{1a} < y_1 \tag{18}$$

where x_{prev} and y_{prev} are previous x and y coordinates of particle 1 before the collision between particle 1 and particle 2. (x_{1a},y_{1a}) gives the adjusted position of particle 1. The center of particle 1 is moved from (x_1,y_1) to (x_{1a},y_{1a}). Thus, sticky (tangential) primary particles are generated. The porosity of the agglomerate can be calculated as follows.

$$V_f = 1 - N\left(\frac{R_0}{R_{g,N}}\right)^2 \tag{19}$$

The algorithm of the DLA used in this study is indicated in Figure 4. The data involves $R_{g,N}$ and D_f of the agglomerate in the flow diagram. Numbers 1 and 2 show two different aggregation modes. If the position of the collided particle cannot be adjusted relative to the agglomerate, there are two ways to follow. The collided particle is annihilated, and a new particle is sent from the circle of the birth for way 1. However, the collided particle is moved and not annihilated for way 2. These ways are called mode 1 and mode 2 below.

Start

Constitute the coordinate system on the screen

counter=1

Form a seed particle at the origin

Calculate the radii of the birth and death circles

Form a particle randomly placed on the birth circle

Annihilate this particle

Move the particle randomly by one particle diameter

1

2

Radius of the death circle < Distance of the particle to the origin

Yes → Annihilate this particle

No

Distance of the particle from each particle of the agglomerate <= Diameter of the particle

No

Yes; Collision

Adjust the position of the particle with respect to the agglomerate

No; If it cannot be adjusted

Yes

Increase the particle number by one (counter = counter + 1)

Calculate agglomerate size, gyration radius, fractal dimension and collision time

Data

Fractal dimension<=Upper limit & Lower limit=<Fractal dimension

No → Decrease the particle number by one (counter = counter - 1)

Yes

Data Storage

The number of particles (counter) == Final particle number (N)

No

Yes

Display the agglomerate containing N particles on the screen

Stop

Fig. 4. The flowchart of the DLA. 1 and 2 show two different paths which are called mode 1 and mode 2 in the text, respectively.

3. Equipment

The equipment used in this study is given in Table 1. As understood from Table 1, the listed items are easy to reach and relatively cheap. Figure 5 shows this equipment.

Table 1. The equipment used for the DLA simulation.

No	Item	Quantity
1	Raspberry Pi 4 Model B (64-bit quad-core Cortex-A72 processor)	1
2	FASTER 64 GB Micro SD Card	1
3	Aluminum case with dual cooling fan for Raspberry Pi 4	1
4	Raspberry Pi DC 5.1V/3A output USB-C Power Supply	1
5	ACER v193w 19-inch LCD monitor coupled with VGA cable and power cord	1
6	Micro-HDMI to HDMI cable	1
7	HDMI to VGA and Audio adapter	1
8	POWERFUL SLE-650 650VA Line Interactive UPS	1
9	TRUST VEZA wireless multimedia keyboard with touchpad	1

Fig. 5. The equipment used for the DLA simulation. The numbers correspond to the parts of the equipment given in Table 1.

4. Results and Discussion

Figure 6 shows the generated aggregates consisting of 500, 1000 and 2000 primary particles via mode 1. As seen from Figure 6, these are dendritic structures (tree-like structures) [16, 17] and are called $D1_{500}$, $D1_{1000}$ and $D1_{2000}$.
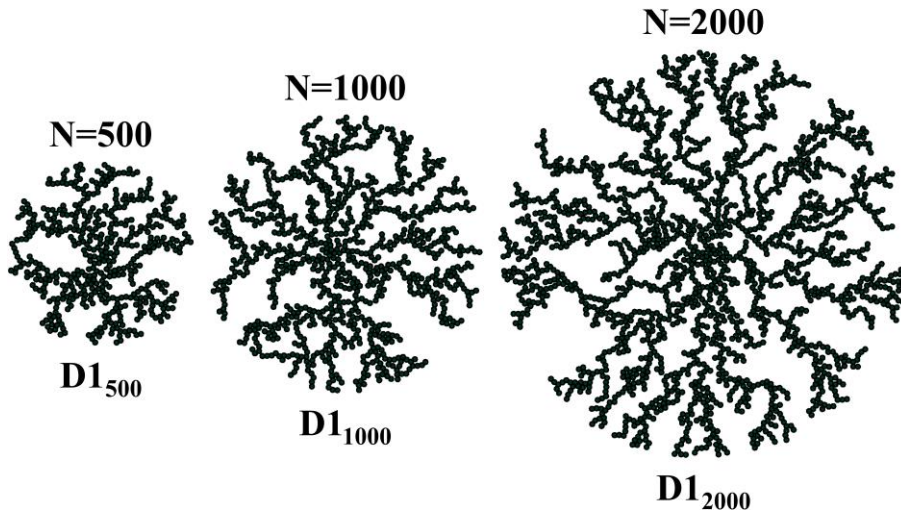
Fig. 6. The dendritic structures generated by the DLA. $D1_{500}$, $D1_{1000}$ and $D1_{2000}$ indicate the dendritic structures consisting of 500, 1000 and 2000 particles, respectively. These structures are generated with mode 1.
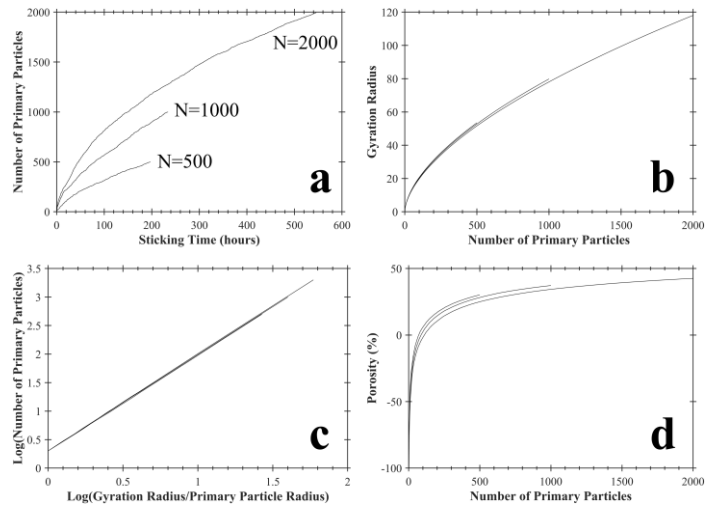
Fig. 7. The plots obtained from $D1_{500}$, $D1_{1000}$ and $D1_{2000}$. a) Number of primary particles versus sticking time, b) Gyration radius versus number of primary particles, c) Log(number of primary particles) versus log(gyration radius/primary particle radius) and d) Porosity versus number of primary particles. The slope gives D_f in Figure 7c.

The plots obtained for these structures are given in Figure 7. $D1_{500}$, $D1_{1000}$ and $D1_{2000}$ are formed at the end of 197 h, 234 h and 546 h, respectively (see Figure 7a). Larger structures need more primary particles, and more particles require more time to form the structure. Their gyration radii evolution is similar (see Figure 7b). It means that the generated structures are analogous. The radii of gyration of $D1_{500}$, $D1_{1000}$ and $D1_{2000}$ are found to be 54, 80, and 118, respectively. Figure 7c shows plot of $Log(N)$ versus $Log(R_g/R_0)$. According to Equation (2), the slope and y-intercept of the linear line in Figure7c give D_f and $Log(k_0)$ of the agglomerate, respectively. The fractal dimensions (D_f) of $D1_{500}$, $D1_{1000}$ and $D1_{2000}$ are 1.69, 1.68 and 1.68, respectively. The scaling prefactors (k_0) of $D1_{500}$, $D1_{1000}$ and $D1_{2000}$ are 1.95, 2.04 and 2.10, respectively. Figure 7d indicates the porosities. The porosities (V_f) of $D1_{500}$, $D1_{1000}$ and $D1_{2000}$ are found to be 30%, 37% and 43%, respectively. As the structure grows, porosity increases, but the increment gradually slows down. The aggregate generated via mode 2 is shown in Figure 8. It contains 2000 primary particles. It is called $D2_{2000}$. It is formed at the end of 710 h. D_f, R_g, and V_f of $D2_{2000}$ are 1.68, 124 and 48%, respectively. $D2_{2000}$ is larger and more porous than $D1_{2000}$. This result can be understood. The primary particle moves inside and outside of the aggregate until it finds a suitable location for sticking. Therefore, as in Figure 8, mode 2 can form a more porous structure than mode 1.

Fig. 8. The dendritic structure generated by using mode 2 of the DLA. It consists of 2000 particles. It is called $D2_{2000}$.

As a result of the combustion of fossil fuels, soot particles are released into the environment. These soot aggregates give rise to global warming due to the absorption and scattering of sunlight. Soot aggregates are shown to have a fractal morphology. This morphology has an impact on their light scattering properties. Hence, the fractal properties of these structures have been investigated by using transmission electron microscopy. For instance, Pang et al. examined different soot aggregates originated from combustion of fuel, burning biomass, and burning coal [18]. D_f values between 1.11-2.19 with k_0 values between 0.25-9.22 were reported for the soot aggregates in the literature [18-21]. Our findings are within these ranges obtained from literature studies. Unlike the studies in literature, porosity has been calculated in this work. The sticking probability of the primary particles is taken as ~1.0 when the algorithm is run. Compact and denser dendritic structures can be generated by defining a sticking probability parameter which is sufficiently smaller than 1.0 in the algorithm. These results are not limited by the soot aggregates and can be expanded to the other natural fractal structures such as manganese dendrites formed on magnesium silicate [22].

5. Algorithmic Art

Algorithmic art is a form of art that uses algorithms. Nowadays, all algorithms are nearly computer algorithms. A computer algorithm consists of computer code written to perform a specific task. Algorists use these computer algorithms to perform their arts. Manfred Mohr, Jean-Pierre Hébert, Vera Molnár and Roman Verostko are among famous algorists [23]. For example, Manfred Mohr uses the edge sets of a cube very well in his works [24].

The dendritic structures created in this study by the DLA algorithm are valuable not only in point of the science but also in terms of algorithmic art. Here, the final pattern can be predicted but it cannot be fully known as the final work of an artist's painting. It is caused by the randomness used in the algorithm. Hence each DLA pattern is unique. Some artistic colorings of $D1_{2000}$ are shown in Figure 9. The primary particles of $D1_{2000}$ are colored from inside to outside by using three different colors and shown on a circular area surrounding it. The circular area is colored in six different colors. All colors in the RGB color palette can be used in the dendritic structure. Other geometric shapes may also be preferred instead of circular area. The size of primary particles is reduced in Figure 10.
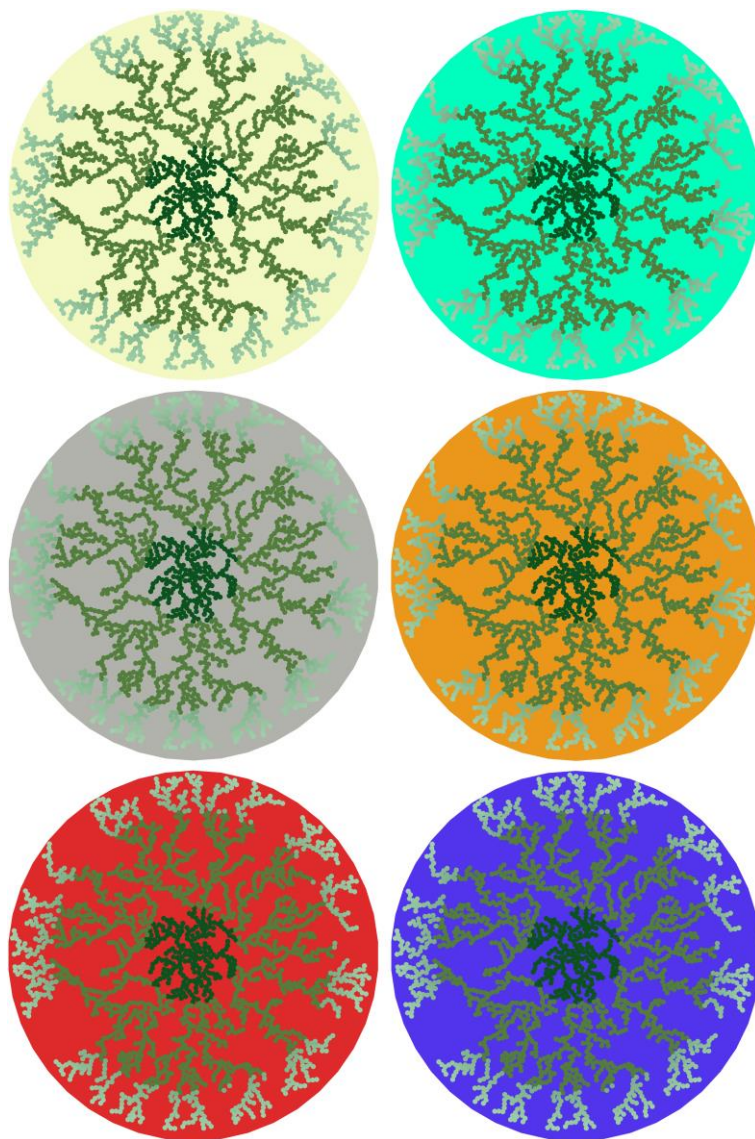
Fig. 9. Colored D1$_{2000}$.
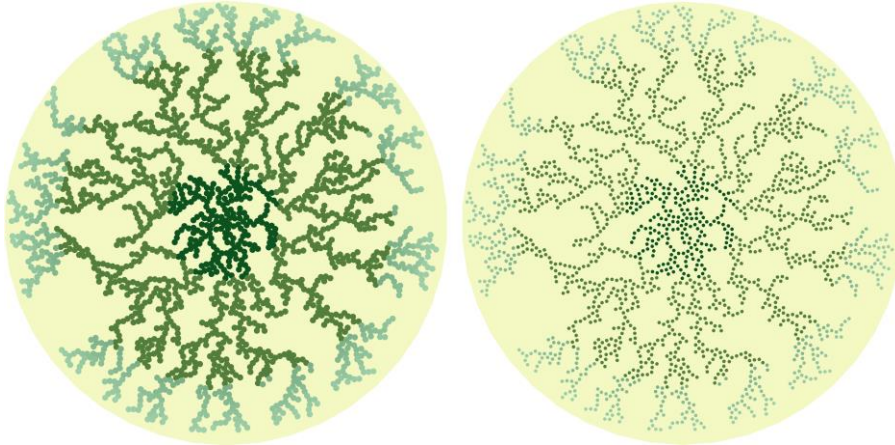
Fig. 10. Colored and reduced primary particles of D1$_{2000}$.

6. Conclusion

The algorithm of DLA is written via Python and it runs on the Raspberry Pi. Turtle library is used to draw the aggregate on the screen. Thus, cheap and portable virtual exhibition platform is created for DLA. Such an exhibition is valuable for classroom and scientific demonstrations and digital exhibitions. Percolation of primary particles towards inside and outside of the aggregate is also considered in the algorithm. Spherical dendritic structures are generated. The fractal dimension of these structures is around 1.68. The porosity increases with the number of primary particles participated to the aggregate, but it is found below 50% for these structures consisting of 2000 particles. The dendritic structures are used for artistic studies. These works are among examples of algorithmic art. Unlimited artworks can be produced by using these dendritic structures.

Acknowledgements

References

[1] J. Nan, M. Yao, T. Chen, Z. Wang, Q. Li and D. Zhan, "Experimental and numerical characterization of floc morphology: role of changing hydraulic retention time under flocculation mechanisms", *Environ. Sci. Pollut. Res.*, vol. 23, pp. 3596-3608, 2016, doi: 10.1007/s11356-015-5539-7.
[2] B. Lim and Y. Xia, "Metal nanocrystals with highly branched morphologies", *Angew. Chem. Int. Ed.*, vol. 50, no. 1, pp. 76-85, 2011, doi: 10.1002/anie.201002024.
[3] H. Tronnolone *et al.*, "Difusion-limited growth of microbial colonies", *Sci. Rep.*, vol. 8, pp. 1-11, 2018, doi: 10.1038/s41598-018-23649-z.
[4] J. Zhang, J. Luo and Z. Liu, "DLA simulation with sticking probability for viscous fingering", in *2011 International Conference on Consumer Electronics, Communications and Networks (CECNet)*, Xianning, China, 2011, pp. 4044-4047, doi: 10.1109/CECNET.2011.5768540.
[5] I. M. Irurzun, P. Bergero, V. Mola, M. C. Cordero, J. L. Vicente and E. E. Mola, "Dielectric breakdown in solids modeled by DBM and DLA", *Chaos, Solitons and Fractals*, vol. 13, no. 6, pp. 1333-1343, 2002, doi: 10.1016/S0960-0779(01)00142-4.
[6] T. A. Witten and L. M. Sander, "Diffusion-limited aggregation", *Phys. Rev. B*, vol. 27, no. 9, pp. 5686-5697, 1983, doi: 10.1103/PhysRevB.27.5686.

[7] M. Wozniak, F. R. A. Onofri, S. Barbosa, J. Yon and J. Mroczka, "Comparison of methods to derive morphological parameters of multi-fractal samples of particle aggregates from TEM images", *J. Aerosol Sci.*, vol. 47, pp. 12-26, 2012, doi: 10.1016/j.jaerosci.2011.12.008.

[8] J. Mroczka, M. Woźniak and F. R. A. Onofri, "Algorithms and methods for analysis of the optical structure factor of fractal aggregates", *Metrol. Meas. Syst.*, vol. XIX, no. 3, pp. 459-470, 2012, doi: 10.2478/v10178-012-0039-2.

[9] D. Liu, W. Zhou, Z. Qiu and X. Song, "Fractal simulation of flocculation processes using a diffusion-limited aggregation model", *Fractal Fract.*, vol. 1, pp. 1-13, 2017, doi: 10.3390/fractalfract1010012.

[10] R. Wang, A. K. Singh, S. R. Kolan and E. Tsotsas, "Fractal analysis of aggregates: correlation between the 2D and 3D box-counting fractal dimension and power law fractal dimension", *Chaos, Solitons and Fractals*, vol. 160, pp. 1-13, 2022, doi: 10.1016/j.chaos.2022.112246.

[11] A. M. Zsaki, "Hardware-accelerated generation of 3D diffusion-limited aggregation structures", *J. Parallel Distrib. Comput.*, vol. 97, pp. 24-34, 2016, doi: 10.1016/j.jpdc.2016.06.009.

[12] N. H. Borzęcka, B. Nowak, R. Pakuła, R. Przewodzki and J. M. Gac, "Cellular automata modeling of silica aerogel condensation kinetics", *Gels*, vol. 7, pp. 1-12, 2021, doi: 10.3390/gels7020050.

[13] M. Polimeno, C. Kim and F. Blanchette, "Toward a realistic model of diffusion-limited aggregation: rotation, size-dependent diffusivities, and settling", *ACS Omega*, vol. 7, no. 45, pp. 40826-40835, 2022, doi: 10.1021/acsomega.2c03547.

[14] O. Tomchuk, "Models for simulation of fractal-like particle clusters with prescribed fractal dimension", *Fractal Fract.*, vol. 7, pp. 1-25, 2023, doi: 10.3390/fractalfract7120866.

[15] S. J. Johnston and S. J. Cox, "The Raspberry Pi: a technology disrupter, and the enabler of dreams", *Electronics*, vol. 6, pp. 1-7, 2017, doi: 10.3390/electronics6030051.

[16] N. Liu *et al.*, "Dynamic mechanism of dendrite formation in Zhoukoudian, China", *Appl. Sci.*, vol. 13, pp. 1-10, 2023, doi: 10.3390/app13042049.

[17] D. D. Ruzhitskaya, S. B. Ryzhikov and Y. V. Ryzhikova, "Features of self-organization of objects with a fractal structure of dendritic geometry", *Moscow Univ. Phys.*, vol. 76, no. 5, pp. 253-263, 2021, doi: 10.3103/S0027134921050143.

[18] Y. Pang *et al.*, "Quantifying the fractal dimension and morphology of individual atmospheric soot aggregates", *J. Geophys. Res. Atmos.*, vol. 127, no. 5, pp. 1-11, 2022, doi: 10.1029/2021JD036055.

[19] A. M. Brasil, T. L. Farias and M. G. Carvalho, "Evaluation of the fractal properties of cluster-cluster aggregates", *Aerosol Sci. Tech.*, vol. 33, no. 5, pp. 440-454, 2000, doi: 10.1080/02786820050204682.

[20] Ü. Ö. Köylü, G. M. Faeth, T. L. Farias and M. G. Carvalho, "Fractal and projected structure properties of soot aggregates", *Combustion and Flame*, vol. 100, no. 4, pp. 621-633, 1995, doi: 10.1016/0010-2180(94)00147-K.

[21] N. Doner and F. Liu, "Impact of morphology on the radiative properties of fractal soot aggregates", *J. Quant. Spectrosc. Radiat. Transf.*, vol. 187, pp. 10-19, 2017, doi: 10.1016/j.jqsrt.2016.09.005.

[22] Z. Merdan and M. Bayirli, "Computation of the fractal pattern in manganese dendrites", *Chinese Phys. Lett.*, vol. 22, no. 8, pp. 2112-2115, 2005, doi: 10.1088/0256-307X/22/8/080.

[23] V. Ceric, "Algorithmic art: technology, mathematics and art", in *ITI 2008, 30th International Conference on Information Technology Interfaces*, Cavtat, Croatia, 2008, pp. 75-82, doi: 10.1109/ITI.2008.4588386.

[24] A. Daudrich, "Algorithmic art and its art-historical relationships", *Journal of Science and Technology of The Arts*, vol. 8, no. 1, pp. 37-44, 2016, doi: 10.7559/citarj.v8i1.220.

RESEARCH ARTICLE

Assessments of GPS satellite orbiting period effects on diurnal and semi-diurnal luni-solar declinations utilizing Galileo satellites

Huseyin Duman[a],*

[a] Sivas Cumhuriyet University, Departments of Geomatics Engineering, 58140 Sivas, Türkiye, ORCID: 0000-0002-7340-7800

Abstract

Global Navigation Satellite Systems (GNSS) can observe a variety of surface deformations on Earth, including periodic oscillations at different frequencies. An example of such phenomena is ocean tide loadings (OTL), which result from the redistribution of water mass. The Global Positioning System (GPS) exhibits orbital geometry that causes its revisit and orbital periods to coincide with the diurnal and semi-diurnal luni-solar declination constituents, known as K1 and K2, respectively. Consequently, the system faces challenges in accurately estimating these periodic oscillations due to its orbital artifacts. This study aims to quantify the extent to which GPS orbital artifacts introduce periodic signals into the K1 and K2 constituents by utilizing the Galileo system and determining the most suitable positioning approach. A dataset from the International GNSS Service (IGS), spanning 40 days in 2024 and covering six stations, was analyzed. Coordinates were estimated using both kinematic positioning every 5 minutes and a 6-hour static precise point positioning (PPP) mode with a 3-hour shift. The power spectra for the east, north, and up components indicated that, on average, the GPS system contributes 52.8% to the K1 constituents and 66.3% to the K2 constituents. Despite expectations that the diurnal K1 and semi-diurnal K2 tidal constituents would be more prominent in the power spectra of the GPS comparing to that of natural signature or of other navigation system (Galileo for this study), the diurnal K1 tidal constituent appeared weak in the kinematic mode power spectra for the GPS system. These findings validate that the overlapped-static PPP mode is a more appropriate approach for estimating these periodic deformations.

© 2023 DPU All rights reserved.
Keywords: GPS; Galileo; Power-spectra; Tidal Loadings; PPP

1. Introduction

The gravitational interactions between the Sun, the Moon, and the Earth induce periodic oscillations on the Earth's surface, manifesting as both solid Earth tides and ocean tides.

These ocean tides cause deformations on the Earth's surface due to the periodic redistribution of water mass, a phenomenon known as ocean tide loadings (OTL) [1]. The OTL deformations are responsive to geodetic measurements such as Global Navigation Satellite Systems (GNSS), Very Long Baseline Interferometry (VLBI), Satellite Laser Ranging (SLR), Doppler Orbitography Integrated by Satellite (DORIS) [2], which means these deformations could also be measurable by the geodetic techniques. However, among the GNSS systems, Global Positioning System (GPS) has a disadvantage of observing diurnal (K1 ~11.97 hours [3]) and semi-diurnal (K2 ~23.93 hours [3]) luni-solar declinations constituents because of aligning these constituents with the GPS revisit period and orbital period [4], [5], [6], although it provides more precise positioning estimates than the other geodetic techniques.

The problematic K1 and K2 luni-solar declination constituents, influenced by the GPS orbital geometry, have been measured more accurately by incorporating other Global Navigation Satellite Systems (GNSS) such as Global'naya Navigatsionnaya Sputnikovaya Sistema (GLONASS) and Galileo [1], [2], [6]. Abbaszadeh et al. [2] utilized the GLONASS system and reported that estimates for all OTL constituents, except K1 and K2, were as precise as those using the GPS system. However, the estimates for K1 and K2 showed improvement when compared to GPS alone. Ait-Lakbir et al. [6] demonstrated that the Galileo and/or GLONASS systems enhanced K1 and K2 estimates by up to 55% compared to GPS. Matviichuk et al. [1] indicated that K1 and K2 estimates are more accurate using GPS+GLONASS for the north and up topocentric coordinate components, whereas the GPS positioning with resolved ambiguities yielded better estimates for the east component than the combined solution. Peng et al. [5], rather than using coordinate time series, examined multi-GNSS interferometric reflectometry to analyze tidal constituents. They found that the bias on the K1 and K2 constituents due to GPS could be reduced by incorporating the Galileo and GLONASS systems. Furthermore, Pan et al. [7] proposed a novel methodology to accurately estimate the problematic K1 and K2 constituents using only the GPS system. This methodology involves fitting a quadratic smooth function to the tidal constituents, benefiting from the unique orbital geometry of other satellite systems in comparison to GPS. Wang et al. [8] benefitted from GPS, GLONASS, Galileo navigation satellites and their combinations to improve ocean tide loading estimates and highlighted that Galileo-only solution and multi-GNSS combinations showed better estimation of solar-related tidal constituents, specifically for K1 and K2 tidals, than GPS-only solutions. Additionally, they stated that resolving ambiguities is a vital role to estimate solar-related tidal constituents.

The studies [1], [2], [6], [9] predominantly processed their observation data using coordinate time series in precise point positioning (PPP) mode [10]. The commonly adopted PPP mode is a kinematic approach. Matviichuk et al. [1] estimated coordinates every 5 minutes in kinematic PPP mode, while Abbaszadeh et al. [2] used kinematic PPP mode with float ambiguities, as described by Penna et al. [11]. Ait-Lakbir et al. [6] processed data in both kinematic and non-overlapping 3-hour static PPP modes, finding the latter more reliable for estimating OTL displacements. Wang et al. [8] also reported similar findings with Ait-Lakbir et al. [6] in terms of data processing strategy. Bogusz and Figurski [9] employed a 3-hour static mode with a 1-hour shift, creating a 2-hour overlapping window, to analyze short-term OTL displacements.

The aforementioned studies primarily concentrate on the precise estimation of K1 and K2 tidal constituents due to the GPS orbital geometry, rather than on the artificial signal contributions to natural phenomena. This paper addresses two key objectives: (i) evaluating the extent to which the signal powers of the diurnal (K1) and semi-diurnal (K2) luni-solar declinations, which coincide with GPS revisit and orbital periods, are contaminated or interfered with by artificial signals induced by GPS orbital geometry; and (ii) determining which PPP mode—kinematic or overlapped-static PPP—is more effective in identifying these artificial signals attributed to GPS orbits. The structure of this paper is as follows. The details of the GNSS data and processing methodologies are elaborated in the following section. Section 3 outlines the preliminary analysis of coordinate time series, including outlier detection and precision assessment, and the transformation of these time series into the frequency domain. Finally, the key findings addressing the research questions are highlighted in the concluding section.

2. GNSS Data Acquisition and Processing

GNSS data from six IGS stations distributed across the Eastern Mediterranean region were employed in this study (Fig. 1). The data were obtained from the online archives of the Crustal Dynamics Data Information System

(CDDIS) (https://cddis.nasa.gov, last accessed: April 7, 2024) in the daily Receiver Independent Exchange (RINEX v3) in Hatanaka format sampled at every 30-seconds [12]. These stations fully include 40 days of data covering January 1, 2024, to February 9, 2024.
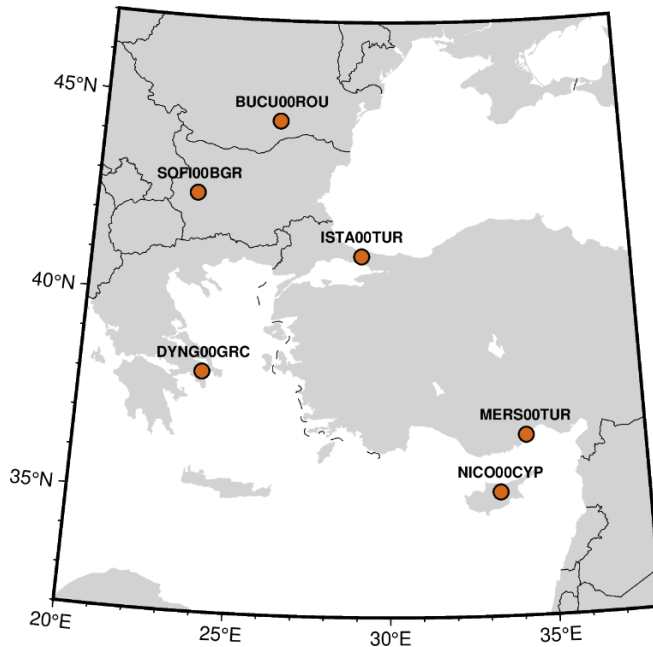
Fig. 1. The six stations operated under the International GNSS Service (IGS) with long name convention.

The PRIDE-PPPAR v3.0 software were utilized to process all 40 days of daily RINEX observation files [13], with processing parameters outlined in Table 1. Coordinates were estimated in both static and kinematic Precise Point Positioning (PPP) modes [10], resolving ambiguities for GPS- and Galileo-only observations [14], [15], [16]. The static PPP strategy entailed a 6-hour session length with a 3-hour session overlap (Fig. 2), while kinematic PPP coordinates were estimated every 300 seconds using non-overlapping observations.
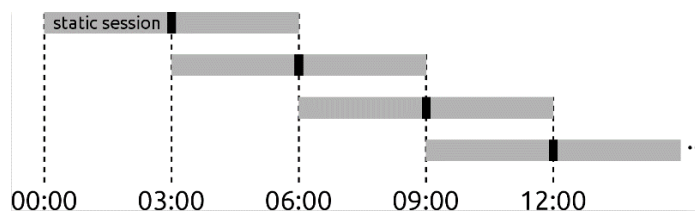
Fig. 2. A 3-hours overlapped 6-hours length static session strategy.

Rapid orbit/clock products, satellite attitude quaternions, observable-specific phase biases, and Earth rotation parameters from Wuhan University were utilized in all processing [15], [17], [18]. The quality of parameter estimates using rapid products has been previously reported by Li et al. [19], showing comparability with final products. Second-order ionospheric effects were mitigated using CODE products [20]. Vienna Mapping Function (VMF1) data were applied [21], with zenith wet delays estimated using a random-walk model, and gradients for horizontal delays estimated using a piece-wise constant model every 12 hours. Pole and Solid Earth tides were accounted for according to International Earth Rotation Service (IERS) conventions [22]; however, ocean tide loadings were not modeled. The GNSS stations in Fig. 1 are far from oceanic boundaries. Even so, they have too

small signal amplitudes for K1 and K2 constituents, this omission was due to clearly exhibiting how much power of the GPS orbital revolution periods adds to the diurnal, semi-diurnal luni-solar declinations (K1 and K2) constituents.

Table 1. PPP processing details for GNSS data

Parameter	Description
Software	PRIDE-PPPAR v3.0
Positioning Strategy	PPP in overlapped-static and kinematic mode.
	Ionosphere-free combinations for code and phase with every 30 seconds
	in static mode and every 300 seconds in kinematic mode
Elevation cut-off angle	7°
Products	Wuhan University rapid products (WUM): Earth rotation
	parameters, observable-specific phase biases, satellite attitude
	Quaternions, orbit and clock products
Phase Center of Satellite/Receiver	IGS20_2290.atx
Phase Ambiguities	Fixing GPS and Galileo satellites above 15° cut-off angle and 15-min arc
	length
Ionosphere	Removed second order effect using CODE products
Troposphere	VMF1
Zenit wet delays	Random-walk
Gradients of horizontal delays	Piece-wise constant at evert 12 hours
Ocean tide loading	Not modelled
Solid earth and pole tides	IERS conventions 2010

3. Results and Discussion

This section presents: (i) a 40-day time series of coordinates for all stations using GPS- and Galileo-only systems in both overlapped static (Fig. 2) and kinematic PPP modes, and (ii) stacked spectra for the east (E), north (N), and up (U) coordinate components in the frequency domain (with frequencies converted to periods) using the Lomb-Scargle algorithm [23], [24]. The analysis evaluates the contribution of the GPS orbiting period to diurnal (K1) and semi-diurnal (K2) luni-solar declinations constituents and compares the efficiency of overlapped static and kinematic positioning strategies.

3.1. GPS- and Galileo-only systems coordinate time series

The three-dimensional cartesian coordinates of the six selected stations aligned to the ITRF2020 reference frame [25] were transformed into the topocentric coordinate system (i.e., east, north, and up), using the average coordinates over the 40-day period as a reference. These averaged reference coordinates were generated using similar processing parameters as detailed in the previous section (see Table 1) but employing a non-overlapped 24-hour session strategy in static PPP mode for both GPS- and Galileo-only system observations.

Outliers in the kinematic and overlapped-static time series for the topocentric coordinate components were removed through median absolute deviation (MAD) method [26], [27], [28], which is of the form:

$$MAD = \begin{cases} \dfrac{1.2533}{N} \times \sum |\boldsymbol{e}|, & median(|\boldsymbol{e}|) = 0 \\ 1.4826 \times median(|\boldsymbol{e}|), & median(|\boldsymbol{e}|) \neq 0 \end{cases} \qquad (1)$$

where, $|\cdot|$ is the absolute operator, and $\boldsymbol{e} = \boldsymbol{y} - median(\boldsymbol{y})$ is normalized observations referencing to the median of observations or observations residuals. N is the number of observations. Any residuals in $|\boldsymbol{e}|$ exceeding $3 \times MAD$ threshold is considered as outliers and removed from the time series.

The analysis results, e.g., the north component of the DYNG00GRC station using GPS- and Galileo-only systems in kinematic and overlapped-static PPP modes (Fig. 3), provide valuable insights into the comparative performance of GPS and Galileo satellite systems. After removing outliers from the coordinate time series (gray solid lines for kinematic mode and black crosses for overlapped-static mode in Fig. 3), the kinematic coordinates align well with the static coordinates. Table 2 presents the outlier percentages and root mean square error (RMSE) comparisons for the east, north (horizontal), and up components. The outlier percentages for kinematic coordinate time series range from 1.40% to 4.41% for GPS and from 1.76% to 4.66% for Galileo, except for the ISTA00TUR station. For this station, the percentages reach up to 15.82% and 45.25% for GPS and Galileo, respectively. The RMSE values for kinematic coordinate time series for GPS vary between 5.00 mm and 9.77 mm for horizontal components and between 16.72 mm and 24.90 mm for vertical components, whereas those for Galileo range from 5.85 mm to 9.98 mm for horizontal components and from 18.58 mm to 47.93 mm for the vertical component. Although the ISTA00TUR station has a high percentage of outliers, its RMSE values are comparable to those of other stations. For the static coordinate time series, both the outlier percentages and RMSE values are generally lower compared to the kinematic time series. The outlier percentages range from 0.00% to 9.43% for GPS and from 0.31% to 14.78% for Galileo. These upper values correspond to the horizontal components of the DYNG00GRC and SOFI00BGR stations and are higher than their kinematic counterparts. The RMSE values for GPS range between 1.59 mm and 2.72 mm for horizontal components, and between 5.98 mm and 12.48 mm for the vertical component. For Galileo, the RMSE values range from 1.74 mm to 2.80 mm for horizontal components and from 6.76 mm to 12.38 mm for the vertical component. The RMSE values for GPS and Galileo across all components are quite close to each other.
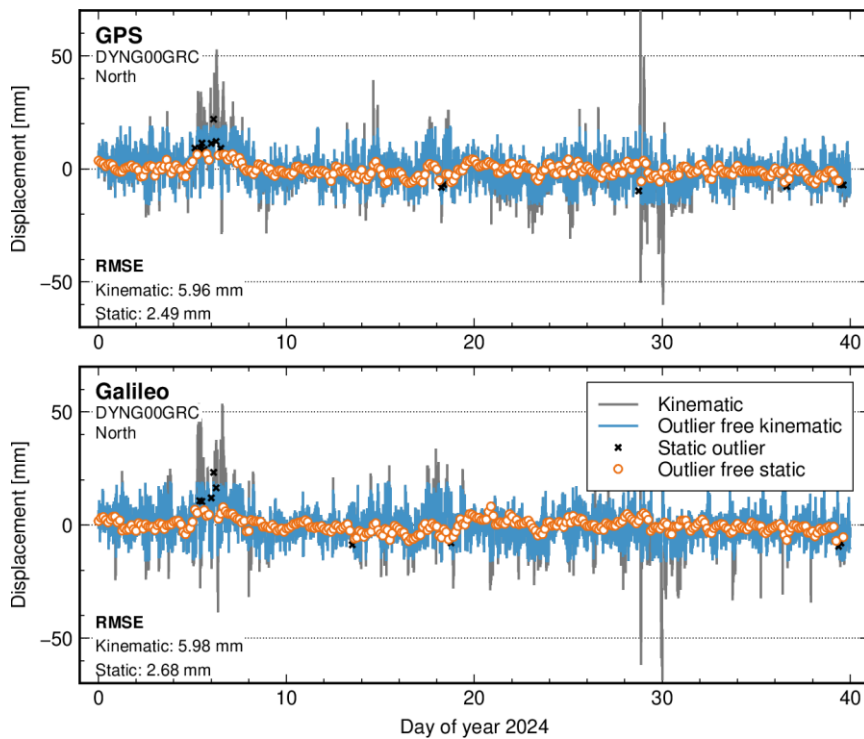
Fig. 3. The north component displacements of station DYNG00GRC, comparing kinematic and static positioning modes with GPS (top) and Galileo (bottom) satellites. The gray solid line represents raw displacements in kinematic positioning, while the blue solid line depicts the same with outliers removed. In static mode, outliers are denoted by black crosses, whereas outlier-free static mode displacements are indicated by orange outlined circles.

Table 2. Outlier percentage and RMSE comparison of east (E), north (N) and up (U) components for kinematic and static positioning modes with GPS and Galileo satellites

| Stations | Outliers [%] | | RMSE* [mm] | |
| | Kinematic-mode | Static-mode | Kinematic-mode | Static-mode |
	E / N / U	E / N / U	E / N / U	E / N / U
GPS				
BUCU00ROU	2.34 / 1.48 / 1.37	1.89 / 0.63 / 0.31	5.17 / 7.27 / 16.92	2.24 / 1.59 / 8.41
DYNG00GRC	4.41 / 3.54 / 2.88	7.23 / 4.40 / 1.89	5.00 / **5.96**[+] / 16.72	2.29 / **2.49**[+] / 6.75
ISTA00TUR	15.82 / 11.87 / 9.83	0.95 / 0.95 / 0.32	6.21 / 7.85 / 20.80	2.12 / 1.94 / 6.97
MERS00TUR	1.61 / 2.01 / 1.47	1.57 / 0.00 / 0.63	6.21 / 8.43 / 21.17	1.95 / 2.00 / 6.97
NICO00CYP	1.93 / 2.60 / 1.40	0.00 / 0.00 / 0.94	5.41 / 7.23 / 21.92	2.00 / 1.95 / 5.98
SOFI00BGR	2.77 / 1.92 / 1.85	9.43 / 3.14 / 1.57	8.63 / 9.77 / 24.90	2.72 / 2.35 / 12.48
Galileo				
BUCU00ROU	2.22 / 1.76 / 1.60	3.46 / 0.94 / 1.26	5.97 / 6.71 / 18.58	2.18 / 1.74 / 9.27
DYNG00GRC	3.58 / 3.94 / 3.01	5.03 / 2.83 / 2.20	5.85 / **5.98**[+] / 19.64	2.70 / **2.68**[+] / 7.51
ISTA00TUR	45.25 / 35.24 / 32.65	3.47 / 0.95 / 0.63	8.56 / 12.65 / 47.93	2.30 / 2.20 / 8.35
MERS00TUR	3.46 / 2.63 / 2.68	0.94 / 0.31 / 2.20	6.93 / 7.71 / 24.74	2.49 / 2.22 / 6.97
NICO00CYP	4.66 / 4.03 / 3.68	2.52 / 1.26 / 0.94	6.19 / 6.93 / 24.81	2.20 / 1.98 / 6.76
SOFI00BGR	3.84 / 2.70 / 2.58	14.78 / 4.40 / 1.26	8.88 / 9.98 / 27.29	2.52 / 2.80 / 12.38

* RMSE is computed using outlier-free time series

[+] These values are depicted in Fig. 3

3.2. Stacked spectra for GPS- and Galileo-only systems

The PPP coordinate time series for GPS- and Galileo-only systems in kinematic and overlapped-static mode elaborated in the previous section are used to examine the GPS system specific orbital period effects on luni-solar declinations. The orbital period equals to $11^h 58^m$, which resulting in two orbital repeats in one sidereal day. This amounts to a 1:2 deep resonant effect on GPS satellites relative to the Earth's rotation [4], [29]. The main luni-solar declinations, i.e., K1 and K2 equivalent either to one sidereal day and its half, coincidence with the GPS orbital period [5]. It means that the signal powers at K1 and K2 frequencies are contaminated by the GPS orbital error, so leading to hinder the detectable natural signature of these frequencies. However, Galileo satellite system has rather a 10:17 shallow resonant effect relative to the Earth's rotation [29]. It means that the Galileo system specific orbital error does not affect the signal powers at the K1 and K2 frequencies, that is, the expected signal powers at these frequencies when using coordinate time series derived only from Galileo system are their detectable natural signature.

To investigate the GPS orbital periodical effect, the coordinate time series for the topocentric coordinate components of all stations were transformed to the frequency domain through the Lomb-Scargle method [23], [24]. The power spectra were generated by stacking the power spectra of each station at equivalent frequencies and subsequently normalizing the powers. This process was performed separately for the east, north, and up components of the kinematic and overlapped-static time series derived from GPS and Galileo systems. Fig. 4 illustrates the corresponding power spectra converted to periods by inverting the frequencies. The K1 and K2 constituents are clearly visible in all components for the overlapped-static mode. For the kinematic mode, these constituents demonstrate a relatively weak presence in all components, except for the K2 in the east component, which shows nearly no signature. In addition to these signals, the 3rd and 4th harmonics of luni-solar declinations (K3 and K4) and the principal lunar semi-diurnal (M2) constituent also appear in the spectra. In the overlapped-static mode, the K3 harmonic has too weak signature in all components, whereas the K4 has no power. The sampling period of the overlapped-static mode is three hours. The Nyquist frequency of this three-hour interval limits the capability to detect the K3 and higher harmonics. The weak presence of K3 despite this limitation could originate from the overlapping strategy. Conversely, in the kinematic mode, these harmonics have distinctive features in the horizontal components, except for the up component due to the sampling interval. The sampling interval of the kinematic mode

(5 minutes) is shorter than that of the overlapped-static mode. The M2 constituent appears in the east and up components, yet it is absent in the north component for both positioning modes.
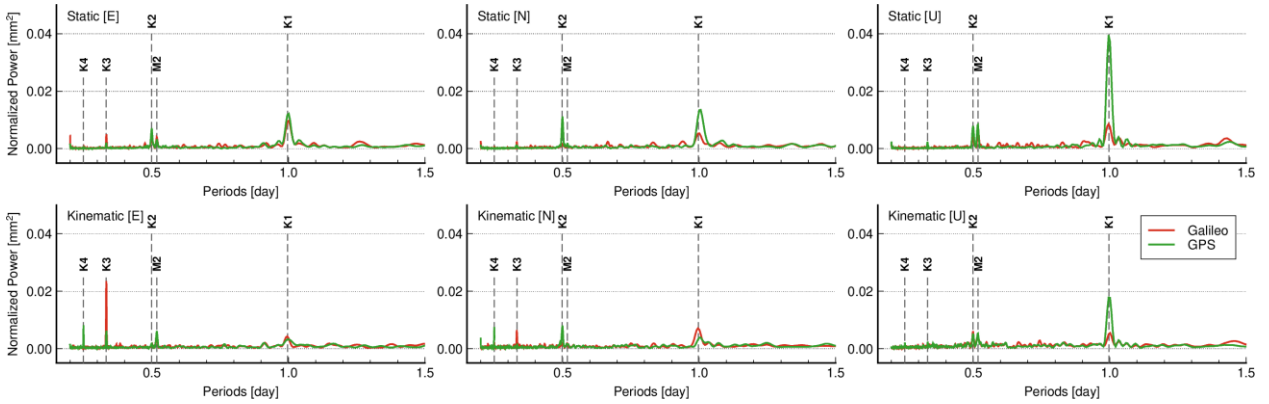
Fig. 4. East (E), north (N) and up (U) components stacked mean power spectra in kinematic and overlapped-static mode for GPS (solid green line) and Galileo (solid red line) satellites. The vertical dashed gray lines represent diurnal, semi-diurnal luni-solar declinations (K1 and K2) and harmonics (K3 and K4), and principal lunar semi-diurnal (M2) constituents.

The K1 and K2 constituents consist of a natural phenomenon of luni-solar declinations and the GPS orbital geometry for the spectra of GPS. But those for the spectra of Galileo include only the natural signature, there is not a system specific artificial error. Therefore, the signal power at the K1 and K2 constituents for GPS system should be higher than those for Galileo system. In the power spectra of the horizontal components for kinematic PPP mode, the signal power at K1 for the Galileo is higher than GPS, which is out of the stated expectation. It clearly implies that the overlapped-static PPP mode has a prior to the kinematic PPP mode.

A difference of the signal power at K1 and K2 between GPS and Galileo systems explains how much signal power is introduced in the natural phenomenon. Assuming the signal power of Galileo is equivalent that of the natural K1 and K2 signal powers, then the contribution of GPS system in percentage (ϕ) is of the form,

$$\phi = \left\{ \frac{P_{GPS}(c) - P_{GAL}(c)}{P_{GPS}(c)} \right\} \times 100\% \tag{2}$$

where, c is the K1 and K2 constituents; $P_{GPS}(c)$ and $P_{GAL}(c)$ are the signal powers at c frequency/period. Using the signal powers in Fig. 4, the GPS orbit periodical effect on the K1 constituents is 19.6%, 60.7% and 78.2% for east, north and up components, whereas that on the K2 constituents is 63.1%, 85.2% and 50.6% in similar order. The statistics show that the signal powers at the K1 and K2 constituents originate mostly from the GPS orbital periodic effect, except for the east component for the K1.

4. Conclusions

The GPS system orbital period coincides with the first two harmonics of lunar-solar declinations, known as K1 and K2. Consequently, a periodic signal resulting from the GPS satellite system's orbital geometry interferes with this natural phenomenon, rendering it undetectable through GPS-only observations. In contrast, the Galileo satellite system, despite its similarities to GPS, has a different orbital period, meaning it does not affect the lunar-solar declinations. This study quantifies the extent to how much the luni-solar declinations are contaminated or interfered with by the GPS satellite system's orbital period, using the Galileo satellite system for comparison. Additionally, the study evaluates the reliability of results produced by either the kinematic or overlapped-static PPP mode. The results demonstrate that the GPS system provides more precise coordinate estimates than the Galileo system by a factor of nearly 1.2. In kinematic PPP mode, the average root mean square errors (RMSE) for the horizontal components are

6.9 / 7.7 mm, and those for the vertical component are 20.4 / 27.2 mm for GPS and Galileo systems, respectively. In overlapped-static PPP mode, these values are significantly lower, and are 2.1 / 2.3 mm and 7.9 / 8.5 mm in similar order. The spectrum analysis reveals notable differences between the GPS and Galileo systems. Specifically, the GPS system exhibits artificial signals corresponding to its orbital period (K2) and revisit period (K1). These artificial signals are more prominent in the power spectra of the overlapped-static PPP mode, validating its superiority over the kinematic PPP mode in isolating GPS system-specific signals. The unexpected presence of the first harmonic of the luni-solar declination (K1) in the horizontal components' power spectra for the kinematic PPP mode further supports this finding. In contrast, assuming that the Galileo system's power spectra predominantly represent natural phenomena, with the artificial signals in the GPS system contributing on average 52.8% and 66.3% to the K1 and K2 periods, respectively. This significant impact of artificial signals induced by the GPS satellite system underscores the necessity for careful consideration in geophysical studies. Overall, this research highlights the advantages of the Galileo system in providing contribution of GPS orbital geometry error into luni-solar declinations and the effectiveness of the overlapped-static PPP mode in extracting these signals.

Acknowledgements

Author Contribution

H.Duman: Data Collection, analysis of data and interpretation results, final manuscript preparation

References

[1] B. Matviichuk, M. King, and C. Watson, "Estimating ocean tide loading displacements with GPS and GLONASS," *Solid Earth*, vol. 11, no. 5, pp. 1849–1863, Oct. 2020, doi: 10.5194/se-11-1849-2020.
[2] M. Abbaszadeh, P. J. Clarke, and N. T. Penna, "Benefits of combining GPS and GLONASS for measuring ocean tide loading displacement," *J. Geod.*, vol. 94, no. 7, p. 63, Jul. 2020, doi: 10.1007/s00190-020-01393-5.
[3] N. T. Penna and M. P. Stewart, "Aliased tidal signatures in continuous GPS height time series," *Geophys. Res. Lett.*, vol. 30, no. 23, p. 2003GL018828, Dec. 2003, doi: 10.1029/2003GL018828.
[4] R. Zajdel, K. Kazmierski, and K. Sośnica, "Orbital Artifacts in Multi‐GNSS Precise Point Positioning Time Series," *J. Geophys. Res. Solid Earth*, vol. 127, no. 2, p. e2021JB022994, Feb. 2022, doi: 10.1029/2021JB022994.
[5] D. Peng, Y. N. Lin, J.-C. Lee, H.-H. Su, and E. M. Hill, "Multi-constellation GNSS interferometric reflectometry for tidal analysis: mitigations for K1 and K2 biases due to GPS geometrical errors," *J. Geod.*, vol. 98, no. 1, p. 5, Jan. 2024, doi: 10.1007/s00190-023-01812-3.
[6] H. Ait-Lakbir, A. Santamaría-Gómez, and F. Perosanz, "Assessment of sub-daily ocean tide loading errors and mitigation of their propagation in multi-GNSS position time series," *GPS Solut.*, vol. 27, no. 3, p. 129, Jul. 2023, doi: 10.1007/s10291-023-01467-9.
[7] H. Pan, X. Xu, H. Zhang, T. Xu, and Z. Wei, "A Novel Method to Improve the Estimation of Ocean Tide Loading Displacements for K1 and K2 Components with GPS Observations," *Remote Sens.*, vol. 15, no. 11, p. 2846, May 2023, doi: 10.3390/rs15112846.
[8] H. Wang, M. Li, N. Wei, S.-C. Han, and Q. Zhao, "Improved estimation of ocean tide loading displacements using multi-GNSS kinematic and static precise point positioning," *GPS Solut.*, vol. 28, no. 1, p. 27, Jan. 2024, doi: 10.1007/s10291-023-01568-5.
[9] J. Bogusz and M. Figurski, "Residual K1 and K2 Oscillations in Precise GPS Solutions: Case Study," *Artif. Satell.*, vol. 46, no. 2, Jan. 2011, doi: 10.2478/v10018-011-0012-4.
[10] J. F. Zumberge, M. B. Heflin, D. C. Jefferson, M. M. Watkins, and F. H. Webb, "Precise point positioning for the efficient and robust analysis of GPS data from large networks," *J. Geophys. Res. Solid Earth*, vol. 102, no. B3, pp. 5005–5017, Mar. 1997, doi: 10.1029/96JB03860.
[11] N. T. Penna, P. J. Clarke, M. S. Bos, and T. F. Baker, "Ocean tide loading displacements in western Europe: 1. Validation of kinematic GPS estimates," *J. Geophys. Res. Solid Earth*, vol. 120, no. 9, pp. 6523–6539, Sep. 2015, doi: 10.1002/2015JB011882.
[12] C. E. Noll, "The crustal dynamics data information system: A resource to support scientific analysis using space geodesy," *Adv. Space Res.*, vol. 45, no. 12, pp. 1421–1440, Jun. 2010, doi: 10.1016/j.asr.2010.01.018.
[13] J. Geng *et al.*, "PRIDE PPP-AR: an open-source software for GPS PPP ambiguity resolution," *GPS Solut.*, vol. 23, no. 4, p. 91, Oct. 2019, doi: 10.1007/s10291-019-0888-1.
[14] J. Geng and S. Mao, "Massive GNSS Network Analysis Without Baselines: Undifferenced Ambiguity Resolution," *J. Geophys. Res. Solid Earth*, vol. 126, no. 10, p. e2020JB021558, Oct. 2021, doi: 10.1029/2020JB021558.
[15] J. Geng, Q. Wen, Q. Zhang, G. Li, and K. Zhang, "GNSS observable-specific phase biases for all-frequency PPP ambiguity resolution," *J. Geod.*, vol. 96, no. 2, p. 11, Feb. 2022, doi: 10.1007/s00190-022-01602-3.

[16] J. Geng, X. Chen, Y. Pan, and Q. Zhao, "A modified phase clock/bias model to improve PPP ambiguity resolution at Wuhan University," *J. Geod.*, vol. 93, no. 10, pp. 2053–2067, Oct. 2019, doi: 10.1007/s00190-019-01301-6.

[17] J. Geng, S. Yang, and J. Guo, "Assessing IGS GPS/Galileo/BDS-2/BDS-3 phase bias products with PRIDE PPP-AR," *Satell. Navig.*, vol. 2, no. 1, p. 17, Dec. 2021, doi: 10.1186/s43020-021-00049-9.

[18] J. Geng, Q. Zhang, G. Li, J. Liu, and D. Liu, "Observable-specific phase biases of Wuhan multi-GNSS experiment analysis center's rapid satellite products," *Satell. Navig.*, vol. 3, no. 1, p. 23, Oct. 2022, doi: 10.1186/s43020-022-00084-0.

[19] W. Li, M. Kačmařík, and D. Kin, "Assessment of the Multi-GNSS PPP Performance Using Precise Products from the Wuhan Analysis Centre," in *Proceedings of conference GIS Ostrava 2021 Advances in Localization and Navigation*, Vysoká škola báňská - Technická univerzita Ostrava, 2021. doi: 10.31490/9788024845050-9.

[20] S. Kedar, G. A. Hajj, B. D. Wilson, and M. B. Heflin, "The effect of the second order GPS ionospheric correction on receiver positions," *Geophys. Res. Lett.*, vol. 30, no. 16, p. 2003GL017639, Aug. 2003, doi: 10.1029/2003GL017639.

[21] J. Boehm, A. Niell, P. Tregoning, and H. Schuh, "Global Mapping Function (GMF): A new empirical mapping function based on numerical weather model data," *Geophys. Res. Lett.*, vol. 33, no. 7, p. 2005GL025546, Apr. 2006, doi: 10.1029/2005GL025546.

[22] G. Petit and B. Luzum, "IERS conventions (2010)," 2010.

[23] N. R. Lomb, "Least-squares frequency analysis of unequally spaced data," *Astrophys. Space Sci.*, vol. 39, no. 2, pp. 447–462, Feb. 1976, doi: 10.1007/BF00648343.

[24] J. D. Scargle, "Studies in astronomical time series analysis. II - Statistical aspects of spectral analysis of unevenly spaced data," *Astrophys. J.*, vol. 263, p. 835, Dec. 1982, doi: 10.1086/160554.

[25] Z. Altamimi, P. Rebischung, X. Collilieux, L. Métivier, and K. Chanard, "ITRF2020: an augmented reference frame refining the modeling of nonlinear station motions," *J. Geod.*, vol. 97, no. 5, p. 47, May 2023, doi: 10.1007/s00190-023-01738-w.

[26] J. W. Tukey, *Exploratory data analysis*. in Addison-Wesley series in behavioral science. Reading (Mass.) Menlo Park (Calif.) London [etc.]: Addison-Wesley publ, 1977.

[27] R. A. Maronna, R. D. Martin, and V. J. Yohai, *Robust Statistics: Theory and Methods*, 1st ed. in Wiley Series in Probability and Statistics. Wiley, 2006. doi: 10.1002/0470010940.

[28] S. Hekimoglu, B. Erdogan, M. Soycan, and U. M. Durdag, "Univariate Approach for Detecting Outliers in Geodetic Networks," *J. Surv. Eng.*, vol. 140, no. 2, p. 04014006, May 2014, doi: 10.1061/(ASCE)SU.1943-5428.0000123.

[29] H. Duman, "GNSS-specific characteristic signals in power spectra of multi-GNSS coordinate time series," *Adv. Space Res.*, vol. 73, no. 12, pp. 5860–5875, Jun. 2024, doi: 10.1016/j.asr.2024.03.016.

[30] P. Wessel *et al.*, "The Generic Mapping Tools Version 6," *Geochem. Geophys. Geosystems*, vol. 20, no. 11, pp. 5556–5564, Nov. 2019, doi: 10.1029/2019GC008515.

RESEARCH ARTICLE

Determination thermal and mechanical properties of Nano Carbon, Graphite and Graphene reinforced recycling Polypropylene composite sample

Ömer Şengül[a,*], Ferhat Çalışkan[b], Menderes Kam[c]

[a,*] *Hatice Bayraktar Vocational and Technical Anatolian High School, Kocaeli, 41000, Türkiye, ORCID: 0000-0002-2253-5064*
[b] *Hatice Bayraktar Vocational and Technical Anatolian High School, Kocaeli, 41000, Türkiye, ORCID: 0009-0002-5517-0034*
[c] *Düzce Üniversitesi, Dr. Engin Pak Cumayeri Vocational Scholl, Düzce, 81000, Türkiye, ORCID: 0000-0002-9813-559X*

Abstract

Polymer-based plastic materials occupy a major place in daily life. However, due to the nature of polymer materials, low thermal resistance and mechanical properties of these products, the need for new and sustainable materials in the industry has increased. With the rapid technological developments in advanced manufacturing industries such as aviation, marine, motor sports and defense industry, lightweight and high-strength composite products have become even more important. In this context, in this study, 1% nano carbon, graphene and graphite particle reinforced Polypropylene (PP) composite material mixed in a twin-screw extruder and MA/G series injection molding machine standard tensile test sample produced. Melt Flow Index (MFI), Heat Deformation Test (HDT), tensile test, Shore-D hardness measurement and density tests performed on these test samples. According to the results obtained from these tests, the mechanical and thermal properties of the test samples produced from different composite materials were determined. The best mechanical and thermal properties occurred in the graphene particle. It formed in graphite and nano carbon, respectively.
© 2023 DPU All rights reserved.

Keywords: Polypropylene, graphene, graphite, nano carbon, injection production, mechanical properties, thermal properties

1.Introduction

Today, due to the increasing need for materials in the industry and the increasing decrease in natural resources, and to meet the need for materials, the search for new materials compatible with the developing technology is becoming increasingly important.

---

* Corresponding author. Tel.: +0-539-214-7527 ; E-mail address: omersengullll@hotmail.com

Polymer materials obtained using petroleum resources are among the most widely used materials in many sectors, such as bags, packaging, pet bottles and rigid plastic products, which are often used in many sectors. Polypropylene (PP) materials are known as polymers materials with the most widespread use from products for the automotive industry, textile products to food packaging [1]. The fact that the field of use of PP material and its mechanical and thermal properties are not particularly good has made it necessary to produce materials suitable for the progress in technology. Composite materials meet the needs of today's industry by combining various and varied materials with appropriate properties and Decently [1-2]. Rapid technological developments and increasing competitiveness and high-strength products in industries such as the aerospace and defense industry have made it mandatory to design and produce lightweight and high-strength materials in these products [3-4]. To meet this need of the industry, composite materials have started to enter the industrial industry since the past years and their usage areas have increased rapidly today [5].

Composite materials are materials created by combining the best properties of two or more materials of different structures to collect them into an original and single material [10-11]. Decoupled materials are materials that formed by combining the best properties of two or more materials of different structures into one original material. The most important criterion in the production of composite materials is the selection of the right matrix and reinforcement elements [12]. The most common composite materials with superior properties produced with polymer-matrices. These composite materials include thermoplastic or thermosetting polymers reinforced with glass, graphite, graphene, aramid, or nano carbon fibers [13]. These materials can produce with different production methods in different shapes and sizes. Composite materials have superior properties because they can use their superior properties such as high strength, hardness, and resistance to corrosion in many different areas [14].

Particles of dimensions, which defined as particles whose dimensions are 100 nm and below, constitute the main basis of nanotechnology. These particles show different and superior properties compared to their forms in micron and larger sizes [2-6]. The most important reasons for the increase in the research of nanoparticle materials are the size dependence of their electronic structure, quantum size effects, high surface-to-volume ratio and the unique characters of their atoms [2-7].

Nano carbon particle reinforced composite products are generally used in the aerospace sector, the automotive sector, and the marine sector [8]. Thanks to the new production techniques that are developing today, operating costs are decreasing and, accordingly, the areas of use are increasing. It has started to be used more widely, especially in the aviation and automotive sector, to reduce the flight costs of new generation aircraft and emission values in motor vehicles [8-9]. The field of use of nano carbon-reinforced composites, which have better mechanical properties than aluminum alloys used in the aerospace sector, has expanded [9]. It is widely preferred in the wings of wind turbines widely used in the renewable energy sector in our country due to its lightness, durability, and ease of production [4-7].

In this study, a homogeneous mixture of nanoparticles with PP made with a twin-screw extruder. Prototypes produced by injection method. Some thermal and mechanical properties of these new composite materials have studied experimentally.

2.Material and Methods

Injection molding method is one of the most important production methods applied in plastic production. In this study, graphene, graphite, nano carbon reinforced Polypropylene (PP) composite samples produced on the injection machine shown in Figure 1. Rectangular cross-sectional samples produced from a single screw sleeve with an injection speed of 45 mm/s and a production pressure of 50 bar.

Fig. 1. Injection Molding Machine.

The dimensions of the tensile test samples made in accordance with the TS ISO 604 standard. The sample dimensions given in Figure 2. The original and recycled PP samples made by subjecting to tensile experiments at a tensile speed of 1 mm/min using Shimadzu brand universal tester Figure 3 with 250 kN capacity load cells. The tensile test repeated three times for each sample and the results averaged. All tests performed by the same operator in a laboratory environment under the same environmental conditions. Figure 4 gives notch throwing device and Figure 5 shows notching measurements.
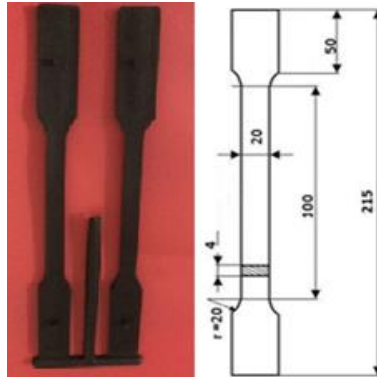
Fig.2. Composite Standard Test Sample.

Fig. 3. Tensile Testing Machine.
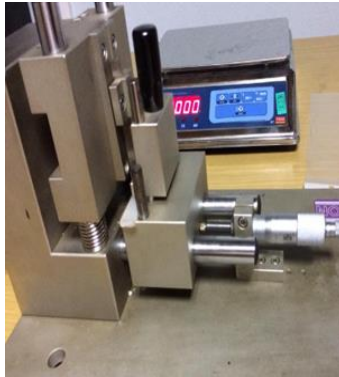
Fig. 4. Notch Throwing Device.
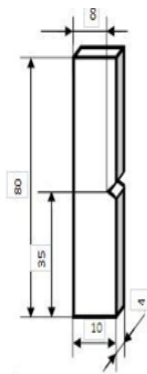
Fig. 5. Notching Measurements [15].

125

The Izod test device and Standard Izod test samples (100x10x4 mm) shown in Figure 6 and Figure 7. The tests were repeated three times for each sample and the average values were taken.

Fig. 6. Izod Test Device.

Fig. 7. Standard Izod test samples.

Shore-D test is a traditional hardness measurement method used to determine the hardness of plastic or flexible materials. It used to indicate the hardness values of polymers, elastomers, and rubber-based materials. Hardness tests of the test samples prepared by injection molding machine performed with the ZWICK brand Shore D durometer device shown in Figure 8. The tests repeated three times for each sample and the average values were taken.

Fig. 8. Shore-D Test Device.

The MFI test performed to determine the fluidity behavior of plastic materials during processing in an extruder and shaping by molding in an injection molding machine [16]. Thermal tests applied to plastics for changes in changes in the physical properties of materials by heating or cooling plastic materials in a controlled manner. Fluidity in polymer materials is of critical importance in the processing and molding of the product. Therefore, control is also an important parameter. The fluid index MFI (ISO 1133) test performed with the Melt Index test device shown in Figure 9.

Fig. 9. MFI Test Device.

Heat Deformation Test (HDT); Heat Deflection Temperature (HDT) used to determine the temperature limit up to which polymer, finished products and semi-finished products are exposed to feverish temperatures. HDT tests performed according to ISO 75 standard. The samples (100x10x4mm) assessed at 3 different stations and their temperatures were measured eight times at an average depth of 0.118 mm and the arithmetic mean of the results was taken. The starting temperature for PP polymer material is determined as 25°C and the starting temperature for composite material is determined as 25°C. The HDT device used in the experiments shown in Figure 10.
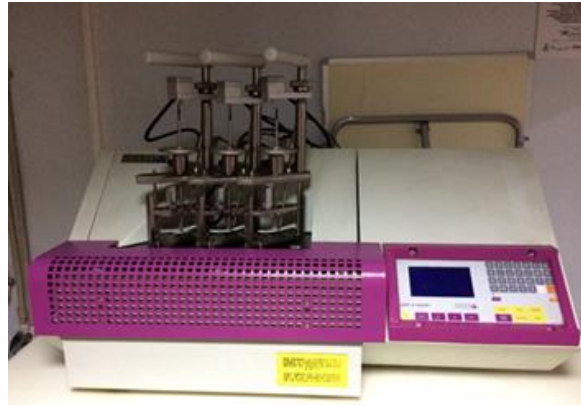
Fig. 10. Heat Deformation (HDT) Testing Machine.

The density test performed to determine the weight of the plastic materials in the unit volume and to determine the density. The tests conducted in accordance with the ISO 1183 test standard with the precision scale RADWAG WAS 220/X model density kit. The Density test device shown in Figure 11.
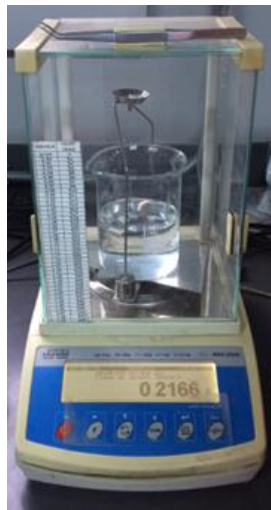
Figure 11. Density Measuring Device.

3.Results and Discussion

It is especially important to know and determine the mechanical and thermal properties of this material before choosing and using any material. In this study, a homogeneous mixture of the new composite material mixed homogeneously with a double-acting extruder, and the production of the prototype conducted by injection production method. For each test, experiments conducted on three distinct products and their average values taken. The Izod Impact Test results for determining the mechanical properties of unadulterated polypropylene and newly created composite material shown in Table 1 and Table 2.

Table 1. Pure PP Samples Izod Test Results.

Test	Material Measurements (mm)	Spent Energy of the Hammer (Joule)	Izod Result(kj/m²)
1	100x10x4	0.087	3.012
2	100x10x4	0,094	3.043
3	100x10x4	0.092	3.035
Average	-	*0.091*	*3.030*

Table 2. Izod Test Results of Composite Samples.

Samples	Material Measurements (mm)	Spent Energy of the Hammer (Joule)	Izod Result(kj/m²)
Recycled PP	100x10x4	0.091	3.030
PP+ Graphene	100x10x4	0.0156	5.136
PP+ Graphite	100x10x4	0.119	4.132
PP+ Nano carbon	100x10x4	0.108	3.750

Izod impact test used to determine the mechanical properties of materials operating under conditions that may cause brittle and fracture. In general. the purpose of the Izod Impact Test is to determine the amount of energy required for materials to break under dynamic stresses. as well as the ductility and brittle transition temperature [10].

In this study. three different Polypropylene composite samples used. The average of the test results taken. and according to the Izod test result of the new composite sample. there was an increase of approximately 70% in graphene-reinforced composite material. 42% in graphite-reinforced composite material. and 24% in nano carbon-reinforced composite material.

Tensile-Rupture test allows determining the shape change that will occur over time when determining the force that must applied to cause a certain shape to change in the material or when a certain force applied to the product [17]. This mechanical test is significant in engineering [13]. The results of the Tensile strength test shown in Table 3, and it shown in Table 4.

Table 3. Tensile Strength Test Results of the Pure PP Samples.

	Tensile Strength (MPa)	Yield Strength (MPa)	Modulus of Elasticity (MPa)	Elongation at Yield (mm)	Elongation at Break (mm)
Test 1	27.96	23.13	1410.9	3.85	17.27
Test 2	27.22	23.22	1965.8	3.33	14.84
Test 3	27.50	23.88	1639.5	3.57	15.93

Average	27.56	23.41	1672.06	3.58	16.01

Table 4. Tensile Strength Test Results in composite material test sample

Samples	Tensile Strength (MPa)	Yield Strength (MPa)	Modulus of Elasticity (MPa)	Elongation at Yield (mm)	Elongation at Break (mm)
Recycled PP	27.56	23.41	1672	3.58	16.01
PP+ Graphene	30.504	26.228	1510.9	3.33	7.93
PP+ Graphite	29.079	25.889	1900.6	3.36	8.97
PP+ Nano carbon	28.156	24.331	1909.8	3.63	9.85

In the tensile test. an increase in the elasticity modulus of the new composite material occurred. According to the tensile test results. in tensile strength values. there was an increase of 11% in graphene-reinforced composite material. 5% in graphite-reinforced composite material. and 2% nano carbon-reinforced composite material. According to these results. it shows the result that the strength values increase. but the shape change forced.

Shore-A test method used for soft polymers such as tires. and Shore-D test method used for other polymers [18]. Shore-D test results given in Table 5 and Table 6.

Table 5. Shore-D Test Result of Pure PP Test Samples.

Samples	Shore-D value
Test 1	69
Test 2	70
Test 3	67
Average	68.66

Table 6. Shore-D Test Results of Composite Test Samples.

Samples	Shore-D value
Recycled PP	68.66
PP+ Graphene	71.12
PP+ Graphite	70.42
PP+ Nano carbon	69.45

Shore-D testing has performed on three different samples s and there has been an increase of about 1.5% in the composite material. i.e., hardening. The density test results are shown in Table 7 and Table 8. According to the test results. there was not much change in the densities of unadulterated PP and composite material.

Table 7. Density Test Results of Pure PP Samples.

Material	Density gr/cm3
Test 1	0.89
Test 2	0.90
Test 3	0.89
Average	*0.89*

Table 8. Density Test Results of Composite Samples.

Samples	Density gr/cm3
Recycled PP	0.89
PP+ Graphene	0.92
PP+ Graphite	0.91
PP+ Nano carbon	*0.90*

Thermal tests are test methods used to determine the lowest and highest temperatures in which the product will be used and to determine properties such as melting temperature. thermal permeability. thermal expansion. decomposition temperature about the materials [22]. MFI test. which is one of the thermal properties. measures the mass or volumetric amount of polymer material flowing from a nozzle with a specified length and known cross-sectional area under certain temperature and loading conditions [12]. MFI test results are shown in Table 9 and Table 10.

Table 9. MFI Test Results of Unadulterated PP Samples.

Material	MFI Result (g/10min)
Test 1.	3.1
Test 2.	3.2
Test 3.	3.1
Average	3.13

Table 10. MFI Test Results of Composite Samples

Samples		MFI Result (g/10min)
Recycled PP		3.13
PP+ Graphene		3.51
PP+ Graphite	3.33	

In the study, three different measurements made and the average of them taken. The viscosity of the new composite material has also been increasing. This also provides a disadvantage in the production of complex structured materials produced by injection molding. New composite materials provide more advantages in 3D printers and as a production method by extrusion. HDT is used to determine the temperature of plastic. durable rubber. nylon insulation materials. reinforced composite and high-strength thermosetting and thermoplastic softening point and temperature determination [11]. HDT test results indicated in Table 11 and Table 12.

Table 11. HDT Result of the Additive PP Samples.

Test	1. Station		2. Station		3. Station	
	Deep (mm)	Temperature (°C)	Deep (mm)	Temperature (°C)	Deep (mm)	Temperature (°C)
1	0.01	26.2	0.01	26.9	0.01	27.1
2	0.04	28.3	0.04	28.5	0.04	29.6

3	0.07	30.0	0.07	31.2	0.07	32.3
4	0.10	32.1	0.10	33.4	0.10	33.1
5	0.13	33.0	0.13	34.9	0.13	34.8
6	0.17	35.2	0.17	35.7	0.17	35.9
7	0.20	36.3	0.20	37.6	0.20	37.8
8	0.23	37.8	0.23	38.5	0.23	38.8
Average	*0.118*	*32.3*	*0.118*	*33.3*	*0.118*	*33.6*

Table 12. HDT Result of Composite Samples.

	1. Station		2. Station		3. Station	
Samples	Deep (mm)	Temperature (°C)	Deep (mm)	Temperature (°C)	Deep (mm)	Temperature (°C)
Recycled PP	0.11	32.3	0.11	33.3	0.11	33.6
PP+ Graphene	0.11	53.11	0.11	53.12	0.11	53.11
PP+ Graphite	0.11	38.71	0.11	38.53	0.11	38.91
PP+Nano carbon	0.11	34.92	0.11	34.13	0.11	35.12

In the study. eight different measurements were made at three stations and the average of the results of these measurements was calculated. Graphene-reinforced composite material increased by 64%. graphite-reinforced composite material increased by 19%. and nano carbon-reinforced composite material increased by 9%. The bending resistance of the new composite material against heat has increased.

In the literature studies [6], according to Izod impact test results, it was observed that the fracture energy increased by 5% in the polyester resin and 0.004% graphene composite material, and when 0.2% graphene was added, the mechanical properties of the new composite material increased by 86% compared to the resin polyester. These data were compatible with our composite material.

In another literature study [2], the deterioration temperature of 0.1% graphene reinforced Polystyrene composite material was observed to be 382 °C, the graphene ratio was observed to be directly proportional to the deterioration temperature and the mechanical properties of the material, and it was observed that the hardness values of the graphene reinforced Polystyrene composite material decreased with the graphene ratio. This led to the conclusion that our study is compatible with the literature.

4. Conclusions

In this study. a composite material formed by adding graphene. graphite and nano carbon material to PP material at a rate of 1-2%. Homogeneous mixture made with two screw extruders. Prototype standard plate tensile test rods have produced on the injection machine. According to the experimental test results, it has been observed that there is an increase in the mechanical properties of the composite material, and it has been observed that there is an increase in the thermal properties of the composite material. We can say that it is positive for test samples produced by extrusion method for 3D printers due to the increase in viscosity of new composite materials.

Acknowledgements

References

[1] T. Dombrowski, "Nano carbonate minerals in wood polymer composites (WPC)". The Chancing Technology in WPCs. The First World Congress on Woodfibre /*Plastics and Related Composites*. San Francisco. CA. pp. 45-60. 2006.

[2] K. Gündoğan, D. Karaağaç, (2020). Grafen Takviyeli PS Kompozitlerinin Yapisal, Isil Ve Mekanik Özelliklerinin İncelenmesi. *Bilge International Journal of Science and Technology Research*, 4(1), 21-26. https://doi.org/10.30516/bilgesci.640084

[3] M.C. Şenel, A. Taşkin, M. Demir, M. Gürbüz, (2024). İndüksiyonla sıcak işlemin Si3N4 ve grafen takviyeli Al6061 matrisli kompozitlerin mekanik ve tribolojik özelliklerine olan etkisi. *Gazi Üniversitesi Mühendislik Mimarlık Fakültesi Dergisi*, 39(3), 1567-1582. https://doi.org/10.17341/gazimmfd.1226420.

[4] T. Türkoğlu, S. Çelik, N. Aslan, E. Atik, (2023). The effect of processing parameters on the wear properties Al6061/GNP composites produced by hot pressing. *Balıkesir Üniversitesi Fen Bilimleri Enstitüsü Dergisi*, 25(1), 1-12. https://doi.org/10.25092/baunfbed.1120301

[5] I. Sudarisman, J.N. Davies, H. Hamada, "Compressive failure of unidirectional hybrid fibre-reinforced epoxy composites containing nano carbon and silicon carbide fibres ". *Composites*. 38:1070-1074. 2007.

[6] A.Subaşi, M. Zurnaci, M. Kahyaoğlu, and E. Demir, "Polyester/Grafen Kompozitlerin Mekanik ve Termal Özelliklerinin İncelenmesi", *ECJSE*, vol. 4, no. 3, pp. 472–481, 2017, doi: 10.31202/ecjse.327707.

[7] G. Hatipoğlu, H. Ünal, S.H. Yetgin, (2023). Karbon Fiber Takviyeli Poli-fital-amit (PPA) Kompozit ve Saf PPA Polimerinin Tribolojik Özelliklerinin Karşılaştırılması. *Gazi University Journal of Science Part C: Design and Technology*, 11(3), 744-755. https://doi.org/10.29109/gujsc.1288917

[8] M. Kam, A. İpekçi, and Ö. Şengül, 2023. Investigation of the effect of FDM process parameters on mechanical properties of 3D printed PA12 samples using Taguchi method. *Journal of Thermoplastic Composite Materials* 36, 1, 307–325.

[9] Ö. Şengül, C. Tugaytimur, M. Şeremet, Experimental investigation of Mechanical and Thermal properties of polyethylene- Graphane-Reinforced Composites. (05.09.2019 -07.09.2019). *Yayın Yeri: International academic research congress (INES 2019)*.

[10] H. Demirer, et al. "Polipropilenin Eğilme Özelliklerine Geri Dönüşümlü EPDM Boyutlarının Etkisi." *European Journal of Science and*

Technology 15 .381–386. 2019.

[11] İ. Kartal, G. Naycı and H. Demirer, "Kestane Gürgen Talaşı Dolgulu Vinilester Kompozitlerin Mekanik Özelliklerinin İncelenmesi." *Avrupa Bilim ve Teknoloji Dergisi*. no. 16. pp. 723–728. 2019.

[12] H. Ünal, S. Yetgin, V.F. Ünal, (2023). Kati Yağlayici Olarak Grafit Katkili Naylon 6 Kompozitlerin Mekanik Ve Tribolojik Performanslari. *Kahramanmaraş Sütçü İmam Üniversitesi Mühendislik Bilimleri Dergisi,* 26(4), 853-865. https://doi.org/10.17780/ksujes.1300407

[13] H. Demirer, İ. Kartal, and A.Yildirim, "The Utilisability of Ground Hazelnut Shell as Filler in Polypropylene Composites." *Presented at the 7. International advances in applied physics and materials science congress*. 2017.

[14] A. Şahin, H. Çinici, E. Mermer, (2023). Bor Elyaf Takviyeli Polimer Kompozit Malzemelerin Termal Özelliklerine Nano Bor İlavesinin Etkileri. *International Journal of Engineering Research and Development*, 15(1), 82-90. https://doi.org/10.29137/umagd.1133717

[15] R. Karslıoğlu, M. Akçil, M. Uysal, G. Bağdatlı , A. Alp and H. Akbulut. "Sıcaklık değişiminin akım sinterleme yöntemi üretilmiş Zn-Al/SiC/Gr hibrit kompozitlerin mikroyapı ve fiziksel özelliklerine etkisi*". Gazi Üniversitesi Mühendislik Mimarlık Fakültesi Dergisi*. vol. 38. no. 4. pp. 2339-2346. Apr. 2023. doi:10.17341/gazimmfd.847323

[16] M.Y. Yazici, (2023). The Effect of Phase Change Temperature of Graphite Matrix Composite on Small-Scale Li-Ion Package Performance Under Square Wave Load. *Yüzüncü Yıl Üniversitesi Fen Bilimleri Enstitüsü Dergisi*, 28(2), 651-666. https://doi.org/10.53433/yyufbed.1175411

[17] M. Gürbüz, T. Mutuk, (2019). Karbon Esaslı Malzeme Takviyeli Titanyum Kompozitler ve Grafen Üzerine Yeni Eğilimler, *Mühendis ve Makina*. 60 (695). 101-118. Retrieved from https://dergipark.org.tr/en/pub/muhendismakina/issue/48382/612537.

RESEARCH ARTICLE

Comparative analysis of machine learning techniques for detecting potability of water

Vahid Sinap[a,*]

[a]Ufuk University, Faculty of Economics and Administrative Sciences, Department of Management Information Systems, 06805, Ankara, Türkiye,
ORCID: 0000-0002-8734-9509

Abstract

This research aims to evaluate the effectiveness of machine learning algorithms in determining the potability of water. In the study, a total of 3276 water samples were analyzed for 10 different features that determine the potability of water. Besides that, the study's consideration is to evaluate the impact of trimming, IQR, and percentile methods on the performance of machine learning algorithms. The models were built using nine different classification algorithms (Logistic Regression, Decision Trees, Random Forest, XGBoost, Naive Bayes, K-Nearest Neighbors, Support Vector Machine, AdaBoost, and Bagging Classifier). According to the results, filling the missing data with the population mean and handling outliers with Trimming and IQR methods improved the performance of the models. Random Forest and Decision Tree algorithms were the most accurate in determining the potability of water. The findings of this research are of high importance to sustainable water resource management and serve as a crucial input for the decision-making process on the quality of water. The study also offers an example for researchers working on datasets that contain missing values and outliers.

* Corresponding author. Tel.: +90-312-586-7378.
  E-mail address: vahidsinap@gmail.com

1. Introduction

Water is an essential resource for sustaining life. Regular monitoring of water quality is important for the health of ecosystems and the human population [1]. Potable water is the water quality that is mainly used for drinking, cooking, and hygiene practices [2]. This water has been stripped of toxic substances and microorganisms through different cleaning and treatment processes. Water is not only a liquid that a human being needs to drink for them to survive. It is also an invaluable commodity in the agricultural, manufacturing, and power generation sectors. So, the safeguarding of water standards is indispensable not only for the health of the people but also for the economic and ecological sustainability [3]. Besides that, some medical practices like kidney dialysis and lens cleaning may require the use of higher quality water. At this point, the protection and monitoring of water quality becomes even more important.

A high-quality drinking-water-supply system greatly enhances people's life quality, whether in small or large towns. The most apparent gain weights the reduction of illnesses caused by polluted water for these initiatives to gain success. Diarrhea, cholera, and typhoid are quite common in rural areas so the availability of clean drinking water can minimize them [4]. In addition, easier access to safe water contributes to the healthy growth and development of children, increasing school attendance rates and expanding educational opportunities. In economic terms, access to safe water supplies allows agricultural and industrial activities to be more efficient and sustainable [5]. This contributes to the development of the local economy. In addition, easier access to clean water resources encourages people to use environmentally friendly water. In this way, natural resources are protected. Increasing access to safe water positively affects the overall well-being, health, and environmental sustainability of a society [6].

Considering the importance of water for life on earth, access to clean drinking water is an important health and development issue at global, national, and local levels. Investments in water supply and sanitation also provide economic benefits through reduced risk of disease and lower health expenditures. This applies to large-scale investments in water supply infrastructure as well as domestic water treatment methods. To protect water quality, supply risks should be assessed, and a comprehensive strategic plan should be developed [7]. This strategy includes the systematic assessment of water-related risks at all stages from the point of supply to the consumer and the development of solutions to mitigate these risks. Several techniques are used to ensure daily assessment of water quality. These techniques analyze the chemical, physical and microbiological properties of water and assess its compliance with drinking and potable water standards [8].

The measurement of dissolved oxygen is essential for the aquatic life among chemical analyses. A low level of dissolved oxygen results in a dangerous situation for aquatic life. The pH meter is among the important monitoring apparatus of drinking water and healthy ecosystems as it can tell if the water is acidic, neutral or alkaline [9]. The TSS test is used to determine the mass of total solids in water and then the number of solids which are either filtered or unfiltered is also determined [10]. Heavy metal analysis is aimed at finding out whether the water has lead, mercury, and arsenic which are some of the harmful heavy metals [11]. With regard to the physical dimension of analysis, there are methods that are used to measure the color and odor properties of water. Color and odor are the direct indicators of the organic and inorganic pollutants, respectively [12]. Temperature measurement is another parameter besides others that can be used to determine ecosystem health as it influences biological activities [13]. Suspended matter refers to the measurement of the number of suspended solid particles in water [14]. Furthermore, microbiological analyses are carried out to check the drinking water quality too. The coliform bacteria that are the indicators of fecal pollution are a big piece of information for the potability of the water. Among the methods used are the analyses of enterococci and Escherichia coli (E. coli) which are the indicators of microbiological pollution in water [15].

Among water quality measurement methods that are currently in use, some have certain advantages as well as some limitations. These methods, in general, operate only on water samples that are collected at a specific moment in time. But then it can be said that water quality is a constantly changing phenomenon. Thus, water quality can be

influenced by many factors such as seasonal changes, weather conditions, and the human impact on the environment [16]. These methods have their limitations in reflecting the instantaneous water quality changes. On the contrary, most of the techniques used for water quality measurement are exorbitantly priced and consume a lot of time. The length of the time and the number of resources required for the whole process of the collection, transportation, and analyzing the water samples for laboratory analysis is considerable [17]. This causes a lot of problems when trying to keep the water quality monitoring system operating continuously and everywhere. Besides that, the water quality measurement techniques used in the past only dealt with samples that were collected at specific points or within certain areas [18]. This makes it impossible to detect local discrepancies in water quality and carry out comprehensive studies over large areas. The other limitation is that traditional methods of analysis tend to focus on a restricted number of parameters and also have limitations in measuring a wider range of parameters [19]. Consequently, these strategies are potentially ineffective in spotting the situations that require prompt help. In order to solve these problems, artificial intelligence (AI) methods are being implemented.

Machine learning's superiority over traditional methods in water quality monitoring is due to the fact that it can use continuous monitoring, large-scale data collection and rapid analysis. Machine learning is the one which employs a more progressive and flexible procedure than the classical ones. Traditional methods are limited in the ability to effectively capture the dynamic changes of the water quality because they get samples at some specific time points [17]. Machine learning techniques can detect sudden spikes of pollution in water, and as a result, monitoring can be done without involving humans [20]. In addition, machine learning is the procedure to follow when it comes to the collection of large-scale data. Instantaneous data streams from extensive geographical areas can be attained through sensors, cameras, and data collection tools [21]. Then the possibility of total monitoring of water quality and comparing quality differences between different regions in detail comes to the surface. Beyond that, machine learning has the capacity to analyze data and thus detect water quality changes quicker than laboratory tests [22]. The unique feature of machine learning is that it can both identify a definite pattern in the water quality and also adjust to environmental changes. This capacity can be employed to find the possible sources of pollution and constantly improve the water quality. The blending of machine learning and remote sensing techniques provides a huge benefit for water quality remote monitoring [23]. The remote sensing data collected from satellite and sensor networks can be processed by machine learning algorithms to get a complete picture of the water quality.

Along with the important benefits of machine learning techniques, there are also some challenges in the case of their usage. Datasets utilized for water quality monitoring are usually very complex and voluminous. Machine learning algorithms suffer from two main problems: firstly, the data may be incomplete or inaccurate, and secondly, the integrity of the data may be compromised. Moreover, the relevant parameters concerning water quality can be very different and hence be required to be checked together for many parameters. The combination of this result with the complexity of the model often leads to the problem of feature selection. The first series of data preprocessing steps is the remedy to these challenges. Moreover, a technique that is particularly developed for feature selection or dimensionality reduction should be utilized to easily cope with the multiple parameters.

In this paper, nine different classification algorithms were used to determine water quality and potability and performance comparisons were made. The methods under consideration are Logistic Regression (LR), Decision Trees (DT), Random Forest (RF), Gradient Boosting Decision Tree (XGBoost), Naive Bayes (NB), K-Nearest Neighbors (KNN), Support Vector Machine (SVM), AdaBoost (ADA) and Bagging Classifier (BAG). The performance of each algorithm is considered in detail in the report for the water quality problem. Apart from this, a major topic of discussion in the paper is the problems machine learning techniques face in water quality assessment as stated in the literature. The research study, however, deals with the performance of machine learning algorithms on water potability analysis, which is too little, and there is a lack of studies in the literature focusing on the performance difference with regard to outlier treatment methods. To overcome these challenges and the lack of knowledge in the literature, we discuss the relationship between different strategies such as feature engineering, outlier detection and processing, data normalization and standardization, and missing values evaluation used in the data preprocessing stages and their effect on the performance of the algorithms. These modern techniques will help

to make the datasets used in the process of water quality monitoring better and the machine learning models more accurate and reliable.

The performance comparisons in the paper provide important insights for decision makers, researchers, and practitioners in the field of water quality monitoring and management. The aim of these analyses is to direct the right choice of algorithms in machine learning so that water resources could be saved and managed more efficiently. The data preprocessing steps in the paper are meant to be a guide to show how to analyze large, multi-parametric, and dynamic datasets.

2. Related work

The literature contains some significant studies focused on water quality classification based on the application of machine learning algorithms. One study conducted using AI techniques in Tayra River in Southwest Iran to predict water quality components showed positive results, using ANN and SVM algorithms. The findings indicated that SVM was the most precise in the aspect of water quality prediction [25]. Another study by [26] developed machine learning algorithms for water quality classification to control water pollution. The three algorithms SVM, KNN and NB were used on a dataset comprising of 7 parameters. Out of the methods used, SVM algorithm recorded the highest accuracy in predicting the water quality. In a study by [27], a dataset with pH, dissolved oxygen, biological oxygen, and electrical conductivity parameters was used to verify the water quality assessment models. Machine learning algorithms such as SVM, DT, and NB were administered in the research. The evaluation results indicated that the DT algorithm had the highest accuracy. Besides, the study done by [28] also confirmed that the DT algorithm was the most successful algorithm with the same result. The performance of classification algorithms was analyzed to classify and compare the water quality of Kinta River in Perak Malaysia. NB, J48, and BAG were the algorithms that were used. NB was the best of the three models [29].

[30] sought to uncover the relationship between agricultural chemicals and the Salton Sea's water quality degradation over time. Regression and machine learning algorithms including linear regression, random forest, SVM, and Long Short-Term Memory (LSTM) were employed for the estimation of salinity and other parameters. LSTM was utilized here as it provided flexibility and accuracy in its output and was a major factor in the management of freshwater.

[31] had a goal of using machine learning algorithms such as SVR and XGBoost to predict water quality factor and assess the accuracy of those algorithms. The two algorithms were used to forecast nine separate factors with the accuracies in the range of 79% to 99%.

[32] proposed an innovative technique of water quality forecasting which is a Long Short-Term Memory Neural Network (LSTM NN). For training, the monthly mean values of the water quality indicators of Lake Taihu from 2000 to 2006 were used. The method was compared with other techniques and the results showed that the LSTM NN outperformed the Back Propagation Neural Network (BP NN) and Online Sequential Extreme Learning Machine (OS-ELM) in water quality prediction.

[33] focused on the use of AI techniques for the optimization of the water supply and sanitation systems, the control of the water quality standards compliance and the efficient operation of monitoring drinking water for the sustainable, environmentally friendly use. As for the study, the adaptive neuro-fuzzy inference system (ANFIS) algorithm was then used for WQI (water quality index) prediction and feed-forward neural network (FFNN) and KNN (K Nearest Neighbor) algorithms for water quality classification. The results showed that ANFIS model was the most precise in predicting the values of WQI with an accuracy of 96.17%, while the FFNN algorithm completely classified water quality data with 100% accuracy. The research revealed that the advanced AI technique proposed by the research team can immensely help in the activities of water treatment and management.

[34] aimed at employing a very sophisticated AI algorithm to approximate and assess water quality. The study set up models for WQI prediction and classified water quality using the artificial neural networks (NARNET and LSTM) for WQI prediction and SVM, KNN, and NB for WQC prediction. The dataset consisted of seven main

parameters and the models were evaluated according to statistical criteria. The results indicated that NARNET slightly outperformed LSTM in WQI prediction, whereas SVM gained the best accuracy (97.01%) for WQC prediction. Both NARNET and LSTM had almost the same accuracy when testing, with a small difference in regression coefficients.

[35] proposed a feature selection method that combines the weighted entropy and the Pearson correlation coefficient to estimate the water quality. This approach developed the prediction to be more precise and secure by taking into consideration the information content and the feature correlation. They examined various machine learning algorithms for the water quality prediction and found out that SVM was the one that performed well in the DO prediction, while MLP was the one that was successful in the nonlinear modelling. The RF and XGBoost methods were quite weak, but the LSTM method was very good at capturing dynamic patterns.

[36] aimed to predict WQI and Water Quality Classification (WQC) using machine learning models. They optimized parameters for models like RF, XGBoost, and others. Data preprocessing included mean imputation and normalization. The dataset had 7 features and 1991 instances. GB model achieved 99.50% accuracy in WQC prediction, while MLP regressor model had 99.8% R2 for WQI prediction, outperforming other models.

[37] aimed to predict river water quality and categorize the WQI based on water quality standards using machine learning models. Data from eleven sampling stations along the Bhavani River were used, considering 27 parameters. MLP regressor predicted WQI efficiently with a root mean squared error of 2.432, and MLP classifier classified the WQI with 81% accuracy.

[38] utilized machine learning models to predict total dissolved solids (TDS), sodium absorption ratio (SAR), and total hardness (TH) in the Karun River. Models included multiple linear regression (MLR), M5P model tree, support vector regression (SVR), and random forest regression (RFR), with principal component analysis (PCA) for variable reduction. Results showed RFR, SVR, and MLR had the lowest errors in predicting TDS, SAR, and TH, respectively, indicating the effectiveness of machine learning models in water quality prediction.

[39] emphasized the importance of water quality prediction due to water pollution's increasing impact. They developed a model using machine learning algorithms to predict the WQI and quality class based on four parameters: temperature, pH, turbidity, and coliforms. Multiple regression algorithms are effective in predicting WQI, while ANN is the most efficient in classifying water quality.

[40] focused on developing deep learning algorithms to predict WQI and WQC. They used the long LSTM algorithm to predict WQI and a convolutional neural network (CNN) for WQC. The study considered seven water quality parameters: DO, pH, conductivity, biological oxygen demand (BOD), nitrate, fecal coliform, and total coliform. Experimental results demonstrated that LSTM predicted water quality with superior robustness, achieving a 97% accuracy in WQI prediction.

[41] developed a machine learning model using adaptive boosting to evaluate drinking water quality. They used a Kaggle dataset and experimented with different machine learning techniques, finding that their ensemble model achieved 96.4% accuracy, outperforming individual models like LR (88.6%), CHAID (93.1%), XGBoost tree (94.3%), and multi-layer perceptron (95.3%).

Table 1 summarizes the key studies, the algorithms used, the datasets or parameters involved, and the results obtained.

Table 1. Summary of studies on water quality classification.

Study	Algorithms used	Parameters/Dataset	Best algorithm	Accuracy/Result
[25]	ANN, SVM	Tayra River, Iran	SVM	SVM gave the most accurate results
[26]	SVM, KNN, NB	Dataset with 7 parameters	SVM	Highest accuracy in water quality prediction
[27]	SVM, DT, NB	pH, DO, BOD, EC	DT	DT achieved the highest accuracy

Study	Algorithms used	Parameters/Dataset	Best algorithm	Accuracy/Result
[28]	DT	-	DT	DT was the most successful algorithm
[29]	NB, J48, BAG	Kinta River, Malaysia	NB	NB was the best model
[30]	LR, RF, SVM, LSTM	Salton Sea, USA	LSTM	LSTM provided flexible and accurate predictions
[31]	SVR, XGBoost	Various water quality factors	-	Success rates ranging from 79% to 99%
[32]	LSTM NN	Taihu Lake, China	LSTM NN	Outperformed BP NN and OS-ELM
[33]	ANFIS, FFNN, KNN	Water supply and sanitation systems	ANFIS (WQI), FFNN (classification)	ANFIS: 96.17%, FFNN: 100% accuracy
[34]	NARNET, LSTM, SVM, KNN, NB	7 parameters	NARNET (WQI), SVM (WQC)	NARNET outperformed LSTM, SVM achieved 97.01%
[35]	SVM, MLP, RF, XGBoost, LSTM	Feature selection with entropy weighting and Pearson correlation	SVM (DO), MLP (nonlinear), LSTM (dynamic patterns)	-
[36]	RF, XGBoost, GB, MLP	7 features, 1991 instances	GB (WQC), MLP (WQI)	GB: 99.50%, MLP: 99.8% R2
[37]	MLP	Bhavani River, India	MLP	RMSE: 2.432, accuracy: 81%
[38]	MLR, M5P, SVR, RFR	Karun River, Iran	RFR (TDS), SVR (SAR), MLR (TH)	-
[39]	Multiple regression, ANN	4 parameters: temperature, pH, turbidity, coliforms	ANN	Effective for classifying water quality
[40]	LSTM, CNN	7 parameters: DO, pH, conductivity, BOD, nitrate, fecal coliform, total coliform	LSTM	LSTM: 97% accuracy in WQI prediction
[41]	LR, CHAID, XGBoost, MLP, adaptive boosting	Kaggle dataset	Adaptive boosting	96.4% accuracy

In general, most previous studies have focused on sea or river water classification, and their impact on drinking water and the importance of variables have not been sufficiently examined. Since drinking water is of vital importance, especially for human life, it is evaluated under more diverse parameters. Therefore, classifying drinking water quality is seen as a more challenging task. Moreover, the target class that studies try to predict is usually based on the WQI value. This study, on the other hand, directly tries to predict the potability or non-potability of water. Furthermore, none of the studies have focused on the effect of outliers on the performance of machine learning algorithms. This study will focus on different outliers processing methods and examine their impact on machine learning algorithms.

3. Material and methods

In this section, explanations of the machine learning algorithms used in the research, the performance criteria used in the comparison of the algorithms, the characteristics of the dataset and information about the data preparation process are given.

3.1. Algorithms used

Machine learning is a sub-branch of AI and involves computers making intelligent decisions by learning from data [42]. Machine learning uses various methods depending on the nature of the data and the objectives of the features. Among these methods, three approaches can be singled out such as supervised learning, unsupervised learning, and reinforcement learning. Supervised learning is an approach that has the machine learning model to come to terms with the relationship between the input and the target output [43]. Supervised learning can be classified basically into two types: classification and regression. The purpose of classification is to find out if an input belongs to a given category. Regression deals with the continuous numerical output of a prediction related to the input data. In this research, the context is given to using supervised classification algorithms for water quality assessment. Classification of water quality is done through a physical, chemical, and biological inspection of water samples. Through this assessment, the potential of the water is decided.

Algorithms for supervised classification could title the samples in a short time using the information from the historic data [44]. This is a feature that makes it possible to quickly and correctly classify the water samples collected in the water quality assessment. Water quality assessment plays a critical role in water resource protection and environmental sustainability. Therefore, it is foreseen that using machine learning algorithms will contribute to the creation of a powerful system for the effective assessment of water quality and protection of water resources.

3.2. Supervised classification algorithms

In this study, a total of nine supervised classification algorithms were used for water quality assessment. These algorithms include Logistic Regression, Decision Trees, Random Forest, XGBoost, Naive Bayes, K-Nearest Neighbors, Support Vector Machine, AdaBoost and Bagging Classifier.

3.2.1. Logistic regression

LR is a statistical modelling technique and is used to estimate the probability of a two-category dependent variable. LR is a widely used technique, especially in classification problems. LR limits linear regression by using the logit transformation of the probability distribution [45].

The mathematical formula of LR is given in Equation 1. When the equation is analyzed, $P(Y=1)$ represents the probability that the dependent variable is 1. e is the Euler number and the coefficients b_0, b_1, b_2, ... b_k are the parameters estimated by the model. X_1, X_2, ... X_k are the independent variables.

$$P(Y = 1) = \frac{1}{1 + e^{-(b_0 + b_1 X_1 + b_2 X_2 + \ldots + b_k X_k)}} \tag{1}$$

3.2.2. Decision trees

DT algorithm, as a machine learning method, is used to classify or regress a dataset by dividing it according to features. The algorithm first creates a tree structure. Each internal node is associated with a feature in the dataset and each leaf node is associated with a class. The tree divides the dataset into homogeneous subsets and makes predictions in this way [46]. DT use various criteria to select features that best summarize the information in the data. These criteria include concepts such as entropy, gain ratio and Gini index [47].

3.2.3. Random forest

RF is a machine learning algorithm used to solve classification and regression problems. This algorithm is constructed by combining multiple decision trees. Each decision tree is used to generate randomly selected subsets (bootstrap samples). RF aims to create more reliable and accepted models by taking the prediction of the majority of these trees. By training each tree on different subsets, the RF algorithm reduces overfitting and increases the generalizability of the model [48]. In addition, by averaging the predictions of each tree, the errors of the individual trees are balanced. Mathematically, the prediction formula of the RF algorithm is given in Equation 2.

$$\acute{Y} = \frac{1}{B} \sum_{j=1}^{B} f_i(X) \tag{2}$$

In the formula in Equation 2, $\acute{Y}$ is the predicted value, B is the number of trees, $f_i(X)$ is the prediction number j of each tree.

3.2.4. Gradient boosting decision tree

Gradient Boosting Decision Tree (XGBoost) creates a powerful forecasting model by successively adding decision trees. The first tree attempts to predict the dataset, and then an error correction process is performed on the errors of this tree, allowing the next tree to focus on them. This process continues by adding a series of trees, each tree correcting previous errors and improving the overall performance of the model. XGBoost learns iteratively, focusing on correcting the errors of the previous trees as each tree is added [49]. The formula of the XGBoost algorithm is given in Equation 3.

$$F(x) = \sum_{m=1}^{M} \gamma_m h_m(x) \tag{3}$$

In Equation 3, $F(x)$ is the total prediction model, M is the number of trees, γ_m is the learning rate of each tree and $h_m(x)$ is the prediction of each tree.

3.2.5. Naive bayes

NB works based on Bayes' Theorem and accepts the assumption of independence between features when classifying. This assumption states that the features are independent of each other, hence the name "naive" [50]. Basically, NB uses the probabilities of features to determine the class to which a data point belongs. Using these probabilities, NB makes predictions for each class and selects the class with the highest probability. The basic mathematical formula of NB is given in Equation 4.

$$P(C \mid X) = \frac{P(X \mid C) \cdot P(C)}{P(X)} \tag{4}$$

When the above equation is analyzed:

- $P(C \mid X)$ is the probability that a given class (C) is determined by the given feature set (X),
- $P(X \mid C)$ is the probability that the feature set (X) belongs to the given class (C),
- $P(C)$ is the probability of belonging to a given class (C),

- $P(X)$ is the probability of observing the feature set (X).

3.2.6. K-Nearest neighbors

The basic principle of the KNN algorithm is to use the influence of its k-nearest neighbors to determine the class or value of a data point. The algorithm measures the distances of each point in the dataset to each other according to their position in the feature space and then determines the class or value of a given data point by the label or value of its k-nearest neighbor [51]. The KNN algorithm uses measurement metrics such as Euclidean Distance or Manhattan Distance to measure the distances of data points. The user-specified value of k is determined interactively, and it is generally preferred that it is not an even number. The basic mathematical formula of KNN is given in Equation 5.

$$\acute{Y} = \text{argmax} \left(\sum_{i=1}^{k} I(y_i = j) \right) \tag{5}$$

In Equation 5, $\acute{Y}$ represents the predicted class, k represents the number of neighbours specified by the user, y_i represents the class of the i-th neighbor, and j represents the class index.

3.2.7. Support vector machine

The main purpose of the SVM algorithm is to classify data points into two or more classes using a hyperplane. SVM performs particularly effectively on datasets that cannot be separated linearly. The algorithm selects a hyperplane to classify data points and places this hyperplane in such a way as to maximize the margin between classes [52]. The mathematical formula of the algorithm is expressed in Equation 6.

$$f(x) = \text{sign}(\mathbf{w} \cdot \mathbf{x} + b) \tag{6}$$

In Equation 6, $f(x)$ represents the estimation function, $\mathbf{w}$ represents the weight vector, $\mathbf{x}$ represents the input feature vector, and b represents a constant term or plane.

3.2.8. AdaBoost

AdaBoost (Adaptive Boosting) is an ensemble learning algorithm for classification problems. ADA creates a strong classifier by combining weak learners together. Its basic principle is to iteratively strengthen the model by adjusting the weights of the examples in the dataset, focusing on the points where a learner is weak. In each iteration, the weight of the misclassified examples is increased so that the next learner focuses more on these examples [53]. The mathematical formulation of the algorithm is expressed in Equation 7.

$$F(x) = \sum_{t=1}^{T} \alpha_t f_t(x) \tag{7}$$

When Equation 7 is analyzed, $F(x)$ is the total prediction model, T is the number of iterations, is the weight of each learner, $f_t(x)$ is the prediction of each learner.

3.2.9. Bagging classifier

Bagging Classifier (Bootstrap Aggregating) is an ensemble learning algorithm used for classification problems. Its main goal is to create a more powerful and generalizable classifier by aggregating many weak learners trained on different subsets [54]. The algorithm trains each learner using different bootstrap samples (repeated sampling). In this way, learners trained on different samples increase the diversity of the model and reduce the risk of overfitting. BAG is based on weak learners such as SVM or KNN. Since each learner is trained on different subsets of the dataset, it contributes to making the model more general and stable [55].

3.3. Data validation method

In the context of water potability prediction, the k-fold cross-validation method was used. The dataset is divided into k parts and uses each of them as a test set respectively. The remaining k-1 parts are considered the training set. This is done k times, and all the parts are used once as a test set. The model performance is evaluated based on the average of the results.

In this study, the dataset is divided into 5 parts, which is a common practice in k-fold cross-validation where k is set to 5. The fiber count k is which intuitively assures computational efficiency and statistical robustness. When k=5, every fold has a data part that corresponds to 20%. This ensures that all the samples are diverse in all folds while still having enough data to train and test. In addition, 5-fold cross-validation method enables researchers to reliably estimate the model's performance on different subsets of the data and thereby assess its generalization capability. The flowchart of the model designed based on k-fold cross-validation is shown in Figure 1.
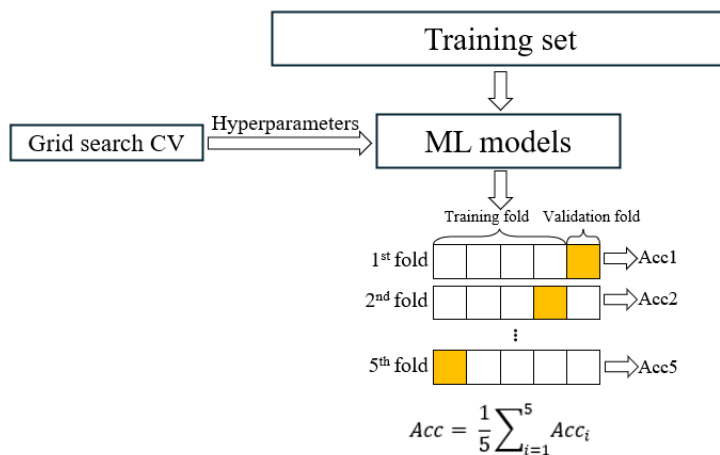
Fig. 1. K-fold cross-validation method.

3.4. Performance metrics

The process of checking the performance of machine learning models is extremely crucial to the process of building and putting models into practice. In this regard, performance metrics are utilized for the consideration and appraisal of model quality regarding the accuracy, precision, sensitivity, and performance of a particular model. The measures that are fundamental such as True Positives (TP), True Negatives (TN), False Positives (FP), and False Negatives (FN) provide metrics that help understand the model behavior characteristics and overall quality of model

results respectively. Additionally, techniques such as ROC curves, confusion matrices, and F1-Score can give a different view by combining various metrics. A thorough grasp of this data is of fundamental importance to the fact that the model is not only functioning well but is also very dependable.

3.4.1. Accuracy

Accuracy is the measure that reflects how close the prediction made by a classification model would be to the actual class. Thus, accuracy is the extent of the number of correct decisions to the total decision number [56]. The formula for calculating accuracy is expressed in Equation 8.

$$Accuracy = \frac{TP + TN}{TP + FP + TN + FN} \tag{8}$$

3.4.2. Precision

Precision is a measure of how many of the cases that a classification model predicts as positive are actually true positive. Precision is the ratio of false positive predictions to the total number of positive predictions. A high precision value indicates that the model's positive predictions are reliable, while a low precision value indicates a high rate of false positive predictions. This metric can be expressed using Equation 9 in its formula.

$$Precision = \frac{TP}{TP + FP} \tag{9}$$

3.4.3. Recall

Recall is a quality index that is used to find out how well the positive samples have been recognized by the model. Recall is the proportion of true positive predictions and total positive samples. A high recall value points to the fact that the model is very good at detecting positive instances. Recall formula is given in Equation 10.

$$Recall = \frac{TP}{TP + FN} \tag{10}$$

3.4.4. F-Measure/F1-Score

The F-measure or F1-score is a gauge utilized to determine the success of a classification model by fusing two measures of precision and recall. The F-measure, which combines these two measures at a balanced point, evaluates how well the model can both minimize the number of false positive predictions and accurately identify the true positives. F-measure is calculated by the following formula:

$$F1 = 2 * \frac{(precision * recall)}{(precision + recall)} \tag{11}$$

3.4.5. Receiver operating characteristic curve

Receiver Operating Characteristic (ROC) Curve a tool in graphical form is which used for assessment of model performance, particularly in classification problems. The ROC curve demonstrates the relationship between the probability of the correct classification (rate of recall) and the probability of the incorrect classification (rate of false positives). This is a means of determining whether the efficiency of the model is governed more by sensitivity or specificity. The ROC curve is a graph showing the effectiveness of the model when using various cut-off values. It goes from the corner where the perfect case is to the line at 45 degrees which is random guessing. A perfect model's ROC curve will rest in the upper left section of the graph, indicating that the true positive rate is high while the false negative rate is low [57]. The ROC curve has two inputs - True Positive Rate (TPR) and False Positive Rate (FPR). True Positive Rate (TPR) is determined the use of the Equation 12 given and whereas for False Positive Rate (FPR) the formula in Equation 13 is provided.

$$TPR = \frac{TP}{TP + FN} \tag{12}$$

$$FPR = \frac{FP}{FP + TN} \tag{13}$$

3.4.6. The area under the curve

The Area Under the Curve (AUC) can be considered as the measurement of the area under the ROC curve. AUC measures the model performance for various thresholds by looking at the size of the area under the ROC curve [58]. AUC can take on any value from 0 to 1. A high AUC value indicates that the model has a good trade-off between high true positives and low false negatives. This means that the model is quite skilled in classifying the data.

3.4.7. Area under the precision-recall curve

The Area Under the Precision-Recall Curve (AUPRC) is a metric that tells the degree to which a classification model strikes a balance between accuracy and recall. The Precision-Recall curve is showing an image of the model's precision and recall over the entire range of cut-off points. The trick is AUPRC, which is the process of measuring the model's performance at different cut-off points, and this is done by getting the area under the curve [59]. High AUPRC of the model shows its ability to pinpoint true positives as well as false positives which indicates that the learner is capable of detecting true positive predictions as well as true positives. AUPRC is a method that is mainly applied to imbalanced classification problems.

3.5. Dataset

In this research we utilized "Water Quality and Potability" dataset available online, a renowned dataset disseminated in the Kaggle platform. The accuracy of features in the dataset predicting the potability of water was verified by two faculty members working in Departments of Water Science Engineering consulting them. They stated that the samples in the dataset meet the standards of WHO (World Health Organization). The dataset consists of 3276 water samples and 10 features that provide essential information about the water quality parameters. These parameters include:

1. pH Value: Indicates the water's acidity or alkalinity, with values within WHO standards (6.52−6.83).
2. Hardness: Reflects the water's calcium and magnesium salt content, impacting its raw hardness.
3. TDS (Total Dissolved Solids): Reflects the water's mineralization, adhering to WHO limits (desirable: 500 mg/l, maximum: 1000 mg/l).
4. Chloramines: Result from ammonia added to chlorine for water disinfection, with safe levels up to 4 mg/L.
5. Sulfate: Naturally occurring in minerals, with concentrations within the 3–30 mg/L range in freshwater.
6. Conductivity: Reflects water's ion concentration, following WHO's 400 µS/cm limit.
7. Organic Carbon: Measures carbon content in water's organic compounds, complying with US EPA standards (< 2 mg/L).
8. THMs (Trihalomethanes): Found in chlorinated water, with levels within the safe limit of 80 ppm.
9. Turbidity: Reflects solid matter quantity in water, with values meeting WHO's recommended limit (0.98 NTU).
10. Potability: Binary indicator (1 for Potable, 0 for Not Potable), determining water's safety for human consumption.

Figure 2 shows the potability distribution of the water samples in the dataset. There is an imbalance in the target variable in the dataset. This should be taken into account in the modeling process. The imbalanced distribution of the target variable (Potable (1) or Not Potable (0)) requires a careful approach to avoid biasing the model towards the majority class.
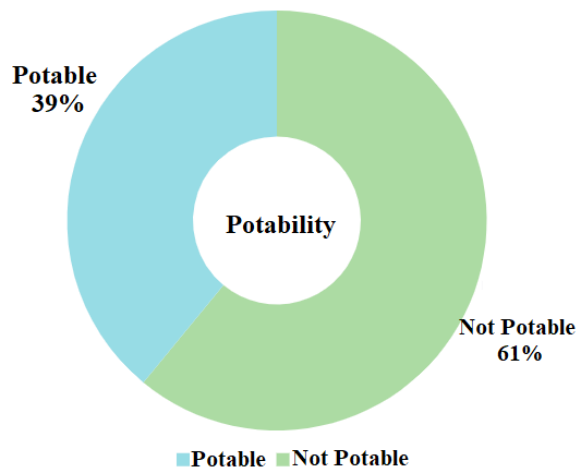
Fig. 2. Potability distribution of water samples in the dataset.

Figure 3 demonstrates the distribution of missing values across different features in the dataset. Notably, a significant number of missing values are observed in the 'ph', 'Sulfate', and 'Trihalomethanes' features. Missing values can negatively affect the accuracy and reliability of the model. Effectively handling these missing values and optimizing the dataset allows the model to learn more robustly and reliably. Solving the missing value problem relies on strategies such as selecting appropriate imputation methods or choosing algorithms that are sensitive to missing values.
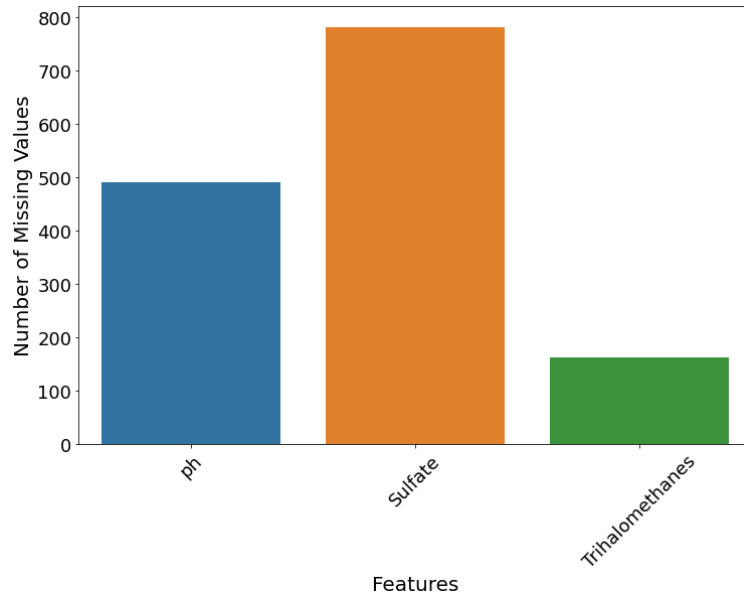
Fig. 3. Missing values in the dataset.

Figure 4 shows the correlation matrix of the dataset. According to the correlation matrix, there is no linear relationship between the features that can explain the target variable. Therefore, linear models may not be effective on this problem. Considering this situation, it would be more appropriate to experiment with probabilistic models. Such models can handle the complexity and relationships in the dataset in a more flexible way, and therefore solve the problem better.
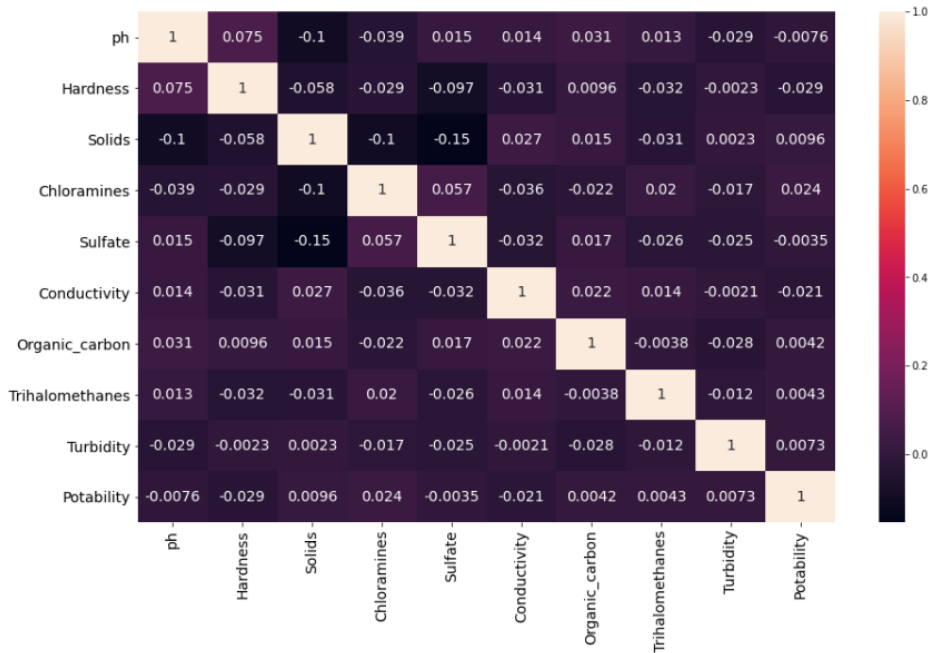
Fig. 4. Correlation matrix.

3.6. Data preparation

Data preparation is a fundamental step in the machine learning process and, when performed correctly, can significantly impact the performance of the model. In this context, three main topics come to the fore: the imbalanced structure of the dataset, missing values and outliers. In the research, the imbalance of the dataset was first addressed and resampling was performed. As the next step, missing values were identified and completed using appropriate imputation techniques. Then, outliers were identified, and solutions were generated with various methods. These three topics are discussed in more detail below.

3.6.1. Class imbalance reduction strategy

To address class imbalance, instances with values 0 and 1 in the 'Potability' column were treated separately. From the DataFrame of instances with value 0 ("zero") and a DataFrame of instances with value 1 ("one"), we found two instances. Resampling was then used to increase the instances of the minority class "one" to a larger size. Here, the technique used is to increase the number of instances in the minority class which is then used to balance the classes. Through this step, the samples of the minority class are randomly and accordingly selected and then this process is repeated. Ultimately, the resulting augmented minority class is put together with the majority class so that the new balanced DataFrame (the "df") can be created. This balancing technique seeks to enhance the model's performance through the equalization of the learning curves between the classes.

3.6.2. Review and processing of missing values

According to features like pH, Sulfate, and Trihalomethanes that were analyzed, missing values were detected. Missing values stand for data values that are not saved for certain observations in a dataset which can cause different problems in statistical analyses and modeling processes. In the case of the dataset being too correlative and the analysis being too confident, missing data can make the dataset incompletable and thus lower the quality, generalizability, and reliability of the results [61]. It can be a cause of such problems as analysis results and modeling accuracy becoming misleading and decision-making being faulted [62]. In turn, proper imputation methods and data preparation techniques should be adopted to effectively cope with missing data.

Since the missing values in the dataset used in this study were covered both classes, these missing values were taken as the population mean. The population mean is a statistical method that shows the sum of the values of a population divided by the population size [63]. Mathematically, the population mean (μ) is expressed as:

$$\mu = \frac{\sum_{i=1}^{N} X_i}{N} \tag{14}$$

This step adds a homogeneity level to the dataset. Thus, making the data more uniform by substituting missing values with population averages of estimates. Also, different statistical techniques for imputing missing data were used. In mean imputation, the absent values were replaced by the average of the whole dataset. Additionally, median and mode are used to finish off the missing entries. In case of median imputation missing values were replaced with the median. The median is the middle number when the numbers are arranged in order. If the mode imputation was employed, the missing values would be replaced by the mode which is the most common value in the dataset. These methods were selected due to the various distributions of the variables. For instance, pH values are typically nearly a normal distribution. Hence, the mean was used for missing values. This is due to the mean being a good representation of central tendency in a normal distribution. However, for variables with more complicated distributions, like Sulfate or Trihalomethanes, it was more appropriate to use the median or mode instead. The median entails the median of the data thus it is more robust than the mean. The mode is the most common value in the dataset and thus shows the most typical position of the distribution. Therefore, it was decided that the mean would be appropriate for pH and the median or mode for Sulfate or Trihalomethanes when filling in missing values. The process of imputing the median with missing values for an X variable can be expressed as shown in Equation 15:

$$\hat{X}_{median} = \text{Median}(X) \tag{15}$$

For a variable X with missing values, the mode imputation process can be expressed as:

$$\hat{X}_{mode} = \text{Mode}(X) \tag{16}$$

In Equation 16 $\hat{X}_{mode}$ is the imputed value and $\text{Mode}(X)$ is the mode of the observed values of X.

3.6.3. Review and processing of outliers

The very nature of the outlier problem in machine learning may lead to the disrupted functioning of a dataset. According to some researchers, if data with unprocessed outliers is included in the dataset, the model's performance results can drop by more than half [64]. So the detection and treatment of the outliers are of the primary importance of the model building process.

Trimming and Standard Deviation methods were used to remove outliers. Trimming involves removing a certain percentage of outliers to improve the accuracy of the results [65]. Standard Deviation is a statistical technique that shows how closely the values of a dataset are to the average. Outlier values correspond to the data beyond a specified standard deviation [66]. In the research, a few features that were outlier indicators, for example, 5% trimming was applied for 'Sulfate'. In this manner, 2.5% values were added up to both extremes and the rest of the data, which was 95%, were used. More so, outlier computation was done using the deviation calculation method for the 'hardness' feature in the dataset. The threshold value was determined by the average hardness value and adding two times the standard deviation for the two values to finish the process.

The second treatment for outliers in this research is the use of IQR (Inter-Quartile Range) method. As per the method, the real data of the highest and lowest values of the dataset are replaced with a certain threshold value, thus, the extreme values will not have a great influence on the model performance [67]. So, according to the IQR method, the data points that are outside the normal range are determined by setting a certain threshold value. This threshold is usually associated with a certain percentile. After that, all the values beyond the threshold are replaced with this threshold value. It is worth noting the fact that in analyses of water quality, the pH values are restricted to a specific range limiting the extreme values to a certain threshold. Thus, it is aimed to increase the certainty of the results by minimizing the probability of extreme values affecting the model's performance. While examining the pH values in the original dataset, a specific threshold value (pH = 9) was chosen and IQR was applied.

The percentile method was also applied to deal with outliers. This method is used to detect outliers by setting a threshold value at a certain percentile [68]. Here, the threshold value may be set at the range of 2%-98%, thus, any value beyond that will be regarded as a misfit. Nevertheless, the application of such a method produced some obstacles in doing the experiment, which resulted in not getting the expected correct results. The method of the percentile requires human instruction to set a particular number and set the limit. Nevertheless, the dataset is complicated and has had different values over time, which makes it hard to find the appropriate threshold value. The disparity in the dataset is illustrated by the water samples drawn from diverse geographical locations. These samples coming from urban water treatment systems to natural water sources in grouped areas are as such. The fact that the water properties are different makes it more difficult to study the effect of the factors involved. An example is the pH of the water in the city which is different from water in the rural area. The complexity is that every dataset feature is a result of many factors which differ in their independence. Hardness of water can be a mix-up of the geographical and the seasonal variability. This complexity makes the assignment of the threshold value of each characteristic more difficult, as the factors influencing them are expected to vary more widely. Furthermore, the percentile method uses a specific percentile range when identifying outliers. However, the threshold value set in the dataset, especially on the TDS (Total Dissolved Solids) value, reflects the mineralization of the water samples. Geographical differences of water sources and intended uses can cause significant variations in TDS values. Natural water sources in rural areas may have higher mineral content, while urban water supply systems may have lower levels of mineralization. This means that although the TDS threshold value is in accordance with generally established WHO standards, it may not be fully compatible with the specific characteristics of water samples from geographical areas. Therefore, it can be difficult to achieve an accurate agreement in defining or interpreting the TDS value as an outlier in water samples from specific geographical areas.

4. Experimental study and findings

In this study, nine supervised classification algorithms including LR, DT, RF, XGBoost, NB, KNN, SVM, ADA and BAG were used to determine the potability of water. GridSearchCV hyperparameter optimization technique was used to determine the hyperparameters of the models. Hyperparameters are manually determined parameters that affect the performance of the model. GridSearchCV is one tool for hyperparameter tuning. It is a systematic way to tune hyperparameters so that machine learning models can be better able to perform. This hyperparameter optimization process consists of certain steps to obtain the best performance of the machine learning models [69].

First, we specify the hyperparameters to be optimized along with a set of values for them. Next, the combination of hyperparameter values is generating the different models and then all the models are evaluated using a predefined metric. The selection of the best performing combination of hyperparameter values is made through a process of trying out different options and sorting out the models. A last model is constructed using the optimal hyperparameter values, and this model is now ready to be utilized on a more extensive dataset. Cross-validation (CV) is the technique used in GridSearchCV, facilitating the model's being tested on different portions of the data, thus improving its generalizability [70]. This process makes the model aware of such tendencies as over-fitting and under-fitting thereby providing reliable and superior results.

While creating the model, the dataset was divided into two parts, 75% for training and 25% for testing. In all algorithms used, the random state was set to 42. The number of trees in RF was defined as 9. The number of neighbors in KNN was set as 5. In the XGBoost algorithm, the learning rate was set as 0.01, the number of predictors as 8 and the number of seeds as 25. The kernel used in SVM is Radial Basis Function (RBF) and C parameter is set as 2. In SVM optimization, the C parameter indicates the extent to which misclassification of each training sample is prevented. For the ADA algorithm, 100 weak learners and a learning rate of 0.1 were used. For the BAG algorithm, 50 base classifiers and sampling strategies were determined. Figure 5 shows the confusion matrices of the algorithms used in the research.

When Figure 5 is analyzed, confusion matrices are used to examine the performance of each algorithm in detail. The BAG algorithm achieved the highest success in correctly identifying the potability status of water, exhibiting the highest True Negative value. On the other hand, the DT algorithm showed a significant performance in correctly classifying the potential risks related to the potability of the water, achieving the highest True Positive value. The LR algorithm has higher False Negative values. This indicates that it performs poorly in classifying the potability of water. Concerning the RF algorithm, it exhibits a well-balanced performance, effectively identifying both potable and non-potable water samples. The RF algorithm's contributions to True Positive and True Negative values contribute to its overall success in classifying water samples.

Fig. 5. Confusion matrices (based on trimming method).
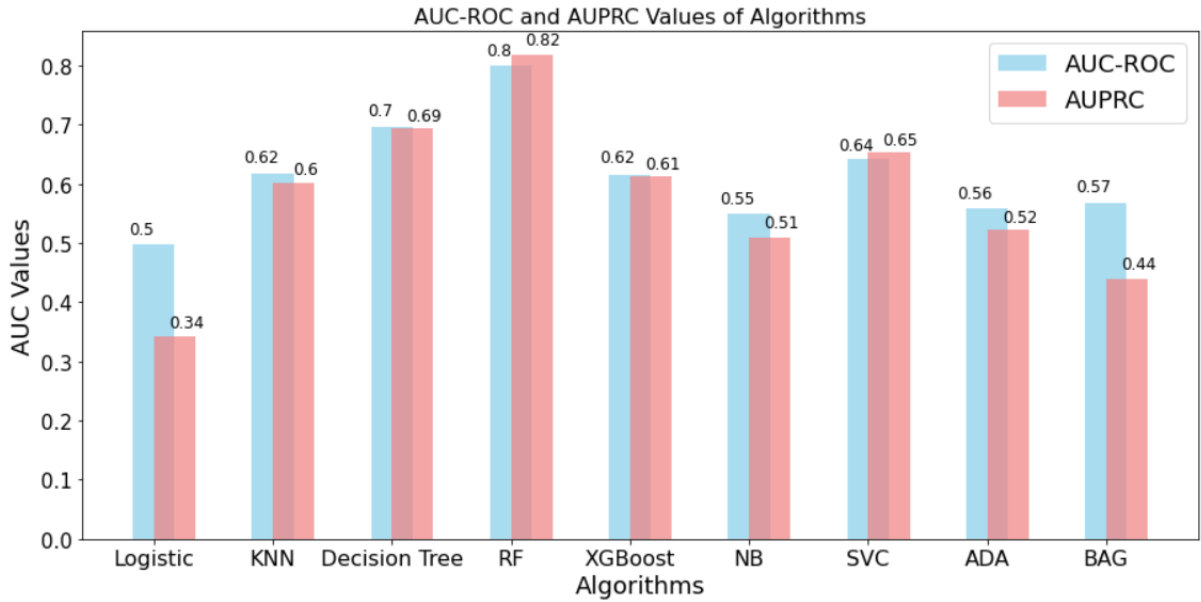
Fig. 6. AUC-ROC and AUPRC values of algorithms (based on trimming method).

Figure 6 shows the AUC-ROC and AUPRC scores of the water potability detection system that was used machine learning. These scores are very important benchmarks to be used for the assessment of the quality of classification models. AUC-ROC is the computation of the trade-off between the false positive rate and the true positive rate and a representation of the capacity of the model to be able to correctly classify non-potable water and at the same time having minimal false positives. AUC-ROC is a key metric with a higher score than the others indicative of better performance classification [71]. Moreover, AUPRC is a metric that investigates the relationship between precision and recall and it is particularly important for the case of the analysis of classification problems with imbalanced data. A high AUPRC score implies that the model can detect the non-potable water samples successfully and thus, it will reduce the probability of false positives [72].

The graph shows the obvious result that the RF algorithm has the highest AUC-ROC (0.80) and AUPRC (0.82) scores and the other algorithms have lower ones. In this instance, it can be stated that the RF algorithm is the top one in both accurately classifying potable water cases and the non-potable ones. In the same way, the DT algorithm is the one that has the most outstanding ability in demonstrating the exact results of the water samples with the AUC-ROC (0.70) and AUPRC (0.69) scores. On the other hand, the LR algorithm is the one that has some possible drawbacks in classifying the water samples correctly, as it has lower AUC-ROC (0.50) and AUPRC (0.34) scores than the other algorithms.

Table 2. Performance metrics according to the outlier treatment methods.

Classifier	Accuracy			Precision			Recall		
	Trim.	IQR	Per.	Trim.	IQR	Per.	Trim	IQR	Per.
LR	0.62	0.47	0.51	0.30	0.47	0.40	0.01	0.49	0.25
KNN	0.66	0.65	0.58	0.54	0.65	0.55	0.46	0.65	0.45
DT	0.72	0.74	0.65	0.56	0.70	0.68	0.73	0.82	0.50
RF	**0.83**	0.80	0.75	**0.84**	0.81	0.72	0.67	**0.79**	0.75
XGBoost	0.69	0.75	0.54	0.65	0.74	0.60	0.34	0.78	0.50
NB	0.63	0.53	0.51	0.50	0.54	0.40	0.23	0.42	0.38
SVC	0.71	0.67	0.60	0.70	0.66	0.55	0.38	0.66	0.60

| ADA | 0.63 | 0.56 | 0.52 | 0.49 | 0.56 | 0.45 | 0.30 | 0.56 | 0.38 |
| BAG | 0.64 | 0.77 | 0.53 | 0.62 | 0.75 | 0.65 | 0.03 | **0.80** | 0.52 |

Table 3. Performance metrics according to the outlier treatment methods.

Classifier	F1-Score			AUC-ROC			AUPRC		
	Trim	IQR	Per.	Trim	IQR	Per.	Trim	IQR	Per.
LR	0.02	0.48	0.45	0.50	0.47	0.30	0.34	0.48	0.42
KNN	0.49	0.65	0.50	0.62	0.65	0.55	0.60	0.60	0.53
DT	0.63	0.75	0.60	0.70	0.74	0.68	0.69	0.66	0.58
RF	0.75	**0.80**	0.70	**0.80**	**0.80**	0.72	**0.82**	0.74	0.65
XGBoost	0.44	0.76	0.45	0.62	0.75	0.60	0.61	0.69	0.55
NB	0.32	0.47	0.48	0.55	0.53	0.35	0.51	0.51	0.41
SVC	0.49	0.66	0.55	0.64	0.66	0.55	0.65	0.61	0.50
ADA	0.37	0.56	0.45	0.56	0.56	0.40	0.52	0.53	0.42
BAG	0.05	0.77	0.48	0.57	0.77	0.60	0.44	0.70	0.51

Table 2 and Table 3 demonstrates the effects of machine learning algorithms for evaluating water quality and its potability. Various outlier treatment methods were applied for the calculation of the performance of the algorithms. "Trimming" refers to the process of clearing the dataset usually by deleting the points from the lowest and highest percentiles. The "IQR" method is the process of limiting the outliers in the dataset and bringing the values above or below a certain threshold to that threshold. The method of the "Percentile" is the process of the ranking of the values in the dataset according to certain percentiles and intervening on values that are either within or outside a certain percentile. In particular, the RF and DT algorithms have strong potential in this area. RF was the most successful algorithm with an accuracy score of 0.83 with the trimming method. According to a precision score of 0.84, the recall is 0.67 (F1-Score = 0.75). The trimming method's recall of the RF algorithm is 0.67 while IQR has a score of 0.79. Because the trimming technique is mainly concerned with low values, the model gets more sensitive to low values and thus has a smaller recall. A lower recall means that occurrences, particularly in the positive class, are found with a success rate that is lower. These scores show the skill of the RF in the differentiation of the potable and non-potable water samples. The model was confirmed to be effective with respect to the classification task and prediction reliability by high values of precision and recall even for imbalanced datasets. DT was the second-best algorithm, thus, via IQR method, the accuracy score of 0.74 was reached. The DT algorithm, which was used to classify water samples correctly, recorded the performance which was represented by a precision score of 0.70 a recall score of 0.82 and an F1-Score of 0.75. The RF algorithm demonstrated high competence in the water potability detection task when the trimming method was applied. The IQR method increased the recall value; however, a balanced adjustment may be needed to increase this value further. Both IQR and trimming methods are efficient methods that can be used to control the outliers that degrade the performance of the model. These methods are important in balancing the model's sensitivity to certain values and its success rate. When the Percentile method was applied, a decrease in the overall performance of the algorithms was observed.
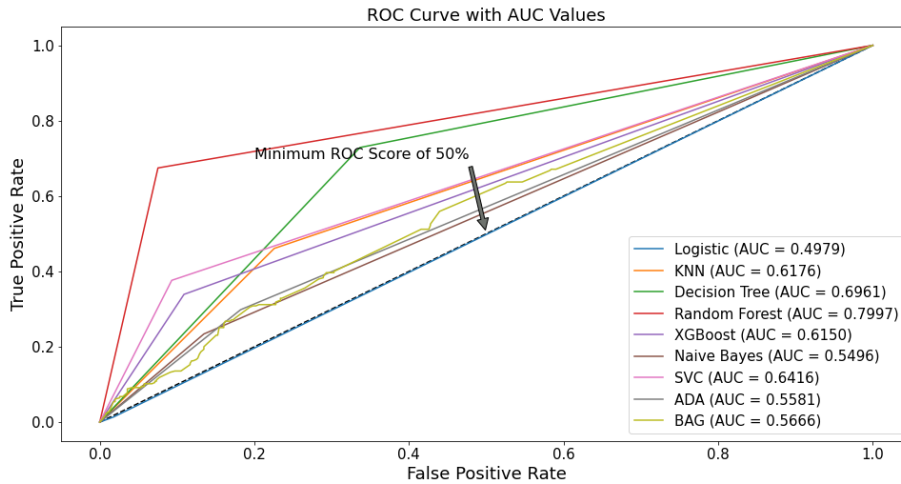
Fig. 7. ROC curve with AUC values (based on trimming method).

When the ROC curve plot is analyzed, it can be seen that certain classifiers perform strongly. The ROC curve provides a visual representation of how a model's sensitivity (true positive rate) and specificity (true negative rate) change at various thresholds. High AUC values indicate the ability of the models to effectively discriminate between different classes [73]. In this context, RF is the algorithm that stands out with a significant difference compared to other algorithms (AUC = 0.80). RF algorithm has demonstrated its competence in data classification by obtaining a very high AUC score. The AUC score obtained emphasizes the effectiveness in classifying the potability of water while maintaining the balance between precision and recall.

5. Discussion

This study compares the performance of various machine learning algorithms to determine water potability status. When the literature is examined, the target class that is tried to be estimated is usually on the WQI value. While many studies aim to estimate the WQI value using machine learning algorithms, this research addresses the practical need to classify water samples as potable or non-potable, which is crucial for ensuring safe drinking water. Furthermore, the multitude of parameters defining water potability, the variability of datasets, and the difficulty in comparing findings across different datasets add complexity to water quality research. This study's unique contribution lies in its use of a dataset that, to our knowledge, has not been previously employed in the literature. The dataset's novelty presents both opportunities and challenges. On one hand, it allows for the exploration of water quality classification using diverse parameters specific to the dataset, potentially uncovering insights that may not be evident in studies using different datasets. On the other hand, this uniqueness makes direct comparisons with other studies challenging, as each dataset may have its own characteristics and biases. Although studies directly focusing on binary classification of water potability may be limited, comparisons have been made between the findings of this study and existing literature based on specific features.

In this study, it was found that algorithms such as RF and DT are effective in accurately determining the potability status of water. A study by [74] suggests that Gradient Boosting algorithms are effective for a similar water quality analysis. Which algorithm to choose may vary depending on the intended use in a particular context, the characteristics of the dataset, and the problem domain to be solved. Algorithms such as RF and DT can achieve successful results, especially on high-dimensional and complex datasets, while Gradient Boosting algorithms can

learn more complex relationships [75]. Therefore, a decision should be made by considering the requirements of the model to be applied and the characteristics of the analyzed water samples.

When the findings from other studies focusing on water quality analysis in different geographical regions are examined, a study conducted in South America showed high accuracy of the KNN algorithm in determining the potability of water [76]. Geographical factors such as climatic conditions, rainfall, type of water sources are important parameters affecting water quality. Therefore, it is important to evaluate whether an algorithm shows the same success in another geographical region. Furthermore, the characteristics of the dataset used to evaluate differences in water quality analysis performance between geographical regions are important [77]. Factors such as regional characteristics, minerals in the water, pollution levels, etc. can affect the success of the analysis algorithms. Furthermore, geographic region-specific parameter settings may be required to optimize the success of the algorithm.

[30] used LSTM to estimate salinity in Salton Lake, emphasizing its accuracy and flexibility. Nevertheless, this research revealed that RF was the most efficient algorithm for the purpose of classifying drinking water. The difference in the observed results is due to the peculiarities of the datasets and the characteristics of the variables used. Chawla et al. concentrated on salinity, which may have different predictors than water potability. Exactly the same, [31] and [32] succeeded in high rates using SVR, XGBoost, and LSTM to forecast the water quality factors. In this work, the results of the SVC and XGBoost were low, however, the RF outcome was high. The different performance of SVC, XGBoost, and RF algorithms in this research and the studies [31] and [32] may be due to several things. Initially, the datasets used in each research may have had differences in size, complexity, and feature selection. RF is recognized for its strong performance on high-dimensional and complex datasets as well as noisy features, which might be the case in this research. In contrast, SVC and XGBoost may be more appropriate for the datasets for which they obtained the highest success rates in [31] and [32]. In addition, the differences in the hyperparameters selected for each algorithm, data preprocessing methods, and model evaluation techniques may have also played a role in the performance differences. RF's performance on such a diverse array of feature types and its strong generalization capacity have likely made it outperform SVC and XGBoost in this study. It should be emphasized that the performance of machine learning methods can be different in relation to the particular features of the dataset and the problem being tackled.

In the case of the study at hand, just like in [39], it can be noted that ensemble methods like Random Forest (RF) were found to be bieng excellent for drinking water quality prediction. This is a good example of the effectiveness of ensemble models for several reasons. One of the advantages of ensemble models is that they make the predictions more stable and reduce overfitting by combining several base learners, thus, they are suitable for complex datasets with non-linear relationships, e.g. water quality data. The ensemble models' high performance might come from the fact that they are capable of capturing the diverse and sometimes conflicting patterns that are present in the data. Through pooling the predictions of multiple models, ensemble models can successfully reduce both bias and variance and consequently, get more accurate and precise predictions. Also, ensemble models are able to deal with the different kinds of features and data distributions, thus, they are flexible and can be used for different datasets. Here, the ensemble model may have combined the information from temperature, pH, turbidity, and coliforms which consequently led to a more precise water quality prediction. Furthermore, the effectiveness of ensemble models can be related to some characteristics of the dataset and the problem domain. The dataset used in the current research may have had intricate relationships and patterns that are suitable for community modeling.

This research also analyzed the impact of outlier treatment methods (Trimming, IQR, Percentile) on performance of the algorithms. The best results of 83% accuracy were achieved via the RF algorithm implemented with the trimming method. This means that the RF algorithm is an expert in differentiating between samples of water that can be consumed and those that cannot be consumed. Meanwhile, it was noted that the recall value of the trimming method increased from 67% to 79%. The reason being, the trimming method mainly excludes a few values, hence the model becomes more sensitive to low values resulting in a lower recall value. The DT algorithm had 74% accuracy with the IQR method, but higher accuracy with the trimming method. In these cases, the IQR and trimming

methods obviously controlled the effect of outliers on the algorithm's performance. Nevertheless, the algorithms performance on the percentile method was decreased when the method was applied. The reason for this phenomenon is that assigning ranks to the values in the dataset according to some percentiles and intervening according to this is less effective than other methods.

A study analyzing the influence of outlier handling methods on algorithms shows that specifically, trimming can increase the performance by increasing the sensitivity of the model to low values [78]. This also means that trim can reveal the presence of crucial components at low concentrations of water, especially in the quality analysis of water. However, the high recall value with the IQR method may ignore critical features at low concentrations in the case of water quality analysis [79]. Consequently, the application of the IQR method should be exercised with care measuring the characteristics to be analyzed. The clear performance deterioration of the Percentile method agrees with some results in the literature [80]. Researchers have pointed out that this approach usually corrupts the overall configuration of a dataset and not so useful for complex datasets. In other words, applying the percentile method may result in the natural structure, distribution, or pattern of the dataset being changed. This is possible when the percentile method does its magic by ranking the values in the dataset according to some percentiles. Taking this into account, this method frequently has the tendency of limiting or modifying the values in the dataset to a certain percentile ranking. Disassembly of data in this way can have unintended consequences, particularly when it is necessary to grasp or keep intact the intricate structures that are part of the dataset. In case of the water potability analysis, applying concentrating or diluting of water properties to a certain percentile may produce results that are less relevant to real-world conditions.

6. Conclusion

This research was conducted to evaluate the performance of nine different machine learning algorithms in determining the potability of water. Through the study of the accuracy of the algorithms in water sample potability detection, it became evident that the purpose of the study was fulfilled successfully.

Through data preparation stages, the procedures performed in this study are the main steps to ensure reliable and effective training of machine learning models. Taking care of the issue of class imbalance, deciding on how to treat missing values, cleaning potential mistakes in the dataset and properly treating outliers were pointed out as main strategic decisions to augment the accuracy of analysis and modeling. To balance the dataset's classes, two sets of samples with different data values (0 and 1) for the 'Potability' column were treated separately. Resampling was utilized to magnify the number of instances in the minority category, and the augmented minority group was coupled with the majority group to make a balanced Data Frame.

Analysis of missing values was carried out to find out the missing values of critical features such as pH, sulfate, and trihalomethanes. For the gaps in this regard, statistical imputation techniques chosen according to how each variable was distributed were used. For instance, the pH values were normally distributed so the mean was used as a central measure. On the other hand, the commonly used median and mode were more appropriate in the case of variables with complex distributions like sulfate or trihalomethanes. In these situations, the median is the value in the middle and the mode is the value that is the most frequent, thus giving more reliable solutions to the mean. The mean was used for pH and the mode or median for sulfate or trihalomethanes. They were successfully tackled this way which consequently led to model reliability improvement.

The process of outlier examination and treatment is the crucial one that is related to the irregularities of the dataset removal. The methods of Trimming, IQR, Standard Deviation, and Percentile were used to remove outliers. In this way, the machine learning model is less likely to be influenced by the outliers thus, the model becomes more generalizable. The dataset received through the data preparation steps provided the machine learning algorithms that were used for the determination of water potassium successful training.

The RF and DT algorithms were discovered to be efficient in potable water detection as a result of the analysis. The RF algorithm was the best method in terms of accuracy and AUC-ROC scores that cutting and trimming were

used for potable water and non-potable water sample classification. DT algorithm has been successful with IQR outlier processing, but the result is not as high as RF. In contrast, the Percentile method often resulted in inferior algorithm performance. The importance of these outcomes shows the potential of machine learning algorithms to be able to distinguish between potable and non-potable water reliably and accurately, as well as identify the outlier treatment methods used in pre-processing of the dataset. Moreover, it was revealed that the algorithms' performance can be distorted by the geographical factors when the comparison is made with other studies in the literature and in the other geographical regions. These are the issues that illustrate the effects of geographical differences in water quality analysis and should be considered in model selection.

The results give crucial data for people who make decisions on the preservation of water resources and the management of water quality. It is suggested that future studies should carry out such analyses in different regions of the world, and the performance of the various algorithms should be compared in more detail and the use of more advanced machine learning models for the water quality analysis should be developed. Moreover, more research needs to be carried out on issues like the efficient handling of the missing values, the inclusion of the imbalanced distribution of the dataset, and the further investigation of the model's sensitivity to the geographical differences. Such recommendations would bring about more stable and transferable results of machine learning-based methods in the field of water quality analysis.

Acknowledgements

References

[1] X. Wen et al., "Microbial indicators and their use for monitoring drinking water quality—A review," *Sustainability*, vol. 12, no. 6, pp. 2249, 2020.
[2] S. E. Hrudey and E. J. Hrudey, *Safe Drinking Water*. IWA publishing, 2004.
[3] W. J. Cosgrove and D. P. Loucks, "Water management: Current and future challenges and research directions," *Water Resources Research*, vol. 51, no. 6, pp. 4823-4839, 2015.
[4] H. G. Peterson, "Rural drinking water and waterborne illness," *Saskatoon, SK: Safe Drinking Water Foundation*, pp. 162-91, 2001.
[5] T. Russo, K. Alfredo, and J. Fisher, "Sustainable water management in urban, agricultural, and natural systems," *Water*, vol. 6, no. 12, pp. 3934-3956, 2014.
[6] S. A. Esrey, "Water, waste, and well-being: a multicountry study," *American Journal of Epidemiology*, vol. 143, no. 6, pp. 608-623, 1996.
[7] World Health Organization**,** "Guidelines for drinking-water quality (Vol. 1)," *World Health Organization*, 2004.
[8] J. DeZuane, *Handbook of Drinking Water Quality*, John Wiley & Sons, 1997.
[9] S. J. Kulkarni, "A review on research and studies on dissolved oxygen and its affecting parameters," *International Journal of Research and Review*, vol. 3, no. 8, pp. 18-22, 2016.
[10] C. Jingsheng, Y. Tao, and E. Ongley, "Influence of high levels of total suspended solids on measurement of COD and BOD in the Yellow River, China," *Environmental Monitoring and Assessment*, vol. 116, pp. 321-334, 2006.
[11] S. Morais, F. G. Costa, and M. D. L. Pereira, "Heavy metals and human health," *Environmental Health–Emerging Issues and Practice*, vol. 10, no. 1, pp. 227-245, 2012.
[12] A. K. Singh and R. Chandra, "Pollutants released from the pulp paper industry: Aquatic toxicity and their health hazards," *Aquatic Toxicology*, vol. 211, pp. 202-216, 2019.
[13] P. Nannipieri, S. Greco, and B. Ceccanti, "Ecological significance of the biological activity in soil," *Soil Biochemistry*, pp. 293-356, 2017.
[14] D. Eisma, *Suspended Matter in the Aquatic Environment*, Springer Science & Business Media, 2012.
[15] S. Some, R. Mondal, D. Mitra, D. Jain, D. Verma, and S. Das, "Microbial pollution of water with special reference to coliform bacteria and their nexus with environment," *Energy Nexus*, vol. 1, pp. 100008, 2021.
[16] I. Delpla, A. V. Jung, E. Baures, M. Clement, and O. Thomas, "Impacts of climate change on surface water quality in relation to drinking water production," *Environment International*, vol. 35, no. 8, pp. 1225-1233, 2009.
[17] T. Dube, O. Mutanga, K. Seutloali, S. Adelabu, and C. Shoko, "Water quality monitoring in sub-Saharan African lakes: a review of remote sensing applications," *African Journal of Aquatic Science*, vol. 40, no. 1, pp. 1-7, 2015.
[18] D. T. E. Hunt and A. L. Wilson, *The Chemical Analysis of Water: General Principles and Techniques (Vol. 2)*, Royal Society of Chemistry, 1986.

[19] C. E. Hatch, A. T. Fisher, J. S. Revenaugh, J. Constantz, and C. Ruehl, "Quantifying surface water–groundwater interactions using time series analysis of streambed thermal records: Method development," *Water Resources Research*, vol. 42, no. 10, pp. 1-14, 2006.

[20] I. Yaroshenko et al., "Real-time water quality monitoring with chemical sensors," *Sensors*, vol. 20, no. 12, pp. 3432, 2020.

[21] H. B. Glasgow, J. M. Burkholder, R. E. Reed, A. J. Lewitus, and J. E. Kleinman, "Real-time remote monitoring of water quality: A review of current applications, and advancements in sensor, telemetry, and computing technologies," *Journal of Experimental Marine Biology and Ecology*, vol. 300, no. 1-2, pp. 409-448, 2004.

[22] K. T. Peterson, V. Sagan, P. Sidike, E. A. Hasenmueller, J. J. Sloan, and J. H. Knouft, "Machine learning-based ensemble prediction of water-quality variables using feature-level and decision-level fusion with proximal remote sensing," *Photogrammetric Engineering & Remote Sensing*, vol. 85, no. 4, pp. 269-280, 2019.

[23] L. F. Arias-Rodriguez et al., "Integration of Remote Sensing and Mexican Water Quality Monitoring System Using an Extreme Learning Machine," *Sensors*, vol. 21, no. 12, pp. 4118, 2021.

[24] V. Gudivada, A. Apon, and J. Ding, "Data quality considerations for big data and machine learning: Going beyond data cleaning and transformations," *International Journal on Advances in Software*, vol. 10, no. 1, pp. 1-20, 2017.

[25] U. Ahmed, R. Mumtaz, H. Anwar, A. A. Shah, R. Irfan, and J. Garc´ıa-Nieto, "Efficient water quality prediction using supervised machine learning," *Water*, vol. 11, pp. 2210, 2019.

[26] S. Kouadri, A. Elbeltagi, A. R. M. T. Islam, and S Kateb, "Performance of machine learning methods in predicting water quality index based on irregular data set: application on Illizi region (Algerian southeast)," *Applied Water Science*, vol. 11, no. 12, pp. 190, 2021.

[27] J. P. Nair and M. S. Vijaya, "Predictive models for river water quality using machine learning and big data techniques - a Survey," in *Proceedings of the 2021 International Conference on Artificial Intelligence and Smart Systems (ICAIS)*, IEEE, Coimbatore, India, March 2021.

[28] M. M. Hassan, M. M. Hassan, L. Akter et al., "Efficient prediction of water quality index (WQI) using machine learning algorithms," *Human-Centric Intelligent Systems*, vol. 1, no. 3-4, pp. 86–97, 2021.

[29] B. Charbuty and A. M. Abdulazeez, "Classification based on decision tree algorithm for machine learning," *Journal of Applied Science and Technology Trends*, vol. 2, no. 01, pp. 20–28, 2021.

[30] P. Chawla, X. Cao, Y. Fu, C. M. Hu, M. Wang, S. Wang, and J. Z. Gao, "Water quality prediction of Salton Sea using machine learning and big data techniques," *Int. J. Environ. Anal. Chem.*, vol. 103, no. 18, pp. 6835–6858, 2023.

[31] K. Joslyn, "Water quality factor prediction using supervised machine learning," *REU Final Reports*, vol. 6, 2018.

[32] Y. Wang, J. Zhou, K. Chen, Y. Wang, and L. Liu, "Water quality prediction method based on LSTM neural network," in *2017 12th International Conference on Intelligent Systems and Knowledge Engineering (ISKE)*, Nov. 2017, pp. 1-5.

[33] M. Hmoud Al-Adhaileh and F. Waselallah Alsaade, "Modelling and prediction of water quality by using artificial intelligence," *Sustainability*, vol. 13, no. 8, pp. 4259, 2021.

[34] T. H. Aldhyani, M. Al-Yaari, H. Alkahtani, and M. Maashi, "Water quality prediction using artificial intelligence algorithms," *Applied Bionics and Biomechanics*, 2020.

[35] X. Wang, Y. Li, Q. Qiao, A. Tavares, and Y. Liang, "Water quality prediction based on machine learning and comprehensive weighting methods," *Entropy*, vol. 25, no. 8, pp. 1186, 2023.

[36] M. Y. Shams, A. M. Elshewey, E. S. M. El-kenawy, A. Ibrahim, F. M. Talaat, and Z. Tarek, "Water quality prediction using machine learning models based on grid search method," *Multimedia Tools and Applications*, pp. 1-28, 2023.

[37] J. P. Nair and M. S. Vijaya, "River water quality prediction and index classification using machine learning," *Journal of Physics: Conference Series*, vol. 2325, no. 1, pp. 012011, Aug. 2022.

[38] A. Nouraki, M. Alavi, M. Golabi, and M. Albaji, "Prediction of water quality parameters using machine learning models: A case study of the Karun River, Iran," *Environmental Science and Pollution Research*, vol. 28, no. 40, pp. 57060-57072, 2021.

[39] M. Azrour, J. Mabrouki, G. Fattah, et al., "Machine learning algorithms for efficient water quality prediction," *Model. Earth Syst. Environ.*, vol. 8, pp. 2793-2801, 2022.

[40] S. Dharshini, "Deep learning approach for prediction and classification of potable water," *Analytical Sciences*, vol. 39, pp. 1179-1189, 2023.

[41] S. Dalal, E. M. Onyema, C. A. T. Romero, L. C. Ndufeiya-Kumasi, D. C. Maryann, A. J. Nnedimkpa, and T. K. Bhatia, "Machine learning-based forecasting of potability of drinking water through adaptive boosting model," *Open Chemistry*, vol. 20, no. 1, pp. 816-828, 2022.

[42] Z. H. Zhou, *Machine Learning*. Springer Nature, 2021.

[43] V. Sinap, "Prediction of Counter-Strike: Global Offensive round results with machine learning techniques," *Journal of Intelligent Systems: Theory and Applications*, vol. 6, no. 2, pp. 119-129, 2023, doi: 10.38016/jista.1235031.

[44] S. Keskin, O. Sevli, and E. Okatan, "Comparative analysis of the classification of recyclable wastes," *Journal of Scientific Reports-A*, vol. 055, pp. 70-79, 2023.

[45] D. Böhning, "Multinomial logistic regression algorithm," *Annals of the Institute of Statistical Mathematics*, vol. 44, no. 1, pp. 197-200, 1992.

[46] C. Kingsford and S. L. Salzberg, "What are decision trees?," *Nature Biotechnology*, vol. 26, no. 9, pp. 1011-1013, 2008.

[47] K. Mathan, P. M. Kumar, P. Panchatcharam, G. Manogaran, and R. Varadharajan, "A novel Gini index decision tree data mining method with neural network classifiers for prediction of heart disease," *Design Automation for Embedded Systems*, vol. 22, pp. 225-242, 2018.

[48] S. J. Rigatti, "Random forest," *Journal of Insurance Medicine*, vol. 47, no. 1, pp. 31-39, 2017.

[49] T. Chen and C. Guestrin, "Xgboost: A scalable tree boosting system," in *Proceedings of the 22nd ACM SIGKDD International Conference on Knowledge Discovery and Data Mining*, 2016, pp. 785-794.

[50] G. I. Webb, J. R. Boughton, and Z. Wang, "Not so naive bayes: aggregating one-dependence estimators," *Machine Learning*, vol. 58, pp. 5-24, 2005.

[51] L. E. Peterson, "K-Nearest neighbor," *Scholarpedia*, vol. 4, no. 2, pp. 1883, 2009.

[52] H. Bhavsar and M. H. Panchal, "A review on support vector machine for data classification," *International Journal of Advanced Research in Computer Engineering & Technology (IJARCET)*, vol. 1, no. 10, pp. 185-189, 2012.

[53] A. Taherkhani, G. Cosma, and T. M. McGinnity, "AdaBoost-CNN: An adaptive boosting algorithm for convolutional neural networks to classify multi-class imbalanced datasets using transfer learning," *Neurocomputing*, vol. 404, pp. 351-366, 2020.

[54] L. Breiman, "Bagging predictors," *Machine Learning*, vol. 24, pp. 123-140, 1996.

[55] X. Zhu, C. Bao, and W. Qiu, "Bagging very weak learners with lazy local learning," in *2008 19th International Conference on Pattern Recognition*, 2008, pp. 1-4.

[56] P. Baldi, S. Brunak, Y. Chauvin, C. A. Andersen, and H. Nielsen, "Assessing the accuracy of prediction algorithms for classification: an overview," *Bioinformatics*, vol. 16, no. 5, pp. 412-424, 2000.

[57] N. R. Cook, "Use and misuse of the receiver operating characteristic curve in risk prediction," *Circulation*, vol. 115, no. 7, pp. 928-935, 2007.

[58] J. Myerson, L. Green, and M. Warusawitharana, "Area under the curve as a measure of discounting," *Journal of the Experimental Analysis of Behavior*, vol. 76, no. 2, pp. 235-243, 2001.

[59] K. Boyd, K. H. Eng, and C. D. Page, "Area under the precision-recall curve: Point estimates and confidence intervals," in *Machine Learning and Knowledge Discovery in Databases: European Conference, ECML PKDD 2013, Prague, Czech Republic, September 23-27, 2013, Proceedings, Part III*, 2013, pp. 451-466.

[60] Kaggle, *Water Quality and Potability*, 2021 [Online]. Available: https://www.kaggle.com/datasets/uom190346a/water-quality-and-potability.

[61] R. J. Little and D. B. Rubin, *Statistical Analysis with Missing Data*, vol. 793. John Wiley & Sons, 2019.

[62] T. D. Pigott, "A review of methods for missing data," *Educational Research and Evaluation*, vol. 7, no. 4, pp. 353-383, 2001.

[63] G. Rose and S. Day, "The population mean predicts the number of deviant individuals," *BMJ: British Medical Journal*, vol. 301, no. 6759, pp. 1031, 1990.

[64] R. K. Pearson, "Outliers in process modeling and identification," *IEEE Transactions on Control Systems Technology*, vol. 10, no. 1, pp. 55-63, 2002.

[65] V. Tkachev, M. Sorokin, C. Borisov, A. Garazha, A. Buzdin, and N. Borisov, "Flexible data trimming improves performance of global machine learning methods in omics-based personalized oncology," *International Journal of Molecular Sciences*, vol. 21, no. 3, pp. 713, 2020.

[66] N. E. Huang, M. L. C. Wu, S. R. Long, S. S. Shen, W. Qu, P. Gloersen, and K. L. Fan, "A confidence limit for the empirical mode decomposition and hilbert spectral analysis," *Proceedings of the Royal Society of London. Series A: Mathematical, Physical and Engineering Sciences*, vol. 459, no. 2037, pp. 2317-2345, 2003.

[67] H. P. Vinutha, B. Poornima, and B. M. Sagar, "Detection of outliers using interquartile range technique from intrusion dataset," in *Information and Decision Sciences: Proceedings of the 6th International Conference on FICTA*, Springer Singapore, pp. 511-518, 2018.

[68] N. Aravind, S. Nagajothi and S. Elavenil, "Machine learning model for predicting the crack detection and pattern recognition of geopolymer concrete beams," *Construction and Building Materials*, *297*, pp. 123785, 2021.

[69] D. Kartini, D. T. Nugrahadi and A. Farmadi, A, "Hyperparameter tuning using GridsearchCV on the comparison of the activation function of the ELM method to the classification of pneumonia in toddlers," in *2021 4th International Conference of Computer and Informatics Engineering (IC2IE)*, IEEE, pp. 390-395, Sep. 2021.

[70] C. Schaffer, "Selecting a classification method by cross-validation," *Machine Learning*, vol. 13, p.135-143, 1993.

[71] S. Narkhede, "Understanding AUC-ROC curve," *Towards Data Science*, vol. 26, no. 1, pp. 220-227, 2018.

[72] V. J. Lei et al., "Model performance metrics in assessing the value of adding intraoperative data for death prediction: Applications to noncardiac surgery," in *MedInfo*, 2019, pp. 223-227.

[73] J. A. Hanley and B. J. McNeil, "the meaning and use of the area under a receiver operating characteristic (ROC) curve," *Radiology*, vol. 143, no. 1, pp. 29-36, 1982.

[74] M. Durairaj and T. Suresh, "Enhanced gradient boosting tree classifier using optimization technique for water quality prediction," *Annals of the Romanian Society for Cell Biology*, pp. 3860-3873, 2021.

[75] T. Kavzoglu and A. Teke, "Predictive performances of ensemble machine learning algorithms in landslide susceptibility mapping using random forest, extreme gradient boosting (XGBoost) and natural gradient boosting (NGBoost)," *Arabian Journal for Science and Engineering*, vol. 47, no. 6, pp. 7367-7385, 2022.

[76] D. Dezfooli et al., "Classification of water quality status based on minimum quality parameters: Application of machine learning techniques," *Modeling Earth Systems and Environment*, vol. 4, pp. 311-324, 2018.

[77] S. Shrestha and F. Kazama, "Assessment of surface water quality using multivariate statistical techniques: A case study of the Fuji River Basin, Japan," *Environmental Modelling & Software*, vol. 22, no. 4, pp. 464-475, 2007.

[78] V. Tkachev, M. Sorokin, C. Borisov, A. Garazha, A. Buzdin and N. Borisov, "Flexible data trimming improves performance of global machine learning methods in omics-based personalized oncology," *International Journal of Molecular Sciences*, vol. 21 no. 3, pp. 713, 2020.

[79] P. Ukkonen and A. Mäkelä, "Evaluation of machine learning classifiers for predicting deep convection," *Journal of Advances in Modeling Earth Systems*, vol. 11 no. 6, pp. 1784-1802, 2019.

[80] C. Mantel, F. Villebro, G. A. dos Reis Benatto, H. R. Parikh, S. Wendlandt, K. Hossain, ... and S. Forchhammer, "Machine learning prediction of defect types for electroluminescence images of photovoltaic panels," in *Applications of Machine Learning*, vol. 11139, SPIE, p. 1113904, Sep. 2019.

RESEARCH ARTICLE

Noise and frequency propagation in natural stone processing plants

Zekeriya Duran[a,*], Bülent Erdem[b], Tuğba Doğan[c], Mehmet Genç[d]

[a]*Sivas Cumhuriyet University, Sivas Vocational School of Technical Sciences, Sivas, 58140, Türkiye, ORCID: 0000-0002-9327-8567*
[b]*Sivas Cumhuriyet University, Geophysics Engineering Department, Sivas, 58140, Türkiye, ORCID: 0000-0002-1226-9248*
[c]*Sivas Cumhuriyet University, Industrial Engineering Department, Sivas, 58140, Türkiye, ORCID: 0000-0002-2628-4238*
[d]*Malatya Turgut Ozal University, Hekimhan Mehmet Emin Sungur Vocational School, Malatya, 44400, Türkiye, ORCID: 0000-0002-9950-0720*

Abstract

In this study, 510 noise measurements recorded in eight natural stone processing plants operating in Sivas City, Turkey were evaluated and the noise levels and dominant frequency bands of 11 different processing machines used in these plants were determined. The daily equivalent noise level of all natural stone processing plants was around or above the exposure limit value (87 dBA) specified in relevant regulations. Considering the machines and plant environment, the frequency ranges for the highest noise levels were mostly between 630 Hz - 5000 Hz, centering around 3150 Hz. Variations in the noise level of the processing machines in separate plants where similar processes were carried out was primarily related to the plant size and machine layout, the number of machines operating simultaneously and the type of natural stone processed. While the difference between the noise levels of gangsaws, bridge cutting, ST cutting, head/side cutting, trimming, cement filling, slab polishing, narrow polishing, chamfering and splitting machines were statistically significant, aging machines generated similar noise levels.

Keywords: ⅓ octave band frequency, Hypothesis testing, L_{Aeq}, $L_{EX,8h}$, Noise and frequency mapping, Natural stone processing machinery

1. Introduction

   Natural stone mining depends on intense manpower. There are many large and small natural stone quarries and processing plants in Turkey. Noise-induced hearing loss is an irreversible but preventable occupational disease. Employees in natural stone processing facilities are more exposed to the harmful effects of noise than other mining

   * Corresponding author. Tel.: (346)4875520
     E-mail address: zduran@cumhuriyet.edu.tr

activities. Noise is a type of energy that can be transmitted through the air as pressure waves. Human ear can perceive these pressure waves that it feels as sound or noise. A normal and healthy young person can hear sounds in the frequency range of 20 Hz - 20000 Hz, but the human ear cannot respond equally to all frequencies [1]. Therefore, simply measuring the physical density of a sound pressure level is not sufficient to evaluate the potentially harmful effect of noise. High frequency noise has been reported to be more harmful than low frequency noise [2, 3]. Noise exposure may cause several negative health effects on people, including stress, cardiovascular diseases, hypertension, respiratory and neurological problems, and sleep disturbance. It is stated that high frequency sounds have effects such as high blood pressure, fatigue, hearing loss, headache, tinnitus, dizziness and nausea, depending on personal sensitivity and aging [4-6]. It is also reported that prolonged exposure to occupational and/or environmental noise may contribute to an increased risk of cardiovascular disease [7-10]. Hearing tests performed in natural stone processing facilities have revealed that the employees suffered from moderate to severe hearing loss [11-13]. It is necessary to identify the frequency distribution of the noise in terms of engineering controls [14]. Noise control through frequency analysis has been described as a vital tool widely used for the selection of hearing protectors and for environmental or communal noise assessment [15]. Controlling high frequency noise is both easier and cheaper than low frequency noise [16, 17]. The amount of sound transmitted from the outside of the buildings to the inside is greater in low frequency sound than in high frequencies. Therefore, thicker sound-absorbing materials are required compared to high-frequency sounds, as low-frequency sounds can pass through obstacles more easily [18]. Thus, it can be inferred that measures to be taken against noise propagation may be easier since the dominant frequencies are in the high frequency range in natural stone processing plants.

There are various approaches to define the frequency ranges that the human ear can hear as low, medium and high frequency ranges. The low frequency limit can be set at 200 Hz [19-23] or 250 Hz. According to an approach, sounds between 250 Hz - 2000 Hz fall into the medium frequency range and sounds with a higher frequency from 2000 Hz fall into the high frequency range [24, 25]. Bilgili et al [26] proposed the following scheme to identify the frequency of the sound considering the A and C-weighted sound levels: generally low frequency when (dBC – dBA $\geq$ 2), broadband equal sound level frequency when (dBC - dBA = 0) and generally high frequency when (dBC – dBA $<$ 2). The World Health Organization (WHO) recommends C-weighted measurement along with A-weighted measurement in the examination of low and high frequency noise [26, 27]. In a study examining the effect of sound frequency on hearing loss, 48 % of 152 personnel with an average age of 32 had hearing loss due to noise, and it was revealed that the frequency of hearing loss started in the 6000 Hz region, especially in the left ear. In another study, it was stated that 40.4 % of the employees in this sector had a hearing loss and the maximum equivalent noise level was in the region of 4000 Hz [28]. The blocks supplied from quarries are handled in the slab and tile lines in the processing facilities, and are brought to the product sizes and specifications desired by the market. A series of equipment including gangsaws, bridge cutting, block cutting, head/side cutting, trimming, chamfering, polishing, cement filling and aging machines are generally used throughout the whole processing stages. It should be noted that the noise level to which the personnel working in natural stone processing facilities are exposed is above the limits specified in international standards [29-35]. It was reported that noise generated in stone processing facilities poses a risk to human health [32, 33, 36]. Researchers suggest that natural stone processing facilities be established away from residential areas [29, 31]. Employees should use personal ear protection equipment when working with high-noise emitting machinery like marble cutting machines, marble saws and polishing equipment [30, 31, 37]. Huang et al [35] reported that the noise levels that employees in natural stone processing plants are exposed to mostly correspond to the high frequency range (2000 Hz - 4000 Hz). The noise emitted in the cutting process varies according to the type of natural stone being processed. Şengün et al [38] recorded higher noise levels with andesite and basalt type rocks. Table 1 enumerates the detrimental impacts of noise on human health. Workers at natural stone processing plants are more exposed to second and third degree noise, which can have a major physiological impact, given the detrimental effects of noise on human health.

Table 1. Effects of noise on humans [26, 39, 40].

Level of Noise	Exposure range (dB)	Health Effects
1st level noises	30–65	Discomfort, uneasiness, anger, fury, sleep disorder, and attention deficit.
2nd level noises	65–90	Physiological reactions; increase in blood pressure, acceleration in heart rate and respiration, decrease in pressure in the cerebral fluid, sudden reflexes.
3rd level noises	90–120	Physiological reactions, headaches.
4th level noises	120–140	Permanent damage to the inner ear, deterioration of balance.
5th level noises	>140	Serious brain damage, burst eardrum.

2. Material and methods

In this study a total of 510 noise recordings were taken from eight natural stone processing facilities located in Sivas city, Turkey and its vicinity. Processing plants, which were coded between A and H to avoid a positive or negative bias, operated some or all of the following 11 machines: gangsaws, bridge cutting, ST block cutting, head/side cutting, trimming, cement filling, slab polishing, narrow polishing, aging, chamfering and splitting. At the time of measurement, the following natural stones were processed in the plants; limestone at plants A, C, F, G and H, yellow travertine at plants B and E and classic travertine at plant D. Noise exposure measurements were carried out in accordance with TS EN ISO 9612 [41] "Acoustics - Determination of occupational noise exposure - Engineering method", calibration for IEC 60942 : 2003 [42] and TS 2607 ISO [43] "Acoustics - Determination of occupational noise exposure and estimation of noise-induced hearing impairment" (Fig. 1). The task-based measuring method was used in this work for measurement purposes, and it was also used to eliminate uncertainties. As a result, for each assignment, measurements were taken three times for a minimum of five minutes. The microphone was positioned between 0.1 and 0.4 meters from the external auditory canal entry, in the middle plane of the employee's head, level with the eyes, and on the side of the ear that was most exposed. The individual taking the measurement positioned himself behind and next to the employee, maintaining this position throughout [44]. In both standards, the root-mean-square (RMS) of the frequency-weighted sound pressure values is defined for a nominal 8-hour working day ($L_{EX,8h}$) for assessing the noise exposure of workers during a working day. The frequency-noise relationship was also studied. A high-precision noise level meter equipped with an ⅓ octave band filter and suitable for all noise measurements specified in the annexes of the "Environmental Noise Assessment and Management Regulation" of the Ministry of Environment and Urbanization was used in field measurements. Noise measurements were carried out with A, C and Z (linear) frequency weightings over three profiles. The noise meter was calibrated before and after each measurement round as per the relevant directives. Frequency analyses were made of the noise levels recorded in the natural stone processing plants and the frequency and noise propagation maps were drawn taking into account the plant layout. The Surfer (Golden Software) application was used to create noise propagation maps [45].

Fig. 1. Noise measurements at a marble plant.

3. Results and discussion

A noise-vibration analysis package [46] was utilized for extracting the ⅓ octave frequency-noise relation of the recordings. Fig. 2 illustrates the frequency-noise relationship of the aging machines in natural stone processing facilities B and E using the A measurement scale in the event that the topic is discussed through an example. While workers in these factories who operate aging machines are subjected to similar dominant frequencies of noise, workers in other natural stone processing facilities may be exposed to different prominent frequency ranges. Because natural stone processing plants have a lot of machinery and industrial settings, the frequencies with the highest noise levels fall primarily between 630 Hz and 5000 Hz, with a concentration in the 3150 Hz frequency range. There is no natural stone processing plant with dominant low frequency ranges (Table 2).
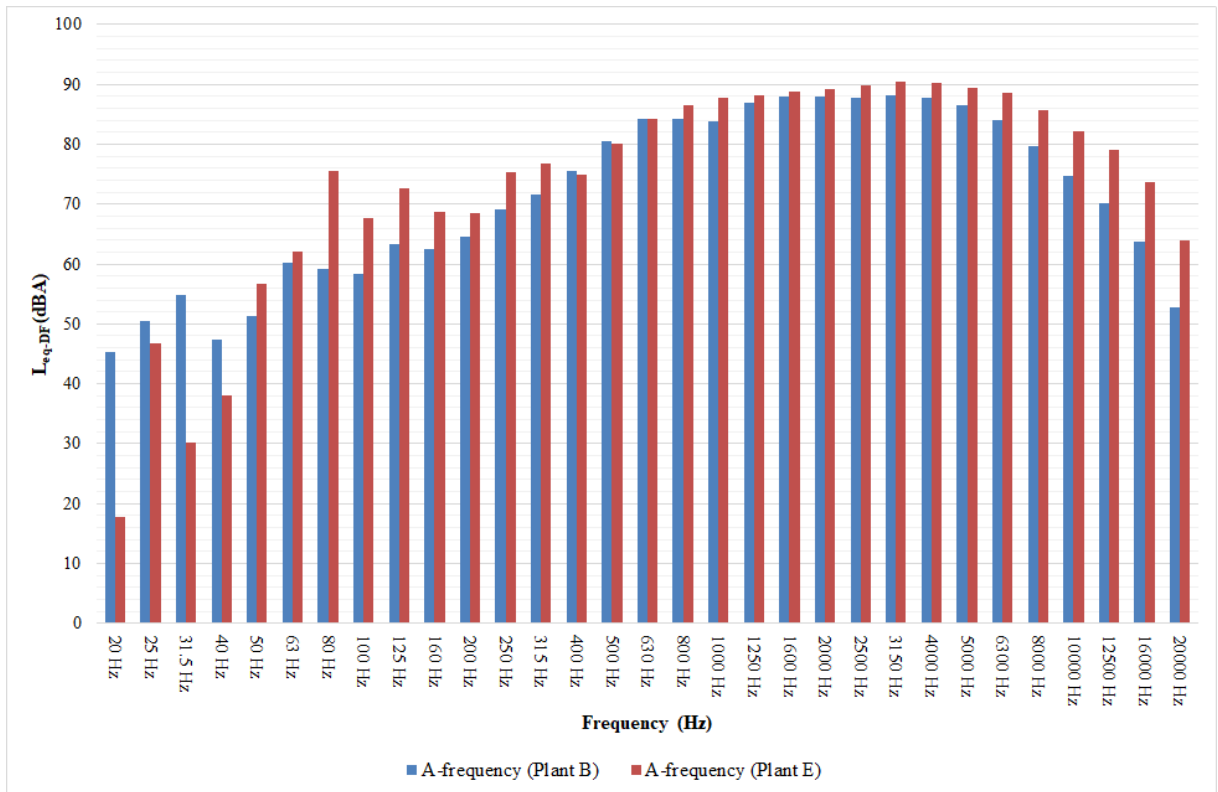
Fig..2. Frequency-noise relationship of aging machine groups.

A, C and Z-weighted equivalent continuous sound levels (L_{eq}) and daily personal noise exposure of workers along with dominant frequencies (DF) for processing machines at all plants are presented in Table 2. The following conclusions have been reached by evaluating the noise data. Among the six plants using gangsaws, there were no significant differences between the $L_{EX,8h}$ levels of the gangsaws in natural stone processing plants A, B, D and H. There were no high-noise machines in the vicinity of the gangsaws and the $L_{EX,8h}$ fluctuated around 89 dBA. The highest and lowest $L_{EX,8h}$ were from plants C and E with 94.4 dBA and 84.1 dBA, respectively. The main reason for the high noise level in plant C was that the gangsaw had been placed in a separate compartment with ST block cutting and head/side cutting machines nearby with high noise intensity (Fig. 3). On the other hand, the noise intensity in plant E was low compared to others due to the small number of machines spread across the large facility. Considering the A-frequency weighting, the highest noise level in the gangsaws corresponded to the medium frequency range in plants A and C (Fig. 4), and to the high frequency range in others. The results obtained were consistent with the literature. Çınar and Şensöğüt [32] reported the noise level of gangsaw machines as 87.51 dBA in two marble factories operating in Konya city, Türkiye.

Table 2. Noise levels and corresponding dominant frequencies (DF) at plants.

Machine [Code]	Plant	A - weighted				C - weighted				Z - weighted			
		$L_{eq\text{-}DF}$ dBA	L_{eq} dBA	$L_{EX,8h}$ dBA	DF (Hz)	$L_{eq\text{-}DF}$ dBC	L_{eq} dBC	$L_{EX,8h}$ dBC	DF (Hz)	$L_{eq\text{-}DF}$ dBZ	L_{eq} dBZ	$L_{EX,8h}$ dBZ	DF (Hz)
Gangsaw [1]	A	80.8	90.1	89.8	630	82.6	91.5	91.2	400	82.6	92.4	92.1	400
	B	80.9	89.5	89.2	4000	82.5	90.9	90.6	400	84.1	92.1	91.8	400
	C	86.1	94.7	94.4	630	88.8	94.7	94.4	500	88.8	96.0	95.7	500
	D	82.3	89.3	89.0	4000	80.5	89.3	89.0	4000	81.3	89.5	89.2	4000
	E	76.5	84.4	84.1	4000	78.2	84.4	84.1	2500	79.0	86.7	86.4	5000
	H	80.2	90.0	89.7	4000	83.6	91.5	91.2	315	83.6	92.3	92.0	315
Bridge cutting [2]	A	88.1	94.5	94.2	3150	86.7	95.0	94.7	3150	87.2	94.9	94.6	3150
	B	87.3	95.3	95.0	2000	88.3	95.4	95.1	1600	88.6	95.8	95.5	1600
	C	79.6	87.8	87.5	800	80.4	87.8	87.5	800	80.4	89.0	88.7	800
	D	92.9	96.0	95.7	4000	91.0	96.7	96.4	2500	91.9	100.2	99.9	4000
	H	75.7	84.9	84.6	2500	75.1	85.6	85.3	2500	75.2	86.3	86.0	2500
ST block cutting [3]	A	90.0	96.6	96.3	3150	87.5	96.8	96.5	3150	87.9	97.5	97.2	3150
	B	90.9	98.4	98.1	3150	95.9	102.6	102.3	100	96.3	103.0	102.7	100
	C	90.9	99.1	98.8	1600	89.6	98.7	98.4	1000	89.9	98.8	98.5	1000
	D	94.7	96.8	96.5	1000	94.7	97.4	97.1	1000	94.7	97.4	97.1	1000
	E	85.3	92.9	92.6	3150	85.0	94.4	94.1	3150	85.5	94.4	94.1	3150
	F	93.7	100.1	99.8	3150	92.0	98.9	98.6	3150	92.5	99.7	99.4	3150
	G	92.3	98.8	98.5	3150	90.3	97.8	97.5	3150	90.8	98.3	98.0	3150
Head/side cutting [4]	A	88.2	94.3	94.0	3150	91.2	93.7	93.4	3150	91.6	95.1	94.8	3150
	B	92.7	99.2	98.9	3150	94.8	99.8	99.5	3150	95.2	100.6	100.3	3150
	C	89.1	97.4	97.1	3150	87.5	96.7	96.4	1250	88.0	97.2	96.9	2150
	D	92.5	99.9	99.6	4000	90.7	99.9	99.6	4000	91.5	99.9	99.6	4000
	F	82.5	91.8	91.5	3150	82.3	92.8	92.5	100	82.6	93.6	93.3	100
	G	88.7	95.3	95.0	4000	86.9	94.6	94.3	4000	87.7	95.2	94.9	4000
	H	83.2	90.4	90.1	4000	81.0	92.1	91.8	160	81.0	92.6	92.3	1660
Trimming [5]	A	86.2	93.7	93.4	1000	86.2	93.7	93.4	1000	86.2	94.0	93.7	1000
	B	87.7	95.7	95.4	3150	92.0	96.5	96.2	25	95.0	98.7	98.4	25
	C	81.4	90.5	90.2	3150	83.0	92.5	92.2	3150	83.0	91.0	90.7	3150
	E	94.4	100.2	99.9	5000	92.6	100.2	99.9	5000	93.9	100.4	100.1	5000
	G	87.4	94.8	94.5	4000	85.7	94.2	93.9	4000	86.4	94.7	94.4	4000
Cement filling [6]	A	78.5	86.7	86.4	3150	82.6	90.3	90.0	25	87.0	91.8	91.5	25
	B	63.6	68.0	67.7	500	66.8	68.0	67.7	500	66.8	79.0	78.7	500
	H	77.2	84.4	84.1	800	72.7	86.4	86.1	800	72.7	86.9	86.6	800
Slab polishing [7]	A	78.0	86.7	86.4	3150	79.5	89.7	89.4	250	83.9	90.0	89.7	250
	C	80.4	89.7	89.4	800	85.8	90.3	90.0	800	85.8	91.4	91.1	800
Narrow polishing [8]	A	80.6	89.1	88.8	3150	83.2	92.5	92.2	250	83.8	93.3	93.0	250
	B	85.9	93.3	93.0	3150	86.9	94.1	93.8	1000	87.0	94.7	94.4	1000
	C	79.5	86.5	86.2	800	80.3	87.8	87.5	800	80.3	87.5	87.2	800
	D	89.4	97.3	97.0	2500	87.8	97.3	97.0	2500	88.1	97.4	97.1	2500
	F	79.6	87.2	86.9	1250	80.3	89.2	88.9	800	80.3	89.3	89.0	800
	G	85.6	93.0	92.7	3150	84.6	93.2	92.9	3150	84.9	93.7	93.4	3150
Aging [9]	B	90.4	99.3	99.0	3150	96.4	101.7	101.4	80	96.9	102.4	102.1	80
	E	88.1	97.2	96.9	3150	91.3	101.8	101.5	31.5	95.8	102.0	101.7	20
In-plant [10]	A	81.3	88.1	87.8	3150	80.6	90.5	90.2	100	82.8	91.0	90.7	100
	C	79.6	86.3	86.0	1000	79.9	87.4	87.1	1000	79.9	87.6	87.3	1000
	D	83.0	92.9	92.6	2500	83.1	92.8	92.5	2500	83.3	93.6	93.3	2500
	E	74.3	88.5	88.2	4000	72.9	89.6	89.3	1000	74.3	89.7	89.4	1000
	H	76.9	86.7	86.4	3150	75.6	88.8	88.5	400	75.6	89.7	89.4	400

Chamfering [11]	A	83.0	90.0	89.7	3150	81.3	91.3	91.0	3150	82.8	91.8	91.5	3150
	C	78.7	86.8	86.5	1600	79.5	86.8	86.5	800	79.5	88.0	87.7	800
Splitting [12]	B	94.7	101.6	101.3	3150	93.0	101.6	101.3	3150	93.5	101.5	101.2	3150
	C	85.6	93.8	93.5	3150	79.7	95.6	95.3	3150	79.9	93.8	93.5	3150
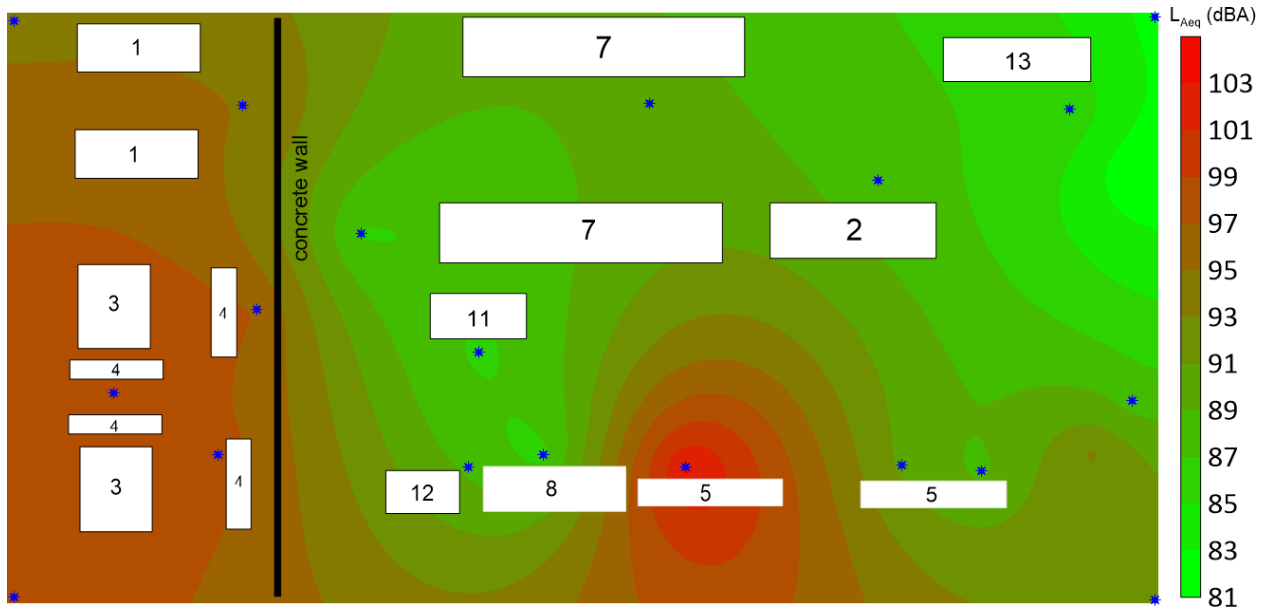
Fig. 3. A-weighted L_{Aeq} map of Plant C (storage area [13], measuring point [✳]).
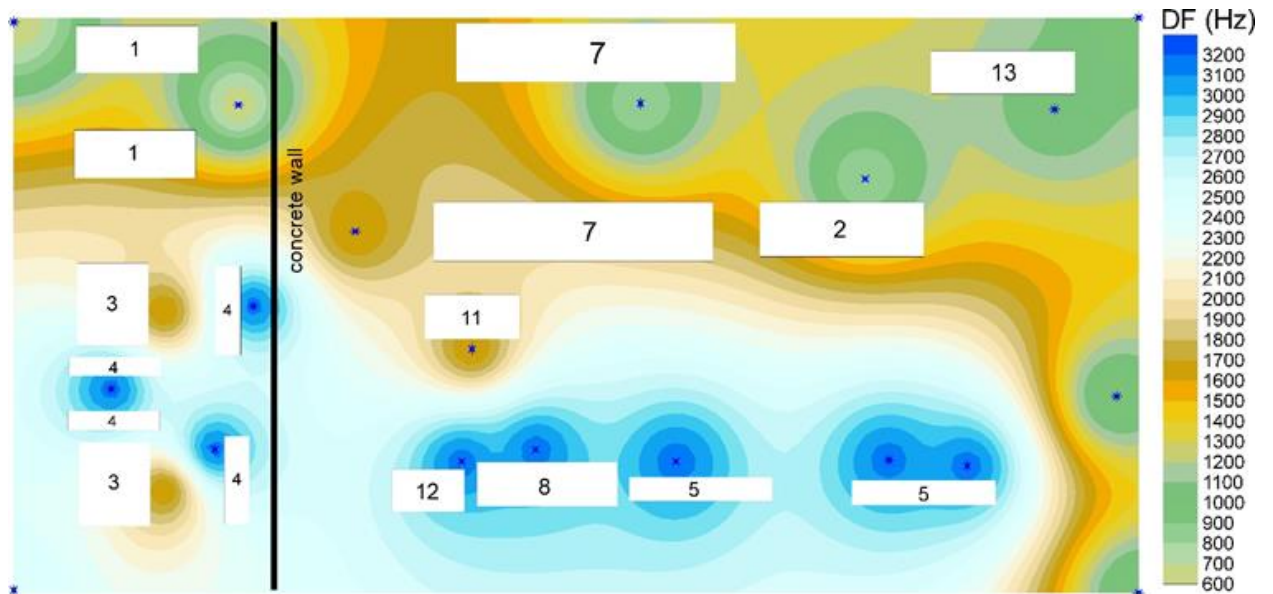
Fig.4. A-weighted frequency map of Plant C (a).

Five bridge cutting machines were monitored within the scope of the study. The lowest daily equivalent noise level of 84.6 dBA was from plant H, where a small number of processing machines had been spread over a relatively large factory area (Fig. 5). Similar to gangsaws, the bridge cutting machines in plants A, B and D were placed in such a way that there were no other high-noise processing machines nearby. The average $L_{EX,8h}$ of the bridge cutting machines in these three plants was 95 dBA. The highest noise levels in bridge cutting machines fell into the medium frequency range in natural stone processing plants B and C, and to the high frequency range in other plants. Fig. 6 illustrates the A-frequency weighted dominant frequency distribution across plant H.

Fig. 5. A-weighted L_{Aeq} map of Plant H.
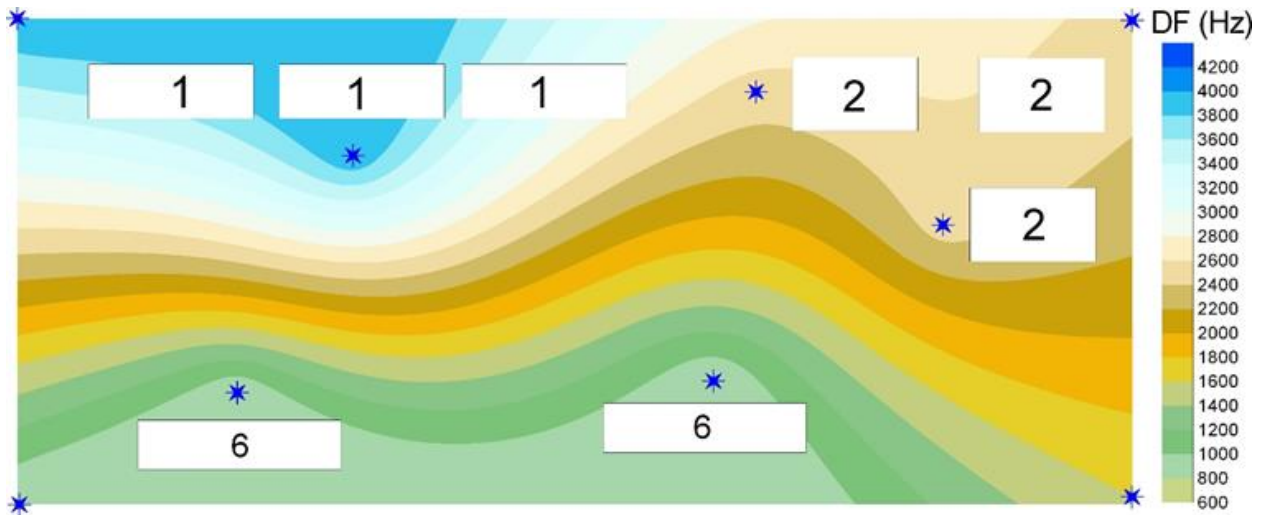
Fig. 6. A-weighted frequency map of Plant H.

One of the most widely monitored equipment in the study was the ST block cutting machine with seven units. The $L_{EX,8h}$ of ST block cutting machines ranged between 96.3 dBA and 99.8 dBA averaging at 98 dBA in all plants except plant E. Adjacent to the ST machines in these plants, there were head cutting machines that produced high

levels of noise. These findings are consistent with the noise level of the ST machine of 96 dBA at a marble factory in South Aceh, Indonesia by Lindawati et al [34]. However, the $L_{EX,8h}$ in plant E, where the processing machines had been scattered over wide open spaces, has decreased to 92 dBA (Fig. 7). Considering the A-frequency weighting, the highest noise levels in the ST machines were in the medium frequency range in plants C and D, and in the high frequency range in other processing plants. The dominant frequency distribution of the processing machines in plant E is presented in Fig. 8.
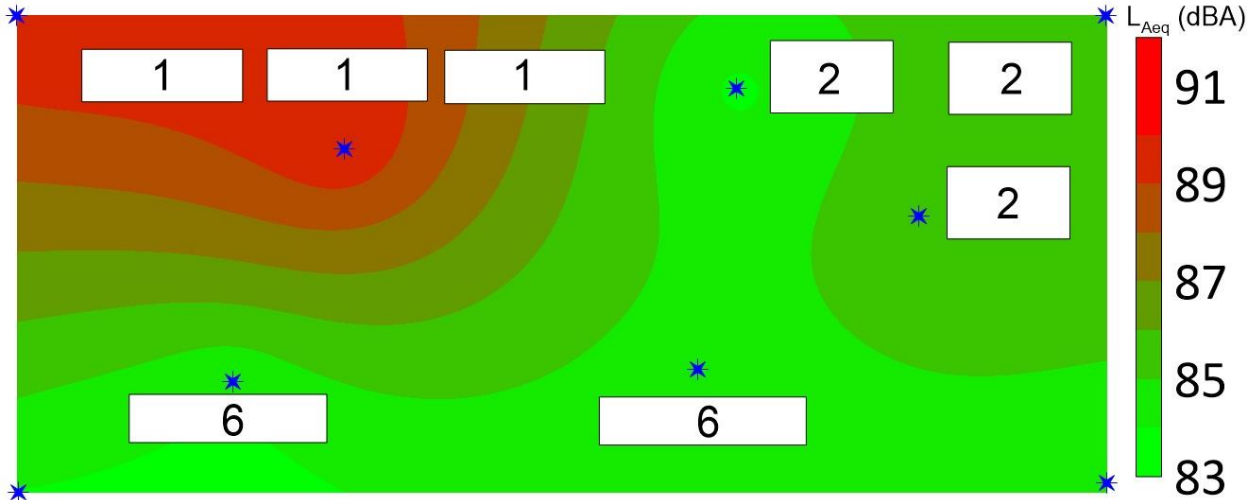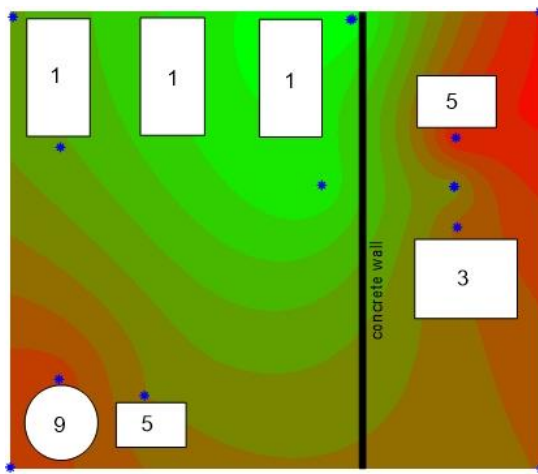

Fig. 7. A-weighted L_{Aeq} map of Plant E.   Fig. 8. A-weighted frequency map of Plant E.
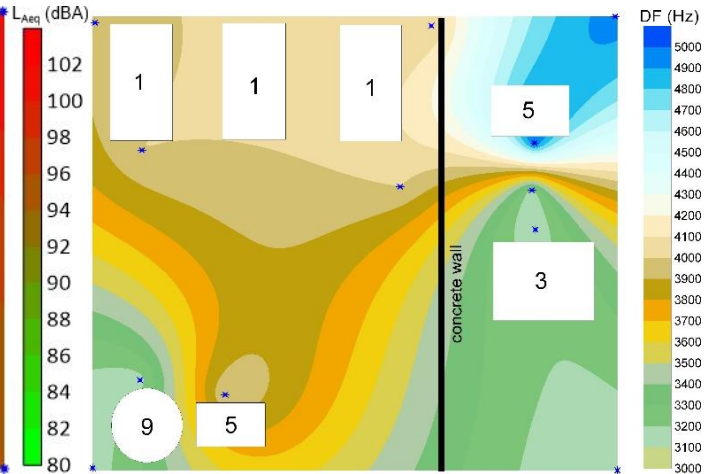
Another machine with the highest noise measurement rounds is the head/side cutting machine with 7 units. Again, as the head/side cutting machines operating in plants B, C and D were placed in isolated locations together with the ST machines, their noise levels were higher than those in other natural stone processing plants. Daily equivalent noise levels of the machines varied between the lowest 90.1 dBA (plant H) and the highest 99.6 dBA (plant D). The highest noise level of the machines in all plants fell into the high frequency region.

Among the five plants with trimming machines, the equivalent daily noise levels of plants B and E were found higher than the others as they were located adjacent to the aging machines. The $L_{EX,8h}$ values of the trimming machines varied between 90.2 dBA and 99.9 dBA with an average of 94.7 dBA, which is consistent with the study of Çınar and Şensöğüt [32] in which the average daily equivalent noise level of the trimming machine was 96.7 dBA. Except for the natural stone processing plant A, where the highest noise level is in the medium frequency region, the highest noise level is in the high frequency region in all other processing plants. As a typical example, the noise and dominant frequency maps of plant G are given in Fig.9.– Fig.10.
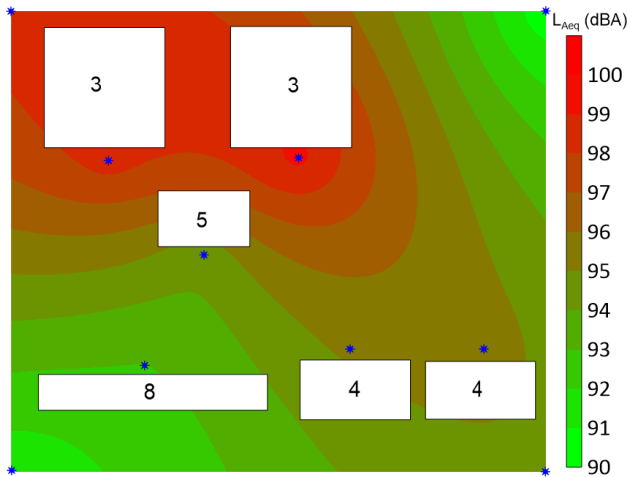
Fig. 9. A-weighted L_{Aeq} map of Plant G.
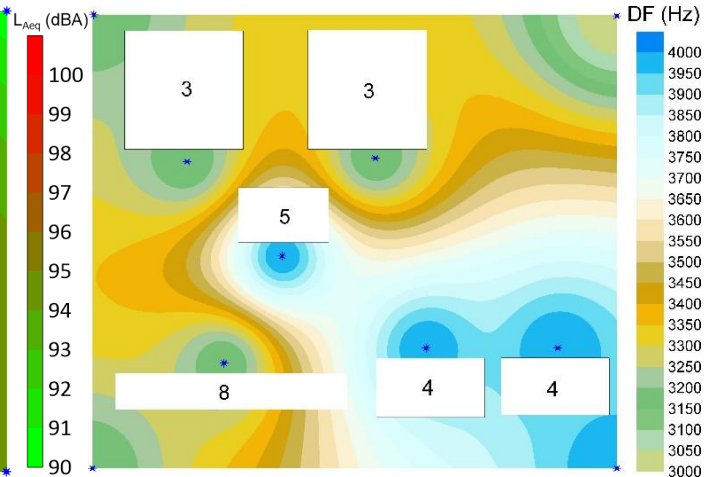
Fig. 10. A-weighted frequency map of Plant G.

The noise levels of the narrow polishing machines in the six plants changed from 86.2 dBA at plant C with no high-noise emitting machine alongside narrow polishing line to 97.0 dBA at plant D with ST, head cutting and bridge cutting machines located near the narrow polishing line. Excluding plant D, where high-noise processing machines were located together, the noise levels in other natural stone processing plants were fairly balanced and averaged at 90.7 dBA. With reference to previous studies, Çınar and Şensöğüt [32] measured the noise level of the polishing machine as 89.55 dBA in two marble factories. As for the dominant frequency distribution, the highest noise levels were in the medium frequency range in plants C and F, and in the high frequency range in other natural stone processing plants.

Three cement filling machines were sampled in the study. The $L_{EX,8h}$ in plants A and H was found to be quite close to each other due to the fact that filling machines were in a location with other natural stone processing machines of the same type. As for the cement filling machine at plant B, which operated in a separate compartment, the $L_{EX,8h}$ was as low as 67.7 dBA. For the cement filling machines, the maximum noise levels fell into the medium frequency range in plants B and H, and to the high frequency range in plant A.

The daily equivalent noise levels in the slab polishing machines that operated in wide and open places in plants A (Fig. 11) and C were similar. The maximum noise level was in the high frequency range in plant A (Fig. 12) while it was in the medium frequency range in plant C.
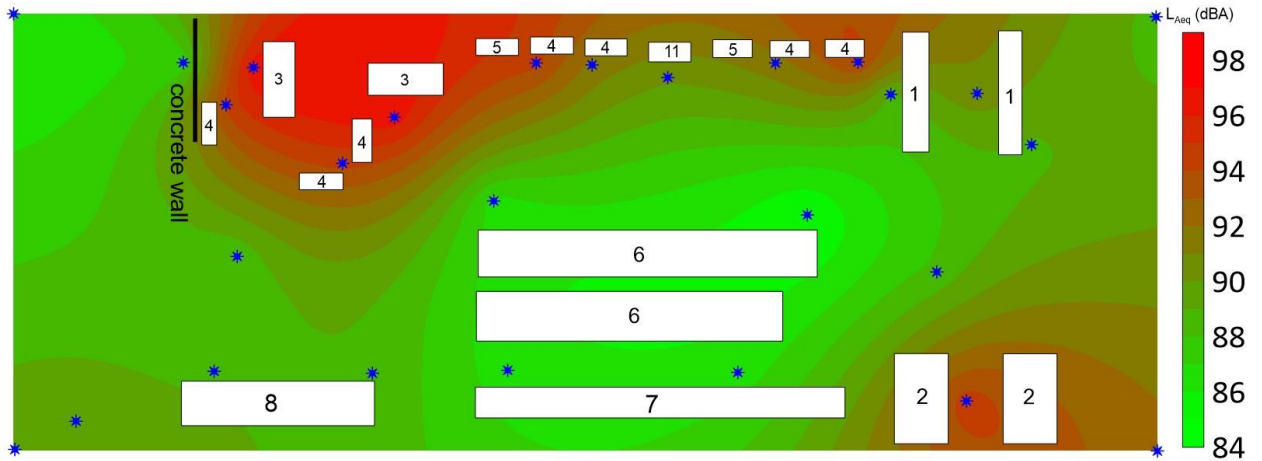
Fig. 11. A-weighted L_{Aeq} map of Plant A.
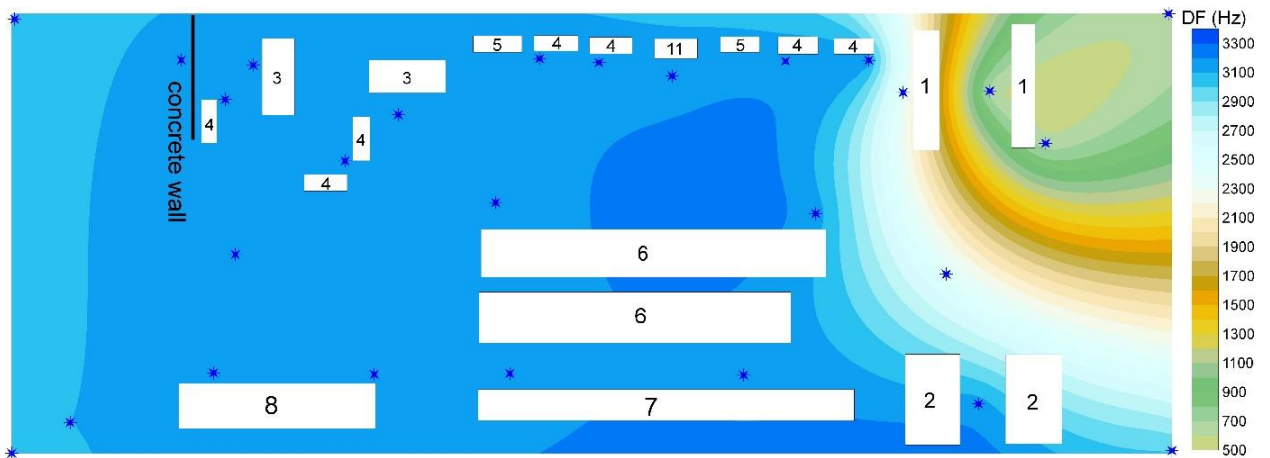
Fig. 12. A-weighted frequency map of Plant A.

The equivalent daily noise levels of the two chamfering machines operating in plants C and A were 86.5 dBA and 89.7 dBA, respectively. The tighter layout of plant A was reflected in the higher noise level. The highest noise level in plant A was in the high frequency range while it was in the medium frequency range in plant C.

In the study, splitting machines used in plants B and C were also sampled. $L_{EX,8h}$ levels were calculated as 101.3 dBA at plant B and 93.5 dBA at plant C. The high noise level at plant B has been attributed to the splitting machine being in an obstructed environment with high-noise emitting head cutting and ST machines. Referring to previous studies, Çınar and Şensöğüt [32] reported the noise level of two splitting machines in marble plants in Konya, Turkey as 94.44 dBA. Noise generated by both machines were in high frequency range. Comparable $L_{EX,8h}$ levels were achieved of the aging machines used in plants B (Fig. 13) and E. This condition was attributed to the fact that the aging machines were surrounded by other high-noise emitting machines. The highest noise level of the machines in two plants were located in the high frequency region (Fig. 14).
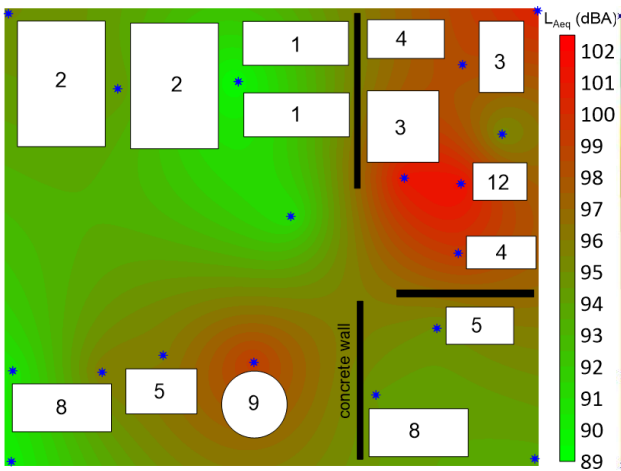
Fig. 13 A-weighted L_{Aeq} map of Plant B.
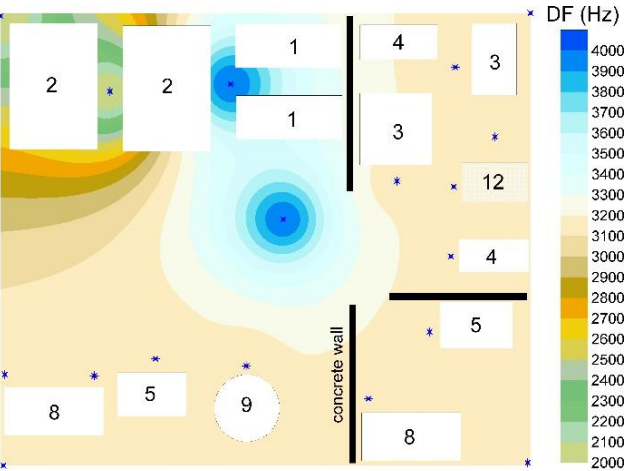
Fig. 14. A-weighted frequency map of Plant B.

Representative ambient noise levels varied between 86.0 dBA and 92.6 dBA, with an average of 88.2 dBA for the processing plants. Nevertheless, differences in the layout planning of natural stone processing machines and the use of equipment with varying noise levels were also reflected as significant variations in the sound level ranges (lowest to highest) in the plants, as follows: 7 dBA at plant H, 10 dBA at plant G, 11 dBA at plant D, 13 dBA at plants A and F, 17 dBA at plant B, 21 dBA at plant E and 22 dBA at plant C.

Considering the A frequency weighting, the dominant frequency range of natural stone processing plants was as follows: 630 Hz - 3150 Hz at plant A, 500 Hz - 4000 Hz at plant B, 630 Hz - 3150 Hz at plant C, 1000 Hz - 4000 Hz at plant D, 3150 Hz - 5000 Hz at plant E, 1250 Hz - 3150 Hz at plant F, 3150 Hz - 4000 Hz at plant G and 800 Hz - 4000 Hz at plant H. Thus, plants E and G were characterized by high frequency noise, while other natural stone processing plants were characterized by medium and high frequency noise.

Again, taking into account the A frequency weighting, the dominant frequency range of natural stone processing machinery among plants is as follows; gangsaws: 630 Hz - 4000 Hz, bridge cutting machines: 800 Hz - 4000 Hz, ST block cutting machines: 1000 Hz - 3150 Hz, head/side cutting machines: 3150 Hz - 4000 Hz, trimming machines: 1000 Hz - 5000 Hz, cement filling machines: 500 Hz - 3150 Hz, slab and narrow polishing machines: 800 Hz - 3150 Hz, aging and splitting machines: 3150 Hz and chamfering machines: 1600 Hz - 3150 Hz. From these findings, which are in line with Engin et al [37], it is evident that regardless of operational and occupational parameters, aging and splitting machines consistently produced the same high-frequency noise, while different types of polishing machines also produced noise in the same frequency range. Head/side cutting machines operated in a narrow band of the high frequency range, while other processing machines were spread over the medium-to-high frequency ranges.

Effects of the natural stone processing machine types, the layout of the machines within plants and the types of natural stones on the noise generated were investigated through hypothesis tests on a statistical analysis package [47]. The level of significance was set at 5 %. The compliance of the data with normal distribution was determined by applying the Kolmogorov-Smirnov test and the one-way variance analysis was utilized in hypothesis tests. The mean and standard deviation of the $L_{Ex,8h}$ representing some 510 measurements was 92.80 dBA ± 5.21 dBA.

The variation of and the differences between noise levels of natural stone processing plants were analyzed using all the data recorded in each facility. Plants B, D, F and G generated averaged noise levels in excess of 95 dBA, while plant H appeared as the quietest one with an average daily equivalent noise level of 86.95 dBA. The results of one-way variance analysis presented in Table 3 reveal that there are statistically significant differences between daily equivalent noise exposures ($pL_{EX,8h} < 0.001$). Accordingly, while the difference between the $L_{EX,8h}$ levels at

plants H (group a), A, C and E (group b) and B, D, F and G (group c) was not statistically significant within a specific group, it was significant on an intergroup basis.

Table 3. Hypothesis testing on plant-based daily equivalent noise exposure.

Test	A	B	C	D	E	F	G	H	p
Duncan	92.38 ± 3.42[b]	95.42 ± 6.02[c]	92.10 ± 5.25[b]	95.35 ± 4.52[c]	90.98 ± 6.19[b]	95.68 ± 6.19[c]	95.51 ± 2.38[c]	86.95 ± 5.22[a]	<0.001

a-c: Means sharing a letter in their superscript are not significantly different at the .05 level.

Table 4 summarizes the results of hypothesis tests showing that the difference between the daily equivalent noise levels of all machine categories in the different plants was statistically significant ($p < 0.001$). Considering the gangsaws, three groups with low (plant E), medium (plants A, B, D, H) and high (plant C) noise levels emerged, with a statistically significant difference between the $L_{EX,8h}$ levels. Bridge cutting machines were divided into three groups with low (plants C and H), medium (plants A and B) and high (plant D) noise levels through hypothesis tests. Though plants within each group did not differ in terms of $L_{EX,8h}$ levels, groups showed statistically significant differences ($p < 0.001$). ST block cutting machines were also divided into groups as low (plant E), lower-medium (plants A, D, G), upper-medium (plants C, F, G) and high (plant B), where intergroup differences were statistically significant. Hypothesis tests revealed a statistically significant difference in $L_{EX,8h}$ levels between head/side cutting machine groups of low (plants A, F, G and H), medium (plants A, B, C and G) and high (plants C and D) at the 0.05 level. Considering plants A and G equivalent, there was a statistically significant difference between $L_{EX,8h}$ levels of trimming machines. Similarly, statistically significant differences were found between the $L_{EX,8h}$ levels of all cement filling machines. Hypothesis tests categorized the narrow polishing machines into groups of low (plant C), medium (plants A, B, F, G) and high (plant D) $L_{EX,8h}$ levels. While there was no statistically significant difference between the $L_{EX,8h}$ levels of the narrow polishing machines within each group, there was a significant difference between the groups at the 0.05 level. Hypothesis tests were used to investigate whether there was a statistically significant difference between the $L_{EX,8h}$ levels across working environments. Plants C, E and H; A, E and H; D and H were classified in low, medium and high-noise groups, respectively. That plant H is included in all groups has shown that the $L_{EX,8h}$ levels in the working environment of this plant can be considered equivalent to other facilities. Nevertheless, the difference between the $L_{EX,8h}$ levels of the groups was found to be statistically significant at the 0.05 level.

Table 4. Hypothesis testing on machine-based daily equivalent noise exposure.

Machine	Test	A	B	C	D	E	F	G	H	p
Gangsaw	Tukey	91.05 ± 1.65[b]	90.54 ± 3.18[b]	94.83 ± 0.75[c]	89.07 ± 0.12[b]	84.90 ± 4.15[a]	-	-	91.00 ± 1.05[b]	<0.001
Bridge cutting	Tukey	94.51 ± 1.88[b]	95.03 ± 1.06[b]	87.90 ± 0.69[a]	99.85 ± 3.93[c]		-	-	85.31 ± 1.59[a]	<0.001
ST cutting	Duncan	96.75 ± 0.99[b]	101.03 ± 3.07[d]	98.58 ± 0.96[c]	96.70 ± 0.35[b]	92.38 ± 1.97[a]	99.23 ± 1.48[c]	97.98 ± 0.79[bc]	-	<0.001
Head/side cutting	Duncan	94.29 ± 3.16[ab]	99.57 ± 2.03[b]	96.84 ± 3.24[bc]	99.60 ± 0.00[c]		92.43 ± 0.90[a]	94.73 ± 1.40[ab]	91.40 ± 1.15[a]	<0.001
Trimming	Duncan	93.50 ± 0.17[b]	96.73 ± 1.72[c]	90.29 ± 2.48[a]	-	99.97 ± 0.12[d]	-	94.27 ± 0.69[b]	-	<0.001
Cement filling	Tukey	89.28 ± 2.88[c]	71.37 ± 6.35[a]		-		-	-	85.66 ± 1.37[b]	<0.001
Narrow polishing	Duncan	90.61 ± 2.16[b]	93.66 ± 2.90[b]	86.73 ± 0.92[a]	97.03 ± 0.06[c]		88.27 ± 1.19[b]	93.01 ± 1.79[b]	-	<0.001
In-plant	Duncan	89.52 ± 1.46[b]	-	86.45 ± 1.89[a]	92.84 ± 3.46[c]	88.59 ± 4.74[ab]	-	-	88.10 ± 1.54[abc]	<0.001

a-d: Means sharing a letter in their superscript in a row are not significantly different at the .05 level.

The effect of the natural stone type on the noise level has also been investigated. Table 5 illustrates that rocks processed at five plants and categorized under the limestone group had lower $L_{EX,8h}$ levels, while the group consisting of yellow and classical travertines caused higher noise emission. The difference between the $L_{EX,8h}$ levels of the groups was statistically significant.

Table 5. Hypothesis testing on natural stone type-based daily equivalent noise exposure.

Test	Yellow travertine	Limestone	Classic Travertine	p
Tamhane	94.46 ± 6.03^b	92.00 ± 4.61^a	97.01 ± 4.90^b	<0.001

a-b: Means sharing a letter in their superscript are not significantly different at the .05 level.

Independent sample t-tests were applied to decide whether there was a statistically significant difference between the $L_{EX,8h}$ levels of slab polishing, chamfering, splitting and aging machines. There is statistically no significant difference between the aging machines in plants B and E (p = 0.280), at the 0.05 level (Table 6). On the contrary, there is a statistically significant difference between the slab polishing machines in plants A and C (p = 0.016), chamfering machines in plants A and C (p < 0.001) and splitting machines in plants B and C (p < 0.001).

Table 6. Independent sample t-tests on machine-based daily equivalent noise exposure levels.

Machines	Plant	N	Mean ± SD	Test statistic	p^1
Slab polishing	A	9	88.21 ± 1.71	-2.682	0.016
	C	9	90.30 ± 1.60		
Chamfering	A	9	90.68 ± 0.89	6.643	< 0.001
	C	3	86.90 ± 0.69		
Splitting	B	3	101.27 ± 0.06	6.210	< 0.001
	C	9	93.27 ± 3.86		
Aging	B	9	100.82 ± 1.49	1.386	0.280
	E	3	98.50 ± 2.77		

[1] Independent sample t-test

4. Conclusions and Recommendations

The results obtained in this study, which covered a total of 510 noise exposure measurements recorded from processing machinery used in eight natural stone processing plants in Sivas, Turkey and its surroundings, are given below.

ST block cutting, trimming, splitting, aging, bridge cutting, narrow polishing and head/side cutting machines have produced high levels of noise. Gangsaws, chamfering, slab polishing and cement filling machines emitted relatively lower levels of noise. However, differences were detected between the noise levels of a certain type of processing machinery in different natural stone processing plants. This discrepancy was attributed to the change in the types of natural stones processed, plant layout and the number of processing machines operating simultaneously during the measurements.

In all other production plants except plant E, the noise level in gangsaw machines exceeded 85 dBA, the highest exposure action value, according to the *Regulation on the Protection of Employees from Noise-Related Risks*. Every plant except H had noise levels in bridge cutting machines that above 85 dBA, the highest exposure action value. The noise level in ST block cutting, head/side cutting, trimming, slab polishing, narrow polishing, aging, chamfering, and splitting machines measured in all natural stone production facilities exceeds the maximum exposure action value. Regarding the cement filling machines, the noise level at Plant B was lower than the lowest exposure action value set in the applicable regulation, owing primarily to the fact that the filling machine in this facility was located in a different compartment. In contrast, the noise level in plant A exceeds the maximum exposure action value.

When the noise exposed by the workers in natural stone processing plants is evaluated with the A-frequency weighting, the highest noise levels varied between 630 Hz - 5000 Hz and concentrated at 3150 Hz. Thus, the dominant frequencies fluctuated between medium and high frequency ranges. It should be noted that no machines in any natural stone processing plants have produced noise in the low frequency region.

Considering the C-frequency weighting, the noise generated in the plants was distributed over all frequency ranges. Also, in C and Z-frequency weightings, the frequency regions with the highest noise level were close.

Examining $L_{EX,8h}$ values revealed that a difference of less than 2 dB was found between $L_{EX,8h}$ values based on A and C-frequency weightings (dBC − dBA ≤ 2), and less than 1 dB between C and Z-frequency weightings (dBZ - dBC ≤ 1). Therefore, it would be beneficial to conduct high frequency sound measurements with A and C-frequency weightings. But, it may not be necessary to measure noise based on Z-frequency weighting.

The noise levels that employees in natural stone processing plants are exposed to were mostly in the 3rd degree noise class, which may cause physiological reactions and headaches on the employees.

Employees in natural stone processing industries are exposed to noise levels that much exceed the maximum exposure action value specified in the *Regulation on the Protection of Employees from Noise-Related Risks*. Employees should be informed at regular intervals on the steps that will be taken to prevent noise-induced hearing loss from progressing to an occupational disease. Permanent hearing loss cannot be treated, although temporary hearing loss can. Facilities that process natural stone should periodically assess the noise levels and implement the appropriate safety measures. The battle against noise needs to be initiated at the source, carried out between the source and the recipient, and then concluded at the receiver. Training on the proper and regular use of personal protective equipment should continue, checks should be performed, and workers should be trained on how to perform the checks. Furthermore, the frequency of noise at the source must be considered while selecting personal protection equipment and materials to reduce noise at the source. Wearing ear protection with muffs is advised because the noise that employees in natural stone processing factories are typically exposed to is in the high frequency range. Depending on their age and level of sensitivity, workers in these facilities who do not wear ear protection could have side effects such headaches, tinnitus, fatigue, dizziness, and nausea in addition to elevated blood pressure and headaches. When developing the layout of machines in newly built natural stone processing facilities, it is more appropriate in terms of worker health to plan the facility while taking into account the noise and dominant frequency values of the machines as well as the production line.

Acknowledgements

Author Contributions

Zekeriya Duran and Bülent Erdem envisioned and planned the research project. Zekeriya Duran, Tuğba Doğan and Mehmet Genç carried out the material preparation and data gathering tasks. Zekeriya Duran and Tuğba Doğan conducted the statistical analyses. Zekeriya Duran, Bülent Erdem, Tuğba Doğan and Mehmet Genç all contributed to the preparation of the article format. All authors commented on the final form of the manuscript.

References

[1] Brüel & Kjær, "Environmental Noise", Nærum: Brüel & Kjær Sound & Vibration Measurement A/S, 2001.
[2] EASHW, "Noise in Figures", Luxembourg: Office for Official Publications of the European Communities, 2005.
[3] A. A. Erdoğan, "Hearing Loss and Approaches to Hearing Loss in Elderly", (In Turkish), *TJFMPC*, vol. 10, no. 1, pp. 25–33, Jan. 2016.
[4] K. Reinhold et al., "Exposure to High or Low Frequency Noise at Workplaces: Differences between Assessment, Health Complaints and Implementation of Adequate Personal Protective Equipment", *Agron. Res.*, vol. 12, no. 3, pp. 895–906, May. 2014.

[5] B. Smagowska and M. Pawlaczyk-Łuszczyńska, "Effects of Ultrasonic Noise on the Human Body—A Bibliographic Review", *Int. J. Occup. Saf. Ergon.*, vol. 19, no. 2, pp. 195-202, Jan. 2015, doi: 10.1080/10803548.2013.11076978.

[6] M. D. Fletcher et al., "Effects of Very High-Frequency Sound and Ultrasound on Humans. Part I: Adverse Symptoms after Exposure to Audible Very-High Frequency Sound", *J. Acoust. Soc. Am.*, vol. 144, no. 4, pp. 2511–2520, Oct. 2018, doi: 10.1121/1.5063819.

[7] W. Babisch et al., "Traffic Noise and Risk of Myocardial Infarction", *J. Epidemiol.*, vol. 16, no. 1, pp. 33–40, Jan. 2005, doi: 10.1097/01.ede.0000147104.84424.24

[8] W. Babisch, "Road Traffic Noise and Cardiovascular Risk", *Noise Health*, vol. 10, no. 38, pp. 27–33, Jan. 2008, doi: 10.4103/1463-1741.39005

[9] S. A. Stansfeld and M. P. Matheson, "Noise Pollution: Non-Auditory Effects on Health", *Br. Med. Bull.*, vol. 68, no. 1 pp. 243–257, Dec. 2003, doi: 10.1093/bmb/ldg033

[10] M. Kaltenbach et al., "Health Consequences of Aircraft Noise", *Dtsch. Arztebl. Int.*, vol. 105, no. 31-32, pp. 548–556, Aug. 2008, doi: 10.3238/arztebl.2008.0548

[11] M. R. H. C. Harger and A. Barbosa-Branco, "Effects on Hearing due to the Occupational Noise Exposure of Marble Industry Workers in the Federal District, Brazil", *Rev. Assoc. Med. Bras.*, vol. 50, no. 4, pp. 396–399, Oct-Dec. 2004, doi: 10.1590/s0104-42302004000400029.

[12] S. Kumari et al., "The Effect of Noise Pollution on Hearing in Marble Factory Workers of Ajmer, Rajasthan: A Case Study", *Int. J. Clin. Biomed. Res.*, vol. 1, no. 4, pp. 34–38, Oct. 2015.

[13] A. Jain et al., "Impact of Noise Exposure on Hearing Acuity of Marble Factory Workers", *Indian J. Physiol. Pharmacol.*, vol. 61, no. 3, pp. 295–301, Mar. 2017.

[14] L. Chen and S. E. Brueck, "Noise and Lead Exposures at an Outdoor Firing Range – California", Cincinnati: National Institute for Occupational Safety and Health, Sep. 2011.

[15] D. P. Driscoll, *"Noise - Measurement and its Effects"*, Evergreen: Associates in Acoustics Inc, 2009.

[16] J. P. Guyer, "Introduction to Building Acoustics and Noise Control", New Jersey: Continuing Education and Development, Inc., 2009.

[17] S. Wise and G. Leventhall, "Active Noise Control as a Solution to Low Frequency Noise Problems", *J. Low Freq. Noise. V. A.*, vol. 29, no. 2, pp. 129–137, Jun. 2010, doi: 10.1260/0263-0923.29.2.129.

[18] E. R. Reeves et al., "Noise Control in Underground Metal Mining", Pittsburgh: National Institute for Occupational Safety and Health, Dec. 2009.

[19]   H. Møller and C. S. Pedersen, "Hearing at Low and Infrasonic Frequencies", *Noise Health*, vol. 6, no. 23, pp. 37–57. Apr-Jun. 2004.

[20] K. Bolin et al., "Infrasound and Low Frequency Noise from Wind Turbines: Exposure and Health Effects", *Environ. Res. Lett.*, vol. 6 pp. 1–6, Sep. 2011, doi: 10.1088/1748-9326/6/3/035103

[21] J. A. Alves et al., "The Influence of Low–Frequency Noise Pollution on the Quality of Life and Place in Sustainable Cities: A Case Study From Northern Portugal", *Sustde.*, vol. 7, no. 10, pp. 13920–13946. Jun. 2015, doi.org/10.3390/su71013920.

[22] P. Thorsson et al., "Low–Frequency Outdoor–Indoor Noise Level Difference for Wind Turbine Assessment", *J. Acoust. Soc. Am.*, vol. 143, no. 3, pp. 206–210, Mar. 2018, doi: 10.1121/1.5027018.

[23] C–H. Chiu and C.S–C. Lung, "Assessment of Low–Frequency Noise from Wind Turbines under Different Weather Conditions", *J. Environ. Health. Sci. Eng.*, vol. 18, pp. 505–514, May. 2020, doi: 10.1007/s40201-020-00478-9

[24] BRD, "Technical Discussion", Wind Gap: BRD Noise and Vibration Control, Inc., 2017.

[25] Z. Duran, et al., "Frequency–Noise Relation of Mining Machines", (In Turkish), *SUJEST*, vol. 6, no. 4, pp. 737–752, Jan. 2018, doi.org/10.15317/Scitech.2018.164.

[26] S. Bilgili et al., "Environmental Noise Measurement and Assessment Guide", (In Turkish), Ankara: Ministry of Labor and Social Security, 2011.

[27] Z. Özçetin, "Noise Control Analysis of Conservatory Buildings and a Case Study: Conservatory Building of Mamak Municipality Ankara Musiki Muallim Mektebi", (In Turkish), Ankara: Gazi University, Oct. 2011.

[28] M. E. Boger et al., "The Noise Spectrum Influence on Noise–Induced Hearing Loss Prevalence in Workers", *Braz. J. Otorhinolaryngol.*, vol. 75, no. 3, pp. 328–334, May-Jun. 2009, doi: 10.1016/s1808-8694(15)30646-7.

[29] F. J. Aukour and M. I. Al–Qinna, "Marble Production and Environmental Constrains: Case Study from Zarqa Governorate", *Jordan J. Earth Environ. Sci.*, vol. 1, no. 1, pp. 11–21, Mar. 2008.

[30] R. P. Neto et al., "Quantitative Noise Analysis at Two Marble Finishing Plants in Olinda, Pernambuco, Brazil", *Work*, vol. 41, pp. 5850–5852, 2012, doi: 10.3233/WOR-2012-0972-5850.

[31] A. A. Hanieh et al., "Sustainable Development of Stone and Marble Sector in Palestine", *J. Clean. Prod.*, vol. 84, pp. 581–588, Oct. 2013. doi.org/10.1016/j.jclepro.2013.10.045.

[32] İ. Çınar and C. Şensöğüt, "Determination of Exposure Value of Noise on Workers in Marble Processing Plant", (In Turkish), *Proc. Symp. Occup. Health Safe'2015*, Turkey, Adana, pp. 335–344, 2015.

[33] A. E. Arıtan and M. Tümer, "Investigation of Environmental Conditions in a Natural Stone Factory Using Monolamella Machine", (In Turkish), *J. Fac. Eng. Arch. Cukurova Univ.*, vol. 32, no. 4, pp. 185–192, Dec. 2017.

[34] L. Lindawati et al., "Analysis of Noise Level Generated by Stone Cutter Machine: A Case Study in Marble Production Unit, South Aceh", *J. Tech. Eng. Innov.*, vol. 3, no. 1, pp 53–58, January-June 2018, doi: 10.31572/inotera.Vol3.Iss1.2018.ID48.

[35] F–J. Huang et al., "The Assessment of Exposure to Occupational Noise and Hearing Loss for Stoneworkers in Taiwan", *Noise Health*, vol. 20, no. 95, pp. 146–151, Jul-Aug. 2018, doi: 10.4103/nah.NAH_45_17.

[36]   H. T. Taştan, "Assessment of Noise Exposure in Granite Factories", (In Turkish), Ankara: Ministry of Labor and Social Security, 2016.

[37] İ. C. Engin et al., "Determination of Risky Areas at the Marble Workshops in Terms of Noise", *Acoust. Aust.*, vol. 47, pp. 79–90, Nov. 2018,

doi: 10.1007/s40857-018-0146-7.

[38] N. Şengün et al., "Investigation into Variations of Saw Rotation and Noise Level in Cutting by Circular Saw", (In Turkish), *PAJES*, vol. 19, no. 3, pp. 121–126, Oct. 2012, doi: 10.5505/pajes.2013.98698.

[39] A. Fişne, "Investigation of Noise Conditions, Statistical Analysis of Noise Exposure Levels and Risk Assessment in Turkish Hard Coal Enterprise", İstanbul: Istanbul Technical University Institute of Science and Technology (PhD thesis), 2008.

[40] S. K. Akın and M. Alptekin, "Examining the performance of thermal insulation materials used in buildings for noise insulation", *Case Studies in Thermal Engineering,* vol, 51, pp.1–8, Nov. 2023, https://doi.org/10.1016/j.csite.2023.103556.

[41] TS EN ISO 9612, "Acoustics – Determination of Occupational Noise Exposure – Engineering Method", Ankara: Turkish Standards Institution, 2009.

[42] TS EN IEC 60942 ISO, "Electroacoustics – Sound Calibrators"*,* Ankara: Turkish Standards Institution, 2018.

[43] TS 2607 ISO, "Acoustics – Determination of Occupational Noise Exposure and Estimation of Noise–induced Hearing Impairment", Ankara: Turkish Standards Institution, 1999.

[44] A. Özmen, "Explain the Provisions of the Regulations Regarding the Protection of Employees from Noise – Related Risks with Examples and Field Applications"*,* (In Turkish), Ankara: Ministry of Labor and Social Security, 2014.

[45] Golden Software, "Surfer User's Guide", Golden: Golden Software, LLC, 2019.

[46] Svantek, "SvanPC++ User Manual", Warsaw: SVANTEK Sp. z o.o., 2015.

[47] IBM, "IBM SPSS Statistics 23 Core System User's Guide", New York: IBM Corporation, 2018.

REVIEW ARTICLE

Evolving trends and advanced applications of engineering materials in contemporary aircraft: a review

Muhammad Hasan Izzuddin[a], Merve Akin[b], Muhammed Bekmezci[c], Guray Kaya[d]*, Fatih Sen[e]

[a]*Sen Research Group, Department of Biochemistry, Kütahya Dumlupinar University, 43100, Kutaya, Türkiye, ORCID:0009-0005-1635-0309*
[b]*Sen Research Group, Department of Biochemistry, Kütahya Dumlupinar University, 43100, Kutaya, Türkiye, ORCID: 0000-0001-6003-0613*
[c]*Sen Research Group, Department of Biochemistry, Kütahya Dumlupinar University, 43100, Kutaya, Türkiye, ORCID: 0000-0003-3965-6333*
[d]*Kütahya Dumlupinar University, Department of Metallurgical and Materials Engineering, 43100, Kutahya, Türkiye,*
ORCID: 0000-0002-6721-9598
[e]*Sen Research Group, Department of Biochemistry, Kütahya Dumlupinar University, 43100, Kutaya, Türkiye, ORCID:0000-0001-9929-9556*

Abstract

This review article discusses the engineering materials used in aircraft, with a focus on aluminum alloys, titanium alloys and composite materials, including where and why they are most used in aircraft. There are many research papers that deal in detail with materials such as aluminum alloys, titanium alloys and composites used in an aircraft, including theoretical and experimental results. However, the author felt that a review of aircraft materials was necessary, both for himself and to help others interested in similar topics. In addition, the author felt the need of thinking back to the past on what materials used to be prevalent and what materials have superseded them. One such example written in this study is the case of Aluminum that used to be the predominant material in aircraft structural components, has been increasingly supplanted by polymer composites in recent years due to their advantageous properties. It is hoped that from this review article the reader will be able to understand the general trend of recent developments in aeronautical engineering materials and be able to choose which path to follow and which area to focus on in their future research.
© 2023 DPU All rights reserved.

* Corresponding author.
E-mail address: guray.kaya@dpu.edu.tr

1. Introduction

In the past decades a focus on developing better aircraft materials and a trend to use more composite materials are seen in Aerospace Industry and this leads to the need of aircraft material review for both researchers and industrial manufacturers alike [1–4]. Prime example for this is the Boeing 787 that uses 50% composite materials compared to its predecessor Boeing 777 that only uses 11% [5]. Boeing 787 only uses about 20% aluminum alloys compared to 70% in Boeing 777 [6]. The reason for using composite materials instead of metal alloys such as aluminum alloys is because the driving force in many airline companies is cost reduction for aircraft purchase and operation [7-9]. This cost reduction is derived from reducing weight of the aircraft by using composites instead of aluminum alloys [10]. The reduction of weight means less fuel needed for aircraft operation which in turn means less operating cost [11,12]. It should be noted that the material selected should not increase the cost of production by more than the cost reduction resulting from the reduction in weight [13,14]. Another way to reduce total cost is to build a more durable aircraft with very high tensile strength, elastic modulus, and/or damage tolerance [15]. This way less maintenance is needed and less cost will be incurred [16,17]. Several design trials have been made and the result shows that reducing the weight is 3-5 times more effective than increasing the durability [18].

Following the consideration that aircraft materials need to be lightweight while not compromising its strength, polymer matrix composites came to a rise [19,20]. Polymer Matrix Composites or commonly known as PMC have better mechanical properties such as higher specific modulus, normalized-by-density specific strength, fatigue, and corrosion resistance than aluminum alloys [21,22]. Nevertheless, there are instances where the PMC is unable to provide protection due to its relatively low resistance to impact and inability to withstand extremely high temperatures like the turbine blades inside the engine [23]. Engine pylon also requires high-strength material capable of supporting the engine weight and thrust and thus, steel and titanium are chosen [24]. Figure 1 shows the materials used in the Boing 787 aircraft and the distribution of these materials in the aircraft components conforming to the fact that not all aircraft parts can be made out of PMC. Certain parts like the leading edge (colored red in Figure 1), the joining between wings and fuselage (colored green in Figure 1) and engine pylon (colored yellow in Figure 1) are using aluminum, fiberglass, and steel/titanium respectively.
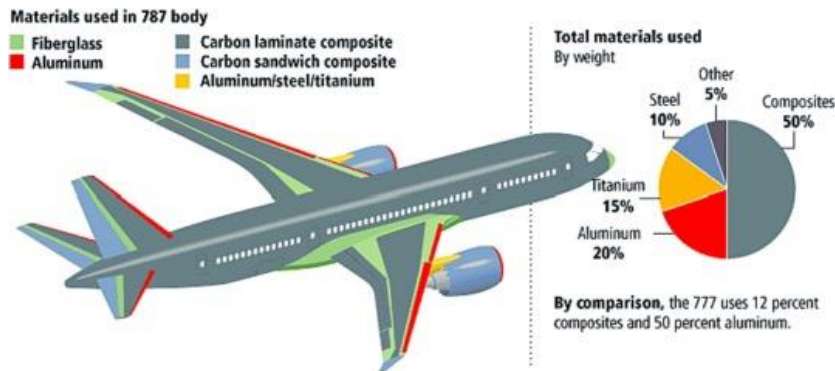
Fig. 1. Boeing 787 materials. It was adapted and reprinted by B. Parveez et al. in MDPI in 2022 [25].

When an aircraft is flying, various parts of the aircraft are affected by different types and amounts of loads [26]. The atmospheric pressure above sea level will be lower than that on the sea level (when aircraft is on ground) [27]. Human would prefer a stable and not too low atmospheric pressure otherwise some medical complications could

happen such as difficulty in breathing and in extreme case, the bubbling of blood due to very low atmospheric pressure [28]. For this reason, typical commercial aircraft that flies high will have a pressurized cabin for both aircraft crew and passengers [29]. The cabin is inside the fuselage, and thus fuselage will be like a pressurized vessel [30]. Fuselage is being held by the wing during flight, this in turn causes the fuselage to experience bending load too [31]. To summarize this part, the fuselage of an aircraft will experience bending compression and tension loads and shear stress due to pressure difference [32]. These loads will mostly be loaded to the skin of the fuselage and to alleviate some of them, stringers and frames are added to the fuselage [33]. Stringer help holding the compression and tension loads transferred from skin [34]. In addition, frames help give the fuselage shape and maintain it [34]. Also, for the fuselage, the front of the cockpit will be more exposed to pressure from airflow than the sides of the fuselage [35].

The same situation cannot be mentioned on the wings. The wing of an aircraft can be thought of as a cantilever beam extending from the fuselage, subject to bending and torsion during flight due to the lift force acting on the wings [36]. Think of it like a wide beam hanging from a building that is given an upward force to lift said building but the force is not distributed evenly hence the torsion of the beam [37]. Additional wing loads may also occur during taxiing, take-off, and landing due to the position of the landing gear and due to the use of flaps and slats on the trailing edges [38]. Aircraft on ground will put most of its weight on the landing gear hence there will be force concentration around it [39]. Think of it like the wide beam from before is now getting supported by pillars and the building is floating because the pillars lifted the building up [40]. The wing of an aircraft has weight too, so in the absence of lifting force this cantilever beam will instead feel the downward force from its own weight [41]. This means the wing will experience bending in both up and down direction, and thus the upper and lower wing will also experience compression and tension due to the different bending alternatingly [42].

Also, landing gear strut and wheels will mostly deal with the impact during landing and to hold the aircraft on ground [43]. The more an aircraft weight the higher requirement the landing gear will have [44]. It is apparent that although a soft landing is preferred for passenger safety and comfort, a hard landing will occur due to environmental reasons or some unforeseen emergency situations [45]. Therefore, landing gear must be able to withstand severe impact loads to ensure that the integrity of the aircraft is not compromised [46]. Evidently, the plane is also expected to have a braking system so that it can stop after landing. The aircraft braking system is also important to ensure that the aircraft can land safely [47]. The disc brake will need to be designed in a way that it can withstand high pressure and high temperature during this braking [48].

The engine of an aircraft is an intricate and delicate system of propulsion, air circulation, and electric power generation [49]. Different parts of this engine will experience different loads in different temperature and requires different materials [50]. Generally, when discussing about the aircraft engine materials, the turbine and compressor blades, combustion chamber, and the nozzle are the three most discussed components [51]. The turbine and compressor blades are rotating in high speeds and experience high temperature. This requires materials that have high specific strength even when subjected to high temperature. As for the combustion chamber, the main concern will be the very high pressure and very high temperature produced from the combustion of fuel and air in a contained space. The materials used in this section must not melt and still maintain their shape integrity [52].

This review article will discuss the types of materials commonly used as aircraft materials and why they are used in the part of the aircraft. Table 1 provides information about the materials used in aircraft.

Table 1. Materials used in an aircraft [53].

No	Material		Application
1	Aluminum Alloys	Aluminum-Copper (Al-Cu) alloys	Fuselage skin and lower-wing skin
		Aluminum-Zinc (Al-Zn) alloys	Upper-wing skin, stringers, stabilizers
		Aluminum-Lithium (Al-Li) alloys	Fuselage skin and upper-wing skin
2	Titanium Alloys	Alpha-Titanium (α-Ti) alloys	Fan blade

		Beta-Titanium (β-Ti) alloys	Landing gear, springs
		Alpha-Beta Titanium alloys	Disc blade of the compressor
3	Composite	Polymer Matrix Composite (PMC)	Fuselage, ailerons, flaps, landing gear door
		Metal Matrix Composite (MMC)	Fuselage skin and wide-body wing
		Ceramic Matrix Composite (CMC)	Exhaust nozzle, aircraft brakes

2. Aluminum alloys

Aluminum alloys have been used as aircraft materials for many years due to its mechanical behavior, ease of design, well-developed manufacturing process and material inspection techniques [54]. Material properties such as density, strength, Young's modulus, fatigue resistance, fracture toughness and corrosion resistance are the important parameters that need to be tailored according to the particular component of the aircraft [55]. For this reason, different types of aluminum alloys are introduced. Aircraft fuselage's main design criterion is damage tolerance, thus aluminum-copper alloy is used for fuselage [56]. While the upper-wings main design criterion is compressive strength and fatigue resistance, thus aluminum-zinc alloy is used for upper-wings [57]. Aluminum-lithium alloys are specially made to reduce weight without reducing strength and replaced the conventional Al-Cu and Al-Zn alloys in their respective application areas [58].

2.1. Aluminum-Copper (Al-Cu) alloys

The most well-known among aluminum alloys are aluminum-copper (Al-Cu) alloy. Al-Cu alloys, commonly referred to as the Aluminum 2000 (Al-2XXX) series, are designated by a four-digit code starting with '2' to indicate their series, followed by three additional digits to indicate other alloying elements and properties [59]. Certain alloys in this series undergo specialized tempering processes, which is reflected in their names with an appended '-Txx' [60]. A notable feature of these alloys, as indicated in the Table 2, is their substantial magnesium content [61]. This is of particular importance because the inclusion of magnesium in the 2000 series alloys enhances their resistance to fatigue crack propagation, a property that aligns with the critical design requirement of damage tolerance in aircraft fuselage structures [62].

Table 2. Chemical composition of two 2000-series aerospace aluminum alloys [63].

Components (wt. %)	Al 2024	Al 2524
Al	remainder	remainder
Cr	⩽0.1	⩽0.05
Cu	3.8 – 4.4	4.0 – 5.5
Fe	⩽0.5	⩽0.12
Mg	1.2 – 1.8	1.2 – 1.6
Mn	0.3 – 0.9	0.45 – 0.7
Si	⩽0.5	⩽0.06
Ti	⩽0.15	⩽0.1
Zn	⩽0.25	⩽0.15

Of these alloys, the oldest historically aluminum alloy, Al 2024-T351, was the material of choice for the construction of aircraft fuselages due to its robust yield strength, superior resistance to fatigue crack growth, and impressive fracture toughness [57]. However, this type had limited use in high-stress areas of aircraft due to its low

yield stress [64]. By reducing contaminants such as iron and silicon, significant improvements in fracture toughness and resistance to fatigue crack initiation and growth have been achieved as shown in Table 3 when comparing the number of impurities (Fe, Si, Cr, Ti) [65].

Table 3. Mechanical properties of two 2000-series aerospace aluminum alloys [63].

Mechanical Properties	Al 2024-T351	Al 2524-T3
Ultimate Tensile Strength	428 MPa	434 MPa
Yield Strength	324 MPa	306 MPa
Fracture Toughness	37 MPam$^{1/2}$	40 MPam$^{1/2}$
Elongation	21 %	24 %

The Al 2524-T3 alloy, known for its high damage tolerance and outstanding fatigue characteristics, has shown a 15-20% increase in fracture toughness and a 30-40% extension in lifespan before failure compared to the Al 2024-T351 alloy, all while maintaining strength and corrosion resistance [66]. These advancements have contributed to weight reductions and an extended service life for the Boeing 777, leading to the replacement of Al 2024-T351 with Al 2524-T3 [67].

Further studies involving observation and microstructural analysis have been conducted to investigate the fatigue crack behavior of the Al 2524-T3 alloy [68–71]. The microstructure, which encompasses inclusions and grain orientations, revealed that inclusions significantly influence fatigue crack progression, forming large voids that act as conduits for accelerated crack propagation [66].

In the aircraft industry, protective coatings are commonly applied to surfaces to mitigate corrosion damage, however, such coatings can diminish mechanical performance and incur high production and maintenance costs [72]. Nickel fluoride sealed anodic films on aluminum alloys offer stable passivity and robust resistance in neutral and basic NaCl solutions. Yet, their effectiveness is compromised in acidic NaCl environments, where passivity and resistance are notably weaker [73].

2.2. Aluminum-Zinc (Al-Zn) alloys

Aluminum-Zinc alloys, categorized under the Aluminum 7000 series, exhibit greater strength compared to the 2000 series [74]. Consequently, they are the preferred choice for critical aircraft structures such as the upper-wing skin, stringers, and stabilizers [75]. These components primarily handle the stresses of compression and tension due to bending forces [76]. Stringers serve as structural reinforcements that fortify the aircraft's skin [77]. The empennage, or tail section of a conventional aircraft, comprises horizontal and vertical stabilizers, which are primarily influenced by aerodynamic lift forces, leading to bending [78]. Table 4 gives information on the chemical composition of aluminum alloys for the two 7000 series of aircraft.

Table 4. Chemical composition of two 7000 series aerospace aluminum alloys [63].

Components (wt. %)	Al 7075	Al 7475
Al	remainder	remainder
Cr	0.18 – 0.28	0.18 – 0.25
Cu	1.2 - 2	1.2 – 1.9
Fe	⩽0.5	⩽0.12
Mg	2.1 – 2.9	1.9 – 2.6
Mn	⩽0.3	⩽0.06

Si	≤0.4	≤0.1
Ti	≤0.2	≤0.06
Zn	5.1 – 6.1	5.2 – 6.2

The Al 7075 alloy boasts greater strength compared to Al 2024 [79]; however, its fatigue resistance is compromised by its susceptibility to corrosion [80]. The onset of corrosion markedly diminishes the ultimate strength of the aluminum alloy [81,82]. Following the initiation of corrosion, there is a consistent decline in strength coupled with an escalation in mass loss [83,84]. As the mass loss progresses, the fatigue life of the alloy decreases exponentially [85]. Al 7075 was used extensively in the past before the problem with corrosion induced fatigue crack was unveiled, and were either replaced or treated with anti-corrosion protection [86].

The Al 7475 alloy, an advancement over the earlier Al 7075, exhibits enhanced strength, fracture toughness, and fatigue crack propagation resistance [87,88]. This progress stems from the reduction of iron and silicon impurities as shown in Table 4. Characterized by a fine grain structure and optimal dispersion, the Al 7475 alloy achieves the highest levels of toughness [89]. Moreover, Al 7475 T7351 plates maintain strength comparable to Al 7075 while offering fracture toughness values that are up to 40% higher [80].

2.3. Aluminum-Lithium (Al-Li) alloys

Weight reduction is a primary objective in optimizing materials for aircraft construction [90]. At this point, another Al alloy; Al containing lithium (Li), come into play. Li stands out as one of the rare elements that has low density as well as good solubility in Al [91]. The incorporation of each 1% increment of Lithium leads to a 3% reduction in the alloy's density [92]. While Lithium is effective for density reduction, it has been noted that adding merely 1% can significantly diminish the alloy's specific strength [93]. On the other hand, enriching the alloy with 2%-3% Lithium can enhance the specific strength by 60%-80% [93].

The first and second generations of Al-Li alloys primarily aimed at density reduction, offering benefits such as decreased density, higher modulus of elasticity, and prolonged fatigue life [94]. However, they suffered from lower fracture toughness in short-transverse and plane stress conditions due to increased tensile property anisotropy [95]. The third-generation alloys are crafted with refined composition and tempering to balance density, strength, and toughness, while also enhancing fatigue crack growth resistance, corrosion resistance, thermal stability, and ease of manufacturing [96].

Al 2198 alloy, developed to supersede Al 2024 and Al 2524 where damage tolerance is critical, contains 2.9%-3.3% Cu and 0.9%-1.1% Li [97]. Stress rates for these structures are also evaluated. With a stress ratio (R=0.1), the fatigue endurance limit is only 8% below the yield stress compared to the 40% below the limit of Al 2024 and also has a reduced density [98]. Under equivalent normalized stresses, Al 2198-T351 can absorb 2-3 times more energy before fracturing than Al 2024, showcasing enhanced damage tolerance [99].

The Al 2060 alloy, belonging to the latest third-generation Al-Li alloys, consists of 3.95% Cu, 0.75% Li, and 0.85% Mg [100]. This generation's application to fuselage skin can lead to a 7% weight saving, and a 14% saving for upper-wing skin, relative to the conventional Al 2524 and Al 2024 alloys [101]. Test results (III generation) have shown that incorporating advanced structural designs not only enhances material properties and damage tolerance in critical areas but also supports fusion welding [102]. The standardized tooling, established assembly techniques, and streamlined repair and maintenance procedures, coupled with the recyclability of Al-Li alloys, enable them to rival polymer composites in the aerospace industry [103].

3. Titanium alloys

Between the 1960s and the 2010s, the application of titanium-based alloys in aircraft manufacturing has surged from 1% to 19% [104]. These alloys are utilized in both the structural framework and engines of aircraft, owing to their high specific strength, exceptional corrosion resistance, and superior performance at elevated temperatures [105]. Titanium alloys are classified into three types: alpha, beta, and alpha-beta [106]. The distinct properties of each type are determined by their microstructure, which in turn is influenced by their chemical makeup and the thermomechanical processes they undergo [107].

3.1. Alpha-titanium alloys

One of the most well-known structures among Ti alloys is Alpha titanium alloys. Alpha titanium (α-Ti) alloys are predominantly composed of the α phase, supplemented by neutral elements or α stabilizers [108,109]. These alloys are typically employed in aircraft components that encounter severe corrosive environments but are not exposed to intense mechanical or thermal stress, such as support structures [109]. For instance, CP-Ti is utilized in support structures and environmental control systems functioning around 230 °C, whereas Ti-6-2-4-2S is applied in gas turbine engine components operating at temperatures up to 540 °C [110]. Incorporating aluminum into alpha titanium alloys not only enhances their strength but also contributes to a lighter alloy composition [111].

3.2. Beta-titanium alloys

Another one in this structure is Beta Titanium (β-Ti) alloys. B- Ti alloys, which are primarily made up of the β phase and contain β stabilizers, are integral to the manufacture of high-stress aircraft components like landing gear and springs [112]. For instance, the Ti-13-11-3 alloy has been extensively utilized in the SR-71 aircraft, while the Ti-10-2-3 alloy is predominantly employed in the Boeing 777's landing gear, offering a significant weight saving of 270 kg over traditional steel [110,113].

3.3. Alpha beta-titanium alloys

The most preferred alloy among Ti alloys is Alpha beta Ti alloy. This is the most widely used Ti-based alloy because of the excellent combination of strength, fracture toughness, and ductility [114]. In alpha-beta Ti-based alloys, the flow stress escalates as the strain rate rises at a constant temperature, and conversely, it diminishes as the temperature increases at a steady strain rate, leading to a more pronounced flow softening effect in the stress-strain curves of alpha-beta Ti-based alloys compared to those composed solely of alpha or beta phases [115]. The alloy that is sold and used extensively in the United States is Ti-6Al-4V which is most used in high-temperature compressor part of the engine and most other aircraft parts that requires high strength-to-weight ratio material [110,116].

Table 5. Mechanical properties of three alpha, beta, and alpha-beta aerospace titanium alloys [110].

Mechanical Properties	Ti-6-2-4-2S	Ti-10-2-3	Ti-6Al-4V
Ultimate Tensile Strength	1010 MPa	1000-1400 MPa	900-1200 MPa
Tensile Modulus	114 GPa	110 GPa	110-140 GPa
Yield Strength	990 MPa	1000-1200 MPa	800-1100 MPa
Hardness	340 HV	300-470 HV	300-400 HV

Several mechanical properties for all three titanium alloys are shown in Table 5 above. Ti-6-2-4-2S is the example for alpha titanium alloy, Ti-10-2-3 is the example for beta titanium alloy. Meanwhile Ti-6Al-4V is the example for alpha-beta titanium alloy. It can be inferred that beta titanium alloys are the strongest among the three types.

4. Composites

Another structure most used in aircraft is composites. A composite is a material structure that consists of at least two macroscopically identifiable materials that work together to achieve a better result [117,118]. The matrix of composite determines the major characteristics while the other material(s) reinforces it [118]. The purpose of having matrix with reinforcements is to get the best properties and to reduce the negatives [119]. An example of composite material engineering is when a strong, yet brittle substance is combined with a ductile and lightweight matrix resulting in a material that retains toughness while being less brittle and still maintaining its lightweight characteristic [120]. Based on the material of the matrix, we can categorize composite into three types: polymer matrix, metal matrix, and ceramic matrix composites [121]. We can infer from Fig. 2 that Polymer Matrix Composite (PMC) has the highest specific strength (strength divided by density) among other materials but has the lowest temperature. For this reason, composites capable of higher temperature like Metal Matrix Composite (MMC) and Ceramic Matrix Composite (CMC) are also developed despite having lower specific strength than PMC [122].
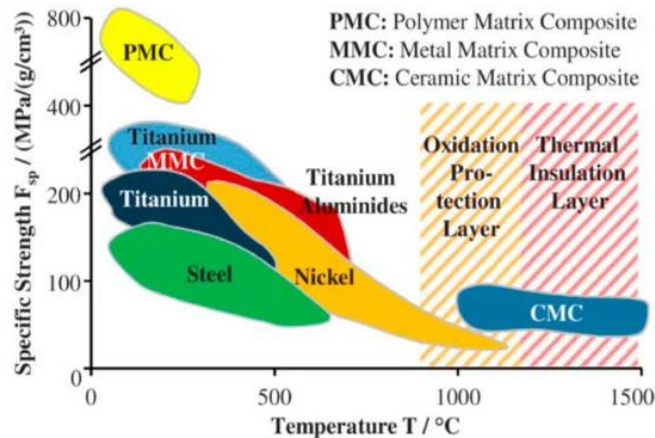
Fig. 2. Specific strength and temperature potential of PMC, MMC, CMC. It was adapted and reprinted by B. Parveez et al. in MDPI in 2022 [25].

Composite materials came to a rise in recent years due to the advancement in health monitoring of composite structures by having a good understanding of the aerodynamic forces-induced wave propagation through the materials [123]. This numerical analysis allows aircraft engineers to implement more composite structures [124].

4.1. Polymer Matrix Composite (PMC)

In composite materials with a polymer matrix, fibers are embedded within a polymer, referred to as the 'matrix' [125]. This integration slightly diminishes the inherent strength and stiffness of the fibers due to their combination with the polymer, thus production methods generally aim to minimize the polymer content to retain the fibers' robust characteristics [126]. The primary purpose of the polymer matrix is to serve as a binder, securing the fibers in place, which then make them capable of withstanding greater compressive forces and distributing loads more

effectively from one fiber to another via shear stresses [127]. This results in a more efficient spread of external loads across the fibers in the composite, as opposed to a mere aggregation of dry fibers [117]. Research has corroborated that the matrix plays a crucial role in load transfer between fibers, significantly enhancing the material's overall strength [128].

Moreover, the polymer in a composite material plays a pivotal role in defining its responsiveness to external factors like moisture, chemicals, and ultraviolet radiation [129,130]. It frequently influences attributes such as color, surface finish, opacity, and fire resistance [131,132,133]. Polymers utilized in composites fall into two main groups: thermoplastics, which can be reshaped with heat, and thermosets, which solidify permanently after being heated [134].

Thermoplastics are polymers that melt when heated and thus can be remolded. Thermosets are polymers that disintegrate when heated, cannot be remolded. Most commonly used polymers are thermoplastics, but the drawback of using thermoplastic is its viscosity that makes it hard to penetrate evenly throughout the fibers [134]. Some special manufacturing techniques is thus required to make sure the fibers are wetted properly [135]. In the end, the distinction between thermosets and thermoplastics is not clear as some polymers such as polyesters, usually behave like a thermoset but can also be thermoplastic [136]. While some other polymer like phenolic resins behave thermoplastics up to a certain temperature where it behaves like a thermoset [117].

The production techniques for composites significantly influence the final product's quality. Fibers that are not adequately saturated can become points of stress concentration, diminishing the composite's overall ultimate tensile strength [137]. These areas may also serve as origins for crack formation, while regions with dry fibers — those not encapsulated by the polymer matrix due to manufacturing flaws — can hasten and direct the path of crack propagation [138].

The sustainability and recyclability of materials are pressing issues in today's material industry [139,140]. Plastics are notorious for their environmental impact due to prolonged decomposition times [140]. Nevertheless, advanced recycling and re-manufacturing techniques for composites have been developed, with many processes maintaining a high level of mechanical properties, and several commercial-scale facilities are now operational [141].

Polymer Matrix Composites (PMCs) are commonly utilized in various aircraft components such as fuselage skin, wing skin, ailerons, flaps, and landing gear doors [142,143]. The advantage of PMCs lies in their density, which is roughly half that of aluminum alloys, coupled with a modulus of elasticity and tensile strength that are two to three times greater [144]. These properties enable significant weight reductions in aircraft and lessen the reliance on aluminum alloys. However, PMCs have their limitations, particularly regarding the service temperature constrained by the polymer matrix. Ongoing research aims to identify alternative matrix materials that can achieve further weight savings while meeting design requirements [25].

Table 6. Mechanical properties of two Carbon Fiber Reinforced Polymer (CFRP) composites [145].

Mechanical Properties	CFRP 50%	CFRP 60%
Ultimate Tensile Strength	443 MPa	512 MPa
Tensile Modulus	39.0 GPa	51.1 GPa
Compressive Strength	352 MPa	391 MPa
Density	1.36 g/cm^3	1.39 g/cm^3

PMC manufacturing methods affect the mechanical properties heavily. One such empirically-determined material properties for tensile test is shown in Table 6 above. CFRP 50% meant that there are 50% v/v carbon fiber / polymer fraction in the composite. It can be inferred that having more carbon fiber means more strength at the cost of weight.

4.2. Metal Matrix Composite (MMC)

Metals such as steel, titanium, and nickel alloys are considered for matrix materials due to their ability to withstand temperatures significantly higher than those tolerated by Polymer Matrix Composites (PMC) [146]. Metal Matrix Composites (MMC) are created by embedding ceramic materials within a metal matrix, enhancing the composite's yield strength, fracture toughness, thermal expansion coefficient, creep resistance, and wear resistance [147]. Consequently, MMCs are emerging as alternatives to traditional aluminum alloys [148].

Research on MMCs has particularly focused on aluminum matrices reinforced with silicon-carbide (Si-C) ceramics [149,150]. A major challenge has been the welding of these materials, which previously limited MMCs' application in aircraft [151]. However, recent studies have demonstrated that employing harder tools can significantly improve the wear resistance of the welds, thus overcoming this obstacle [152].

Some other recent studies have revealed that metal composites reinforced with nanoparticles outperform those with microscale reinforcements, leading to the development of nanocomposites [153,154]. It is apparent that nanoparticles are used in sensors, pharmaceutical research, fuel cells, etc. [155–161]. It is used in many areas as well as in aircraft materials. Among these nanostructures, carbon structures are encountered due to their abundance and superior properties. Graphene, graphite, carbon nanotubes and fullerenes can be given as examples. Also, research indicates that the inclusion of nanotubes and graphene nanosheets significantly bolsters the stiffness and strength of these materials [162]. Despite the challenges in achieving optimal integration of the reinforcements within the metal matrix, progress is being made. Achieving a uniform distribution of nanoparticles is crucial for balancing the rigidity of ceramic reinforcements with their spacing, thus optimizing yield strength and creep resistance while preserving ductility [154].

Metal Matrix Composites (MMCs) are employed in areas of aircraft such as fuselage and wing skins, where high temperatures due to air friction and pressure are prevalent, replacing Al 7000 series alloys [163]. Advanced aluminum alloy composites include Al A356 with 4 wt.% nano Al2O3, produced via stir casting, which boasts a compressive strength of 630.5 MPa, and Al 2009 reinforced with 1 wt.% and 3 wt.% carbon nanotubes through friction stir processing, yielding a strength of 385 MPa and an ultimate tensile strength of 477 MPa [164]. Additionally, there are MMCs based on aircraft aluminum alloys such as Al 2024 and Al 7075; for example, Al 2024 combined with 5 wt.% graphite and 20 wt.% SiC via powder metallurgy has a density of 2.94 g/cm³ and a hardness of 63 BHN (approximately 68 Hv), while Al 7075 with 7 wt.% SiC and 3 wt.% graphite, created through stir casting, has a density of 2.784 g/cm³ and a hardness of 219 Hv [164].

4.3. Ceramic Matrix Composite (CMC)

Ceramics are highly regarded for their application in components that endure extreme stress and temperatures [165]. Yet, their widespread adoption is limited due to their inherent brittleness, which leads to low fracture toughness, and a susceptibility to vibration-induced damage, culminating in a reduced ability to withstand fatigue from such vibrations [166]. To enhance their performance and mitigate brittleness, ceramics are being reinforced with nanoparticles. The most prevalent nanocomposite materials used in Ceramic Matrix Composites (CMCs) are Graphene Nanoparticles (GNPs) and Carbon Nanotubes (CNTs) [167,168]. This in turn produces a good strength to weight ratio at really high temperature where no metal alloys can manage [169]. Most polymer matrix composites and aluminum alloys cannot manage more than 350-400 °C while Titanium alloys and Nickel-based superalloys cannot manage more than 700 °C and 1000 °C respectively [170].

Recent studies have shown that GNPs exhibit better nanocomposites than CNTs due to the difficulty in ceramic matrix dispersion in CNT reinforced composites. GNPs are well dispersed in ceramic matrix microstructure. Exact measurement of GNPs fraction is a must to ensure porosity is not too much and fracture toughness is not compromised [166,171].

Extensive testing and analysis on carbon fiber-reinforced ceramic matrix composites for nozzle applications have demonstrated that the C/SiC material endures temperatures up to approximately 2300 K (around 2022 °C) while preserving its structural integrity without any deformation and when compared to traditional metal alloy nozzles, this composite material offers a substantial 60% reduction in weight, attributable to its exceptional thermophysical and mechanical properties [169,172,173].

Ceramic Matrix Composites (CMCs) are employed in areas of aircraft that are exposed to extremely high temperatures, such as the engine nozzle and the disc brakes of the landing gear [174]. Key components include combustion lines, ducts, nozzle flaps, acoustic liners, turbine vanes, blades, and discs, among others. However, the application of Ceramic Matrix Composites (CMCs) faces challenges such as insufficient manufacturing and processing technologies, a need for standardized design methodologies, and advanced maintenance evaluation techniques [175].

Machining plays a crucial role in the manufacturing of products and influences the operational performance of components. Given the harsh conditions that Ceramic Matrix Composites (CMCs) are subjected to, any production flaws could significantly shorten their expected service duration [176]. The conventional machining process of carbon fiber reinforced ceramic matrix composites includes matrix crushing, interfacial debonding, and fiber fracture that concludes in brittle fractures [177]. There is a need to develop better machining tools suitable for ceramic matrix composites to ensure quality and performance of said material [178].

Traditionally, ceramics are recognized for their brittleness, especially when contrasted with metals, and this characteristic persists in ceramic matrix composites. To mitigate this, the composites are reinforced with fibers engineered to distribute loads uniformly and effectively. This is achieved by fine-tuning the fiber-matrix interaction to prevent microcracks within the matrix itself. Instead, these microcracks are allowed to develop in the interphase, the boundary layer between the fibers and the matrix. This strategic design results in a composite that exhibits greater ductility than its ceramic counterpart [179].

5. Conclusions

The progress of aircraft material development has been tremendous these last few years and it cannot be denied that composites are becoming more prevalent and are replacing the conventional metal alloys. Aluminum alloy used to be the bread-and-butter material for an aircraft until composites were developed. This is because, at first, composites were very costly to produce. In addition, the limitation in design capacity prevented the widespread use of composite materials in the aircraft industry. However, developments in the fields of material production and development have produced important results in overcoming these limitations. After the R&D studies carried out in these composite materials in recent years, cheaper and easier production of polymer matrix composites has become widespread, and they are taking on the role of Al alloys in aircraft structures. In addition, polymer matrix composites that have an impressive strength-to-weight ratio in a low-temperature environment, as well as ductility that provides sufficient flexibility, can be used for aircraft skins and structural supports. Meanwhile, ceramic matrix composites have become a better option for engine components formerly dominated by titanium and nickel-based superalloys. Because these ceramic matrix composites have a higher temperature threshold and are also lighter than their metal alloy counterparts.

The author believes that the future of aircraft materials will be determined predominantly by composites, and therefore research and development should focus on making non-destructive testing on composites more accessible to make composites cheaper and easier, while also ensuring a good service life. In addition, it is evident that there is a significant increase in the popularity of Nanocomposites. In the light of these findings, it can be inferred that composite materials should be developed and taken further. Magnesium alloys, superalloys, smart materials and light weight steels are also gaining importance in response to the rise of composite materials. One research heading recommended by the author is to focus the research on composites and nanocomposites.

Acknowledgements

None

Author Contribution

M.H.I., and F.S.; Conceptualization, Methodology. M.H.I., M.A., M.B.; Data curation, Writing- Original draft preparation. G.K.; Visualization, Investigation. M.H.I., M.A., M.B., G.K., and F.S.; Writing- Reviewing and Editing.

References

[1] P. D. Mangalgiri, "Composite Materials for Aerospace Applications," *Bulletin of Materials Science*, vol. 22, no. 3, pp. 657–664, 1999, doi: 10.1007/BF02749982.
[2] K. Shivi, "Polymer Composites in Aviation Sector: A Brief Review Article," *International Journal of Engineering Research & Technology (IJERT)*, vol. 6, no. 06, p. 518, 2017.
[3] M. Mrazova, "Advanced composite materials of the future in aerospace industry," *Incas Bulletin*, vol. 5, pp. 139–150, 2013, doi: 10.13111/2066-8201.2013.5.3.14.
[4] R. Nedelcu and P. Redon, "Composites Materials for Aviation Industry," *International Conference of Scientific Paper AFASES*, May 2012.
[5] X. Zhang, Y. Chen, and J. Hu, "Recent Advances in the Development of Aerospace Materials," *Progress in Aerospace Sciences*, vol. 97, pp. 22–34, Feb. 2018, doi: 10.1016/j.paerosci.2018.01.001.
[6] T. Dursun and C. Soutis, "Recent Developments in Advanced Aircraft Aluminium Alloys," *Materials & Design (1980-2015)*, vol. 56, pp. 862–871, Apr. 2014, doi: 10.1016/j.matdes.2013.12.002.
[7] R. Curran, S. Raghunathan, and M. Price, "Review of Aerospace Engineering Cost Modelling: The Genetic Causal Approach," *Progress in Aerospace Sciences*, vol. 40, no. 8, pp. 487–534, Nov. 2004, doi: 10.1016/j.paerosci.2004.10.001.
[8] Y.-H. Chang and P.-C. Shao, "Operating Cost Control Strategies for Airlines," *African Journal of Business Management*, vol. 5, no. 26, pp. 10396–10409, 2011, doi: 10.5897/ajbm11.625.
[9] I. Kilinc, M. A. Oncu, and Y. E. Tasgit, "A Study on the Competition Strategies of the Airline Companies in Turkey," *Tourismos: An International Multidisciplinary Journal of Tourism*, vol. 7, no. 1, pp. 325–338, 2012, doi: 10.26215/tourismos.v7i1.271.
[10] F. W. J. Van Hattum, F. Regel, and M. Labordus, "Cost Reduction in Manufacturing of Aerospace Composites," *Plastics, Rubber and Composites*, vol. 40, no. 2, pp. 93–99, Mar. 2011, doi: 10.1179/174328911X12988622801052.
[11] M. Kaufmann, D. Zenkert, and P. Wennhage, "Integrated Cost/Weight Optimization of Aircraft Structures," *Structural and Multidisciplinary Optimization*, vol. 41, no. 2, pp. 325–334, Mar. 2009, doi: 10.1007/s00158-009-0413-1.
[12] R. C. Holzwarth, "The Structural Cost and Weight Reduction Potential of More Unitized Aircraft Structure," *39th AIAA/ASME/ASCE/AHS/ASC Structures, Structural Dynamics, and Materials Conference and Exhibit*, vol. 3, pp. 2218–2227, 1998, doi: 10.2514/6.1998-1872.
[13] A. J. Beck, A. Hodzic, C. Soutis, and C. W. Wilson, "Influence of Implementation of Composite Materials in Civil Aircraft Industry on reduction of Environmental Pollution and Greenhouse Effect," *IOP Conf Ser Mater Sci Eng*, vol. 26, no. 1, p. 012015, Dec. 2011, doi: 10.1088/1757-899X/26/1/012015.
[14] S. A. Morrison, "An Economic Analysis of Aircraft Design," *Journal of Transport Economic and Policy*, vol. 18, no. 2, pp. 123–143, May 1984.
[15] M. Kaufmann, D. Zenkert, and C. Mattei, "Cost Optimization of Composite Aircraft Structures Including Variable Laminate Qualities," *Compos Sci Technol*, vol. 68, no. 13, pp. 2748–2754, Oct. 2008, doi: 10.1016/j.compscitech.2008.05.024.
[16] M. N. Beltramo, D. L. Trapp, B. W. Kimoto, and D. P. Marsh, "Parametric Study of Transport Aircraft Systems Cost and Weight," Apr. 1977.
[17] W. Wei and M. Hansen, "Cost Economics of Aircraft Size," *Journal of Transport Economics and Policy (JTEP)*, vol. 37, no. 2, pp. 279–296, May 2003.
[18] F. C. Campbell, *Manufacturing Technology for Aerospace Structural Materials*. Elsevier, 2006.
[19] P. Balakrishnan, M. J. John, L. Pothen, M. S. Sreekala, and S. Thomas, "Natural Fibre and Polymer Matrix Composites and Their Applications in Aerospace Engineering," *Advanced Composite Materials for Aerospace Engineering*, pp. 365–383, Jan. 2016, doi: 10.1016/B978-0-08-100037-3.00012-2.
[20] J. S. Tomblin, Y. C. Ng, and K. S. Raju, "Material Qualification and Equivalency for Polymer Matrix Composite Material Systems," 2001.
[21] S. Sajan and D. Philip Selvaraj, "A Review on Polymer Matrix Composite Materials and Their Applications," *Mater Today Proc*, vol. 47, pp. 5493–5498, Jan. 2021, doi: 10.1016/j.matpr.2021.08.034.
[22] C. Zweben, "Advanced Composites for Aerospace Applications: A Review of Current Status and Future Prospects," *Composites*, vol. 12, no. 4, pp. 235–240, Oct. 1981, doi: 10.1016/0010-4361(81)90011-2.
[23] H. Liu, J. Sun, S. Lei, and S. Ning, "In-Service Aircraft Engines Turbine Blades Life Prediction Based on Multi-Modal Operation and

Maintenance Data," *Propulsion and Power Research*, vol. 10, no. 4, pp. 360–373, Dec. 2021, doi: 10.1016/j.jppr.2021.09.001.

[24] M. Stefanovic and E. Livne, "Structural Design Synthesis of Aircraft Engine Pylons at Certification Level of Detail," *J Aircr*, vol. 58, no. 4, pp. 935–949, Apr. 2021, doi: 10.2514/1.C035953.

[25] B. Parveez, M. I. Kittur, I. A. Badruddin, S. Kamangar, M. Hussien, and M. A. Umarfarooq, "Scientific Advancements in Composite Materials for Aircraft Applications: A Review," *Polymers (Basel)*, vol. 14, no. 22, p. 5007, Nov. 2022, doi: 10.3390/polym14225007.

[26] J. R. Wright and J. E. Cooper, *Introduction to Aircraft Aeroelasticity and Loads*, vol. 20. John Wiley & Sons, 2008.

[27] T. L. Grigorie and O. Grigorie, "Aircrafts' Altitude Measurement Using Pressure Information: Barometric Altitude and Density Altitude," *WSEAS Transactions on Circuits and Systems*, vol. 9, no. 7, pp. 503–512, 2010.

[28] A.-L. Paul, "The Biology of Low Atmospheric Pressure - Implications for Exploration Mission Design and Advanced Life Support," *Gravitational and Space Biology*, vol. 19, no. 2, pp. 3–17, Aug. 2006.

[29] J. Affleck *et al.*, "Cabin Cruising Altitudes for Regular Transport Aircraft," *Aviat Space Environ Med*, vol. 79, no. 4, pp. 433–439, Apr. 2008, doi: 10.3357/asem.2272.2008.

[30] A. P. Singh, R. Saxena, and S. Verma, "Aircraft Cabin Temperature and Pressure Management System," University of Petroleum & Energy Studies India, Dehradun, 2013.

[31] C. Hao, C. Y. Nan, Z. Peng, and L. Lei, "Research on Buckling and Post-buckling Characteristics of Composite Curved Stiffened Fuselage Panel under Hoop Bending load," *IOP Conf Ser Mater Sci Eng*, vol. 531, no. 1, Sep. 2019, doi: 10.1088/1757-899X/531/1/012045.

[32] C. Hao, C. Y. Nan, Y. Z. Bo, and L. Lei, "Experimental Research on the Stability behavior of Composite Curved Stiffened Fuselage Panel under Four-Point-Bending load," *IOP Conf Ser Mater Sci Eng*, vol. 563, no. 2, Jul. 2019, doi: 10.1088/1757-899X/563/2/022005.

[33] D. R. Ambur and M. Rouse, "Design and Evaluation of Composite Fuselage Panels Subjected to Combined Loading Conditions," *J Aircr*, vol. 42, no. 4, pp. 1037–1045, May 2012, doi: 10.2514/1.18994.

[34] R. D. Young, C. A. Rose, and J. H. Starnes, "Skin, Stringer, and Fastener Loads in Buckled Fuselage Panels," *19th AIAA Applied Aerodynamics Conference*, 2001, doi: 10.2514/6.2001-1326.

[35] T. L. Lomax, "Structural Loads Analysis for Commercial Transport Aircraft," *Structural Loads Analysis for Commercial Transport Aircraft*, 2012, doi: 10.2514/4.862465.

[36] A. Demirtaş and M. Bayraktar, "Free Vibration Analysis of an Aircraft Wing by Considering as a Cantilever Beam," *Selçuk Üniversitesi Mühendislik, Bilim Ve Teknoloji Dergisi*, vol. 7, no. 1, pp. 12–21, Mar. 2019, doi: 10.15317/Scitech.2019.178.

[37] K. Kim and T. Strganac, "Aeroelastic Studies of a Cantilever Wing with Structural and Aerodynamic Nonlinearities," *43rd AIAA/ASME/ASCE/AHS/ASC Structures, Structural Dynamics, and Materials Conference*, Apr. 2012, doi: 10.2514/6.2002-1412.

[38] A. Gopalarathnam and R. K. Norris, "Ideal Lift Distributions and Flap Angles for Adaptive Wings," *J Aircr*, vol. 46, no. 2, pp. 562–571, May 2012, doi: 10.2514/1.38713.

[39] S. S. Rao, "Optimization of Airplane Wing Structures Under Landing Loads," *Comput Struct*, vol. 19, no. 5–6, pp. 849–863, Jan. 1984, doi: 10.1016/0045-7949(84)90186-X.

[40] R. S. Swati and A. A. Khan, "Design and Structural Analysis of Weight Optimized Main Landing Gears for UAV under Impact Loading," *Journal of Space Technology*, vol. 4, no. 1, pp. 96–100, 2013.

[41] F. Gambioli *et al.*, "Experimental Evaluation of Fuel Sloshing Effects on Wing Dynamics," *18th Int. Forum Aeroelasticity Struct. Dyn. IFASD*, 2019.

[42] F. Hürlimann, R. Kelm, M. Dugas, and G. Kress, "Investigation of Local Load Introduction Methods in Aircraft Pre-Design," *Aerosp Sci Technol*, vol. 21, no. 1, pp. 31–40, Sep. 2012, doi: 10.1016/j.ast.2011.04.008.

[43] P. W. Chen, S. H. Chang, and C. M. Chen, "Impact Loading Analysis of Light Sport Aircraft Landing Gear," *Applied Mechanics and Materials*, vol. 518, pp. 252–257, 2014, doi: 10.4028/www.scientific.net/amm.518.252.

[44] B. Milwitzky and F. E. Cook, "Analysis of Landing Gear Behavior," Vancouver, 1952.

[45] D. H. Chester, "Aircraft Landing Impact Parametric Study with Emphasis on Nose Gear Landing Conditions," *J Aircr*, vol. 39, no. 3, pp. 394–403, May 2012, doi: 10.2514/2.2964.

[46] X. H. Wei and H. Nie, "Dynamic Analysis of Aircraft Landing Impact Using Landing-Region-Based Model," *J Aircr*, vol. 42, no. 6, pp. 1631–1637, May 2012, doi: 10.2514/1.6801.

[47] R. F. Swati, A. A. Khan, and L. H. Wen, "Weight Optimized Main Landing Gears for UAV Under Impact Loading for Evaluation of Explicit Dynamics Study," *Advanced Materials, Structures and Mechanical Engineering*, no. 1, pp. 371–376, Apr. 2016, doi: 10.1201/B19693-81.

[48] Jan Robert Wright and Jonathan Edward Cooper, *Introduction to Aircraft Aeroelasticity and Loads*. 2007.

[49] G. C. (Ed.) Oates, *Aircraft Propulsion Systems Technology and Design*. AIAA Education Series, 1989.

[50] I. Moir and A. Seabridge, *Aircraft Systems: Mechanical, Electrical, and Avionics Subsystems Integration*. John Wiley & Sons, 2011.

[51] C. T. Yucer, "Thermodynamic Analysis of the Part Load Performance for a Small Scale Gas Turbine Jet Engine by Using Exergy Analysis Method," *Energy*, vol. 111, pp. 251–259, Sep. 2016, doi: 10.1016/j.energy.2016.05.108.

[52] R. Atilgan and Onder Turan, "Economy and Exergy of Aircraft Turboprop Engine at Dynamic Loads," *Energy*, vol. 213, p. 118827, Dec. 2020, doi: 10.1016/j.energy.2020.118827.

[53] R. Soni, R. Verma, R. Kumar Garg, and V. Sharma, "A Critical Review of Recent Advances in The Aerospace Materials," *Mater Today Proc*, Aug. 2023, doi: 10.1016/j.matpr.2023.08.108.

[54] E. A. Starke and J. T. Staley, "Application of Modern Aluminum Alloys to Aircraft," *Progress in Aerospace Sciences*, vol. 32, no. 2–3, pp. 131–172, Jan. 1996, doi: 10.1016/0376-0421(95)00004-6.

[55] A. Heinz, A. Haszler, C. Keidel, S. Moldenhauer, R. Benedictus, and W. S. Miller, "Recent Development in Aluminium Alloys for Aerospace Applications," *Materials Science and Engineering: A*, vol. 280, no. 1, pp. 102–107, Mar. 2000, doi: 10.1016/S0921-5093(99)00674-7.

[56] J. C. Williams and E. A. Starke, "Progress in Structural Materials for Aerospace Systems," *Acta Mater*, vol. 51, no. 19, pp. 5775–5799, Nov. 2003, doi: 10.1016/j.actamat.2003.08.023.

[57] P. Rambabu, N. Eswara Prasad, V. V. Kutumbarao, and R. J. H. Wanhill, "Aluminium Alloys for Aerospace Applications," *Aerospace Materials and Material Technologies*, pp. 29–52, Nov. 2016, doi: 10.1007/978-981-10-2134-3_2.

[58] R. K. Gupta, N. Nayan, G. Nagasireesha, and S. C. Sharma, "Development and Characterization of Al–Li Alloys," *Materials Science and Engineering: A*, vol. 420, no. 1–2, pp. 228–234, Mar. 2006, doi: 10.1016/j.msea.2006.01.045.

[59] M. S. Kenevisi, Y. Yu, and F. Lin, "A Review on Additive Manufacturing of Al–Cu (2xxx) Aluminium Alloys, Processes and Defects," *Materials Science and Technology*, vol. 37, no. 9, pp. 805–829, Jun. 2021, doi: 10.1080/02670836.2021.1958487.

[60] J. R. Davis, *Aluminum and Aluminum Alloys*. ASM Specialty Handbook, ASM International, Materials Park, OH, USA, 1994.

[61] N. Akhtar and S. J. Wu, "Macromechanics Study of Stable Fatigue Crack Growth in Al–Cu–Li–Mg–Ag Alloy," *Fatigue Fract Eng Mater Struct*, vol. 40, no. 2, pp. 233–244, Feb. 2017, doi: 10.1111/ffe.12489.

[62] J. S. Warner and R. P. Gangloff, "Alloy Induced Inhibition of Fatigue Crack Growth in Age-Hardenable Al–Cu Alloys," *Int J Fatigue*, vol. 42, pp. 35–44, Sep. 2012, doi: 10.1016/j.ijfatigue.2011.04.013.

[63] *International Alloy Designations and Chemical Composition Limits for Wrought Aluminum and Wrought Aluminum Alloys*. The Aluminium Association, 2018.

[64] P. Dwivedi, A. N. Siddiquee, and S. Maheshwari, "Issues and Requirements for Aluminum Alloys Used in Aircraft Components: State of the Art," *Russian Journal of Non-Ferrous Metals*, vol. 62, no. 2, pp. 212–225, Mar. 2021, doi: 10.3103/S1067821221020048.

[65] S. M. Amer, R. Y. Barkov, and A. V. Pozdniakov, "Effect of Impurities on the Phase Composition and Properties of a Wrought Al–6% Cu–4.05% Er Alloy," *Physics of Metals and Metallography*, vol. 121, no. 5, pp. 495–499, May 2020, doi: 10.1134/S0031918X20050038.

[66] Y. Q. Chen, S. P. Pan, M. Z. Zhou, D. Q. Yi, D. Z. Xu, and Y. F. Xu, "Effects of Inclusions, Grain Boundaries and Grain Orientations on the Fatigue Crack Initiation and Propagation Behavior of 2524-T3 Al Alloy," *Materials Science and Engineering: A*, vol. 580, pp. 150–158, Sep. 2013, doi: 10.1016/j.msea.2013.05.053.

[67] B. Smith, "The Boeing 777: The Development of the Boeing 777 was Made Possible by the Development of Breakthrough Materials that Allowed Reductions in Structural Weight While Maintaining Affordability.," *Advanced Materials & Processes*, vol. 161, no. 9, pp. 41–45, Sep. 2003.

[68] P. J. Golden, A. F. Grandt, and G. H. Bray, "A Comparison of Fatigue Crack Formation at Holes in 2024-T3 and 2524-T3 Aluminum Alloy Specimens," *Int J Fatigue*, vol. 21, pp. S211–S219, Sep. 1999, doi: 10.1016/S0142-1123(99)00073-0.

[69] J. A. Moreto, E. E. Broday, L. S. Rossino, J. C. S. Fernandes, and W. W. Bose Filho, "Effect of Localized Corrosion on Fatigue–Crack Growth in 2524-T3 and 2198-T851 Aluminum Alloys Used as Aircraft Materials," *J Mater Eng Perform*, vol. 27, no. 4, pp. 1917–1926, Apr. 2018, doi: 10.1007/S11665-018-3244-7.

[70] C. A. R. P. Baptista, A. M. L. Adib, M. A. S. Torres, and V. A. Pastoukhov, "Describing Fatigue Crack Growth and Load Ratio Effects in Al 2524 T3 Alloy with an Enhanced Exponential Model," *Mechanics of Materials*, vol. 51, pp. 66–73, Aug. 2012, doi: 10.1016/j.mechmat.2012.04.003.

[71] W. B. Shou, D. Q. Yi, H. Q. Liu, C. Tang, F. H. Shen, and B. Wang, "Effect of Grain Size on the Fatigue Crack Growth Behavior of 2524-T3 Aluminum Alloy," *Archives of Civil and Mechanical Engineering*, vol. 16, no. 3, pp. 304–312, May 2016, doi: 10.1016/j.acme.2016.01.004.

[72] S. G. Pantelakis, A. N. Chamos, and A. T. Kermanidis, "A Critical Consideration for the Use of Al-Cladding for Protecting Aircraft Aluminum Alloy 2024 Against Corrosion," *Theoretical and Applied Fracture Mechanics*, vol. 57, no. 1, pp. 36–42, Feb. 2012, doi: 10.1016/j.tafmec.2011.12.006.

[73] Y. Zuo, P. H. Zhao, and J. M. Mao, "The Influences of Sealing Methods on Corrosion Behavior of Anodized Aluminum Alloys in NaCl Solutions," *Surf Coat Technol*, vol. 166, no. 2–3, pp. 237–242, Mar. 2003, doi: 10.1016/S0257-8972(02)00779-X.

[74] C. Wolverton, L. W. Wang, and A. Zunger, "Coherent Phase Stability in Al-Zn and Al-Cu FCC Alloys: The Role of the Instability of FCC Zn," *Phys Rev B*, vol. 60, no. 24, Dec. 1999, doi: 10.1103/PhysRevB.60.16448.

[75] B. Zhou, B. Liu, and S. Zhang, "The Advancement of 7XXX Series Aluminum Alloys for Aircraft Structures: A Review," *Metals 2021, Vol. 11, Page 718*, vol. 11, no. 5, p. 718, Apr. 2021, doi: 10.3390/met11050718.

[76] V. Jagdale *et al.*, "Experimental Characterization of Load Stiffening Wing for Small UAV," *Society for Experimental Mechanics Annual Conference*, 2007.

[77] O. Stodieck, J. E. Cooper, and P. M. Weaver, "Interpretation of Bending/Torsion Coupling for Swept, Nonhomogenous Wings," *J Aircr*, vol. 53, no. 4, pp. 892–899, Dec. 2015, doi: 10.2514/1.C033186.

[78] M. Drela, "Method for Simultaneous Wing Aerodynamic and Structural Load Prediction," *J Aircr*, vol. 27, no. 8, pp. 692–699, May 2012, doi: 10.2514/3.25342.

[79] B. L. Smith, A. L. Hijazi, and R. Y. Myose, "Strength of 7075-T6 and 2024-T3 Aluminum Panels with Multiple-Site Damage," *J Aircr*, vol. 39, no. 2, pp. 354–358, May 2012, doi: 10.2514/2.2933.

[80] B. B. Verma, J. D. Atkinson, and M. Kumar, "Study of Fatigue Behaviour of 7475 Aluminium Alloy," *Bulletin of Materials Science*, vol. 24, no. 2, pp. 231–236, 2001, doi: 10.1007/bf02710107.

[81] E. U. Lee, A. K. Vasudevan, and G. Glinka, "Environmental Effects on Low Cycle Fatigue of 2024-T351 and 7075-T651 Aluminum Alloys," *Int J Fatigue*, vol. 31, no. 11–12, pp. 1938–1942, Nov. 2009, doi: 10.1016/j.ijfatigue.2008.11.012.

[82] S. M. A. K. Mohammed, A. Albedah, F. Benyahia, and B. B. Bouiadjra, "Effect of Single Tensile Peak Overload on the Performance of Bonded Composite Repair of Cracked Al 2024-T3 and Al 7075-T6 Plates," *Compos Struct*, vol. 193, pp. 260–267, Jun. 2018, doi: 10.1016/j.compstruct.2018.03.069.

[83] C. Kaynak and A. Ankara, "Short Fatigue Crack Growth in Al 2024-T3 and Al 7075-T6," *Eng Fract Mech*, vol. 43, no. 5, pp. 769–778, Nov. 1992, doi: 10.1016/0013-7944(92)90007-2.

[84] C. E. Celik, O. Vardar, and V. Kalenderoglu, "Comparison of Retardation Behaviour of 2024-T3 and 7075-T6 Al Alloys," *Fatigue Fract Eng Mater Struct*, vol. 27, no. 8, pp. 713–722, Aug. 2004, doi: 10.1111/J.1460-2695.2004.00800.X.

[85] D. A. Necşulescu, "The Effects of Corrosion on the Mechanical Properties of Aluminium Alloy 7075-T6," *Bull., Series B*, vol. 73, no. 1, 2011.

[86] A. Bouzekova-Penkova and A. Miteva, "Some Aerospace Applications of 7075 (B95) Aluminium Alloy," *Bulgarian Academy of Sciences-Space Research and Technology Institute-Aerospace Research in Bulgaria*, vol. 34, pp. 165–179, 2022, doi: 10.3897/arb.v34.e15.

[87] R. D. Carter, E. W. Lee, E. A. Starke, and C. J. Beevers, "The Effect of Microstructure and Environment on Fatigue Crack Closure of 7475 Aluminum Alloy," *Metallurgical Transactions A*, vol. 15, no. 3, pp. 555–563, Mar. 1984, doi: 10.1007/BF02644980.

[88] R. Ramos, N. Ferreira, J. A. M. Ferreira, C. Capela, and A. C. Batista, "Improvement in Fatigue Life of Al 7475-T7351 Alloy Specimens by Applying Ultrasonic and Microshot Peening," *Int J Fatigue*, vol. 92, pp. 87–95, Nov. 2016, doi: 10.1016/j.ijfatigue.2016.06.022.

[89] M. T. Jahn and J. Luo, "Tensile and Fatigue Properties of a Thermomechanically Treated 7475 Aluminium Alloy," *J Mater Sci*, vol. 23, no. 11, pp. 4115–4120, Nov. 1988, doi: 10.1007/BF01106845.

[90] P. Lequeu, P. Lassince, T. Warner, and G. M. Raynaud, "Engineering for the Future: Weight Saving and Cost Reduction Initiatives," *Aircraft Engineering and Aerospace Technology*, vol. 73, no. 2, pp. 147–159, 2001, doi: 10.1108/00022660110386663.

[91] E. J. Lavernia and N. J. Grant, "Aluminium-Lithium Alloys," *J Mater Sci*, vol. 22, no. 5, pp. 1521–1529, May 1987, doi: 10.1007/BF01132370.

[92] T. Dorin, A. Vahid, and J. Lamb, "Chapter 11 - Aluminium Lithium Alloys," *Fundamentals of Aluminium Metallurgy: Recent Advances*, pp. 387–438, Jan. 2018, doi: 10.1016/B978-0-08-102063-0.00011-4.

[93] S. Ud Din *et al.*, "The Synergistic Effect of Li Addition on Microstructure, Texture and Mechanical Properties of Extruded Al–Mg–Si Alloys," *Mater Chem Phys*, vol. 174, pp. 11–22, May 2016, doi: 10.1016/j.matchemphys.2016.02.029.

[94] M. P. Alam and A. N. Sinha, "Fabrication of Third Generation Al–Li Alloy by Friction Stir Welding: A Review," *Sadhana - Academy Proceedings in Engineering Sciences*, vol. 44, no. 6, pp. 1–13, Jun. 2019, doi: 10.1007/S12046-019-1139-4.

[95] D. Y. Rasposienko, L. I. Kaigorodova, V. G. Pushin, and Y. M. Ustugov, "Multicomponent Aging Al-Li-Based Alloys of the Latest Generation: Structural and Phase Transformations, Treatments, Properties, and Future Prospects," *Materials 2022, Vol. 15, Page 4190*, vol. 15, no. 12, p. 4190, Jun. 2022, doi: 10.3390/ma15124190.

[96] R. J. Rioja and J. Liu, "The Evolution of Al-Li Base Products for Aerospace and Space Applications," *Metall Mater Trans A Phys Metall Mater Sci*, vol. 43, no. 9, pp. 3325–3337, Sep. 2012, doi: 10.1007/S11661-012-1155-Z.

[97] S. fei Zhang, W. dong Zeng, W. hua Yang, C. ling Shi, and H. jun Wang, "Ageing Response of a Al–Cu–Li 2198 Alloy," *Mater Des*, vol. 63, pp. 368–374, Nov. 2014, doi: 10.1016/j.matdes.2014.04.063.

[98] R. Sepe, V. Giannella, N. Razavi, and F. Berto, "Characterization of Static, Fatigue and Fracture Behaviour of the Aluminium-Lithium Alloy Al-Li 2198-T851," *Int J Fatigue*, vol. 166, p. 107265, Jan. 2023, doi: 10.1016/j.ijfatigue.2022.107265.

[99] N. D. Alexopoulos, E. Migklis, A. Stylianos, and D. P. Myriounis, "Fatigue Behavior of the Aeronautical Al–Li (2198) Aluminum Alloy Under Constant Amplitude Loading," *Int J Fatigue*, vol. 56, pp. 95–105, Nov. 2013, doi: 10.1016/j.ijfatigue.2013.07.009.

[100] X. Zhang, W. Yang, and R. Xiao, "Microstructure and Mechanical Properties of Laser Beam Welded Al–Li Alloy 2060 with Al–Mg Filler Wire," *Mater Des*, vol. 88, pp. 446–450, Dec. 2015, doi: 10.1016/j.matdes.2015.08.144.

[101] B. Bodily, M. Heinimann, G. Bray, E. Colvin, and J. Witters, "Advanced Aluminum and Aluminum-Lithium Solutions for Derivative and Next Generation Aerospace Structures," *SAE Technical Papers*, vol. 6, Sep. 2012, doi: 10.4271/2012-01-1874.

[102] X. Zhang, T. Huang, W. Yang, R. Xiao, Z. Liu, and L. Li, "Microstructure and Mechanical Properties of Laser Beam-Welded AA2060 Al-Li Alloy," *J Mater Process Technol*, vol. 237, pp. 301–308, Nov. 2016, doi: 10.1016/j.jmatprotec.2016.06.021.

[103] R. J. H. Wanhill, "Aerospace Applications of Aluminum–Lithium Alloys," *Aluminum-Lithium Alloys: Processing, Properties, and Applications*, pp. 503–535, Jan. 2014, doi: 10.1016/B978-0-12-401698-9.00015-X.

[104] M. J. Krane, A. Jardy, R. L. Williamson, and J. J. Beaman, "Proceedings of the 2013 International Symposium on Liquid Metal Processing and Casting (LMPC)," John Wiley & Sons, Oct. 2013.

[105] R. R. Boyer, "Titanium for Aerospace: Rationale and Applications," *Advanced Performance Materials*, vol. 2, no. 4, pp. 349–368, Oct. 1995, doi: 10.1007/BF00705316.

[106] P. Singh, H. Pungotra, and N. S. Kalsi, "On the Characteristics of Titanium Alloys for the Aircraft Applications," *Mater Today Proc*, vol. 4, no. 8, pp. 8971–8982, Jan. 2017, doi: 10.1016/j.matpr.2017.07.249.

[107] M. Peters, J. Kumpfert, C. H. Ward, and C. Leyens, "Titanium Alloys for Aerospace Applications," *Adv Eng Mater*, vol. 5, no. 6, pp. 419–427, Jun. 2003, doi: 10.1002/adem.200310095.

[108] I. Weiss and S. L. Semiatin, "Thermomechanical Processing of Alpha Titanium Alloys—An Overview," *Materials Science and Engineering: A*, vol. 263, no. 2, pp. 243–256, May 1999, doi: 10.1016/S0921-5093(98)01155-1.

[109] de L. Gasperetti and L. Fernando, "Usage of Titanium Alloys in Airframes: Current Situation and Future," *SAE Technical Papers*, Oct. 2011, doi: 10.4271/2011-36-0248.

[110] J. P. Davim, C. Veiga, J. P. Davim, and A. J. R. Loureiro, "Properties and Applications of Titanium Alloys: A Brief Review," *Rev. Adv. Mater. Sci.*, vol. 32, pp. 14–34, Dec. 2012.

[111] X. J. Jiang, R. Jing, C. Y. Liu, M. Z. Ma, and R. P. Liu, "Structure and Mechanical Properties of TiZr Binary Alloy After Al Addition," *Materials Science and Engineering: A*, vol. 586, pp. 301–305, Dec. 2013, doi: 10.1016/j.msea.2013.08.029.

[112] R. R. Boyer, "Aerospace Applications of Beta Titanium Alloys," *JOM*, vol. 46, no. 7, pp. 20–23, Jul. 1994, doi: 10.1007/BF03220743.

[113] R. R. Boyer and R. D. Briggs, "The Use of β Titanium Alloys in the Aerospace Industry," *J Mater Eng Perform*, vol. 14, no. 6, pp. 681–685, Dec. 2005, doi: 10.1361/105994905X75448.

[114] Y. G. Zhou, W. D. Zeng, and H. Q. Yu, "An Investigation of a New Near-Beta Forging Process for Titanium Alloys and its Application in

Aviation Components," *Materials Science and Engineering: A*, vol. 393, no. 1–2, pp. 204–212, Feb. 2005, doi: 10.1016/j.msea.2004.10.016.

[115] W. Jia, W. Zeng, J. Liu, Y. Zhou, and Q. Wang, "On the Influence of Processing Parameters on Microstructural Evolution of a Near Alpha Titanium Alloy," *Materials Science and Engineering: A*, vol. 530, no. 1, pp. 135–143, Dec. 2011, doi: 10.1016/j.msea.2011.09.064.

[116] I. Gurrappa, "Characterization of Titanium Alloy Ti-6Al-4V for Chemical, Marine and Industrial Applications," *Mater Charact*, vol. 51, no. 2–3, pp. 131–139, Oct. 2003, doi: 10.1016/j.matchar.2003.10.006.

[117] R. P. L. Nijssen, *Composite Materials: An Introduction*. Toray Advanced Composites, 2015.

[118] T. W. Clyne and D. Hull, *An Introduction to Composite Materials*, 3rd ed. Cambridge University Press, 2019.

[119] K. K. Chawla, *Composite Materials: Science and Engineering*, 3rd ed. Springer Science & Business Media, 2012.

[120] R. M. Christensen, *Mechanics of Composite Materials*. Courier Corporation, 2012.

[121] B. Harris, *Engineering Composite Materials*. The Institute of Materials, 1999.

[122] F. Klocke, M. Zeis, A. Klink, and D. Veselovac, "Experimental Research on the Electrochemical Machining of Modern Titanium- and Nickel-based Alloys for Aero Engine Components," *Procedia CIRP*, vol. 6, pp. 368–372, Jan. 2013, doi: 10.1016/j.procir.2013.03.040.

[123] C. Pany, "An Insight on the Estimation of Wave Propagation Constants in an Orthogonal Grid of a Simple Line-Supported Periodic Plate Using a Finite Element Mathematical Model," *Front Mech Eng*, vol. 8, p. 926559, Jul. 2022, doi: 10.3389/FMECH.2022.926559.

[124] C. Pany, "Panel Flutter Numerical Study of Thin Isotropic Flat Plates and Curved Plates with Various Edge Boundary Conditions," *Journal of Polytechnic*, vol. 26, no. 4, pp. 1467–1473, Dec. 2023, doi: 10.2339/POLITEKNIK.1139958.

[125] M. Nurazzi, A. Khalina, S. M. Sapuan, D. Laila, M. Rahmah, and Z. Hanafee, "A Review: Fibres, Polymer Matrices and Composites," *Pertanika J. Sci. & Technol*, vol. 25, no. 4, pp. 1085–1102, 2017.

[126] D. D. L. Chung, "A Review of Multifunctional Polymer-Matrix Structural Composites," *Compos B Eng*, vol. 160, pp. 644–660, Mar. 2019, doi: 10.1016/j.compositesb.2018.12.117.

[127] N. H. Mostafa, Z. N. Ismarrubie, S. M. Sapuan, and M. T. H. Sultan, "Fibre Prestressed Polymer-Matrix Composites: A Review," *J Compos Mater*, vol. 51, no. 1, pp. 39–66, Mar. 2016, doi: 10.1177/0021998316637906.

[128] R. Hsissou, R. Seghiri, Z. Benzekri, M. Hilali, M. Rafik, and A. Elharfi, "Polymer Composite Materials: A Comprehensive Review," *Compos Struct*, vol. 262, p. 113640, Apr. 2021, doi: 10.1016/j.compstruct.2021.113640.

[129] S. Huang, Q. Fu, L. Yan, and B. Kasal, "Characterization of Interfacial Properties Between Fibre and Polymer Matrix in Composite Materials – A Critical Review," *Journal of Materials Research and Technology*, vol. 13, pp. 1441–1484, Jul. 2021, doi: 10.1016/j.jmrt.2021.05.076.

[130] M. A. Shaid Sujon, A. Islam, and V. K. Nadimpalli, "Damping and Sound Absorption Properties of Polymer Matrix Composites: A Review," *Polym Test*, vol. 104, p. 107388, Dec. 2021, doi: 10.1016/j.polymertesting.2021.107388.

[131] T. D. Fornes, P. J. Yoon, and D. R. Paul, "Polymer Matrix Degradation and Color Formation in Melt Processed Nylon 6/Clay Nanocomposites," *Polymer (Guildf)*, vol. 44, no. 24, pp. 7545–7556, Nov. 2003, doi: 10.1016/j.polymer.2003.09.034.

[132] C. Liang, Z. Gu, Y. Zhang, Z. Ma, H. Qiu, and J. Gu, "Structural Design Strategies of Polymer Matrix Composites for Electromagnetic Interference Shielding: A Review," *Nano-Micro Letters 2021*, vol. 13, no. 1, p. 181, Aug. 2021, doi: 10.1007/S40820-021-00707-2.

[133] N. Balasubramanian, K. Babu, and T. Ramesh, "Role, Effect, and Influences of Micro and Nano-Fillers on Various Properties of Polymer Matrix Composites for Microelectronics: A Review," *Polym Adv Technol*, vol. 29, no. 6, pp. 1568–1585, Jun. 2018, doi: 10.1002/pat.4280.

[134] N. Balasubramanian, K. Babu, and T. Ramesh, "Role, Effect, and Influences of Micro and Nano-Fillers on Various Properties of Polymer Matrix Composites for Microelectronics: A Review," *Polym Adv Technol*, vol. 29, no. 6, pp. 1568–1585, Jun. 2018, doi: 10.1002/pat.4280.

[135] K. Niendorf and B. Raeymaekers, "Additive Manufacturing of Polymer Matrix Composite Materials with Aligned or Organized Filler Material: A Review," *Adv Eng Mater*, vol. 23, no. 4, p. 2001002, Apr. 2021, doi: 10.1002/adem.202001002.

[136] M. Biron, *Thermoplastics and Thermoplastic Composites*. William Andrew, 2018.

[137] A. Goren and C. Atas, "Manufacturing of Polymer Matrix Composites Using Vacuum Assisted Resin Infusion Molding," *Archives of Materials Science and Engineering*, vol. 34, no. 2, pp. 117–120, 2008.

[138] C. Barile, C. Casavola, and F. De Cillis, "Mechanical Comparison of New Composite Materials for Aerospace Applications," *Compos B Eng*, vol. 162, pp. 122–128, Apr. 2019, doi: 10.1016/j.compositesb.2018.10.101.

[139] V. Goodship, "Recycling Issues in Polymer Matrix Composites," *Failure Mechanisms in Polymer Matrix Composites*, pp. 337–367, Jan. 2012, doi: 10.1533/9780857095329.2.337.

[140] I. Delvere, M. Iltina, M. Shanbayev, A. Abildayeva, S. Kuzhamberdieva, and D. Blumberga, "Evaluation of Polymer Matrix Composite Waste Recycling Methods," *Environmental and Climate Technologies*, vol. 23, no. 1, pp. 168–187, 2019, doi: 10.2478/rtuect-2019-0012.

[141] S. Pimenta and S. T. Pinho, "Recycling Carbon Fibre Reinforced Polymers for Structural Applications: Technology Review and Market Outlook," *Waste Management*, vol. 31, no. 2, pp. 378–392, Feb. 2011, doi: 10.1016/j.wasman.2010.09.019.

[142] R. Yadav, M. Tirumali, X. Wang, M. Naebe, and B. Kandasubramanian, "Polymer Composite for Antistatic Application in Aerospace," *Defence Technology*, vol. 16, no. 1, pp. 107–118, Feb. 2020, doi: 10.1016/j.dt.2019.04.008.

[143] A. L. Zolkin, S. A. Galanskiy, and A. M. Kuzmin, "Perspectives for Use of Composite and Polymer Materials in Aircraft Construction," *IOP Conf Ser Mater Sci Eng*, vol. 1047, no. 1, Feb. 2021, doi: 10.1088/1757-899X/1047/1/012023.

[144] M. H. Al-Saleh and U. Sundararaj, "Review of the Mechanical Properties of Carbon Nanofiber/Polymer Composites," *Compos Part A Appl Sci Manuf*, vol. 42, no. 12, pp. 2126–2142, Dec. 2011, doi: 10.1016/j.compositesa.2011.08.005.

[145] E. C. Botelho, Figiel, M. C. Rezende, and B. Lauke, "Mechanical behavior of carbon fiber reinforced polyamide composites," *Compos Sci Technol*, vol. 63, no. 13, pp. 1843–1855, Oct. 2003, doi: 10.1016/S0266-3538(03)00119-2.

[146] A. Mortensen and J. Llorca, "Metal Matrix Composites," *Annu Rev Mater Res*, vol. 40, pp. 243–270, Aug. 2010, doi: 10.1146/annurev-matsci-070909-104511.

[147] J. W. Kaczmar, K. Pietrzak, and W. Wlosiński, "The Production and Application of Metal Matrix Composite Materials," *J Mater Process*

Technol, vol. 106, no. 1–3, pp. 58–67, Oct. 2000, doi: 10.1016/S0924-0136(00)00639-7.

[148] J. Liu, J. Li, and C. Xu, "Interaction of the Cutting Tools and the Ceramic-Reinforced Metal Matrix Composites During Micro-Machining: A Review," *CIRP J Manuf Sci Technol*, vol. 7, no. 2, pp. 55–70, Jan. 2014, doi: 10.1016/j.cirpj.2014.01.003.

[149] Q. Shi *et al.*, "A Review of Recent Developments in Si/C Composite Materials for Li-Ion Batteries," *Energy Storage Mater*, vol. 34, pp. 735–754, Jan. 2021, doi: 10.1016/j.ensm.2020.10.026.

[150] W. X. Wang, Y. Takao, and T. Matsubara, "Tensile Strength and Fracture Toughness of C/C and Metal Infiltrated Composites Si–C/C and Cu–C/C," *Compos Part A Appl Sci Manuf*, vol. 39, no. 2, pp. 231–242, Feb. 2008, doi: 10.1016/j.compositesa.2007.11.004.

[151] G. G. Chernyshov, S. A. Panichenko, and T. A. Chernyshova, "Welding of Metal Composites," *Welding International*, vol. 17, no. 6, pp. 487–492, 2003, doi: 10.1533/wint.2003.3155.

[152] T. Prater, "Friction Stir Welding of Metal Matrix Composites for Use in Aerospace Structures," *Acta Astronaut*, vol. 93, pp. 366–373, Jan. 2014, doi: 10.1016/j.actaastro.2013.07.023.

[153] M. Malaki *et al.*, "Advanced Metal Matrix Nanocomposites," *Metals (Basel)*, vol. 9, no. 3, p. 330, Mar. 2019, doi: 10.3390/met9030330.

[154] H. Ferkel and B. L. Mordike, "Magnesium Strengthened by SiC Nanoparticles," *Materials Science and Engineering: A*, vol. 298, no. 1–2, pp. 193–199, Jan. 2001, doi: 10.1016/S0921-5093(00)01283-1.

[155] M. Bekmezci, D. B. Subasi, R. Bayat, M. Akin, Z. K. Coguplugil, and F. Sen, "Synthesis of a functionalized carbon supported platinum–iridium nanoparticle catalyst by the rapid chemical reduction method for the anodic reaction of direct methanol fuel cells," *New Journal of Chemistry*, vol. 46, no. 45, pp. 21591–21598, Nov. 2022, doi: 10.1039/D2NJ03209K.

[156] R. Bayat, M. Akin, B. Yilmaz, M. Bekmezci, M. Bayrakci, and F. Sen, "Biogenic platinum based nanoparticles: Synthesis, characterization and their applications for cell cytotoxic, antibacterial effect, and direct alcohol fuel cells," *Chemical Engineering Journal Advances*, vol. 14, p. 100471, May 2023, doi: 10.1016/j.ceja.2023.100471.

[157] M. Bekmezci, R. Bayat, V. Erduran, and F. Sen, "Biofunctionalization of functionalized nanomaterials for electrochemical sensors," *Functionalized Nanomaterial-Based Electrochemical Sensors: Principles, Fabrication Methods, and Applications*, pp. 55–69, Jan. 2022, doi: 10.1016/B978-0-12-823788-5.00003-X.

[158] Y. Wu *et al.*, "Hydrogen generation from methanolysis of sodium borohydride using waste coffee oil modified zinc oxide nanoparticles and their photocatalytic activities," *Int J Hydrogen Energy*, vol. 48, no. 17, pp. 6613–6623, Feb. 2023, doi: 10.1016/j.ijhydene.2022.04.177.

[159] B. Yilmaz, R. Bayat, M. Bekmezci, and F. Şen, "Metal organic framework-based nanocomposites for alcohol fuel cells," *Nanomaterials for Direct Alcohol Fuel Cells: Characterization, Design, and Electrocatalysis*, pp. 353–370, Jan. 2021, doi: 10.1016/B978-0-12-821713-9.00006-8.

[160] M. Bekmezci, R. Bayat, M. Akin, Z. K. Coguplugil, and F. Sen, "Modified screen-printed electrochemical biosensor design compatible with mobile phones for detection of miR-141 used to pancreatic cancer biomarker," *Carbon Letters*, vol. 33, no. 6, pp. 1863–1873, Oct. 2023, doi: 10.1007/S42823-023-00545-9.

[161] R. Bayat, M. Bekmezci, M. Akin, I. Isik, and F. Sen, "Nitric Oxide Detection Using a Corona Phase Molecular Recognition Site on Chiral Single-Walled Carbon Nanotubes," *ACS Appl Bio Mater*, vol. 6, no. 11, pp. 4828–4835, Nov. 2023, doi: 10.1021/acsabm.3c00573.

[162] E. Omanović-Mikličanin, A. Badnjević, A. Kazlagić, and M. Hajlovac, "Nanocomposites: A Brief Review," *Health Technol (Berl)*, vol. 10, no. 1, pp. 51–59, Jan. 2020, doi: 10.1007/S12553-019-00380-X.

[163] N. K. Yusuf, A. S. Medi, M. A. Lajis, B. L. Chan, and S. Shamsudin, "Mechanical Properties of Direct Recycling Metal Matrix Composite (MMC-AlR) AA7075 Aircraft Aluminium Alloy," *International Journal of Integrated Engineering*, vol. 13, no. 7, pp. 89–94, Sep. 2021, doi: 10.30880/ijie.2021.13.07.011.

[164] J. Joel and M. Anthony Xavior, "Aluminium Alloy Composites and its Machinability studies; A Review," *Mater Today Proc*, vol. 5, no. 5, pp. 13556–13562, Jan. 2018, doi: 10.1016/j.matpr.2018.02.351.

[165] P. Spriet, "CMC Applications to Gas Turbines," *Ceramic Matrix Composites: Materials, Modeling and Technology*, pp. 591–608, Nov. 2014, doi: 10.1002/9781118832998.ch21.

[166] I. Ahmad, B. Yazdani, and Y. Zhu, "Recent Advances on Carbon Nanotubes and Graphene Reinforced Ceramics Nanocomposites," *Nanomaterials 2015, Vol. 5, Pages 90-114*, vol. 5, no. 1, pp. 90–114, Jan. 2015, doi: 10.3390/NANO5010090.

[167] J. D. Kiser, J. E. Grady, R. T. Bhatt, V. L. Wiesner, and D. Zhu, "Overview of CMC (Ceramic Matrix Composite) Research at the NASA Glenn Research Center," 2016.

[168] W. Krenkel, *Ceramic Matrix Composites: Fiber Reinforced Ceramics and their Applications*. John Wiley and Sons, 2008. doi: 10.1002/9783527622412.

[169] S. Schmidt, S. Beyer, H. Knabe, H. Immich, R. Meistring, and A. Gessler, "Advanced Ceramic Matrix Composite Materials for Current and Future Propulsion Technology Applications," *Acta Astronaut*, vol. 55, no. 3–9, pp. 409–420, Aug. 2004, doi: 10.1016/j.actaastro.2004.05.052.

[170] Q. Li *et al.*, "A Study of the Hot Salt Corrosion Behavior of Three Nickel-Based Single-Crystal Superalloys at 900 °C," *Crystals (Basel)*, vol. 14, no. 4, p. 307, Mar. 2024, doi: 10.3390/CRYST14040307.

[171] J. Liu, H. Yan, and K. Jiang, "Mechanical Properties of Graphene Platelet-Reinforced Alumina Ceramic Composites," *Ceram Int*, vol. 39, no. 6, pp. 6215–6221, Aug. 2013, doi: 10.1016/j.ceramint.2013.01.041.

[172] D. L. McDanels, T. T. Serafini, and J. A. DiCarlo, "Polymer, Metal, and Ceramic Matrix Composites for Advanced Aircraft Engine Applications," *Journal of Materials for Energy Systems*, vol. 8, no. 1, pp. 80–91, Jun. 1986, doi: 10.1007/BF02833463.

[173] G. Canale, F. Rubino, and R. Citarella, "Design Aspects of a CMC Coating-Like System for Hot Surfaces of Aero Engine Components," *Forces in Mechanics*, vol. 14, p. 100251, Feb. 2024, doi: 10.1016/j.finmec.2023.100251.

[174] S. Fan *et al.*, "Progress of Ceramic Matrix Composites Brake Materials for Aircraft Application," *Rev. Adv. Mater. Sci.*, vol. 44, pp. 313–325, 2016.

[175] H. Ohnabe, S. Masaki, M. Onozuka, K. Miyahara, and T. Sasa, "Potential Application of Ceramic Matrix Composites to Aero-Engine

Components," *Compos Part A Appl Sci Manuf*, vol. 30, no. 4, pp. 489–496, Apr. 1999, doi: 10.1016/S1359-835X(98)00139-0.

[176] Y. Gowayed, G. Ojard, E. Prevost, U. Santhosh, and G. Jefferson, "Defects in Ceramic Matrix Composites and Their Impact on Elastic Properties," *Compos B Eng*, vol. 55, pp. 167–175, Dec. 2013, doi: 10.1016/j.compositesb.2013.06.026.

[177] O. G. Diaz, G. G. Garcia Luna, Z. Liao, and D. Axinte, "The New Challenges of Machining Ceramic Matrix Composites (CMCs): Review of Surface Integrity," *Int J Mach Tools Manuf*, vol. 139, pp. 24–36, Apr. 2019, doi: 10.1016/j.ijmachtools.2019.01.003.

[178] Q. An, J. Chen, W. Ming, and M. Chen, "Machining of SiC Ceramic Matrix Composites: A Review," *Chinese Journal of Aeronautics*, vol. 34, no. 4, pp. 540–567, Apr. 2021, doi: 10.1016/j.cja.2020.08.001.

[179] R. R. Naslain, "The Design of the Fibre-Matrix Interfacial Zone in Ceramic Matrix Composites," *Compos Part A Appl Sci Manuf*, vol. 29, no. 9–10, pp. 1145–1155, Jan. 1998, doi: 10.1016/S1359-835X(97)00128-0.